# Terahertz Desorption Emission Spectroscopy

## Thesis

The Open University

# Terahertz Desorption Emission Spectroscopy

Submitted for the degree of Doctor of Philosophy

in Astronomy

Mr. Olivier Auriacombe

The Open University

In collaboration with the Rutherford Appleton Laboratory

Date of submission : 29th November 2018

**Abstract**

Enhancing our understanding of the formation and evolution of the Universe is strongly dependent upon the observation of matter that exists between the stars and that forms the interstellar medium (ISM). Using Radio-telescopes based on heterodyne detection (such as ALMA), nearly 200 molecules have been detected. Whilst molecules, such as $H_2O$ and $CH_3OH$, can only form in the solid state, the formation of complex organic molecules is not fully known. Moreover many simple species desorb from ices during the star formation process being useful tracers of these astronomical processes, but only if the thermal and non-thermal desorption mechanisms are fully understood.

In this thesis, I have designed, developed, built and proven a new experimental technique, namely Terahertz Desorption Emission Spectroscopy (THz-DES). The basis of THz-DES is to recreate the chemical conditions found in interstellar environments by emulating the astronomical detection techniques. The emission spectroscopy is based on the integration of a total-power Schottky-barrier based radiometer operating between 320-350 GHz (overlapping with ALMA band 7), coupled to a vacuum chamber where interstellar ice analogues can be grown on a 77 K cold-finger, then thermally desorbed, enabling the gas-ice synergy to identify molecular spectra and desorption energies.

I demonstrate the versatility of the technique observing thermal desorption from pure, layered or mixed ices of nitrous oxide, water and methanol. The results are compared to existing literature values of the desorption energies, and the known spectral features. Finally, there is some evidence that certain energy levels of desorbing species are under-populated relative to the population expected in local thermodynamic equilibrium conditions. This impact of surface constrains on the dynamics and internal energy of desorbing molecules, largely ignored in astronomy, shows interesting promise for the future of the THz-DES technique.

# Acknowledgements

Firstly, thank you to my supervisors Dr. Helen Fraser, Prof. Brian Ellison and Dr. Sergio Ioppolo for all their help and support during my PhD. I would especially like to thank Helen for her scientific assistance and knowledge and her help throughout my PhD. Thank you very much Brian for sharing your knowledge and passion on radio-astronomy technology but also for giving me the opportunity to pursue my career with the MMT group on exciting projects. Thank you Sergio for supporting me at Caltech, bringing me with you to FELIX and correcting my writing. I would also like to give a very, very special thanks to my friend and master, Dr. Simon Rea, without whom nothing would have been possible in the lab. and outside, I owe you a lot.

To Pawala, Dan and Aasia who gave precious comments, Diego for enduring my late lamentations and for our weekend's coffee breaks and to Andre for wading with style and panache. Thank you all for reading through my Frenglish but most importantly for your friendships. To the Wayback Crew, Andrew, Chris, Angus, Colin, Fi, Nart, Adrian, Test-E David, thank you for making me feel at home and for the 'unforgettable' time here. GRE-team, Fox-team, Centipede-team, thank you so much for being such great friends, providing very memorable moments and I am sure there are more to come: la jabbagarre! Antho, à toi de jouer! Piebro et Dr. Petru, thank you so much for all the London fun! Merci Max, Margot, François et Clara, pour tout nos moments forts ces dernières années sur Vannes. Thank you to the popolian potato bag for cooking such amazing cakes, it has kept me going through the tsunami of Paté Henaff and those long dark nights. Finalement, Merci Thibaut, Papa et Maman pour votre soutien inconditionnel tout au long de mon périple doctoral et de globe-trotteur.

*There is no way around hard work. Embrace it.*

*by Roger Federer*

# Contents

# Acronyms

**ADCs** Analog-to-degital converters. 67

**AGB** Asymptotic Giant Branch. 36

**ALMA** Atacama Large Millimeter Array. 33, 51

**BT** Brightness temperature. 88

**CCDs** Charge-coupled devices. 67

**CDMS** Cologne Databse for Molecular Spectroscopy. 36

**COMs** Complex organic molecules. 35

**CSM** Circumstellar Medium. 42

**DSB** Double-Sideband. 78

**ESA** European Space Agency. 51

**FFT** Fast Fourier Transform. 66

**FWHM** Full width at half maximum. 65

**HCN** Hydrogen cyanide. 36

**HEB** Hot Electron Bolomters. 52, 73

**IF** Intermediate Frequency. 72

**IQ** In-phase Quadrature. 68

**ISM** Interstellar medium. 31

**JPL** Jet Propulsion Laboratory. 43

**LNA** Low noise amplifier. 79

**LO** Local Oscillator. 52

**LSB** Lower-Sideband. 77

**LTE** Local Thermodynamic Equilibrium. 68

**OAP** Off-axis parabolic. 118

**QMS** Quadrupole mass spectrometer. 45

**RAIRS** Reflection Absorption Infra-Red Spectroscopy. 45

**RF** Radio Frequency. 76

**RFM** Reference Forward Model. 203

**RGB** Red Giant Branch. 36

**SHM** Sub-harmonic mixer. 78

**SIS** Superconductor-Insulator-Superconductor. 52, 73

**SSB** Single-Sideband. 78

**THz-DES** Terahertz Desorption Emission Spectroscopy. 31, 99

**TPD** Temperature Programmed desorption. 45, 95

**UHV** Ultra-High Vacuum. 45

**USB** Upper-Sideband. 77

**VCOs** Voltage controlled oscillators. 114

**WBS** WideBand Spectrometer. 111

# List of Figures

# List of Tables

# Chapter 1

# Introduction

## 1.1 Thesis Overview

In this thesis, I present a novel laboratory experiment I have designed, built and exploited, called **Terahertz Desorption Emission Spectroscopy (THz-DES)**. The title of the experimental system is descriptive of the nature of the system and each element of the terminology is briefly described as follows. **Terahertz** (THz) frequency electromagnetic radiation encompasses the frequency range 300 GHz to 3 THz. In terms of equivalent wavelength, this corresponds to 1 mm to 0.1 mm, i.e. the longer wavelength portion of the submillimetre-wave spectral region. **Desorption** is a process in which molecular species located on a surface transit directly from the solid to gaseous phase, i.e. omitting the liquid state. This process also called sublimation generally occurs under vacuum conditions. In space, particularly in the space between stars, i.e. the so-called 'interstellar medium' (ISM), desorption of species from icy dust grains is a key process that enriches the gas phase with a large variety of molecules including organic complex and pre-biotic species. Most of the complex molecular species detected to date in the gas phase in the ISM are indeed thought to originate from reactions in the ice mantle of dust particles in star forming regions. Thermal and non-thermal processes are believed to cause the desorption of species from the

solid phase. In warmer regions of the ISM (e.g. hot cores and hot corinos), thermal desorption is most likely the mechanism leading grains to eventually loose completely their ice mantle, especially at temperatures higher than 100 K. In dense cold interstellar clouds (T = 10-20 K), thermal processing is negligible, therefore other (non-thermal) mechanisms are needed to explain the presence of complex species in the gas phase. Depending on the desorption process at play, molecules can sublimate in a ro-vibrational excited state different from the ground state (i.e. population of energy levels other than the ground state). Excited gas-phase species will then relax by emitting photons during their transition from an excited state to a lower energy state. In the ISM, low order transitions are excited, emitting signals in the Terahertz frequency range. To observe those electromagnetic **emissions** from species coming off interstellar ice analogues, a total-power radiometer can be used in laboratory experiments against a cold background signal. This technique provides **spectroscopic** information on the molecules desorbing the ice.

The THz-DES is the first ever laboratory experiment to look at direct spectroscopic emission of desorbed species in the Terahertz region. The long term aim of the experiment is:

1. to detect desorbing molecules as a function of ice temperature to investigate thermal desorption with unprecedented detail.

2. to identify whether desorption, especially non-thermal processes, lead to notable excitation of molecules.

3. to identify differences in spin-dominated low energy spectroscopic features, such ortho- para- or A- E- transitions, related to formation and/or desorption.

The THz-DES technique has therefore the potential to move the laboratory astrochemistry field forward by providing complementary information that are traditionally hard to retrieve from conventional experimental techniques employed

in ice-laboratory astrophysics. Moreover the operational frequency of the THz-DES has the advantage of mirroring present telescope frequencies, e.g. Atacama Large Millimetre Array (ALMA) or Herschel Observatory, or future spaceborn instruments. Thus THz-DES data can be used to better interpret observations. Moreover, THz-DES provides absolute intensity measurements, so that the population distribution of the desorbing molecules can be quantitatively determined. The technology used for this new experiment, explained in details in Chapter 2, is based on Schottky-barrier diodes. The main advantage of using Schottky diodes in heterodyne instruments is that they can operate at room temperature making the radiometer design compact without the use of a complex cryogenic system.

The work in this thesis aims at answering questions such: *'Can we design, build and exploit an experiment to emulate the way astronomers detect the gas-phase behaviour of molecules desorbing from interstellar ices, to better understand the gas-ice synergy in interstellar regions? In other words can we build an "ALMA in the Lab"?'*. This thesis describes the steps toward the design, construction, use and potential future applications of a system such a THz-DES. However first, it is of paramount importance to put this work in a astrophysical context. Therefore below a short introduction to the astrochemical topics linked to the subject of the thesis.

## 1.2 The Interstellar Medium

The interstellar medium is defined as the space and material in between distinct star systems in a galaxy. It is composed of silicate and carbon dust particles for about 1% and gaseous molecules for the remaining 99% in mass. Gas phase molecules are predominately hydrogen (90%), helium (8%) and 2% of heavier species.

### 1.2.1 The Stellar Life Cycle

According to Prof. H. Reeves, *'Nous sommes tous des poussières d'étoiles'*, we are all stardust. All molecules from which we are formed have roots in star forming regions. The formation of stars and planets is a process also called 'cycle of dust' and starts in the diluted ISM, leads to the formation of a planetary system with a protostar and eventually ends with the death of the star that re-injects the materials into the ISM to feed new forming stars. The evolution of star forming regions depends on the initial total available mass of the system and therefore is linked to the mass of the star (i.e. high vs low-mass star formation regions). Here, only the cycle of solar-type, i.e. low-mass, stars is discussed and can be seen in Fig. 1.1.

Star formation is a long and complicated process well described by Shu et al.[261]. Since it is a cycle, the starting point can be chosen arbitrary. However, conventionally the cycle of matter starts in the diffuse ISM (see Fig. 1.1). In the first step, stellar winds and/or explosions enrich the diffuse interstellar medium in dust and gas. Supernova shocks can trigger the collapse of diffuse clouds into dense clouds. Typically, interstellar grains pass through different phases of the interstellar medium (e.g., from diffuse to dense ISM) several times on a typical scale of $\sim 3 \times 10^7$ years, before they take part in the formation of a new star.

Molecular clouds made of silicate and carbonaceous grains and gaseous materials (H, He and heavier elements) present temperatures varying between 10 and 100 K with molecular densities of $10^2 - 10^7$ molecules/cm$^3$. UV radiation and cosmic rays interacting with gas and dust are permanently destroying bonds between molecules. However in areas of the cloud with enough density ($10^5 - 10^7$ molecules/cm$^3$), dust grains can shield molecules and protect them from external UV radiation coming from field stars. Gas-phase interactions would convert species into simple molecules such as CO and unsaturated chains. It should be noted that $H_2$ is an exception because although it is the simplest molecule, it

has been proven to form efficiently in the solid phase on dust grains in molecular clouds through surface reactions. In dense molecular clouds, the low temperatures (10 - 20 K) and high densities ($10^6$–$10^7$) of the environment allow molecules to freeze-out onto the dust grains enhancing solid state chemistry that leads to the formation of molecules such as $H_2O$, $CO_2$, $NH_3$, $CH_4$, $CH_3OH$ and even more complex organic molecules (COMs) [271]. The composition and evolution of interstellar ices are explained in more details in Section 1.2.2.

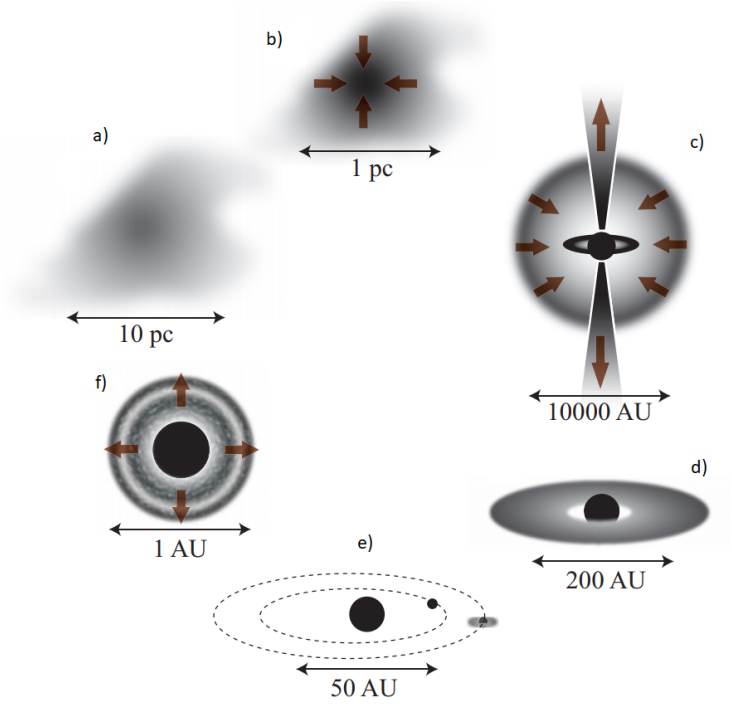


Figure 1.1: Cycle of matter or star formation from a planetary system, such as the Solar System (e). After the death of the star (f), molecular elements and dust particles are diffused in the ISM (a). A dense cloud (b) will collapse due to its own gravitational force to create a new-born protostar (c). At the end of this mechanism, the cloud around the star will disperse and only an accretion disk will remain (d). Collisions and interactions within the accretion disk will form planets and a planetary system rotating around its star (e). Figure taken from Oberg [203].

Over $3.10^7$ years, dense molecular clouds are no more stables as their gravitational potential energies are too high resulting in the collapse of their denser areas, called cores [262] with densities between $10^7$ – $10^8$ molecules/cm$^3$ and temperature around 100 K. During the collapse, the cores are becoming young stellar

objects [81], their dust temperatures increase and because of the conservation of angular momentum, they are rotating and dragging matters towards their central protostar (Fig. 1.1). Moreover the excess of angular momentum will be released by bipolar outflows along the rotation axis of the cores [14, 260] and the creation of an accretion disk [146].

When the temperature of the sun-like protostar is becoming high enough (3000-5000 K) to start the fusion of hydrogen into helium, a new star is born. The materials forming the proto-stellar disk will eventually evolve to form planetary system such as our Solar System. A planetary systems, as the Solar System, will exist for $10^7$ to $10^{10}$ years. Protostars with masses less than roughly 0.08 $M_\odot$ never reach temperatures high enough for nuclear fusion of hydrogen to begin. These are known as brown dwarfs. For $0.08 < M_\star < 8$ $M_\odot$, the star will spend a long time on the main-sequence phase ($10^7$ – $10^{10}$ yr) and nuclear fusion will form elements up to C, O and N. After leaving this phase, stars below 0.23 $M_\odot$ become white dwarfs, while more massive stars will move into the Red Giant and Asymptotic Giant Branch (RGB and AGB) phases and eventually evolve into a planetary nebula with a white dwarf core. Red giant winds and planetary nebulae are important sources of gas and dust enrichment in the ISM. From this material it will take about $2.10^9$ years to create a new low-mass star. This way the cycle of matter of low-mass stars is complete.

### 1.2.2 Interstellar Ices

Many molecules, simple or complex, have been observed in the interstellar and circumstellar medium. The Cologne Database for Molecular Spectroscopy (CDMS)[79] reports more than 200 molecules detected as of November 2018, probing that a very rich chemistry is happening in space. Some molecules are qualified as inorganic (e.g. $H_2O$, $CO_2$, CO or $N_2O$), organic (e.g. $CH_4$ or $CH_3OH$), ions (e.g. $NH_4^+$ or $C_4H^-$), hydrocarbon chain (e.g. Hydrogen cyanide (HCN)) and large

carbonaceous species such as $C_{60}$[100]. Those molecules have all been detected via the observation of their high-resolution rotational, vibrational or electronic spectra. Spectroscopic information brings knowledge on the physical conditions, density, temperature and chemical history of a molecular species.

E. van Dishoeck[299] and Linnartz et al. [174] reviewed the chemistry of the ISM. In brief, there are three main ways (i.e. reaction types) to produce new molecules from smaller/simpler species in space: radiative association (chemical reaction with emission of a photon), associative detachment (anion and neutral react freeing an electron), and dust-grain catalysed surface reaction (chemical reaction onto a dust particle). Bond breaking reactions also can create new molecules either by photodissociation (with a photon), collisional dissociation or dissociative recombination with an electron. Finally, rearrangement reactions may also occur between ion-molecule, charge transfer or neutral reaction.

Under cold dense ISM conditions, collisional rates between two species are still extremely low ($10^{-4}s^{-1}$). Moreover the low temperature of colliding molecules does not bring enough energy to overcome the binding energy needed to form a new species. This makes the radiative association process inefficient suggesting that other mechanisms need to be at play to explain molecular abundances observed in such environments. Therefore solid state chemical reactions are thought to take place on or within ice layers formed on cold dust particles. Ice dust grains can indeed act as a third body receiving energy from species landing onto them and reacting with each other. In hot cores where temperatures are above 90 K, complex gas-phase chemistry can proceed efficiently again.

Several different parameters can affect grain surface chemistry in dense clouds. First of all, the accretion rate, depending on molecular sticking probably, defines the speed at which gas phase species are absorbed onto the grains. The surface migration rate sets the chemical reaction network by diffusion of species on the ice surface. Finally, the desorption rate is the mechanism by which molecules are released from the solid to the gas phase.

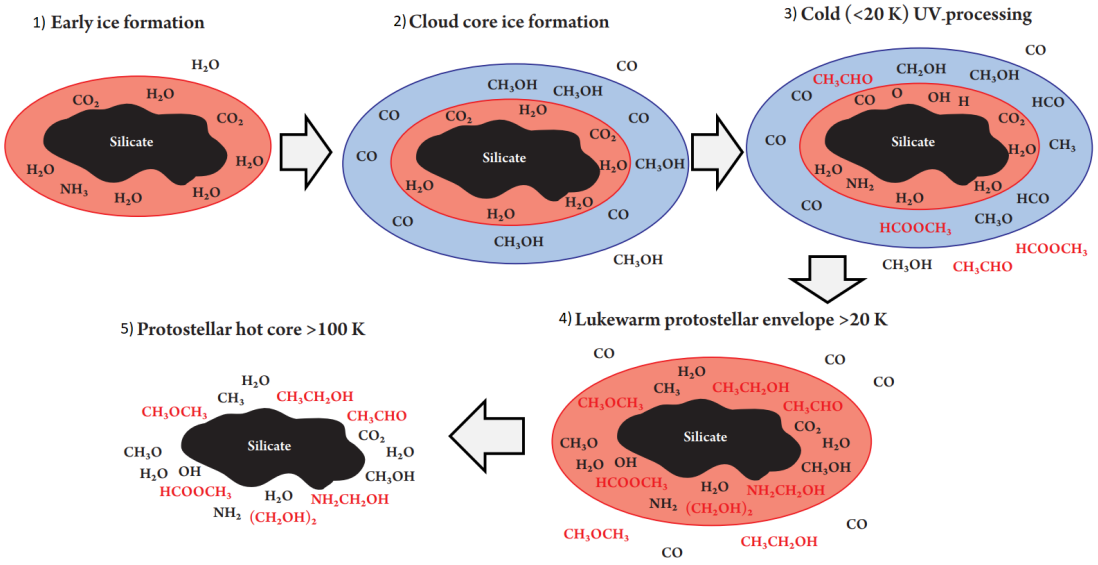


Figure 1.2: Ices evolution during star formation. Early during cloud formation (a) a H2O-rich ice forms. Once a critical density and temperature is reached CO freezes-out catastrophically (b), providing reactants for the formation of species like CH3OH. Energetic processing (UV photolysis and cosmic rays irradiation) of the CO-rich ice results in the production of complex species. Closer to the protostar (c), following sublimation of CO, other complex molecules become abundant. Finally, all ice close to the protostar 100 K desorbs thermally (d). Credit: E. van Dishoeck (2014)[299] adapted from Oberg et al. [205].

The evolution of interstellar ices during star formation can be depicted in 5 steps as shown in Fig. 1.2.

1. Hydrogenation reactions of atoms such as C, O or N and other species occur on dust grains in molecular clouds, as described by van de Hulst for the first time in 1946 [210]. A first layer of ice is thereby formed which, for instance, includes $H_2O$ as its dominant component, $NH_3$ and $CO_2$. This ice layer is called $H_2O$-rich or polar ice. (Fig. 1.2 (1))

2. As the collapse of the molecular cloud proceeds, densities are increasing to about $10^5$ cm$^{-3}$. Substantial amount of CO freezes-out on top of the $H_2O$-rich ice forming a new layer referred to as CO-rich or apolar ice. The hydrogenation of CO produces $CH_3OH$ while its oxygenation generates $CO_2$ [289].

3. While surface hydrogenation processes are continuing [306], cosmic rays and UV photons interacting with the icy dust grains lead to the formation of new molecules [189, 207]. In parallel, non-thermal desorption mechanisms induced by, for instance, cosmic rays and UV photons impinging on ice dust particles release some of the new born molecules in the gas phase [45].

4. At this stage, temperatures surrounding the protostar are rising above 20 K. Above 30 K, thermally activated diffusion and reaction of species occur inducing the formation of COMs. Thermal and non-thermal desorption mechanisms play an important role in bringing molecules into the gas phase [3]. Complex solid state chemistry triggered by energetic processing still happens within the ice as explained in (3).

5. The temperature of the grains eventually exceeds 100 K inducing the sublimation of most of the compounds within the ice mantles. In hot cores, densities and temperatures are much higher than in the cold molecular clouds leading to a richer gas-phase chemistry.

### 1.2.3 Desorption of Interstellar Ices

A list of desorption mechanisms, turning molecules from solid to gas phase, has been reviewed by Collings et al.[183]. They are shown on the diagram of an icy grain (by Fraser et al.[90]) in Fig. 1.3. The dust particle made of a silicate core is covered by an icy mantles made of molecules such as $H_2O$ or $CH_3OH$ as explained in the previous section.

Among others, the main desorption processes leading newly formed solid COMs to the gas phase are:

– Cosmic-Ray induced heating[170]: In cold dense regions and shock regions, cosmic rays, with kinetic energies of keV - MeV range (well above binding energies which are less than 0.5 eV), interact with the ice mantle of dust

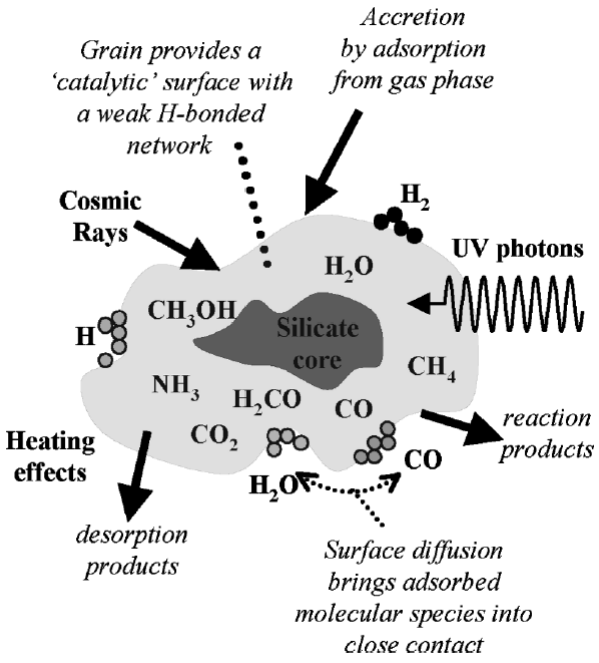


Figure 1.3: Desorption is due to the following main mechanisms: thermal heating, chemical reactions on a surface, photodesorption, interaction with cosmic rays and collisions with other frozen dust particles. Figure from Fraser et al.[90]

grains inducing either a local heating effect desorbing molecules in proximity of the cosmic ray path into the ice grains or a whole grain heating effect which usually occur only for smaller grains [124].

– Exothermicity from chemical reactions[69, 102]: Chemical reactions are happening within the ice mantle as stated previously. For instance, recombination of atoms to form $O_2$ or $N_2$ on the ice surface releases 5.2 and 9.8 eV, respectively, which is much higher than the surface binding energies of such species. The excess energy can be used by molecules to diffuse and desorb from the ice and it can be also partially dissipate within the ice, for instance within the OH-network in water-rich ices [304].

– UV photodesorption[207]: It is the most studied non-thermal desorption mechanism happening in cold dense clouds. UV photons are produced both by the interstellar radiation field, generated by stars outside a molecular cloud [192], and by the interaction between $H_2$ and cosmic rays within a

cold dense molecular cloud [235]. UV radiation can excite certain molecular electronic states of molecules. This is a wavelength dependent process. If enough energy is brought by UV photons into the ice, excited molecules or dissociated fragments can desorb if residing in the top few layers of the ice [206]. Photodissociation, i.e. the dissociation of a species upon interaction with a UV photon, has been widely studied by molecular dynamics simulations[8] and laboratory experiments [86, 209], but will not be the focus of this thesis.

– Thermal sublimation[31, 50]: This mechanism is happening within the protostellar envelop and its range is different depending on the sublimation temperature of the molecules composing the ice and the environmental temperature of the dust grain. As seen in Fig. 1.4, the temperature is increasing from 10 K to above 100 K closer to the protostar. In close proximity of the protostar (below tens of astronomical units), the temperature will be higher than most of the molecular sublimation temperatures. Therefore only gas phase molecules will be present. However, in the mid-plane of the accretion disk around the protostar, densities increase and temperatures drop again. This leads to the formation of snow-lines defined as the limit at which gas phase molecules will be frozen-out on dust grains. This process is called thermal desorption.

Thermal and non-thermal desorption mechanism cause ice molecules to sublimate. Astronomical observations of gases give insights on the chemical evolution of a star-forming region. Over the past decades, many laboratory studies and complex simulations have so far focussed their efforts to characterise desorption mechanisms and understand their impact on the evolution of complex molecules throughout the formation of a star system.

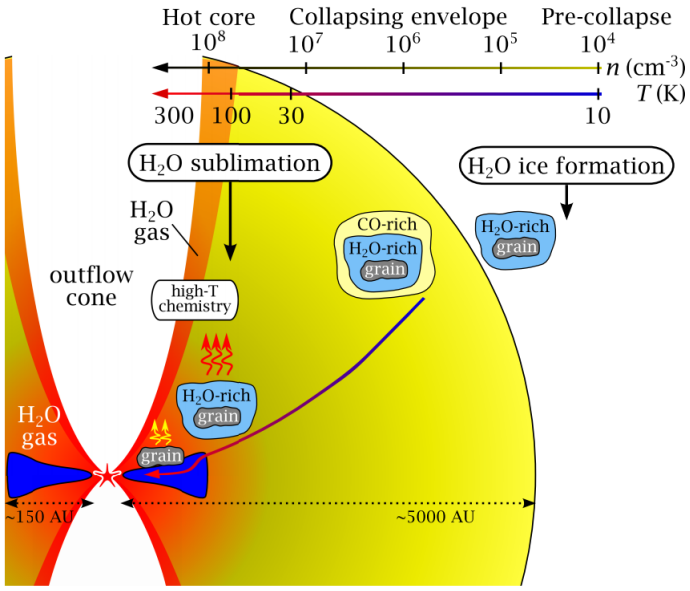


Figure 1.4: Schematic of a protostellar envelope and disk with simple ice evolution from the pre-collapse step to the hot core. Figure by R. Visser, adapted from Herbst and van Dishoeck [125]

## 1.3 Laboratory Experiments

The first report of molecules in space occurred in 1940 when unidentified UV absorption lines were attributed to CH and CN in diffuse interstellar clouds[187]. In 1963 the OH molecule was discovered by a radio telescope[309]. Since then, astronomers observing spectral lines at THz, submm/mm and radio frequencies from gas species in the ISM and circumstellar medium (CSM) realised that spectroscopic information accessible only by laboratory based experiments was required to unambiguously identify molecular species in space. Although to date more than 200 molecules have been identified in space, the search for new molecules in space still poses big challenges to astrochemists. For instance, the majority of data observed so far by ground-, air- and space-based astronomical facilities remain uninterpreted: (i) survey lines cannot be assigned as gas, ice, and dust material databases are incomplete, and mostly populated by lines of atmospheric interest (e.g. JPL catalogue and HITRAN database); (ii) even where molecules are known to exist, observations have clearly detected molecules in vibrationally and rotationally excited states, for which likely no current labora-

tory measurements or theoretical calculations exist. Thus gas-phase observations place major demands on laboratory astrochemists: (i) first, to identify which molecules could be present in space; (ii) second, to understand the formation mechanisms of such molecules, deciphering between solid-state and gas-phase reaction pathways; (iii) and third, to understand non-thermal (non-Boltzmann) excitation mechanisms of molecules. To put next Chapters of this thesis into an astrochemical context, this section will review current gas-phase spectroscopy techniques and will discuss laboratory experiments on thermal desorption.

### 1.3.1 Gas Phase Spectroscopy

The unambiguous identification of chemical molecular species in astronomical observations by means of radio telescopes rely on the availability and completeness of spectroscopic gas-phase databases at the corresponding frequencies of molecular species. A comparison between laboratory data and observations not only leads to the identification of new species but also allows for quantitative studies of the molecules present in the ISM. To date, two main catalogues, which combine laboratory data with large models and fitting functions based on molecular rotation and ro-vibration transitions exists: the Cologne Database for Molecular Spectroscopy (CDMS)[79] and the Jet Propulsion Laboratory (JPL)[219] catalogues.

Laboratory data are routinely obtained via many different absorption techniques, that is THz time-domain spectroscopy[196], backward-wave-oscillator-based fast scan sub-millimeter spectroscopy [188, 255], and chirped-pulse Fourier transform spectroscopy[215]. Recent advances in heterodyne technology allowed for the use of similar receivers in radio astronomy and in laboratory experiments. The heterodyne-based approach to build new detectors has various advantages compared to standard frequency modulation absorption techniques. The instrument is measuring an absolute intensity via the calibration mechanism described

in Chapter 2. All intensities of molecules are assumed to reflect the local thermal equilibrium conditions as they are observed in a static vacuum chamber in pure concentration. Moreover the observed line-shape is not a derivatives and is linked to the amount of molecules within the optical path of the detectors. Commonly for THz receivers (see Section 2.3), quantum-noise-limited detectors, non-linear devices are used such as Schottky-barrier diodes for example. Those detectors have a fast response of several picoseconds (e.g. Schottky-barrier diodes). The digital spectrometers used also permit to have a broad instantaneous frequency coverage. Finally, it is possible to mirror astronomical observations by performing either absorption or emission spectroscopy.

In the past years, THz gas-phase spectroscopy was firstly used to test the good operation of newly developed receivers before being incorporated into satellites or ground-based telescopes, e.g. the Submillimeter Wave Astronomy Satellite [292], ODIN [94] and Herschel [284] (briefly described in the next section). More recently, the gas-phase spectra of Nitrous Oxide at 326.56 GHz and 326.69 GHz, shown in Section 4.4.1, were presented [12] to test the radiometer described in this Thesis. In 2018, an observation of Nitrous oxide at 355.6 GHz was presented using a new digital spectrometer [216]. However to date these spectroscopic data are not published in a peer-reviewed journal yet. It is only in 2017 that Wehres et al.[199] described the design, construction and operation of two laboratory broadband emission spectrometers. The first one is based on Schottky-barrier heterodyne receiver with fast Fourier transform digital spectrometer operating between 80 and 110 GHz whilst the second one is using cryo-cooled SIS technology and operates at higher frequency between 270 and 290 GHz[307]. Pyridine and methyl cyanide features were successfully detected and matching analytic simulations were presented for the observed spectral transitions. Finally in 2018, a new proof-of-concept technique combining terahertz radiometer (41 - 49 GHz) and a vacuum chamber was developed so as to observe the generation of cold plasma and UV photochemistry in the gas phase under low pressure as described by

Tanaroo et al.[282].

The THz-DES proof-of-concept experiment described in this thesis has the same approach as those two new aforementioned experiments. Indeed it combines THz technology used in radio astronomy with laboratory vacuum techniques to look at gas phase molecules under interstellar relevant conditions. However instead of purely characterising emission of gases or the impact of UV light on gas mixtures, the THz-DES project focuses on the observation of the thermal desorption mechanism.

### 1.3.2 Thermal Desorption

Laboratory experiments that study thermal desorption mechanisms are called Temperature Programmed desorption (TPD) experiments. TPD has been commonly used for astrochemistry purposes over the past 20 years. It is a destructive technique which detects the amount of gaseous adsorbate coming from a cold surface as a function of the linear heating applied on this substrate. In the past years, many different experimental ultra-high vacuum (UHV) systems were designed to perform TPD experiments, such as, for instance, the Nottingham Surface Astrophysics Experiment (ICE RIG) by Fraser et al. in 2002[90], the Surface Reaction Simulation Device by Fuchs et al. in 2009 [98, 133] and the InterStellar Astrochemistry Chamber by Munoz Caro et al. in 2010[197]. The ice was grown under UHV conditions ($10^{-10}$ mbar) and monitored with RAIRS instruments. Heaters increase the temperature of the substrate where the ice is formed and the subsequently sublimated materials are detected via a quadrupole mass spectrometer (QMS). A typical results obtained with the TPD method is shown in Fig. 1.5. The x-axis is the substrate temperature. The different curves represent different TPD experiments where the amount of $H_2O$ deposited on the surface is increased. In the experiments, desorption for water starts at 140 K, desorption rate increases for all the ice thicknesses following the same trend

meaning that the concentration of ice molecules does not affect the desorption behaviour (so called multilayer regime). Once all molecules desorb, desorption rates are decreasing to reach the noise floor of the experiment (sub-monolayer regime). This means that all molecules have been released and pumped away by the UHV system. In general, whilst the TPD experiment itself is relatively straightforward, the interpretation of the data is often much more challenging. Under conditions where the pumping speed is sufficiently high, the quadrupole mass spectrometer (QMS) signal for the selected mass is proportional to the rate of desorption of that species, $r_d$ (molecules $cm^{-2}$ $s^{-1}$). The rate of desorption is given by the Polanyi-Wigner equation:

$$r_d = \nu_i N_X^i \exp(-E_d/RT) \tag{1.1}$$

where $\nu_i$ is the pre-exponential factor for the process leading to the desorption, $N_X$ is the surface concentration of adsorbate $X$, $i$ is the desorption order, $E_d$ is the activation energy for desorption per mole, R is the gas constant and T the temperature. Desorption from multilayers of bulk ice is typically close to zero order (i = 0). For perfect zero order desorption, the desorption rate does not depend on the surface concentration. In many cases, desorption of submonolayer coverage results in near first order kinetics (i = 1), *i.e.*, the desorption rate depends linearly on the surface concentration.

The simplest thermal desorption process is the desorption of a pure ice. Desorption of binary or more complex mixtures is less understood. Different desorption trend for mixtures or layered ices have been observed [179] such as co-desorption, when molecules of different sublimation temperature are desorbing at the same temperature, or volcano desorption[268], when a trapped molecules is released at a temperature slightly different to its sublimation temperature without other species. The latter mechanisms likely occurs when other dominant species in the ice are undergoing structural modifications (e.g. restructuring of

the ice from amorphous to crystalline).

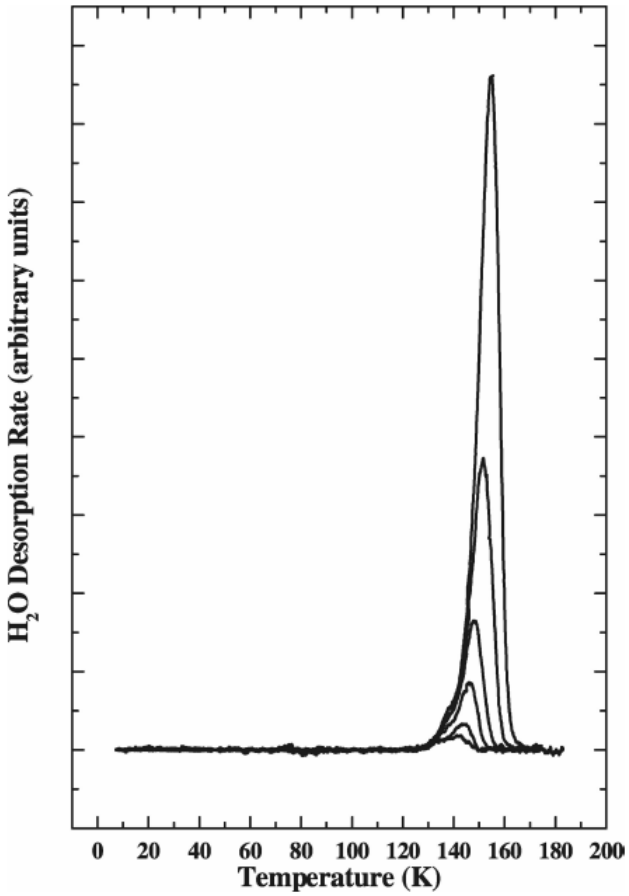


Figure 1.5: Water ice desorbs at around 140 K under ultra-high vacuum conditions with a rate that depends on the number of layer deposited on the substrate surface. Figure from Fraser et al.[90]

At low temperature, ice formed in its amorphous phase rather than in crystalline structure. At 10 K, molecules within the ice do not have enough energy to rearrange themselves into an organize structure on the grain[182]. Low density amorphous ice seems to be the most common type of ice in space[58] and could trap molecules into its mantle. The structure of the ice has a significant impact on mixed ice desorption. For example, Fig. 1.6 presents the desorption of a layered configuration of CO on porous $H_2O$ ice[51, 54]. The TPD curve of CO is rotated for clarity. At 10 K, molecules of CO are adsorbed on top of the porous deposited $H_2O$. Increasing the temperature, CO will start sublimating at 25 K but some molecules will diffuse through the porous water creating a gap in the

desorption rate of CO. The second peak at 40 K corresponds to the desorption of the CO molecules remaining on top of the porous $H_2O$ ice. Up to 140 K, some CO molecules will remain trapped within the pores of $H_2O$ ice and it is only when the water undergoes its structural change from compact amorphous to crystalline at 140 K [182] that the CO molecules trapped are released to the gas phase. The final peak at 160 K is the co-desorption of traces of CO with the remaining $H_2O$ molecules.

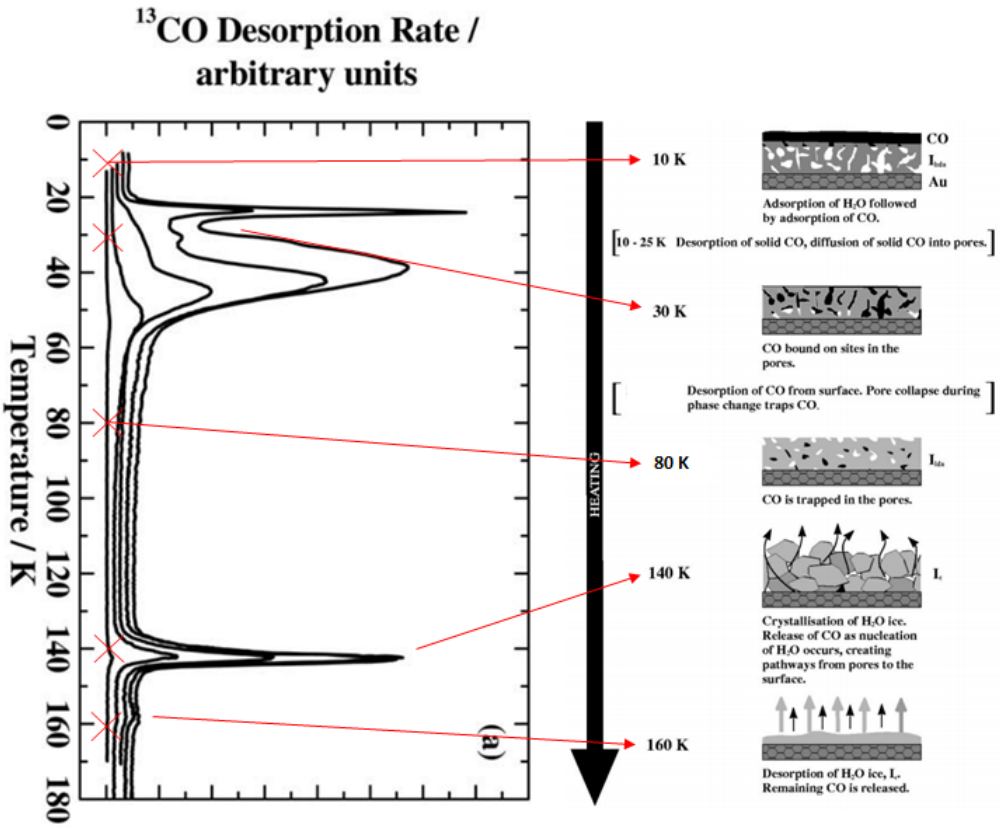


Figure 1.6: Effect of the temperature on layered ice composed of CO and $H_2O$ molecules. Because the temperatures of desorption for CO and $H_2O$ are different, CO partially desorbs first from the surface and then co-desorbs with water at higher temperatures. Credits:[51, 54]

A classification has been made using TPD results[50] for simplifying the treatment of the different desorbing species. Molecules, such as $NH_3$, $CH_3OH$ and HCOOH, are considered to follow the same desorption trend as for $H_2O$ (polar ices). They cannot diffuse much in porous materials and remain within the ice. Some other molecules ($N_2$, $O_2$, $CH_4$, NO) are comparable to CO and are con-

sidered as volatiles (apolar ice). They can be trapped within ice layers and have volcano desorption or co-desorption. Finally some species ($C_2D_4$, $C_2H_2$, $C_2O$, OCS, $CS_2$, $SO_2$, $CH_3CN$, $H_2S$) have behaviour between water-like and CO-like species, less affected by volcano and co-desorption; however traces can still be seen when porous water is desorbing.

Finally, desorption activation energies can be derived as explained in details by Schwarz and Falconer [83], and in Section 2.5. The desorption activation energy ($E_{des}$ in kJ/mol) corresponds to the minimal energy needed by chemical reactants to change their thermodynamic state from solid to gas. If the molecular ice (made of one molecular kind) receives less energy than $E_{des}$, the ice will not sublimate. Desorption energies for various molecules are shown in Table 1.1. They are different depending on the kind of molecules analysed and the kind of ice desorbed.

Table 1.1: Desorption activation energy of $H_2$, $H_2O$, $CH_3OH$, CO, $CO_2$ and $N_2$ (in kJ/mol) from various TPD experiments in the literature.

| **Molecules** | **References** | **Desorption Energy (kJ/mol)** | **Notes** |
|---|---|---|---|
| $H_2$ | Acharyya et al.[1] | $4.0 \pm 0.1$ | Silicate |
| $H_2O$ | Bolina [24] | $39.9 \pm 0.8$ | Graphite |
| | Dulieu et al. [69] | 39.9 | Silicate |
| | Fraser et al.[89] | 46.6 | Amorphous ice |
| | Fraser et al.[89] | $47.5 \pm 0.5$ | Crystalline ice |
| | Collings et al.[50] | $49.3 \pm 2.0$ | Amorphous silica |
| $CH_3OH$ | Sandford et al.[246] | $35.2 \pm 0.1$ | Pure |
| | Bolina et al.[25] | $41.0 \pm 0.8$ | Graphite/multilayer |
| | Bolina et al.[25] | $48.0 \pm 0.8$ | Graphite/monolayer |
| CO | Acharyya et al.[2] | $7.1 \pm 0.1$ | Pure |
| | Collings et al.[50] | $7.3 \pm 0.3$ | Layered |
| $CO_2$ | Sandford et al.[244] | $22.4 \pm 1.2$ | Pure |
| $N_2$ | Fuchs et al.[96] | $6.7 \pm 0.2$ | Pure |

TPD measurements are a really powerful way to obtain information on the sublimation temperature of molecules, desorption rate and order of reaction

for pure and mixed ices. Many interesting molecules, such as CO, $H_2O$ $C_2O$, HCOOH, $CH_3OH$, and various configurations were studied over the years and are still under investigation. Nevertheless, TPD experiments present some limitations. First of all, it is not possible to know with accuracy what the ice layers are made of, i.e. only signals from the mass of molecules directed towards the quadrupole mass spectrometer. Therefore it is not possible to directly identify individual binding sites or packing structures but only indirectly by carefully analysing TPD curves. The second limitation is that data treatment can be complex and mistakes can arise when applying the different methods especially to retrieve desorption activation energies. The main technical issue however is due to the limitation of a quadrupole mass spectrometer. Although QMS can detect pressures down to $10^{-13}$ mbar, different kind of molecules such as isotopes with very close masses or radicals cannot be easily detected. Moreover excited molecules and molecules in their ground states cannot be differentiated so as to determine if thermal desorption mechanisms present different characteristics depending on the transitions level of the icy molecules. The THz-DES technique does not present the aforementioned limits.

## 1.4 Observations of the Interstellar Medium

Most of knowledge gathered over the past decades on the physics and chemistry of the star formation and interstellar medium was obtained using spectroscopic techniques from space or ground-based telescopes. The heterodyne technique, described in details Section 2.3, permits to down-convert high-frequency signals to low frequencies making them easier to detect with high-sensitivity. Radio telescopes are based on this principle so as to characterise the signature of the gases observed in different regions in space.

Sub-mm and radio-telescopes are key instruments to detect molecules in space. A short summary of few missions used for radio astronomy have been listed in

Fig. 1.2 (past and present) and Fig. 1.3 (future) with their respective date of operation and frequency range. In this section, the focus is on describing two systems in details because of their role and impact in astrochemistry and their development using state-of-the-art THz technology. They are the Herschel Space Observatory and the Atacama Large Millimeter Array (ALMA).

### 1.4.1 Herschel Space Observatory

The Herschel Space Observatory was commissioned by the European Space Agency (ESA) and was launched in 2009 and lasted until 2013 when it ran out of liquid helium, necessary to cool the instruments on-board. The heritage from Herschel observations is very important. The key scientific objectives of Herschel were to investigate the formation of stars, planetary-system and galaxies, and increase the scientific understanding of the ISM, our Solar System as well as extra-galactic galaxies. The high spectral resolution of one of its instrument (HIFI) permit to detect more than 100,000 spectral features in a single spectrum [19]. Molecules such as water[301] (through the WISH program of observations in the ISM), carbon monoxide oxygen and many more were detected in different astronomical environments[108].

The Herschel telescope was passively cooled using liquid helium at around 4 K as primary cooling and the dish was 3.5 meter diameter. Three scientific instruments were on-board: a high-spectral resolution heterodyne spectrometer (HIFI, Heterodyne Instrument for the Far Infrared), an imaging photometer (PACS, Photodetector Array Camera) and a medium resolution grating spectrometer (SPIRE, Spectral and Photometric Imaging Receiver). The THz frequency was covered by the HIFI instrument, which is made of several heterodyne receivers: Band 1a (480-552 GHz), band 1b (552-636 GHz), band 2a (640-736 GHz), band 2b (704-792 GHz), band 3a (736-848 GHz), band 3b (852-948 GHz), band 4a (960-1104 GHz), band 4b (1056-1188 GHz), band 5 (1104-1272 GHz), band 6a

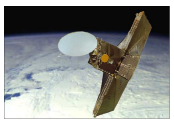

**2001. ODIN**

- Launched in 2001 (Instruments: SMR and OSIRIS)
- Operating frequencies: 100 GHz - 600 GHz (SMR)
- Star formation, Comets

**2003. SMA (Submillimeter Array)**

- Operational since 2003 (Mauna Kea, Hawaii, USA)
- Operating frequencies: 180 GHz - 900 GHz
- Stars formation, Solar System bodies, distant galaxies, protoplanetary disks,...

**2004. ROSETTA**

- Launched in 1989 (Instruments: MIRO, OSIRIS, ALICE, CONSERT, COSIMA, MIDAS, ROSINA, RPC, RSI, VIRTIS)
- Operating frequencies: 190 GHz - 562 GHz (MIRO)
- Comets composition, Solar System evolution, extraterrestrial life

**2005. APEX (Acatama Pathfinder Experiment)**

- Operational since 2005 (Chajnantor, Acatama, CHILE)
- Operating frequencies: 211 GHz - 200 GHz
- Star forming regions, planetary atmospheres, molecular clouds, starbust galaxies

**2009. HERSCHEL (Herschel Space Observatory)**

- Launched in 2008 (Instruments: PACS, SPIRE, HIFI)
- Operating frequencies: 480 GHz - 1908 GHz (HIFI)
- Stars formation, Protogalaxies, Planets formation, Molecular clouds,...

**2010. SOFIA (Stratospheric Observatory for Infrared Astronomy)**

- Operational since 2010 (Instruments: GREAT, CASIMIR, HAWC, SAFIRE,...)
- Operating frequencies: 500 GHz - 1.2 THz (CASIMIR), 450 GHz - 2 THz (SAFIRE), 1.5 - 5 THz (GREAT)
- Star birth and death, planets, comets, nebulae, black holes,...

**2013. ALMA (Atacama Large Millimeter/submillimter Array)**

- Operational since 2005 (Llano de Chajnantor, Acatama, CHILE)
- Operating frequencies: 30 GHz - 950 GHz
- Star formation, galaxies, interstellar medium, protostars, protoplanetary disks,...

Table 1.2: Past and present telescopes operating at THz frequencies.

(1408-1592 GHz), band 6b (1472-1696 GHz), band 6c/d (1704-1908 GHz). The main components used as mixers were HEB and SIS mixers (see Section 2.3) whereas the local oscillator (LO) sources (see Section 2.3) were based on Schot-

**2022. JUICE (JUpiter ICy moon Explorer)**

- Launched scheduled for 2022 (Instruments: SWI, JANUS, UVS, GALA, ...)
- Operating frequencies: 530 - 601 GHz and 1080 - 1275 GHz (SWI)
- Investigations of Jupiter and Galilean satellites: Oceans composition, magnetic field, atmosphere characterisation,...

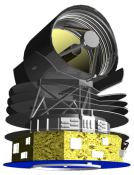

**Late 2020s. SPICA**

- Launched scheduled by end 2030 (Instruments: SAFARI, SMI, POL)
- Operating frequencies: 1.4 - 8.8 THz (SAFARI)
- Star formation, Galaxy Evolution, Proto-planetary Disk Evolution.

**By 2030. LLAMA (Large Latin American Millimeter Array)**

- Installation on-going (Alto Chorrillos, Salta Province, ARGENTINA)
- Operating frequencies: 40 GHz - 900 GHz (SMR)
- Star forming regions, maser emission, galaxies, solar atmosphere, solar flares, ...

Table 1.3: Some of the future telescopes operating at THz frequencies.

tky multiplication principles.

Future space missions that will pick up where Herschel left will be SPICA (developed by the European Space Agency) and the Origins Space Telescope (OST), a Nasa new mission[Origins-Space-Telescope].

### 1.4.2 ALMA

The Atacama Large Millimeter/sub-millimter Array [ALMA] is an international astronomy facility. It was completed in 2013 and is composed of 66 high-precision antennas over 6596 $m^2$ at an altitude of 5000 m in Llano de Chajnantor, Acatama, Chile. The dish antennas are either 12 meters (54 of them) or 7 meters diameter (12 of them). Those sizes combined to the area of the array gives a spatial resolution as low as 0.004 arcseconds (where 1 arcsecond is 1/3600 of a degree), ten times lower than what the Hubble Space Telescope can achieve. The 10 receivers used are based on Schottky LO sources (similarly to Herschel) and SIS mixers cooled at 4 K making it the most sensitive ground based telescope and are covering 10 frequency bands: ALMA band 1 (31.3-45 GHz), ALMA band 2 (69-90

GHz), ALMA band 3 (84-116 GHz), ALMA band 4 (125-163 GHz), ALMA band 5 (163-211 GHz), ALMA band 6 (211-275 GHz), ALMA band 7 (275-370 GHz), ALMA band 8 (385-500 GHz), ALMA band 9 (620-720 GHz), ALMA band 10 (787-950 GHz).

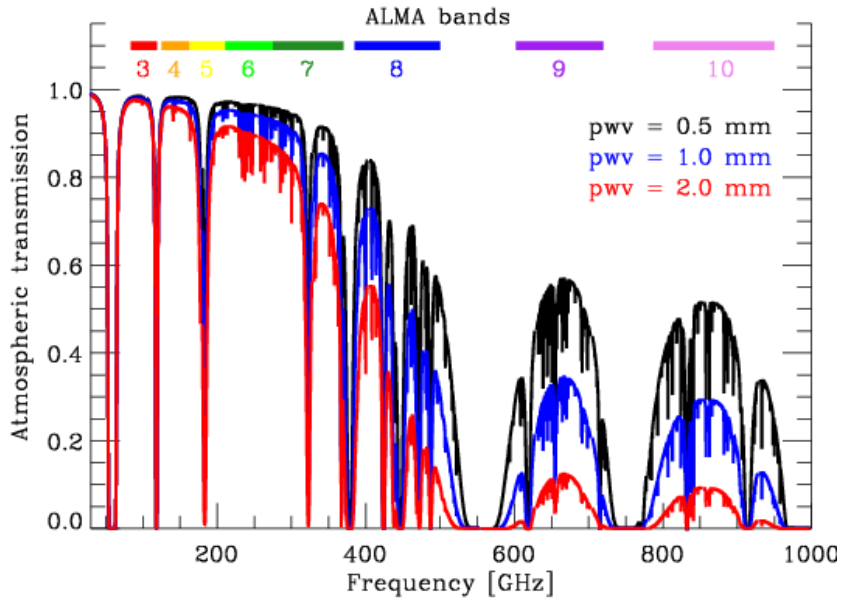


Figure 1.7: Zenith atmospheric absorption of water vapour for the ALMA telescope. Credit:[177]

ALMA is a ground based telescope, therefore the atmospheric transmission has a direct impact on the telescope sensitivity. The frequencies, where atmospheric molecules present strong absorption lines, will appear opaque and no observations further than the atmosphere is possible. Figure 1.7 shows the atmospheric transmission at the ALMA location for three precipitable water vapour[177]: 0.5 mm (black curve), 1.0 mm (blue curve) and 2.0 mm (red curve). From this figure, it appears that the atmosphere absorb almost all signals around 550 GHz and 750 GHz. This is the reason of the frequency gaps between band 8-9 and band 9-10.

ALMA provides unprecedented ability to detect various processes such as the formation of young stars or young planets or faint signals of stars and galaxies

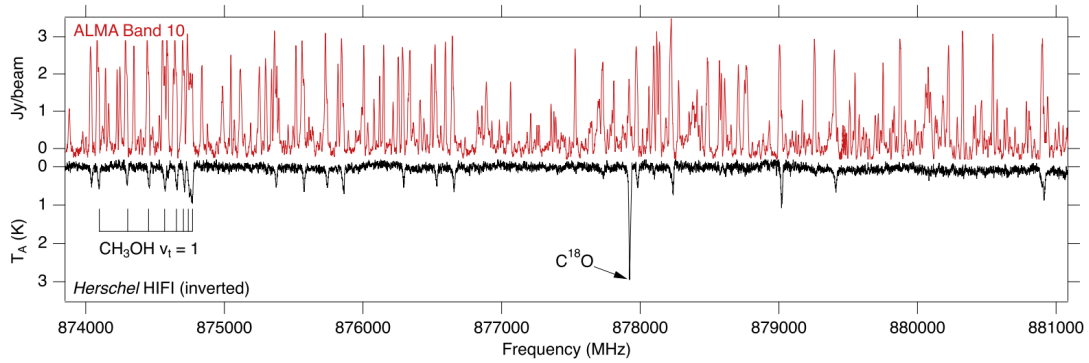


Figure 1.8: Comparison of the spectra acquired by ALMA band 10 and HIFI observing the NGC 63341 region. More informations avalable in McGuire et al. article [186].

at great distances. It is able to detect and map many simple or complex organic molecules within star forming regions in the ISM. Finally, ALMA can observe our own Sun to characterise its structure and its active regions.

For instance, a recent study from 2018 by McGuire et al. [186] shows the first spectral line survey of a high-mass star-forming region using ALMA band 10. They performed a direct detection of water vapour jets from one of the protostars of this region via the detection of HDO around 880 GHz. Moreover a spectral lines survey was carried out with ALMA Band 10 and compared to previous results acquired with HIFI from Herschel, as shown in Fig. 1.8. McGuire et al. discovered a very rich molecular composition observable with ALMA compared to HIFI. This probes the significant advantage of ALMA to characterise the molecular composition of various regions of interest. Finally, the team discovered the presence of $HC(O)CH_2OH$, glycolaldehyde. The technique to assign features to a molecule is to compare them to laboratory based data and quantum mechanical simulations. The authors are pointing out the lack of laboratory spectral information of molecules above 600 GHz. This issue can be potentially solved if the THz-DES technique described in the next Chapters is employed to generate a new laboratory database over the same ALMA spectroscopic range. THZ-DES can also fill in the opaque regions that are inaccessible to ALMA.

### 1.4.3 Observations of Sublimated Ices

In accretion disks of newly formed protostars, snow-lines are the regions where molecules (such as water and carbon monoxide) reach their sublimation temperature. They would appear in the gas phase closer to the protostar and solid phase away from the protostar. Different molecules will present snow-line of different radius as their sublimation temperature will differ. For example, Qi et al. measured the snow-line of CO in the disks surrounding the star TW Hydra at 30 astronomical units ($1.5 \times 10^8$ km) at 20 K[228]. The authors measured the emission of $N_2H+$ to determine the CO snow-line as it is a reactive ion present in large abundance only where CO is frozen-out. The water snow-line (at a sublimation temperature above 100 K) is usually found at a distance less than 5 astronomical units from its star [150] and can be measured via the observation of $H^{13}CO+$ as water is its most abundant destroyer [18].

In 2016, Cieza et al. [48] measured directly for the very first time the water snow line around TW Hydra using the ALMA telescope. The snow-line detected was much further away than in standard protoplanertary disks at about 30 astronomical units. This means that the snow-line shifted away from the star due to a protostellar outburst caused by an increase in the accretion rate [21]. The outburst likely increased the environment temperature above the water sublimation temperature within 30 astronomical units. This shows the potential of ALMA spectroscopic data to analyse sublimation events in combination with models of disk evolution and planet formation.

Finally, methanol is to date the most complex molecule identified on icy mantles. However, complex molecules such as $CH_3CH_2CHO$ that are observed around protostars in the gas phase likely have a solid phase origin [17]. Therefore thermal and non-thermal sublimation processes are needed to explain observations. A laboratory experiment acquiring the rotational spectroscopy of gas phase molecule during interstellar relevant desorption events would provide powerful constraints

on the ice evolution of star-forming regions. The THz-DES system described here will potentially help understanding the evolution and fate of simple ices and complex molecules mirroring warm protostellar region and disk envelope conditions under controlled laboratory conditions and with unprecedented detail.

## 1.5 This Thesis

- **Chapter 2** contains the fundamental theory relative to the THz-DES experiment. In this Chapter, a summary overview of spectroscopic techniques, quasi-optical principles and radiometric technology are explained in detail.

- **Chapter 3** describes the three main parts of the THz-DES experiment which are the desorption chamber, the radiometer and the data acquisition and processing. The mechanism to deposit and desorb the ice is presented together with the different steps of a standard THz-DES measurement.

- **Chapter 4** reviews the radiometric characterisation performed on the radiometer. The impact of different operational parameters (such as integration time and bandwidth) on the radiometer sensitivity and stability are studied in the first section. The THz-DES background signal and some tuning operations are explained before the first gas-phase spectra in the THz-DES frequency range of the targeted molecules (i.e. nitrous oxide, water and methanol) are presented.

- **Chapter 5** presents the first ever THz-DES results observed via emission spectroscopy in the THz frequency range for desorbing pure ices. This Chapter discusses how to interpret THz-DES data and compare it to literature TPD studied. Finally a quantitative method combining THz-DES data and radiative model is used to calculate the desorption activation energy for nitrous oxide, water and methanol.

- **Chapter 6** deals with the thermal desorption of binary ices. Three distinct configurations are analysed. The first one is the desorption of a system composed of nitrous oxide and water ice layers. The second and third configurations studied are a system made of water and methanol observed in a different frequency range, the radiometer Lower-SideBand (LSB) and Upper-SideBand (USB). THz-DES results are validated at other frequencies which would be pivotal to a future radiometer operating at THz frequency, which could be integrated into the next generation of the THz-DES systems.

- **Chapter 8** will bring a conclusion to this Thesis, explaining why THz-DES proof-of-concept is unique and pivotal to a better understanding of interstellar relevant processes. This Chapter deals with how the THz-DES experiment achieved its purpose in the testing phase and describes the potential benefits it will bring to the astrochemistry community. Finally a future work section describes how the THz-DES proof-of-concept experiment will be upgraded next.

# Chapter 2

# Theoretical Background

## 2.1 Introduction

Theoretical background, from which the development of the THz-DES experiment was based on, is presented in this Chapter. Firstly the emission of molecules such as water and methanol is described as long as spectroscopic technique to observe and analyse it. Finally, Gaussian optic principles and radiometer technology are presented as the core of the THZ-DES experiment. Finally, the theory behind the desorption activation energy is described as this parameter will be retrieved from the THz-DES results.

## 2.2 Spectroscopy Techniques

Absorption and emission spectroscopy are two different techniques used to analyse the energetic signature of unknown gases by characterizing their spectra. For absorption spectroscopy, an incoming radiation is absorbed providing enough energy for a molecular transition to a higher quantum energy state. Therefore wavelengths corresponding to those transitions are removed from the spectrum of the incoming light. The transmission of the light depends on the absorption coefficient of the medium, the optical path length or the absorption cross section

and density of absorbers. Emission spectroscopy is based on the de-excitation of a high energy level to a lower one. Radiation (photons) is generated during this process at a discrete frequency.

### 2.2.1 Molecular Spectroscopy

Einstein in 1905[73] showed that the energy of light is quantized and depends on the photon frequency $\nu$ and the Planck constant h such as $E = \nu \times h$. Atoms and molecules also present quantised energetic levels. For a molecule, they are defined as the electronic, vibrational and rotational levels. Electronic levels are associated with the repartition of the electrons between the atoms of the molecule. Vibrational levels are associated to oscillations of the molecular bonds between the atoms. Finally the rotational energy levels corresponds to rotation of the molecule around certain axis defined by its geometry.

Based on the Bohr-Oppenheimer approximation[28], stating that the motion of nuclei and electrons can be separated, molecular energy states may take only certain values defined by their quantum numbers, associated with either electronic, vibrational or rotational states. The spectroscopy rises from either the excitation or de-excitation of levels when interacting with electromagnetic radiations. Absorption features will be observed for excitations, as the energy state of the molecule rises to an higher level. Emission lines are observed during the de-excitation of molecule as it produces a radiation at the frequency corresponding to the difference between the two energy states. The spectroscopic features, either absorption or emission, are in principle characterised by a single frequency. This effect rises from the Heisenberg's Uncertainty Principle ($\Delta E \Delta t \geqslant \hbar/2$, with $\Delta E$ the energy-dispersio of the energy state, $\Delta t$ its lifetime and $\hbar = h/2\pi$, h the Planck constant) which stipulate that the energy and life time of an energy state cannot be known precisely simultaneously. This uncertainty generates broadened spectral line over frequency called natural lineshape, defined as a Lorentzian

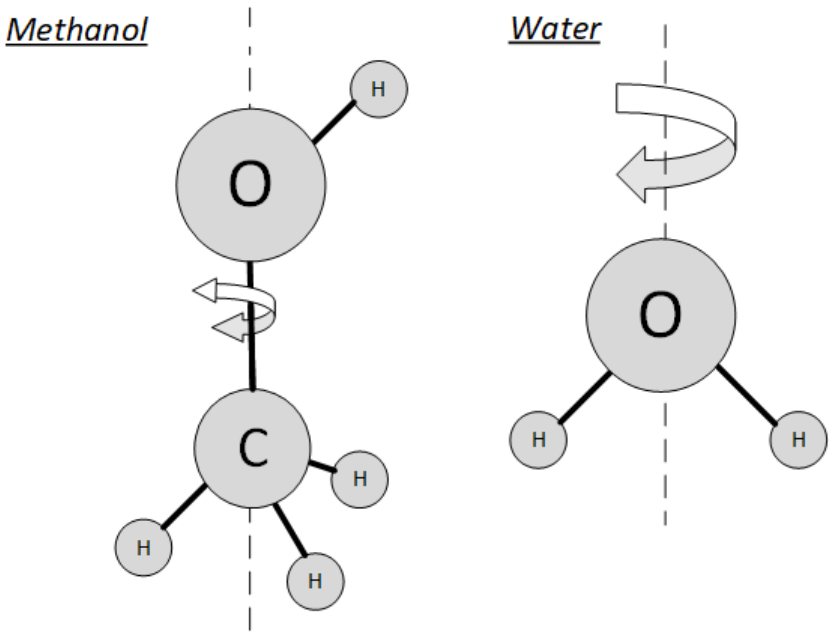


Figure 2.1: Model of the asymmetric top methanol and water molecules. Axis of summetry are shown by the dashed lines. Credit: [140]

curve. The second impact is that some transitions rules link to the quantum number of the molecules appear, defined as the selection rules. Spectroscopic theory are well defined and modelled at present[32, 293]. A small introduction on the rotational spectroscopy of gas phase methanol, water and nitrous oxide is presented in this section. $CH_3OH$ and $H_2O$ molecules are shown in Fig. 2.1.

Two quantum numbers are defined, J corresponding to the rotational quantum number and K which is the projection of J on principal axes of inertia of a molecule [293].

#### 2.2.1.1 Methanol

Methanol, as shown in Fig. 2.1, is an asymmetric rotor where the $CH_3$ group can rotate relative to the OH bond but creating torsional oscillations between those group. An angular momentum is produced resulting in two torsional symmetry states called A-type and E-type. For E-type transitions the quantum number K can either be positive or negative to defined the state levels. For A-type, the levels are torsionally degenerate and represents with K always positive but levels

are refereed to + for +K and - for -K states, as shown in Fig. 2.2. Methanol transitions are labelled $J_K$. The ground state level for A-type methanol is J=0, K=0 whereas it is J=1, K=-1 for E-type methanol.

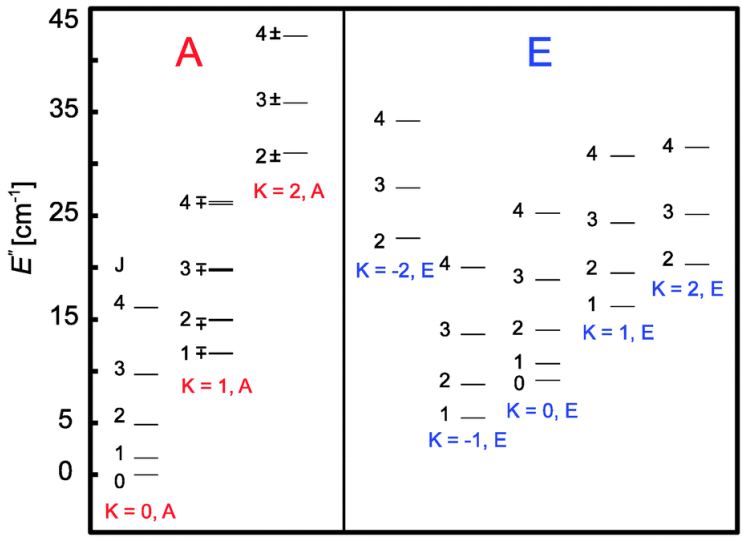


Figure 2.2: Level diagram for vibrational ground state of mehtanol. Credit: [279]

Selection rules exist for methanol such that only transitions between certain energy levels can happen, driven by the conservation of angular momentum. For A symmetry, the selection rules are [148]:

$$\Delta J = 0,\ \Delta K = 0, \pm 1,\ \pm \leftrightarrow \mp \tag{2.1a}$$

$$\Delta J = \pm 1,\ \Delta K = 0, \pm 1,\ \pm \leftrightarrow \pm \tag{2.1b}$$

For E symmetry, they become:

$$\Delta J = 0, \Delta K = 0, \pm 1 \tag{2.2a}$$

$$\Delta J = \pm 1, \Delta K = 0, \pm 1 \tag{2.2b}$$

#### 2.2.1.2 Water

Water is an asymmetric top rotor. The levels are named $J_{K_aK_c}$. To explain the meaning of $K_a$ and $K_c$, prolate and oblate symmetric rotor notions have to be introduced. For symmetric tops, two of their three moment of inertias, from the

principal axis ($I_a$, $I_b$ and $I_c$) through the center of mass, are equals. The prolate configuration is the situation when $I_a < I_b = I_c$ whereas the oblate configuration is when $I_a = I_b > I_c$. $K_a$ and $K_c$ are respectively the projection of the angular momentum on the symmetry axis when the molecules are respectively in prolate and oblate symmetric rotor configurations.

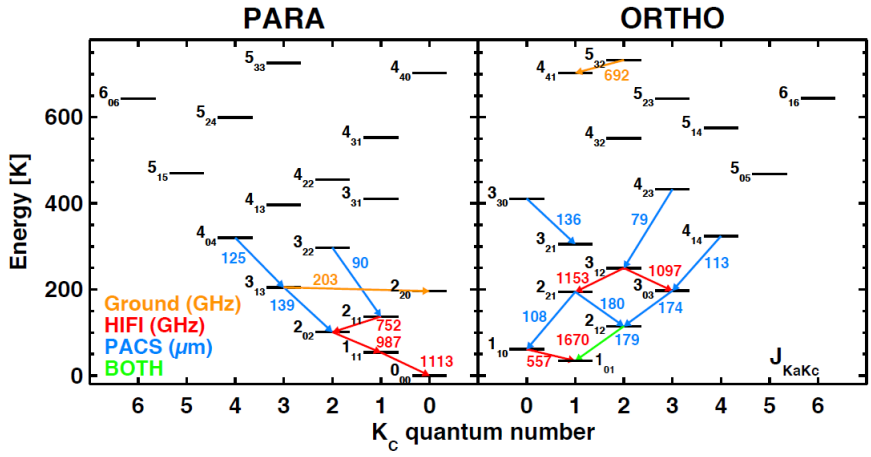


Figure 2.3: Level diagram of ortho- and para-water with observed transitions from the Herschel mission. Credit: [300]

The selection rule for water is $\Delta J = 0$ or $\pm 1$ and a distinction is made depending on the evenness of the $K_a$ and $K_c$ values. Ortho-water is defined when the two nuclear spins of the H atoms are parallel to each other and corresponds to $K_a + K_c$ = odd. When the nuclear spins of the H-atoms are anti-parallel, the molecule is in a para-water configuration where $K_a + K_c$ = even.

Figure 2.3 shows the ortho-/para- water energy levels. The detected transitions from the Herschel mission are highlighted in different colours depending on which instrument was used to detect them.

#### 2.2.1.3 Nitrous Oxide

Nitrous oxide is a non-centrosymmetric linear tri-atomic molecule as seen on Fig. 2.4. It follows the selection rule: $\Delta J = \pm 1$[313]. The rotational spectral features of nitrous oxide appears every 25.12 GHz, corresponding to the J = 0 - 1 transition[222].

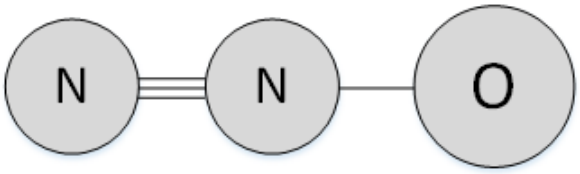


Figure 2.4: Lewis model of the Nitrous Oxide molecule with 2 atoms of nitrogen and one atome of oxygen.

Level energies, transitions frequencies and other spectroscopic information of the molecules studied in this PhD can be found in the JPL[219], Hitran, Cologne spectral line[79] catalogues.

### 2.2.2 Line Broadening

Spectral lines spread over a frequency range depending on environmental factors, pressure, density and temperature. This is called broadening and it can either come from natural line broadening, doppler effect or pressure broadening[41, 193, 194].

- **Natural Broadening**: Natural broadening is an intrinsic phenomena occuring to all transitions. It is based on the Heisenberg uncertainty principle stating that the energy level have finite level time. The transitions will be seen with a Lorentzian line shape: $(\gamma/4\pi^2)/((\nu - \nu_0)^2 + (\gamma/4\pi)^2)$ where $\nu$ and $\nu_0$ are respectively the frequency and the feature frequency and $\gamma$ is the called the damping constant and depends on the line frequency.

- **Pressure or Collisional Broadening**: One of the most important sources of broadening is the variation of the medium's pressure. This effect comes from the collisions between molecules. The concentration of molecules depends on the pressure. They can be seen as oscillators with a life time $\tau$ and with an amplitude decreasing with the time ($a_0 \exp(-t/\tau)$) and a half width of $1/2\pi\tau$, with a Lorentz resonance lineshape (for pressure broadening): $(\Gamma/4\pi^2)/((\nu - \nu_0)^2 + (\Gamma/4\pi)^2)$. The absorption coefficient is narrow for low pressure and the full width at half maximum (FWHM) of the lines

increase when the pressure increases. This is known as the Van Vleck Weisskopf theory (more information in [293]). The intensity of the radiations is also affected by the decrease of pressure and will be lower when there is less molecules.

- **Doppler broadening**: When atoms or molecules (emitting/absorbing radiations) are moving towards or away from the observer. The apparent and measured frequency appear to be slightly shifted. This effect gives a Gaussian distribution to the spectral line. When Doppler and pressure broadening are both considered, a third function is used, often a Gaussian: $1/(\sqrt{\pi}\Delta\nu_D)\times\exp(-(\nu-\nu_0)^2/(\Delta\nu_D)^2)$, where $\Delta\nu_D = (\nu_0/c)\times\sqrt{2kT/m}$ is the doppler width. From measurement of space emission lines, it is possible to understand the kinetics of some molecular species around their stars. When the gas comes in one direction the line would appears at lower frequency whereas it has a higher frequency when moving in the opposite direction from the observer. The voigt profile is the convolution of the two previous functions and is used when both effect should be taken into account.

### 2.2.3 Spectrometers

Nowadays, digital techniques are used in order to process the incoming spectra, mainly because they can give real time Fast-Fourier transform (FFT) with high spectral resolution and have compact sizes. The following comparison of techniques relates to heterodyne system. The idea of such a system was first proposed by Weinreb in 1961 [308] and has improved in speed, power and cost over the past 50 years. Four common systems exist for sampling the signal waveform at periodic intervals of time which are the filter bank, acousto-optical, digital autocorrelation spectrometers and Fast-Fourier transfor (FFT) spectrometers [159, 226]. They are all based on the analogue-to-digital conversion via the Nyquist frequency theorem. This criterion states that the sampling frequency should be at least twice

the highest frequency of the input signal. For a signal coming from the receiver with a bandwidth B, the Nyquist frequency should be: $f_s \geq 2 \times B$. If the sampling frequency is lower than this limit, there are not enough samples so as to capture all the signal shape. This is called aliasing.

Filter banks spectrometers are made of a number of narrow-band filters in parallel discretising the measured frequencies in many channels of spectral resolution defined by the filters. They need the use of detectors at each channels. Therefore those spectrometers are inefficient for high-spectral resolution and large bandwidth measurements. Acousto-optical spectrometers has been used in space mission such as in the HIFI instrument[263]. These spectrometers are based on the diffraction of the signal on Bragg-crystal illuminated by a laser beam and detected by charge-coupled devices (CCDs). However this technique needs space, acquisition time, is costly and is sensitive to temperature fluctuations and vibrations. The other-type of spectrometers are the digital autocorrelation spectrometer[77] and the FFT spectrometers. Both have the advantages to be digital meaning that their acquisition times are fast, with a bandwidth of few GHz and high spectral resolution. Digital auto-correlation can have a bandwidth of few GHz with a spectral resolution below or of few MHz. They are based on the multiplication of a signal by a delayed version of the same signal using a series of delays and when the Fourier transform is applied the measurement of the power spectrum is achieved. They are commonly used in radio-astronomy[78].

FFT spectrometers are based on field programmable gate array (FPGA) chips. Those FPGA are combined with commercially avaiable analog-to-digital converters (ADCs) which give high sampling rate. Their advantages is that they have broad bandwidth, cost effective, a data flow of 3 Gsamples/s and their specifications are still improving. The high number of spectral channels within those devices would decompose their frequency band observrbale into smal section giving a very high sensitivity with insteaneous FFT. Those spectrometers are very sensitive and fast, making them the perfect candidates for radio-astronomy, a 1 GHz

Bandwidth FFT-spectrometer with 32-k channels was installed on APEX[20], and therefore for the THz-DES experiment[Parks]. Moreover, the input of those spectrometers could be in a in-phase/quadrature (IQ) format which would reduce the required sampling frequency by a factor 2, called complex sampling. This is due to the quadrature sampling of the two I/Q signals from the phase offset of the same signal which bring twice more information. As a result, the clock frequency of the two ADC boards can be the same as the observed bandwidth. Finally windowing functions are applied to control the filtering performance of the FFT. Those functions present different performances as explained in [118]. As the sources observed with THz-DES are very faint over the frequency range, the rectangular windowing function was selected and obtain less leakage compared to other windowing functions [278].

### 2.2.4 Brightness Temperature

In 1901, Planck introduced Planck's law[221] which relates the electromagnetic radiation emitted by a black body to its physical temperature. It is considered that any body, in local thermodynamic equilibrium (LTE) with their surroundings, of temperature T above 0 K, radiates electromagnetic energy proportionally to their physical temperature. A blackbody is defined as a perfect emitter which will radiate all absorbed energy in all direction. The LTE can be described[214] in gas as when the energy states of the gas are populated in equilibrium distributions at any locality due to collisions within the gas components (atoms, molecules, ..). If two levels, populated respectively with $N_1$ and $N_2$ electrons, are considered in LTE, the ratio of their level populations will follow a Boltzmann distribution and be written :

$$\frac{N_2}{N_1} = \frac{g_2}{g_1} \times e^{-(E_2 - E_1)/k_B T} \tag{2.3}$$

where $g_i$ is the statistical weight of the level i, $E_i$ the energy level i, $k_B$ the

Boltzmann's constant and T the temperature.

A radiative transfer equation (Equation 2.4) characterises mathematically the intensity of an emitting or absorbing medium[242] where $I_\nu$ is the specific intensity or brightness of an element, $B_\nu(T)$ is spectral emission radiance intensity (source) and $\tau_\nu$ corresponds to the optical depth of the cloud in the observer's line of sight .

$$\frac{dI_\nu}{d\tau_\nu} = -I_\nu + B_\nu(T) \tag{2.4}$$

Kirchoff's law states that the emissivity of a medium in LTE ($\varepsilon_\nu$) is equal to the absorptivity ($A_\nu$). The emissivity is defined as the ratio between the emitting intensity of a body to its Planck function as $\varepsilon_\nu = \frac{I_\nu}{B_\nu(T)}$. For a blackbody, its value is 1 but for a gray-body it is between 0 and 1.

For a blackbody radiation, the term of Equation 2.4, $I_\nu$ and $B_\nu(T)$, will be equal and $B_\nu(T)$ is called the Planck function. The spectral radiance intensity, $B_\nu$, ($W.sr^{-1}.m^{-2}.Hz^{-1}$) can be calculated from the Planck's law, as shown on Equation 2.5 where $h = 6.6260693 \times 10^{-34}$ $W.s^2$ is the Planck's Constant, $c = 2.998 \times 10^8$ $m.s^{-1}$ is the speed of light and $k_b = 1.380658 \times 10^{-23}$ $J.K^{-1}$ is the Boltzmann's Constant.

$$B_\nu(T) = \frac{2h\nu^3}{c^2} \frac{1}{\exp(h\nu/k_bT) - 1} \tag{2.5}$$

According to Equation 2.5, blackbody radiation intensities will depend on their temperature and the frequency of emission. An approximation $h\nu << k_bT$, called the Rayleigh-Jeans law, can be used depending on the values of T and $\nu$ because the term $\exp(h\nu/k_bT)$ can be developed as a Taylor Series. A new expression of $B_\nu(T)$ is obtained (Equation 2.6). Figure 2.5 shows the brightness for 2 blackbodies respectively at 300 K (black curve) and 6000 K (red curve) following Planck (solid lines) and Rayleigh-Jeans (dashed lines) laws. The approximation is valid up to a frequency lower than for the maximum brightness.

This maximum value corresponds to a linear relation between the frequency and the temperature as $\nu_{max} = a \times T$ where $a = 58.789$ GHz/K called the Wien displacement law. Following this law, for a radiation at 400 GHz the Rayleigh-Jeans approximation will be valid only for a temperature higher than 6.8 K. Therefore for microwave frequencies, the Rayleigh-Jeans law is considered valid.

$$\begin{aligned} B_\nu(T) &= \frac{2h\nu^3}{c^2} \frac{1}{(1+h\nu/k_bT+(h\nu/k_bT)^2/2!+...)-1} \\ &= \frac{2h\nu^3}{c^2} \frac{1}{h\nu/k_bT} \\ &= \frac{2\nu^2 k_b T}{c^2} \end{aligned} \tag{2.6}$$

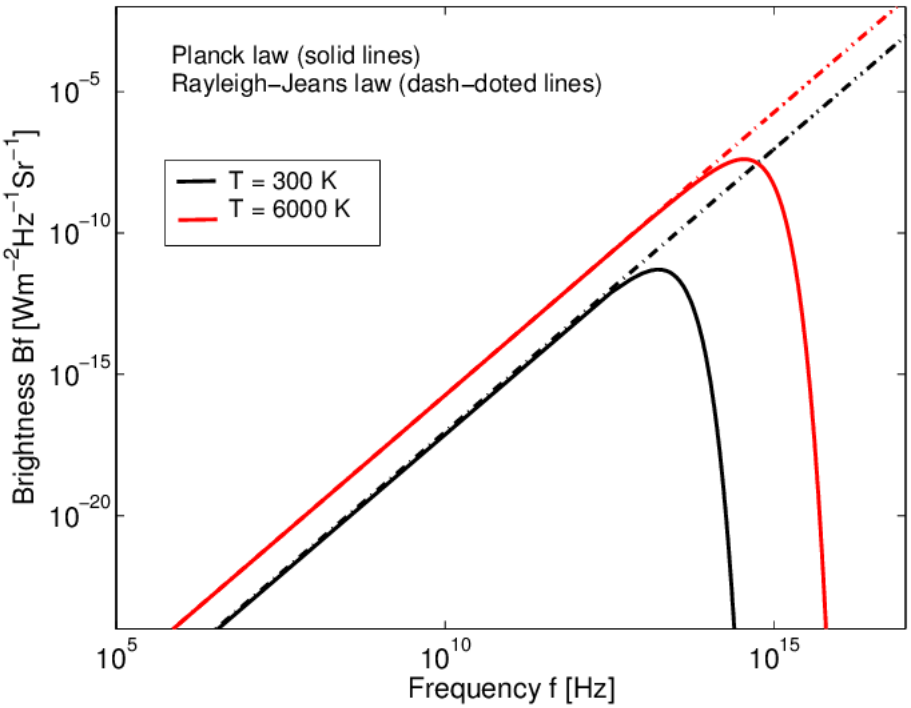


Figure 2.5: Blackbody radiations following Planck law for a body at a temperature of 300 K (black curve) and 6000 K (red curve). The dashed lines are shows the Rayleigh-Jeans law. Credit [114]

By applying the inverse of Planck's law (equation 2.5), the expression of the temperature is obtained:

$$T = \frac{h\nu}{k_b} \ln^{-1}\left(1 + \frac{2h\nu^3}{B_\nu \times c^2}\right) \tag{2.7}$$

Finally using, the definition of the brightness temperature of an element is given by Equation 2.8, by replacing $B_\nu$.

$$BT_\nu = \frac{h\nu}{k_b} \ln^{-1}\left(1 + \frac{2h\nu^3}{(I_\nu/\varepsilon_\nu) \times c^2}\right) \tag{2.8}$$

Introducing the brightness temperature term ($BT_\nu$) in the radiative transfer equation (Equation 2.4), it is possible to define the brightness temperature observed of a molecular cloud against a blackbody source of brightness temperature $BT_{source}$ as shown in Fig. 2.6. The corresponding radiative transfer equation is shown on Equation 2.9.

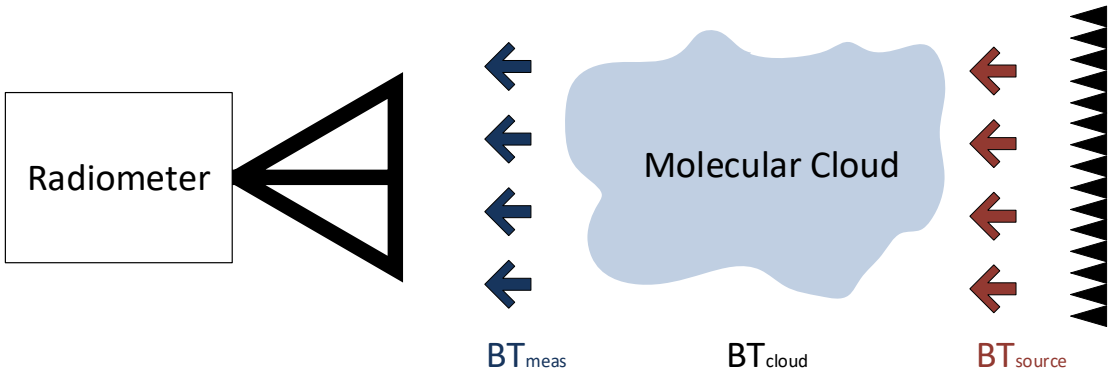


Figure 2.6: A total power radiometer detects the brightness temperature of a molecular cloud and a background source (forming a radiative transfer model).

$$\frac{dBT_{meas}(\tau_\nu)}{d\tau_\nu} = -BT_{meas}(\tau_\nu) + BT_{source} \tag{2.9}$$

By solving the Equation 2.9, the formula of the measured brightness temperature of a radiometer is obtained. The molecular cloud is considered in LTE meaning that its intensity is homogeneous through the entire cloud. Assuming that $BT_{meas}(0) = BT_{cloud}$, different cases can be defined depending on the brightness temperature values of the background source and the molecular cloud. Considering an optically thin gas ($\tau << 1$), if the brightness temperature of the molecules is $BT_{cloud} > BT_{source} > 0$, emission lines will be observed. However if

$BT_{cloud} < BT_{source}$, absorption lines will be detected by the radiometer.

$$\begin{aligned} BT_{meas}(\tau) &= BT_{meas}(0) \times e^{-\tau_\nu} + BT_{source} \times (1 - e^{-\tau_\nu}) \\ &= BT_{cloud} \times e^{-\tau_\nu} + BT_{source} \times (1 - e^{-\tau_\nu}) \end{aligned} \tag{2.10}$$

## 2.3 Radiometer Technology

Heterodyne detection is based on the down-conversion of THz high frequency signals to a lower frequency band, normally a few GHz, which is commonly known as the intermediate frequency (IF) band. In the last 30 years, detectors based on this principle (explained in details in Section 2.3.2) have been developed to perform high resolution spectroscopic studies for mm- and submm- imaging, atmospheric remote sensing or cosmic remote sensing.

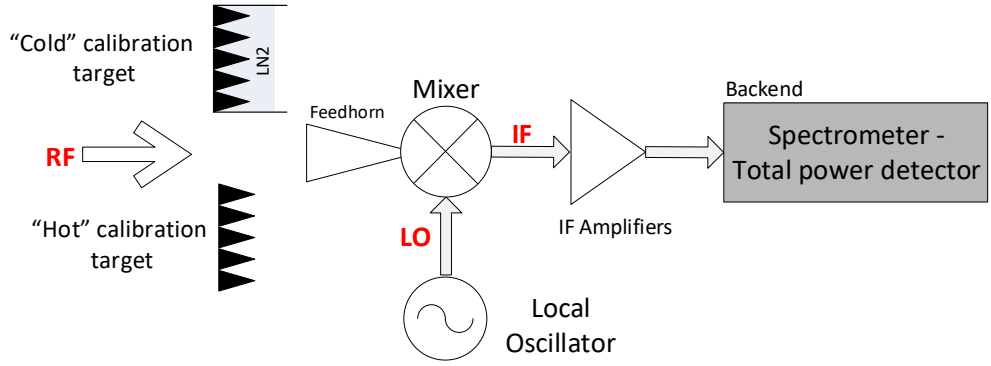


Figure 2.7: Schematic of a total power radiometer, composed of a calibration module, an antenna, mixer device, LO source, Amplifiers, spectrometer or power detector.

Radiometry is a passive technique which measure the microwave blackbody radiation of a desired object or target [224]. A radiometer is composed of various elements such as a calibration module, the antenna (described in Section 2.4), the mixer, the local oscillator (LO), amplifiers and a spectrometer or detector to analyse the IF signal a device measuring the power, as shown in Fig. 2.7. The mixer is the element where the down-conversion occurs (see Section 2.3.3).

There are three main technologies used as mixers: Superconductor-Insulator-

Superconductor (SIS) diodes[162], Hot Electron Bolometers (HEB)[38] and Schottky diodes. State of the art SIS and HEBs show noise temperatures around 5 and 10 times the quantum noise limit, respectively, while Schottky mixers have between 30 to 50 times the quantum noise limit [176]. Despite the higher noise generated by Schottky mixers, they are still the technology of choice for a wide range of applications such as Earth observation and planetary science, due to its ability to operate at both room and cryogenic temperatures, while SIS and HEBs have to be cooled to 4K, leading to complex and costly radiometer designs. In addition, Schottky diodes are a mature and robust technology, with broader bandwidth than SIS and HEBs. Regarding the level of LO power required to 'pump' these mixer, SIS and HEBs required just a few μW, while Schottky diodes require of the order of mW of power. For this thesis, the mixer used was based on Schottky-barrier diodes technology.

Heterodyne detection presents some advantages [239] making it such a powerful spectroscopic method. Firstly it can detect absolute amplitude and phase of the signal via a calibration module. Radiometers developed with a spectrometer are able to measure the real lineshapes of spectroscopic features with large instantaneous bandwidths (several GHz) and fast detection schemes due to the fast response of the detector. A disadvantage would be the difficulty to produce large arrays within a single instrument covering a broad frequency range, for example because of the size of low frequency feedhorns and the design of complex focussing optic.

### 2.3.1 Diode Theory

Schottky-barrier diodes are based on a metal-semiconductor junction(s) named after Walter Schottky for his work on metal-semiconductor interfaces in the 1940s' [257]. For operation in the Terahertz region, Schottky-barrier diodes are fabricated with GaAs because of its high electron mobility, and the high breakdown

voltage of the diodes based on this semiconductor material. When the metal and the semiconductor are joined in the formation of the Schottky contact, some of the electrons in the semiconductor move spontaneously into the metal and collect on its surface, until the Fermi levels of each material aligned. These electrons leave behind a positively charged region created by the ionized donors known as depletion region, which creates an electrostatic barrier in the energy band between the metal and the semiconductor[265, 267]. By applying a forward bias voltage across the diode (positive at metal interface) V, the Fermi level energy of the metal will decrease which will increase the number of electrons going from the semiconductor part to the metal -diffusion of electrons in the semiconductor with enough thermal energy to pass over the Schottky barrier. The non-linear current created by these passing electrons, called thermionic current, $I_d(V)$ is expressed by Equation 2.11, where n is the ideal factor[1], q the electron charge, V the positive bias voltage, T the diode temperature, $k_B$ the Boltzman's constant, $R_s$ the parasitic series resistance and $I_S$ the reverse saturation current. By applying a Taylor expansion on the Equation 2.11, the diode current becomes as stated by Equation 2.12, where $\alpha = \frac{q}{nk_BT}$.

$$I_d(V) = I_S \left( \exp\left( \frac{q(V - I \times R_s)}{nk_BT} \right) - 1 \right) \tag{2.11}$$

$$I_d(V) = I_S(\alpha V + \frac{(\alpha V)^2}{2!} + \frac{(\alpha V)^3}{3!} + ...) \tag{2.12}$$

A lumped equivalent circuit of a Schottky-barrier diode is shown in Fig. 2.8. The parasitic series resistance will reduce the amount of coupled power into the Schottky Junction. It generally depends on the thickness and doping concentration of the epilayer and the substrate used during the diodes fabrication, the ohmic contact resistance and the anode size.

[1]The concept of ideality factor is introduced to describe the deviation of the current from the ideal pure thermionic emission, n=1, due to effects such as barrier lowering due to image force, electron tunnelling or imperfections during fabrication [70]

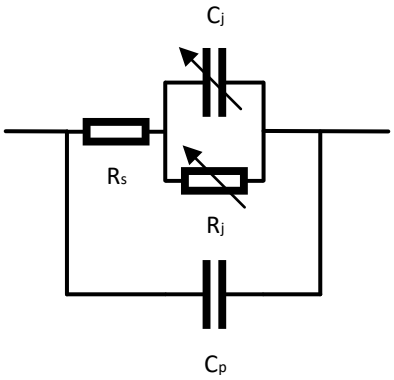


Figure 2.8: Equivalent circuit of a Schottky diode. $C_j$ and $R_j$ are respectively the junction capacitance and the non-linear resistance of the Schottky barrier. $R_s$ corresponds to the series resistance and $C_p$ is the parasitic capacitance.

$C_j$ represents the capacitance appearing in high dielectric material defined as $C_j = \varepsilon_0 \varepsilon_r A/d$ with $\varepsilon_0$ the permittivity of free space ($8.854 \times 10^{-12}$ F/m), $\varepsilon_r = 12.9$ for GaAs, A the effective area and d the thickness of the depletion region. $R_j$ is the non-linear resistance of the Schottky barrier, $R_s$ the series resistance and $C_j$ is the nonlinear junction capacitance due to the depletion region created by the Schottky contact. The junction capacitance depends on the structure and doping of epilayer. The value of $R_s$ increases when the anode size is reduced or the doping concentration is lower, degrading the diode performance when used in frequency mixers and frequency multipliers. However, for high frequency mixer operation, power loss through the non-linear junction capacitance has a very important impact on the performance of the mixer, and it is fundamental to reduce the value of $C_j$ by reducing the anode size and increasing the doping concentration. This phenomenon is commonly known as shunting effect. Also a trade-off between noise performance and bandwidth [84] has to be considered during the diode design process. Design and optimisation of Schottky based circuits is normally carried out by using 3D electromagnetic simulators to describe the filters, matching networks and diode embedding circuits, together with non-linear diode models.

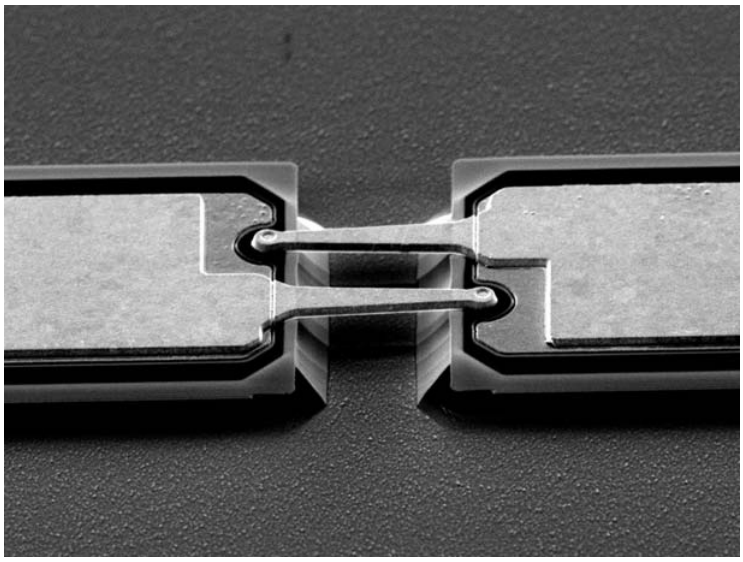

Figure 2.9: Planar anti-parallel Schottky barrier Diodes developped by Teratech Components Ltd. at the Rutherford Appleton Laboratory.

The structure of Schottky diodes was long designed as whisker-contacted diodes[220], having low parasitic capacitance, easy to fabricate but unreliable choice due to their integration complexity. During the past decades, planar Schottky diodes have been developed as an alternative for monolithic mixer devices. An anti-parallel Schottky diodes pair manufactured at RAL is shown in Fig. 2.9. Heterodyne mixing is based on the non-linear resistance of the diodes. Therefore the diode performance is the key part of the performance of the overall mixer. In addition, providing a good impedance matching between the input signals and the diodes is critical to achieve a good mixer performance. The fabrication of Schottky diodes at 1 THz and higher frequencies is technologically challenging, and the development of accurate fabrication techniques is fundamental to provide good performance mixers.

### 2.3.2 Heterodyone Technique

As stated previously, the heterodyne detection consists in the down-conversion of a high frequency or radio-frequency (RF) signal to the IF band (several GHz) by pumping the mixer with a local oscillator signal (LO) of frequency similar to the

RF signal. The analysis of the signal in the IF band is relatively simple since it is possible to use commercially available electronic components. The LO and RF voltages can be described as two simple sinusoidal signals as shown by Equation 2.13. The total voltage excitation $V_{in}$ of the diode is given by the addition of those two voltages together with a bias voltage $V_0$, see eq. 2.13.

$$\begin{cases} V_{LO} = A \times \cos(\omega_{LO} t) \\ V_{RF} = B \times \cos(\omega_{RF} t) \\ V_{in} = V_0 + V_{LO} + V_{RF} \end{cases} \tag{2.13}$$

By injecting $V_{in}$ from Equation 2.13 into Equation 2.12 characteristic of a Schottky diode device, the current can be written as a function of $\omega_{LO} = 2\pi \times f_{LO}$ and $\omega_{RF} = 2\pi \times f_{RF}$, as seen on Equation 2.14 where $a_i = \frac{I_0}{i!}\alpha^i$, $f_{LO}$ the frequency of the local oscillator and $f_{RF}$ the broad RF signal.

$$\begin{aligned} &I_d = a_0(V_0 + V_{LO} + V_{RF}) + a_1(V_0 + V_{LO} + V_{RF})^2 + ... \\ &= a_0 V_0 + a_1 V_0^2 + (a_0 + 2a_1 V_0)V_{LO} + (a_0 + 2a_1 V_0)V_{RF} + a_1 V_{LO}^2 + a_1 V_{RF}^2 + ... \\ &= a_0 V_0 + a_1 V_0^2 + A(a_0 + 2a_1 V_0)\cos(\omega_{LO} t) + B(a_0 + 2a_1 V_0)\cos(\omega_{RF} t) + \\ &\frac{a_1 A^2}{2}(1 + \cos(2\omega_{LO} t)) + \frac{a_1 B^2}{2}(1 + \cos(2\omega_{RF} t)) + \\ &\frac{a_1 AB}{2}\left(\cos[(\omega_{LO} - \omega_{RF})t] + \cos[(\omega_{LO} + \omega_{RF})t]\right) + ... \end{aligned} \tag{2.14}$$

The IF signal is defined by the $|\omega_{LO} - \omega_{RF}|$ terms in Equation 2.14. It has to be noticed that a given IF frequency can be generated by two different RF frequencies for a fixed LO frequency: RF frequencies for which $\omega_{LO} - \omega_{RF} < 0$ are called the Upper-sideband (USB) and RF frequencies where $\omega_{LO} - \omega_{RF} > 0$ are called Lower-sideband (LSB). Figure 2.10 is shows a schematic of the mixing principles where a RF signal made of the LSB and USB is down-converted to a lower frequency IF.

Based on this distinction between USB and LSB, a radiometer can operate in single sideband mode when the unwanted sideband is suppressed before mixing

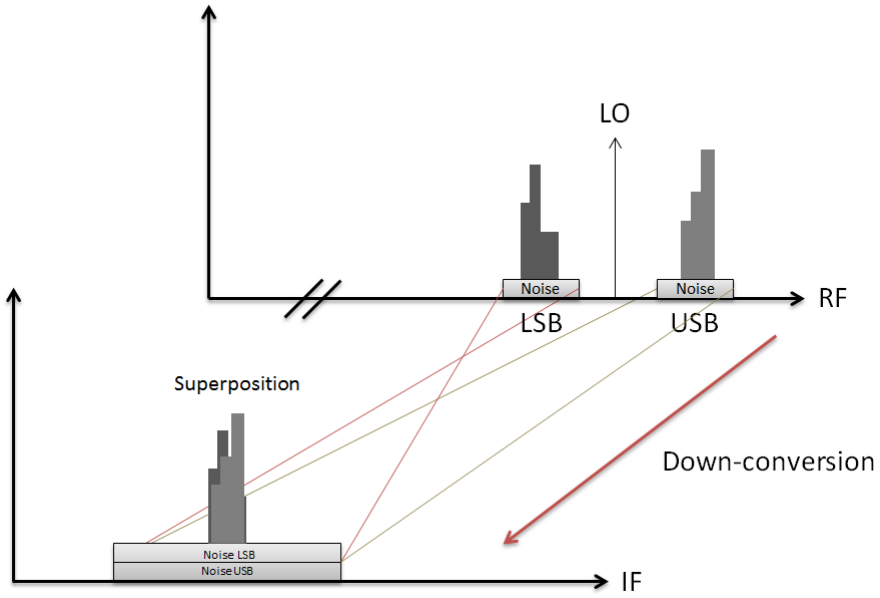


Figure 2.10: Schematic of the mixing heterodyne principle where the RF signal composed of the LSB and USB is down-converted to an intermediate frequency (IF).

with a waveguide, filters or within the mixer device configuration as explained in Section 2.3.3. If none of the sideband is suppressed, the radiometer is operating as a double sideband system where LSB and USB will be observed simultaneously. Both sidebands superposed within the same IF frequency range but the highest frequency values of the LSB will appear as the lowest values in the IF, as shown in Fig. 2.10. The impact of the radiometer operation double sideband (DSB) or single sideband (SSB) on the sensitivity is described in Section 2.3.7.

### 2.3.3 Sub-Harmonically Pumped Image Rejection Mixer

There are two widely used configurations for mixers based on Schottky diodes which are the fundamentally pumped mixers and the sub-harmonically pumped mixer (SHM)[296]. Fundamental mixers down-convert the RF signal with a LO signal to a lower frequency IF, as explained in 2.3.2, such that $f_{IF} = |f_{RF} - f_{LO}|$ and are separated in two main categories, the single-ended and balanced mixers (employing an even number of diodes). Single-ended mixers only have a single port in order to couple the RF and LO signals. Therefore beamsplitters

and couplers are needed ahead of the mixer attenuating both signals[176]. The benefit of such devices is that it is a simple design where a bias circuit can easily be integrated. Balanced mixers require at least 2 diodes and present 2 distinct ports for the RF and LO overcoming the attenuation problem of single-ended mixers. Balanced mixers have the property of rejecting the LO phase and amplitude noise (AM noise) at the IF but are noisier as they have more diodes. The parallel configuration of the diodes at the IF, decrease the impedance facilitating the matching between the IF port and the low noise amplifier (LNA). This has the impact of giving broadband bandwidth performance. Fundamental balanced mixer have been demonstrated for frequencies up to 900 GHz [285, 286]. Balanced configurations require more LO power than single-ended due to the higher number of diodes.

The sub-harmonically pumped mixers are the second kind of mixers. The down-converted IF signal is results from the difference between the RF and the second harmonic of the LO frequency source: $f_{IF} = |f_{RF} - 2 \times f_{LO}|$. Because of this characteristic they do not require a high frequency source delivering few mW of power. Therefore they are widely used in receiver systems. The most common topology for such device is to have an anti-parallel pair of planar Schottky-barrier diodes. Because of the antisymmetric current-voltage present in the diodes pair, all the even harmonics ($mf_{LO} + nf_{LO}$, m+n even) are suppressed[49, 274]. Other benefits of subharmonic mixers are similar to the balanced mixers, RF-LO ports independents, lower IF impedance than single-ended mixers, cancellation of AM noise[256, Wolff]. However the conversion loss of those mixers are slightly higher than fundamental mixers (1 or 2 dB) and the IF bandwidth lower as explained in Section 2.3.4.

Mixers, fundamental or subharmonic, are double sideband detectors (see Section 2.3.2) where the spectrum of RF signals of different frequencies are superposed in the IF. The impact of having superposed spectra is that it is not possible to unequally determine the frequency of the RF signals. It is possible to separate

the USB and LSB by using a procedure known as image rejection. Two techniques exists to perform the rejection of the unwanted sidebands. The first one consists of using a diplexer or optical filter ahead of two DSB mixers. The rejection ratio would depend on the performances of the diplexer. However the filtering method is not efficient to separate the two sidebands near their LO frequency and the diplexer element would add losses increasing the overall conversion loss of the mixers. Another technique is based on a phasing method to obtain a single sideband mixer. The RF or LO signals are phase shifted by 90°. However it is usually recommended to apply the phase shifting on the LO signal to reduce the RF losses and amplitude and phases imbalances because of the narrow bandwidth of the LO [275, 303]. The sub-harmonic image rejection used in the THz-DES was designed at RAL with an operating frequency between 320 - 360 GHz[234].

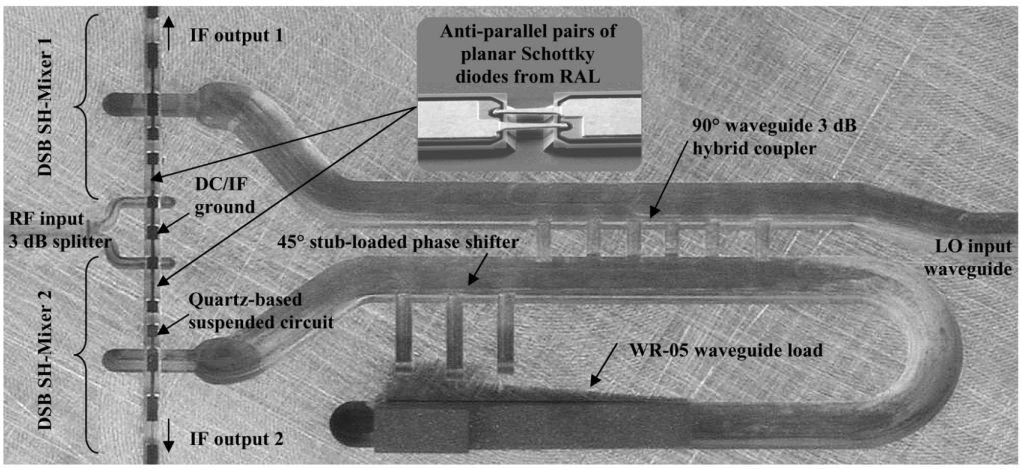


Figure 2.11: Sub-harmonic image rejection Schottky diode mixer manufactured at RAL and used in the THz-DES. Figure taken from Thomas et al.[287].

The components of this mixer are outlined in Fig. 2.11. It comprises two double sideband SHMs, LO- RF waveguides, 90° hybrids and loads in a single micro-machined block. The input RF signal is divided between 2 DSB subharmonic mixers based on an anti-parallel diode pair, by using a 3 dB waveguide power splitter. The single LO signal is separated so as to obtain two outputs via a 90° hybrid coupler [154]. A 45° stub-loaded phase shifter [10] is used at the LO so as to provide a 90° phase shift at the IF output signals. Finally an external 90°

quadrature hybrid is used to recombine the two IF signals. The phase imbalance will produce a signal corresponding to the LSB in one port and to the USB in the other IF port. This techniques is also called IQ conversion (I: in phase and Q: quadrature component). The mathematical equations illustrating this technique are presented below.

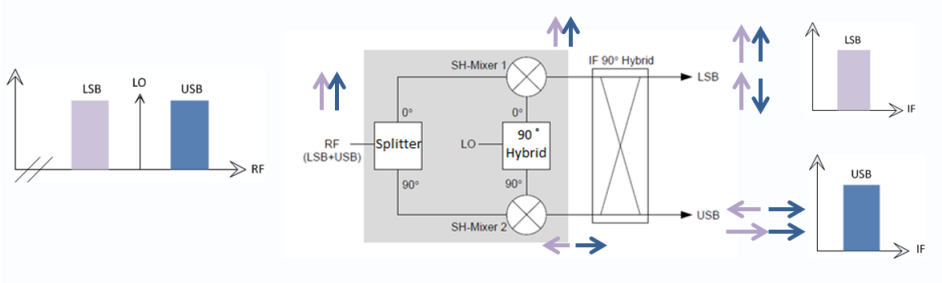


Figure 2.12: Sideband Rejection Principle of the SHIRM. Two side band from the input signal can be detected individually via the rejection mechanism [234]

Figure 2.12 presents the described rejection procedure. The LO signal ($v_{LO}$) and the RF signals ($v_{RF}$, combination of the LSB and the USB) are defined on Equation 2.15, where $A_i$, $B_i$, $C_i$ are constants. After 90° phase shift in the LO and RF signals, will produce the sideband rejection when they are recombined by the hybrid.

$$\begin{cases} v_{RF} = A_0 \times \cos(\omega_{USB} t) + B_0 \cos(\omega_{LSB} t) \\ v_{LO} = C_0 \times \cos(\omega_{LO} t) \end{cases} \tag{2.15}$$

The I and Q branches, corresponding to SHM-1 and SHM-2, have signals noted $v_{SHM-1}$ and $v_{SHM-2}$ on Equation 2.16. In the Q branch, the LSB has a phase of -90° whereas the USB has +90° phase. The final step of the rejection is achieved with the use of the external 90° quadrature hybrid.

$$\begin{cases} v_{SHM-1} = A_1 \times \cos((\omega_{USB} - 2 \times \omega_{LO}) \times t) + B_1 \times \cos((2 \times \omega_{LO} - \omega_{LSB}) \times t) \\ v_{SHM-2} = A_2 \times \cos((\omega_{USB} - 2 \times \omega_{LO})t + \frac{\pi}{2}) + B_2 \times \cos((2 \times \omega_{LO} - \omega_{LSB})t - \frac{\pi}{2}) \end{cases} \tag{2.16}$$

The final IF signals ($v_{IF-1}$ and $v_{IF-2}$) obtained at the two IF ports corresponds

to the down-converted signal of the USB and the down converted signal of the LSB in the other branch as shown on Equation 2.17.

$$v_{IF-1} = \frac{1}{\sqrt{2}}(v_{SHM-1} + v_{SHM-2}[-\frac{\pi}{2}]) = A_{out} \times \cos((\omega_{USB} - \omega_{LO})t) \quad (2.17)$$

$$v_{IF-2} = \frac{1}{\sqrt{2}}(v_{SHM-1}[-\frac{\pi}{2}] + v_{SHM-2}) = B_{out} \times \cos((\omega_{LO} - \omega_{LSB})t - \frac{\pi}{2}) \quad (2.18)$$

### 2.3.4 Radiometric Noise Contribution

In a Schottky-barrier diode, the noise of the device is coming from three main contributors, the shot noise, the thermal noise and flicker noise (detailed description elsewhere [82]). Shot noise is due to the random variations of electrons going through the barrier creating a current seen as a series of random pulses[297]. The shot noise spectral density can be written as below where I is the average current in the barrier, q the elementary charge of an electron ($1.602176634 \times 10^{-19}$ C) :

$$S_{shot}(f) = 2qI \quad (2.19)$$

The impact of the shot is over a broad range of frequency as the time employed by the carriers for surmounting the barrier is very short. It also depends on temperature as the barrier current varies depending on T as shown on Equation 2.11. The evaluation of the available noise power due to shot noise in a Schottky diode (using the previous 2qI performance) can be approximated by $\frac{HT}{2}$ where H is the diode ideality factor, T the temperature.

Flicker noise varies as 1/frequency. Its presence comes from trapped electrons in impurities when they are moving through the diode and can be reduced by the use of an unbiased device, although the observed RF signal will still move electrons within the diode. Its amplitude decreases as the frequency increases but does not totally average to 0. Therefore electronic devices will always present a

sensitivity limit which will be dictated by the flicker noise and the integration time will have no impact on it. The description of the 1/f spectral density is given by:

$$S_{flicker}(f) = \frac{\alpha \times I^2}{N \times f} \tag{2.20}$$

where I is the diode current, N the total number of carrier, $\alpha$ a parameter defined by F. Hooge.[130]. The flicker noise appears predominantly at low frequencies as stated by previous equation. There does not exist a unique and satisfactory theory to describe Flicker noise.

In 1928, J. B. Johnson [145] measured the thermal noise for the first time. Any electronic conductor components at temperature above 0K is containing free thermally excited moving electron. The random motion of those electrons generates a random variation of the electrical voltage and current at the terminals of the device. The corresponding noise power spectral densities is defined as[302]:

$$S_{thermal}(f) = hf\left(\frac{1}{2} + \frac{1}{\exp[(hf)/(k_B T)] - 1}\right) \tag{2.21}$$

where $k_B$ is Botlzmann's constant, h is Planck's constant, T is the temperature and f is the frequency. This term is independent from the frequency (white noise) only if it is assumed that $(hf)/(kT) \ll 1$ and becomes $S_{thermal}(f) = k_B T$. This is applicable, for example, at T = 290 K only if f « 6 THz or at f = 1 THz, only if T » 48 K. Decreasing the temperature of the device will therefore decrease significantly the contribution of the thermal noise.

Another kind of noise plays a significant role in radiometric system. For example, a drift noise often appears with radio-astronomical and laboratory equipment which could be due to environmental noise contributions, mechanical fluctuations within the instrument of measurement, thermal drift. This drift varies as $1/f^2$ or $1/f^3$[254]. The appearance of this noise is predominant when the integration time of the radiometer becomes higher than an optimum value defined by the Allan

variance test described in Section 2.3.8.

### 2.3.5 System Noise Temperature

According to Planck's equation, described in Section 2.2.4, a body of temperature $T_i$, in thermal equilibrium will radiate energy ($N_i$) according to the Equation 2.22 where $N_i$ is in watts, $k_B$ is the Boltzmann constant ($1.38 \times 10^{-23}$ J/K) and B, the bandwidth in hertz.

$$N_i = k_B \times T_i \times B \tag{2.22}$$

The noise performance of electronic elements, such as amplifiers, filters or receiver systems, is measured and defined by the noise factor (F) corresponding to the signal-to-noise ratio before and after the element. The approach was introduced for the first time in 1944 by Harald T. Friis[93] and is commonly used to characterise noise power within radiometer instruments. Any element in the receiver system is assumed to have a gain G and to add a noise contribution ($N_{element}$). Equation 2.23 shows the noise factor as a function of the signal power at the input ($S_{input}$) and output ($S_{output}$) of an element of the receiver and the noise power at the input ($N_{input}$) and output ($N_{output}$) of the element.

$$F = \frac{SNR_{input}}{SNR_{output}} = \frac{S_{input}/N_{input}}{S_{output}/N_{output}} \tag{2.23}$$

Considering the characteristics of the element, the output noise power can be written as a function of its gain and noise contributions as shown on Equation 2.24. By combining Equation 2.22 and 2.24 with Equation 2.23, the noise power density of the element and its output noise signal depends on the gain, the bandwidth and the device temperature (Equation 2.25).

$$\begin{aligned} S_{output} &= G \times S_{input} \\ N_{input} &= k_B \times T_{element} \times B \\ N_{output} &= G \times N_{input} + N_{element} \end{aligned} \tag{2.24}$$

$$\begin{aligned} N_{element} &= (F-1) \times G \times k_B \times T_{element} \times B \\ N_{output} &= F \times G \times k_B \times T_{element} \times B \end{aligned} \tag{2.25}$$

In a multi-stage systems such as a receiver, elements (mixer, filters, and amplifiers) are connected one after the other forming a cascade of devices. Figure 2.13 shows a simple configuration of two devices in cascade, with their gain and noise factors. The signal and noise power at the input of the first element is $S_i$ and $N_i = k_B \times T_i \times B$. The signal and noise power at the output of each element can be calculated using Equations 2.24 and 2.25. Results are shown on Equations 2.26 and 2.28 with the temperature of all the devices considered the same ($T_i$) around 290 K when devices operate at room temperature.

$$\begin{aligned} S_{out1} &= G_1 \times S_i \\ N_{out1} &= F_1 \times G_1 \times k_B \times T_i \times B \end{aligned} \tag{2.26}$$

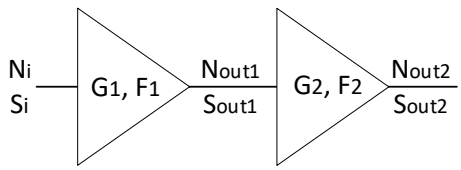


Figure 2.13: System Noise factor for 2 devices in cascade.

$$\begin{aligned} S_{out2} &= G_2 \times S_{out1} = G_2 \times G_1 \times S_i \\ N_{out2} &= G_2 \times N_{out1} + N_2 = G_2 \times F_1 \times G_1 \times k_B \times T_i \times B + (F_2 - 1) \times G_2 \times k_B \times T_i \times B \end{aligned} \tag{2.27}$$

The overall system noise factor is $F = F_1 + \frac{(F_2-1)}{G_1}$ and the overall gain in the system defined by $S_{out2}/S_i = G_1 \times G_2$, as shown on Equation 2.28. It is possible

to generalise this formula to n elements in cascade (Equation 2.29). This is called the Friis formula and can be expressed either as a function of the noise factor or as a function of the noise temperature ($T_{syst}$) as $T_{syst} = T_i \times (F - 1)$.

$$\begin{aligned} F &= \frac{S_i/N_i}{S_{out2}/N_{out2}} \\ &= \frac{S_i}{k_B \times T_i \times B} \times \frac{G_2 \times F_1 \times G_1 \times k_B \times T_i \times B + (F_2 - 1) \times G_2 \times k_B \times T_i \times B}{G_2 \times G_1 \times S_i} \\ &= F_1 + \frac{(F_2 - 1)}{G_1} \\ G_f &= G_1 \times G_2 \end{aligned} \tag{2.28}$$

$$\begin{aligned} F_{syst} &= F_1 + \frac{(F_2 - 1)}{G_1} + \frac{(F_3 - 1)}{G_1 G_2} + ... + \frac{F_n - 1}{G_1 G_2 ... G_{n-1}} \\ T_{syst} &= T_1 + \frac{T_2}{G_1} + \frac{T_3}{G_1 G_2} + ... + \frac{T_n}{G_1 G_2 ... G_{n-1}} \end{aligned} \tag{2.29}$$

The system noise temperature is a key parameter regarding the sensitivity and the good performances of a radiometer. Its importance is presented in more details in Section 2.3.7.

A technique, called Y-factor[119], method is used to measure and calculate the system noise temperature of a radiometer. The term Y refers to the ratio between two noise power levels, one measuring the radiation of a blackbody target at low temperature ("Cold") which is generally a blackbody target placed in a Dewar of liquid nitrogen. The other one is a blackbody target at room temperature or heated ("hot"). Blackbody targets are generally pyramidal shapes considered to have an emissivity close to 1 although the corresponding power reflection coefficient is typically less than -30 dB. Therefore their emission temperature is considered equal to their physical temperatures. They are described in more details in Section 3.5. The liquid nitrogen cooled cold target has an assumed physical temperature of 77.3 K at one atmosphere of pressure. The noise-power radiated by the hot and cold targets at temperatures $T_H$ and $T_C$, respectively are noted by $N_{hot}$ and $N_{cold}$, respectively, in Equation 2.30.

$$\begin{aligned} N_{hot} &= k_b B \times G_{rec} \times (T_H + T_{syst,DSB}) \\ N_{cold} &= k_b B \times G_{rec} \times (T_C + T_{syst,DSB}) \end{aligned} \tag{2.30}$$

The Y-factor corresponds to the ratio of those two power (Equation 2.31) and is calculable from the measurement of the observed output powers.

$$Y = \frac{N_{hot}}{N_{cold}} = \frac{T_H + T_{syst,DSB}}{T_C + T_{syst,DSB}} \tag{2.31}$$

From Equation 2.31, it is possible to retrieve the system noise temperature as shown by Equation 2.32. In this approach, it is considered that the gain of the receiver did not change while the measurement was carried out. This approximation is valid as often hot/cold observation are done faster than gain drift with the receiver, this is defined by the stability of the radiometer as shown in Section 4.2.2.

$$T_{syst,DSB} = \frac{T_H - Y \times T_C}{Y - 1} \tag{2.32}$$

As explained in Section 2.3.2, radiometer can operate in a single-sideband mode instead of double sideband. Kerr et al. described in 1993 [152], the difference between the system noise temperature observed by those two kind of radiometers. Effectively, the SSB noise temperature would be a combination of the measured DSB noise temperature and the power gain at the signal ($G_s$) and image ($G_i$) frequencies, as described by Wengler et al. [312]. A sideband rejection factor can be defined as $R = \frac{G_i}{G_s}$.

$$T_{SSB} = T_{DSB}\left(1 + \frac{G_s}{G_i}\right) = T_{DSB}\left(1 + \frac{1}{R}\right) \tag{2.33}$$

Method to calculate $T_{SSB}$ exist and are well established[55], for example by introducing CW signals of know intensities into the LSB and USB and recording the IF response for each case or measuring ratio of CW signals in each sideband

and measuring the changes in output power at the IF ports as explained in details elsewhere[156].

### 2.3.6 Radiometric Calibration

To retrieve the brightness temperature of the observed desorption cell scene from acquired data; we use a two-point calibration scheme[151], which is a linear radiometer transfer function. The instrument gain (G) and the integrator offset (I) are used to calculate the brightness temperature (BT) of the scene viewed (line-of-sight) by the radiometer. The gain represents the amount by which an incoming signal is amplified before detection and can vary over time due to different noise contribution in the receiver. The $P_{hot}$ and $P_{cold}$ terms represent the radiometer power output readings corresponding to the introduction of the hot ($T_{hot}$) and cold ($T_{cold}$) reference target temperatures into the radiometer signal path.

$$\begin{cases} G = \frac{P_{hot} - P_{cold}}{T_{hot} - T_{cold}} \\ \\ I = P_{cold} - T_{cold} \times G \end{cases} \tag{2.34}$$

The expression of a scene view brightness temperature (line-of-sight), $BT_{scene}$, is given by Equation 2.35. It depends on the previously described terms, G and I, and on the measured radiometer output power corresponding to the scene view $P_{scene}$.

$$BT_{scene} = \frac{P_{scene} - I}{G} \tag{2.35}$$

Variations in environmental conditions can affect the cold target brightness temperature and thereby introduce an error in the radiometer calibration[181, 185]. The characterisation of an error within the calibration targets temperature is presented in Section 4.3.

### 2.3.7 Radiometric Sensitivity

The radiometric sensitivity of a total power radiometer is a key element when performing spectroscopic observation. It will determine the performance of the experiment in terms of noise equivalent temperature difference (NEδT). This term was firstly introduced in 1964[290] and is commonly use for the characterisation of radiometers [135, 248]. In 1979, Dr. James C. Bremer[29] detailed the expression of the NEδT as the sum of three uncorrelated noise power errors, also reviewed by Hersman in 1981 [127].

$$\mathrm{NE\delta T} = (\mathrm{T_{syst}} + \mathrm{T_{scene}}) \times \sqrt{\frac{1}{\mathrm{B} \times \tau_\mathrm{s}} + \frac{1}{\mathrm{B} \times \tau_\mathrm{c}} + (\frac{\Delta \mathrm{G}}{\mathrm{G}})^2} \tag{2.36}$$

The NEδT is shown on Equation 2.36 where B the spectral bandwidth, $\mathrm{T_{syst}}$ and $\mathrm{T_{scene}}$ are respectively the receiver (or system) noise temperature and the apparent temperature at the scene view. The first term ($\frac{1}{\mathrm{B}\times\tau_\mathrm{s}}$) corresponds to the scene noise power error which are fluctuations within the measurement of the power at the scene view with an integration time of $\tau_\mathrm{s}$. The gain of the overall system (G), as described in Section 2.3.4, drift over the experimental time. Therefore noise power fluctuation will appears during the calibration procedure which is corresponding to the second term ($\frac{1}{\mathrm{B}\times\tau_\mathrm{c}}$) where $\tau_\mathrm{c}$ is calibration target integration time. Finally, as calibration view and scene view are not perform simultaneously, a potential drift in gain ($\Delta$G) will create the last term called the gain fluctuation ($\frac{\Delta \mathrm{G}}{\mathrm{G}}$).

Based on this definition of the radiometer sensitivity, the best interests of any instrument is to minimize the gain fluctuation ($\frac{\Delta \mathrm{G}}{\mathrm{G}}$) and maximising $\tau_\mathrm{s}$ and $\tau_\mathrm{c}$ for a give spectral bandwidth. A technique called the Allan Variance is able to determine the optimum integration to use before the gain fluctuation becomes the predominant term. The noise temperature, defined earlier, or the bandwidth are also impacting significantly the NEδT.

### 2.3.8 Allan Variance

The Allan variance technique is commonly used in radio astronomy (for example in ALMA [99]) so as to define the stability of instrumental systems. It was developed in 1966 by D. W. Allan[4] and permits to observe the noises contributions present in a data samples acquired by the instrument as a function of its integration time. The minimum value taken by the Allan variance ($\sigma_y^2(\tau)$) corresponds to the optimal integration time in order to perform observation when the noise level is at its lowest [254, 315], defining the measurement integration in Equation 2.36.

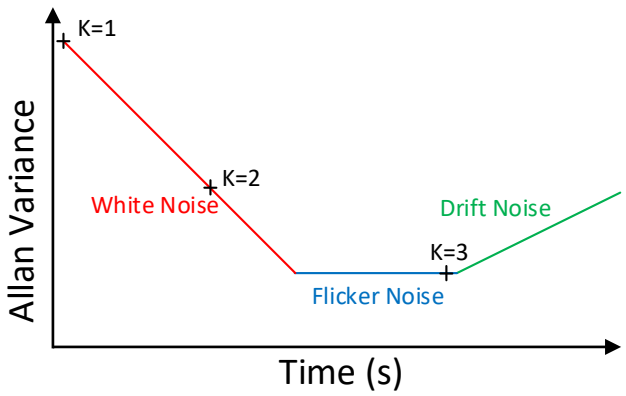


Figure 2.14: Typical Allan variance figure showing the different noise contributions as a function of the integration time, $\tau$.

Figure 2.14 shows the impact of the noise contributions on the Allan variance. It appears that $\sigma_y^2(\tau)$ varies following Equation 2.37, where c is a constant and $\beta$ the slope in the log scale. When $\beta = -1$, the white noise is predominant in the system [16], red curve in Fig. 2.14. The flicker noise (blue curve) with a 1/f dependence appears to have a slope of $\beta = 0$ whereas at higher integration time, the drift noise (green curve) produced by variations over time in temperature, gain fluctuations will present a slope $1 < \beta < 2$.

$$\sigma_y^2(\tau) = c \times \tau^{\beta} \tag{2.37}$$

The procedure to calculate the Allan variance is well established and described in details by Schieder, R. and Kramer, C.[254]. The instrument is set-up to observe a blackbody target of constant temperature with a small integration time ($\tau$). From this raw data it possible to increase the averaging period by selecting a different length of sample, increasing the summing factor seen in Fig. 2.15. For example, K = 1 would corresponds to the data taken every $\tau$ s noted $S_i$, K = 2 would be the average of $S_i$ and $S_{i+1}$, K = 3 would be taking into account the average of $S_i$, $S_{i+1}$ and $S_{i+2}$ for K=1. In this thesis, an overlapping technique was used, decreasing the degree of freedom as data are overlapping each other as shown in Fig. 2.15. This method improves the estimation of the stability point []. The measured Allan variance for K=1, 2 or 3 will then be plotted at a function of the integration, $1 \times \tau$, $2 \times \tau$ and $3 \times \tau$ (Fig. 2.14).

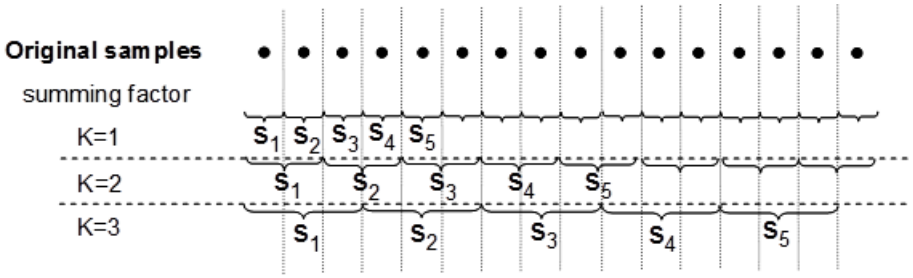


Figure 2.15: Allan variance procedure for a data set. K represents the number of data points per selection. In our case S would be the integration time $\tau$.

The data acquired every $\tau$ s ($S_i$) are constituting a samples of length M. The variable $T = K \times \tau$ as the integration time for each summing factor K as defined by Fig. 2.15), K = 1 to M. The mean value of each sample is calculated $\bar{y}_i(T)$. Finally the Allan variance expression, $\sigma_y^2$, is shown in Equation 2.38.

$$\sigma_y^2(T) = \frac{1}{2(M-1)} \sum_{i=1}^{M-1} \left[\bar{y}_{i+1}(\tau) - \bar{y}_i(\tau)\right]^2 \tag{2.38}$$

## 2.4 Optical Principles

"Quasi-optical systems"[107] are defined as compact optical systems in which diffraction effects are important and where Gaussian beam mode simulates the behaviour of the electromagnetic radiations as neither geometrical optics, due to the diffraction involve at mm-wavelength, nor physical optics (long computational time in systems with many elements) are not appropriate. Antennas and calibration modules for radiometer, are designed on quasi-optical principles.

### 2.4.1 Quasi Optics

The propagation of electromagnetic field radiations can be seen as a Gaussian intensity distribution, which do not change with propagation. It is a well-defined method originally developed for laser beam propagate and is explained by many authors [107, 169]. Gaussian beam mode analysis describes accurately the propagation of the beams and the location of its characteristic depending on the kind of horn used. The advantage is that it determines the depth of filed and beam radius which are necessary to design complex quasi-optical systems [198]. Only the first (fundamental) and single mode of the electromagnetic field propagating is considered as it is an adequate approximation for quasi-optic system.

For a Gaussian beam, R(z) and w(z) represent respectively the wavefront radius of curvature and the beam width of the propagating wave (Equation 2.4.2).

$$\begin{cases} w(z) = w_0 \times \left(1 + \left(\frac{z}{z_0}\right)^2\right)^{\frac{1}{2}} \\ R(z) = z \times \left(1 + \left(\frac{z_0}{z}\right)^2\right) \\ w_0 = \left(\frac{\lambda z_0}{\pi}\right)^{\frac{1}{2}} \end{cases} \tag{2.39}$$

w(z) is the beam radius and $w_0$ is called the waist, the smallest radius of the wave propagation. $z_0$ determines also the spot length where the beam is focused around the waist (Equation 2.40).

$$\begin{cases} I(r,z) = I_0 \left(\frac{w_0}{w(z)}\right)^2 \exp\left(-\frac{2r^2}{w(z)^2}\right) \\ P(r) = \int_0^r I(r,z) \times 2\pi r dr = \frac{1}{2} I_0 \times \left(\frac{w_0}{w(z)}\right)^2 \times \left(1 - \exp\left(-\frac{2r^2}{w_0^2}\right)\right) \end{cases} \tag{2.40}$$

The relative distribution power density of the Gaussian beam's fundamental mode can also be expressed as the edge taper $T_e$ at a radius $r_e$ (Equation 2.41). $T_e$ represents the relative power at a radius re. It is expressed as the ratio between on-axis power of the Gaussian distribution, the preferred unit is dB ( Table 2.1).

$$\left\{ \frac{r_e}{w} = 0.3393 \times (T_e(dB))^{0.5} \right. \tag{2.41}$$

| $T_e$(dB) | $T_e(r_e)$ | $r_e/w$ |
|---|---|---|
| 0.00 | 100 % | 0 |
| 3.00 | 50.11 % | 0.588 |
| 20 | 1.0 % | 1.517 |
| 40 | 0.01 % | 2.146 |

Table 2.1: Fraction of power and ratio between the radius of the beam as a function of the edge taper

Using the Gaussian approximation it is possible to calculate and determine the properties of the input beam light propagating through the instrument. This will permit to define the size of the optic, windows to use and the distance between them so that the beam is not truncated.

### 2.4.2 FeedHorn

Feedhorns are the antennae of the radiometer system. They coupled the radiations emaning from the free space (environment) to a waveguide structure within the mixer block use as detector. The impedance of the free space is different to the one of the waveguide, which create an impedance mismatch. The power of radiations will be reflecting due to this mismatch and only a small amount is coupled into the waveguide, therefore detected. Feedhorns are coupling the radiations

with various efficiency, polarization, bandwidths and are highly directional[122].

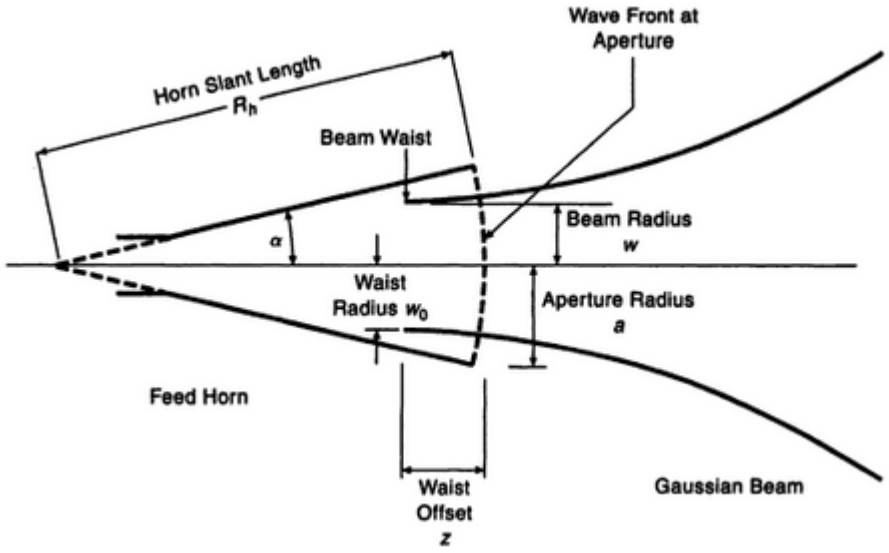


Figure 2.16: Schematic diagram of the Gaussian optics involved in a feedhorn. [107]

Figure 2.16, shows the position of the waist radius ($\omega_0$) and beam waist($\omega$) as a function of the length of the feedhorn and its aperture radius. The beam waist, located at a distance z from the feed horn aperture, depends on the waist radius $\omega_0$ and a coupling parameter ($\varkappa$), see Equation 2.42.

$$\begin{cases} \omega_0 = \dfrac{\varkappa \times a}{\sqrt{1+\left[\frac{\pi \varkappa^2 a^2}{\lambda R_h}\right]^2}} \\ z = \dfrac{R_h}{1+\left[\frac{\lambda R_h}{\pi \varkappa^2 a^2}\right]^2} \end{cases} \tag{2.42}$$

There are different types of feeds such as corrugated circular or diagonal[107]. Corrugated circular feed horn are flared waveguide section with grooves into their internal surface with a transition to rectangular region. Rectangular feedhorns are designed with squared aperture. Parameters for optimum coupling with the incoming electric field can be found depending on the geometry of the feed itself. It is defined as the ratio between the beam radius at the exit of the feed horn ($\omega_a$) and the aperture radius (a): $\varkappa = \frac{\omega_a}{a}$. Table 2.2 below represents this parameter for various design of feed.

Diagonal horns were one of the first designed horn structures[144]. However

| FeedHorn | $\varkappa$ |
|---|---|
| Corrugated circular | 0.644 |
| Diagonal | 0.43 |

Table 2.2: Coupling parameter of different kinds of feedhorn.

that type of horn has some limitations such as an asymmetrical beam pattern, relatively high side lobes in the $45^{o}$ plane which are cross polarised, making it unsuitable for polarisation sensitive detections for example. A corrugated circular horn generally delivers high beam efficiency, low side lobe levels, great return loss and the same phase in every cut of antenna angle with a very good axial symmetry. Therefore it is a desired choice for receivers system[143, 283].

## 2.5 Desorption Activation Energy

Temperature programmed desorption (TPD) is a very powerful and simple technique used in surface science, first described by Apker in 1948[9]. It has been used for the study of many astrophysical interesting molecules and ice systems over the past decades. Generally the adsorption of metal surfaces is a non-activated process, meaning that the differential heat of adsorption is equal to the desorption activation energy ($E_{des}$)[157]. As explained in Section 1.3.2, laboratory based TPD cannot fully reproduce the thermal desorption occurring on interstellar dust particles but it gives qualitative values on sublimation temperature, order of reaction, chemical reactions and desorption energy.

There are three kinetic orders of desorption, $0^{th}$, $1^{st}$ and $2^{nd}$. The $0^{th}$ order of desorption is generally observed for multilayer ice configurations where the slopes of desorption are similar for different surface coverage (as seen in Chapter 5). The $1^{st}$ order occurs when deposited molecules are adsorbed by the substrate and then desorb without dissociating, leading to a desorption temperature independent of coverage. The $2^{nd}$ order of desorption appears when adsorbed molecules are dissociating on the surface prior to their desorption[165]. Only the $0^{th}$ order will

be considered here as all THz-DES results are compliant with this order of the desorption.

The rate of desorption, as defined in Section 1.3.2, can be described as a function of the surface coverage ($\vartheta$), the desorption rate constant ($k_{des}$) and the kinetic order of desorption (m)[175, 322] and the time (t) as shown on Equation 2.43[157].

$$R_{des} = k_{des} \times \vartheta^{m} = -d(\vartheta)/dt \tag{2.43}$$

Adsorption is an activated process following Arrhenius law and equations. Therefore the desorption rate can written as:

$$k_{des} = \nu(\vartheta) \times \exp\left(-\frac{E(\vartheta)}{RT}\right) \tag{2.44}$$

where $\nu(\vartheta)$ is the pre-exponential factor, T the temperature and R the gas constant (1.9823 cal/(mol.K)).

Thermal desorption is usually described via the Polanyi-Wigner equation[223] defining the rate of desorption of molecular species from a surface. Equation 2.45 is the combination of Equations 2.43 and 2.44, giving the rate of desorption (r) as defined by De Jong et al.[60] where $\vartheta$ is the adsorbate coverage, t the time, $\nu$ the pre-exponential factor of desorption, n the order of desorption, E the activation energy of desorption and T the temperature.

$$r(\vartheta) = -\frac{d\vartheta}{dt} = \nu(\vartheta)\vartheta^{m}\exp\left(-\frac{E(\vartheta)}{RT}\right) \tag{2.45}$$

It possible to express the rate of desorption as a function of the temperature ($R_m(\vartheta)$) instead of the time as t and T are related by the heating rate $\beta = \frac{dT}{dt}$, as shown on Equation 2.46.

$$R_m(\vartheta) = -\frac{d\vartheta}{dT} = -\frac{d\vartheta}{dt} \times \frac{dt}{dT} = \frac{\nu(\vartheta)\vartheta^{m}}{\beta}\exp\left(-\frac{E(\vartheta)}{RT}\right) \tag{2.46}$$

De Jong et al.[60] is presenting various ways to calculate the desorption energy from TPD data depending on the desorption order. In our case only two methods can be used as THz-DES desorption assumed to follow a $0^{th}$order. A complete analysis[157], can be applied on the TPD results by directly fitting the desorption rate using the Equation 2.46. From the fitting function, the desorption energy is calculated. The second method is called Leading edge analysis[72]. It consists in applying a logarithmic function to the desorption rate. Then plotting it as a function of (1/T) will give to a straight line with a slope of -$E_{des}$/R as shown by Equation 2.47:

$$\ln(R_0) = \ln\left(\frac{\nu(\vartheta)}{\beta}\right) - \frac{E_{des}}{RT} \tag{2.47}$$

## 2.6 Summary

This chapter presented the theoretical background in order to understand the concepts explained in details in this thesis. Spectroscopic techniques are at the centre of the THz-DES technique. Emission spectra will be shown in Chapter 4. Quasi-optics was used to development the interfaces within the THz-DES instrument in Chapter 3. The desorption energy is first introduced in Chapter 5 and is used as the quantitative parameter retrieve from THz-DES results. Finally the heart of the THz-DES is the instrument used based on the radiometry technology described in this chapter. Those concepts will be used in Chapters 3 and 4.

# Chapter 3

# Terahertz Desorption Emission Spectroscopy (THz-DES)[1]

A scientific experiment has been developed to study the gas phase emission spectroscopy of molecules in the terahertz frequency range (320-350 GHz). The measurement technique is called "Terahertz Desorption Emission Spectroscopy" (THz-DES). In this chapter, an overview of the technique is provided, detailing each element of the experiment and its methodology. The aim is to determine the feasibility of the technique, i.e. detecting molecules in the gas phase after they have thermally sublimated from an ice surface, held at high vacuum.

## 3.1 Introduction

To realise the novel THz-DES experiment a total-power radiometer was interfaced with a vacuum chamber, coupled to a dosing line, and ices were formed on a 77 K

[1]Auriacombe, O. et al, Review of scientific Instruments, in prep.

cold finger in the vacuum, heated, desorbed and the resulting molecules detected by ultra-high resolution emission spectroscopy. The sensitive, high-spectral resolution radiometer at the core of the THz-DES instrument was originally developed by the Millimetre Wave Technology Group at Rutherford Appleton Laboratory (RAL Space) for atmospheric remote sensing of the Earth. Its main purpose was to observe water emission in the atmosphere at 325 GHz [233] but will now be used to perform gas-phase emission spectroscopy of molecules sublimating from interstellar ice analogues through thermal desorption mechanism. As such, it provides a unique way of analysing thermal desorption whilst producing data resembling direct astrophysical observations of molecules in star forming regions. That is, the excitation level of species evolving from the ice mantle is directly measured by the radiometer in the gas phase and can be linked to emission features observed in space by ground-based observational facilities.

## 3.2 THz-DES Experimental Overview

The THz-DES system comprises 3 main elements (see Fig. 3.1):

- (A) Desorption chamber.
- (B) THz radiometer.
- (C) Data acquisition and Processing

The desorption Chamber ((A) in Fig. 3.1) consists of the combination of a vacuum cell, a dosing line, a cold trap and a background source. The vacuum cell is actively pumped to high vacuum, conditions under which it is possible to form (or deposit) ices on a cold trap and subsequently desorb the material into the gas phase by heating it. The ice are typically formed by condensating a fixed amount of gas (from an external dosing line) onto the pre-cooled 77 K surface of the cold trap by opening a needle to the chamber. In order to maximise the measurement signal-to-noise ratio a cold background is required and achieved by terminating

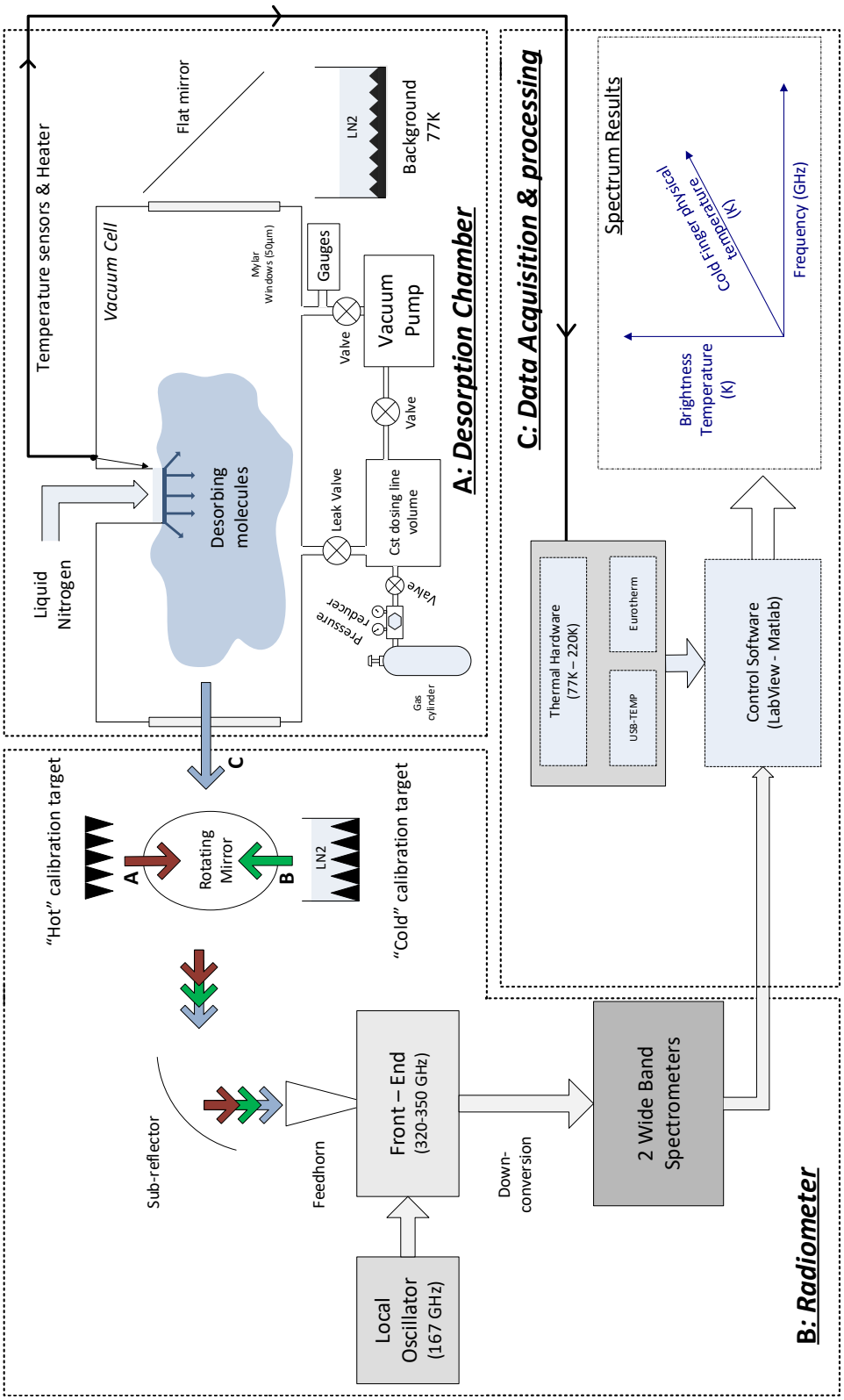


Figure 3.1: Schematic of the THz-DES experiment, showing the desorption chamber (A), the THz radiometer (B) and the data acquisition and processing module (C). See text for full details.

the vacuum cell with a 77 K blackbody background target. All molecules will emit radiations a temperature higher than the background target, hence enabling the molecules to be detected in emission.

The THz radiometer ((B) in Fig. 3.1) is a total-power heterodyne instrument operating at room temperature which incorporates a down-converting receiver operating in the frequency band 320-350 GHz, two spectrometers and a calibration sub-system with two blackbody targets (maintained at 300 K and 77 K). The receiver formed of a front-end and a local oscillator has a novel architecture enabling single-sideband observations. The ultra-high spectral resolution is achieved with the use of the spectrometers units. Finally, calibrated spectra can be generated of the observed optical path through the vacuum cell, (called scene-view, optical path C in Fig. 3.1) by measuring the brightness temperature of the calibration targets (Optical paths A and B for 'hot' and 'cold' targets) and using the linear transfer function of the receiver to derive the 'scene' brightness temperature. This means that the spectroscopic data are not only accurate frequency informations but have an absolute intensity measurement, explained in more details in Section 3.6.1.

The data acquisition and processing module ((C) in Fig. 3.1) is used to control the overall experiment, acquire and save the data, generate the spectral brightness temperature of the molecules and retrieve physical parameter such as the desorption energy (explained in Chapter 5). Custom LabVIEW software is used to configure and control the THz radiometer, measure intensity for various optical paths (A, B or C)and to set and monitor the cold trap temperature. The resulting data are processed using Matlab scripts, giving calibrated, frequency-resolved, brightness temperature of the emitted radiations from gas molecules, versus the surface temperature of the cold trap and the spectral frequency.

In Figure 3.2, a proof-of-concept THz-DES set-up is shown to indicate the desorption chamber and dosing line (left) and the THz radiometer (right).

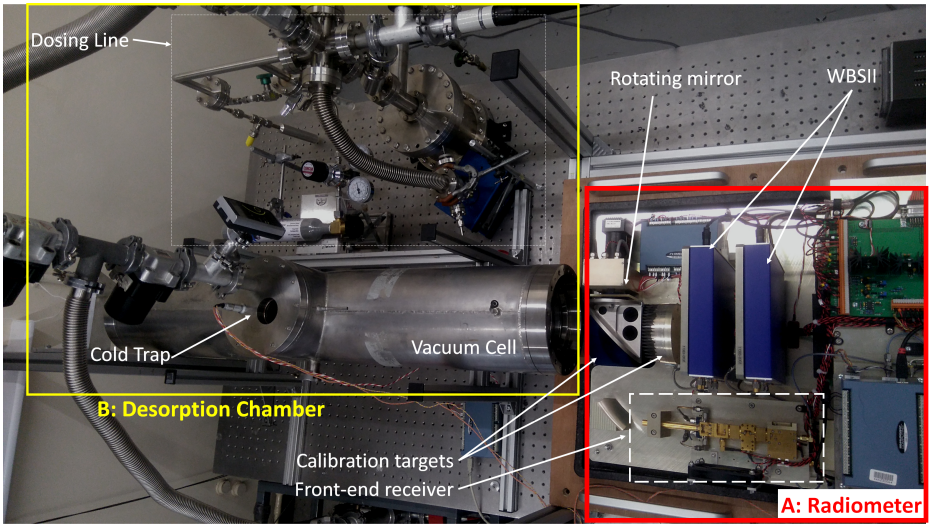


Figure 3.2: The prototype THz-DES experiment. Desorption chamber (left), THz radiometer (right).

## 3.3 The Desorption Chamber

The desorption chamber is the central element of the experimental set-up, see Fig. 3.3. It comprises a vacuum cell, a dosing line and a cold trap which are necessary to grow and sublimate ices to mirror thermal desorption. Moreover a background source, made of a blackbody target in a dewar filled of Liquid Nitrogen ($LN_2$), is completing the desorption chamber.

### 3.3.1 The Vacuum Cell

The vacuum cell is a 1 m long stainless steel cell with circular apertures of 130 mm diameter at each end. Two 50 μm thick Mylar window films (Goodfellow) are located at either end of the cell. Mylar is transparent between 320-350 GHz with a refractive index between 1.58 and 1.64. Consequently each window provides a signal transmission of typically 93%[167] within the spectral range of the experiment. However since the overall path incorporates both windows, a Fabry-Perot interference effect is introduced that results in a frequency dependent variation of the spectral noise floor baseline (see Section 4.3.2). In addition, Mylar has a relatively high permeability coefficient, dominated by water ($100.\frac{cm^2}{s.Pa}.10^{-13}$ at 298

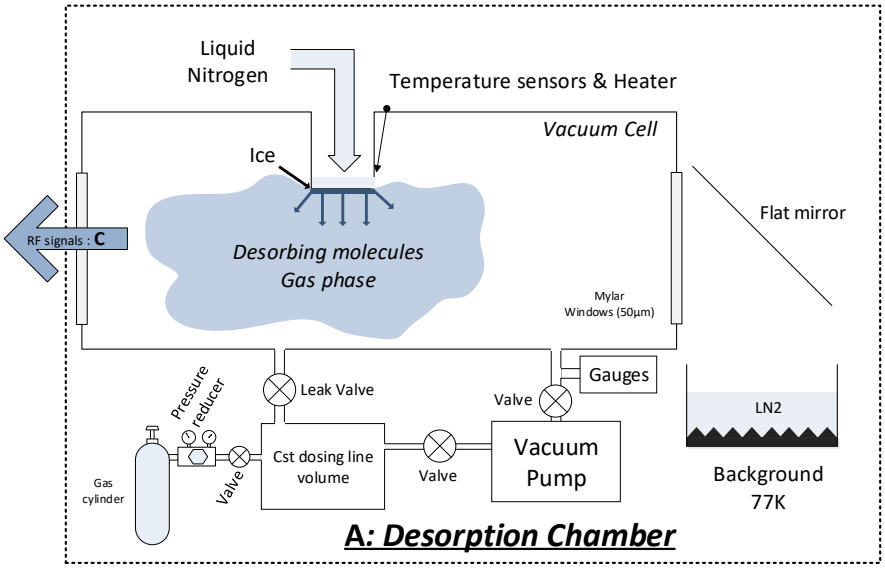


Figure 3.3: The desorption chamber of the THz-DES experiment. See text for details.

K), which means water molecules preferentially leak into the cell over time. This effect is explained in details in Chapter 4.4.2 and the water leak was measured of $1.73 \times 10^{-4}$ mbar/s in a static mode (no pumping on the cell). Because the base pressure during a THz-DES experiment is around $10^{-5}$ mbar (measured via pirani and penning gauges (PR10-K Edwards and Penning CP25-K Edwards)) and THz-DES is operating in a dynamic mode (permanent pumping on the vacuum cell), this leak do not impact the THz-DES results. However, it will have a small impact during the ice deposition as explained in Section 3.3.4.

### 3.3.2 The Dosing Line

The dosing line is shown in Fig. 3.3. Its purpose is to calibrate a known volume of gas in a constant volume (3.2 L) at 25 mbar prior to its release into the vacuum chamber. The quantity of gaseous material is monitored by Pirani gauges (Leybold Diavac-N and PR010 Balzers). For the current THz-DES three lecture bottles where selected containing $N_2O$, $H_2O$ and $CH_3OH$ in gaseous and liquid phases. Those gaseous molecules will eventually enter the vacuum cell at a con-

stant rate determined via a precise needle valve. The deposition procedure of the gaseous molecules in the dosing to form ice inside the vacuum cell is detailed in Section 3.3.4. Between two deposition cycles, the valve connecting the dosing line to the pump is opened to achieve a pressure below $10^{-4}$ mbar so as to 'clean' the volume using rotary and turbo pumps (Leybold vacuum, Turbotronik NT-50).

### 3.3.3 The Cold Trap

Figure 3.4 shows the cold trap used in the THz-DES experiment. It has been designed and manufactured in order to match the requirement of the THz-DES proof-of-concept experiment, a surface temperature of the trap of 77 K.

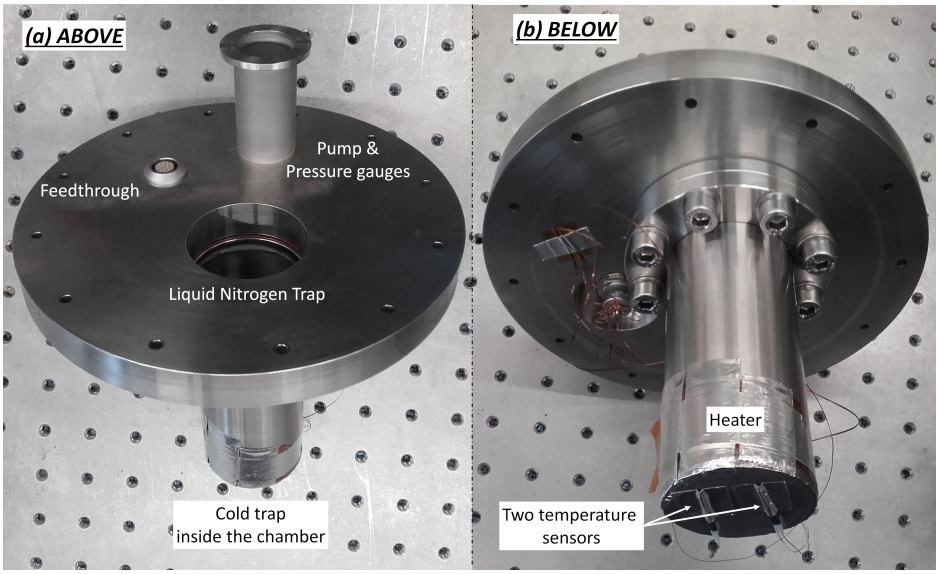


Figure 3.4: Pictures of the cold trap. (a) View from above (outside the vacuum cell), where the feedthrough output, the CF flange and the trap entry are visible. (b) Below view, inside the vacuum cell with the temperature sensors and the heater. The bottom of the flange is where the ice is grown.

Figure 3.4 (a) shows the feedthrough (LEMO), a CF-flange where the gauges and pumps are connected and the trap into which liquid nitrogen is introduced. The trap is a CF stainless steel half nipple with a diameter of 50.8 mm and height of 120 mm. A very thin piece of stainless steel is welded to the bottom of trap in order to contain the liquid nitrogen, which is inserted from the outside of the chamber into the trap. A kapton insulated heater is mounted to the half nipple

wall, and two platinum resistance temperature sensors (PT100) are mounted to the bottom surface of the trap (Fig. 3.4 (b)). A Eurotherm PID controller, in conjunction with the heater and one of the PT100 sensors, is used to control the trap temperature. The second PT100 is connected to an external data acquisition device (USB-TEMP-AI) for continuous logging of the trap temperature. All electrical wiring inside the chamber is made from 36AWG phosphor-bronze wires suitable for cryogenic use, ensuring a low thermal conductivity at low temperature.

### 3.3.4 Ice formation

Three methods exist for growing ice on the cold finger. The first two methods introduce a defined amount of gas into the vacuum cell when the cold finger is already cooled to a base temperature of 77 K. In the first method the valve between the cell and the pump is closed (static regime) and in the second this valve remains open (dynamic regime) and the pumping continues on the cell. Due to the non-directional nature of the deposition, the advantage of the static regime is a higher level of ice growth. This is because continual pumping on the cell results in gas being pumped out of the cell before it can be deposited on the cold trap. The third method introduces the gas into the cell in the static regime (valve closed) before the cold trap is cooled to 77 K. This means that the cell is filled to a known pressure before the ice layers are grown on the cold trap. This technique cannot be used to form binary ice - ice made of two molecular species. As their sublimation points are different they will always grow the same manner: the bottom layer will be formed of the molecules having the highest sublimation point, and the top layer with molecules having the lowest sublimation point.

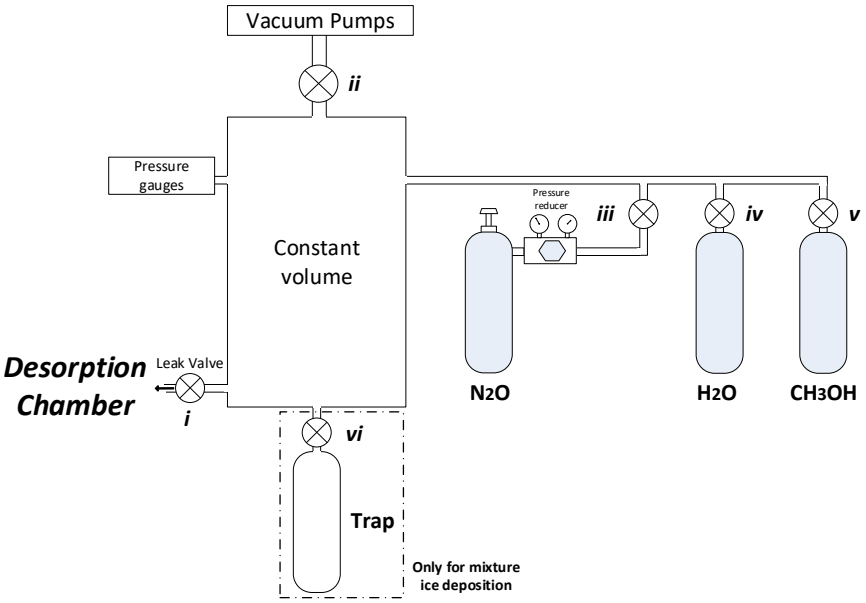


Figure 3.5: THz-DES dosing line configuration for nitrous oxide, water or methanol molecules. The dosing line after being put under high vacuum, is filled with the desired molecules. The cold trap in the desorption is cooled down to 77 K. The desorption chamber is isolated and molecules from the dosing line are depositing on the cold surface.

Based on the above rationale the first option was selected for the experiment. The deposition mechanism of the ice has been introduced in Section 3.3.2. The dosing line is shown in Fig. 3.5. Only pure deposition is presented in this Section for $N_2O$, $H_2O$ and $CH_3OH$, meaning that valve *vi* is close as only needed for mixture deposition. Prior to the deposition, desorption chamber and dosing line are kept separately under vacuum with a rotary pump to a pressure lower than $10^{-3}$ mbar (valve *i* close). The standard procedure is referred as 1 exposure time deposition:

- Introduce 25 mbar of gaseous molecules in the constant volume: valves *i and ii* close; opening valve *iii* for $N_2O$ or freeze-pump-thaw cycle via valve *iv or v* for $H_2O$ or $CH_3OH$.

- Cool down the cold finger temperature to 77 K while still pumping on the desorption chamber: valves *i and ii* close.

- Once the surface temperature reached 77 K, isolate the desorption from its pumping system and open valve *i*.
- Keep valve *i* open until the pressure in the dosing valve reaches $1.10^{-2}$ mbar. Then close valve *i*.
- Wait until the pressure in the desorption chamber reaches $1.10^{-3}$ mbar. The minimum number of molecules deposited onto the cold trap was estimated to be $2 \times 10^{20}$molecules/cm$^2$. Open valve *ii* so as to clean the dosing line.
- Connect the pumping system to the desorption chamber to reach $10^{-5}$ mbar.

The way gaseous molecules are obtained in the dosing line depends on their forms, liquid or gaseous in the lecture bottle. $N_2O$ is commercially available in the gas phase in a lecture bottle and is easily introduced with the right quantity (monitoring with the pressure gauge) in the dosing line with valve *iii*. $H_2O$ and $CH_3OH$ molecules are stored in their liquid phase. A freeze-pump-thaw cycle is applied on their containers to remove residual molecules which sublimate at low temperature - low pressure. Liquid molecules are firstly frozen in their sample cylinders with liquid nitrogen (valve *iv or v* close). Once all $H_2O$ or $CH_3OH$ froze, the lecture bottle was put under vacuum (valves *ii* and *iv or v* open). The pressure will drop and the temperature will increase accordingly to their phase diagram. As soon as the pressure increases, it means that the sublimation of $H_2O$ or $CH_3OH$ is happening. At that moment, the valve *iv or v* is closed and a new cycle is performed. In general, it takes 3 cycles to remove all impurities in the liquid [89]. For the last cycle, when the desired molecules starts to sublimate in the dosing volume, the valve *ii* is closed and the desired quantity is monitored using the pressure gauge while the liquid - vapour equilibrium settles.

### 3.3.5 Ice Desorption

Figure 3.6 shows a typical set-point THz-DES temperature curve over time. Once all the liquid nitrogen in the cold trap has passively boiled off (at t=50 s), the temperature of the cold trap rises, as the thermal control system, controlled by the Eurotherm PID controller, is trying to reach the predefined temperature set-point previously defined. Even with no heater power applied the temperature of the trap will still rise to room temperature due to thermal conduction between the flange and the chamber walls and the air convection in the cold trap.

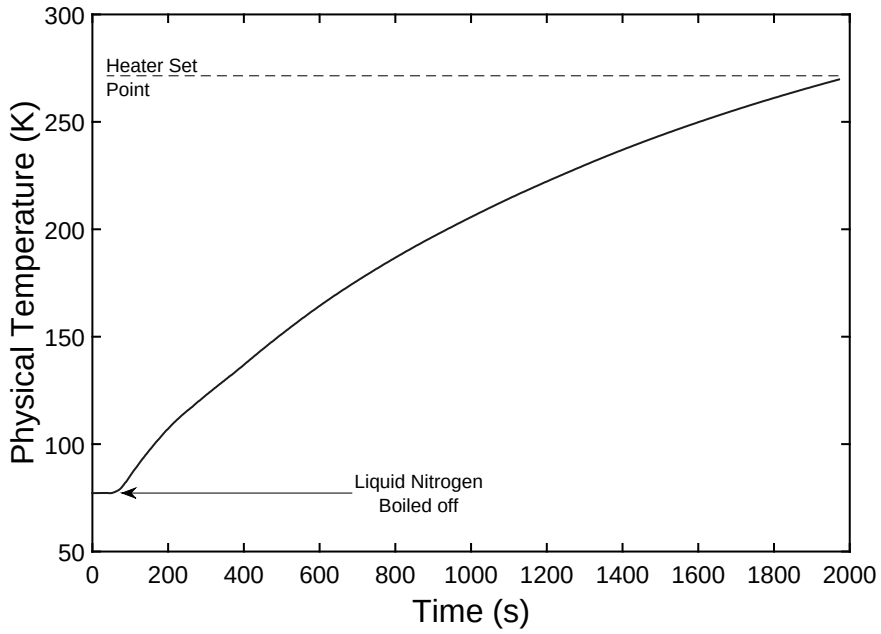


Figure 3.6: Physical temperature of the cold trap over time during a desorption experiment. The temperature stays constant at 77 K as the liquid nitrogen passively boils off from the trap. Once the liquid nitrogen has completely boiled off, the resistor heats the trap to the set point chosen.

The present thermal control system can only apply heat at a fixed power, resulting in a non-linear positive temperature curve profile without cooling system to regulate the temperature. A more sophisticated control system would enable variable heating and cooling enabling a user-defined temperature curve to be applied as for TPD experiment[90]. Thus the current thermal control system has the effect of limiting the desorption achievable as the time to reach the sublimation

point is fixed. The impact of the temperature curve profile has been carefully analysed on the THz-DES results presented in Section 6.4.3.

### 3.3.6 Background Source

At the rear of the vacuum cell, in Fig. 3.3, a cold blackbody target is positioned in order to maximise the signal-to-background scene noise ratio of the measurement. The radiometer views the liberated gas through the length of the vacuum cell against this liquid nitrogen (77 K) cooled blackbody background target that has, in a similar manner to the calibration targets, been especially designed to present a high emissivity within the THz frequency range. The effective gas temperature is greater than that of the external target and thus spectral features are recorded in emission against the cold blackbody background. However other contributions are also occurring, increasing this background temperature (see Section 4.3.2). The cold target comprises a foam pyramidal blackbody target placed in a liquid nitrogen dewar and a flat metallic mirror at 45 deg angle to reflect the target emission to the vacuum cell window.

## 3.4 The Terahertz Radiometer

The THz radiometer, Fig. 3.1 (B), is the detection element of the experimental system. The instrument was originally developed to demonstrate a single-sideband detection system with high spectral resolving capability operating in the band 320-350 GHz for applications in atmospheric science. Fig. 3.7 shows a schematic representation of the instrument. The instrument comprises the receiver, which is made up of a number of discrete modules, the calibration subsystem and the power and control electronics. Each of these will be described in the following sections.

### 3.4.1 Receiver Sub-system

The receiver sub-system is composed of four modules; the local oscillator (Fig. 3.7 (I)); the front-end (Fig. 3.7 (II)), core of the heterodyne principle, see Chatper 2); the IQ-down conversion module (Fig. 3.7 (III)) and the wideband spectrometer (WBS) module (Fig. 3.7 (VI)). This system is vital for the heterodyne detection and the acquisition of raw spectra. The description of the radiometer is presented assuming a spectrometer bandwidth of 2 GHz. The impact of the spectrometer bandwidth on the instrument bandwidth is described in Section 3.4.6.

### 3.4.2 Local Oscillator

A local oscillator (LO) signal is required for the heterodyne down-conversion process, because combining the LO signal with the RF incident signal (THz radiation) generates an intermediate frequency signal (IF) at lower frequency. The IF frequency is difference between the RF and LO, meaning that the LO frequency has to be set close to the frequency of the RF signal. The input RF signal, between 320 and 350 GHz, is the electromagnetic radiation to be detected from the experiment. Different approaches are available for the generation of a high frequency LO. In our case because a sub-harmonic mixer [264] is used in the front-end, it requires a local oscillator input frequency at half the RF frequency (see Chatper 2). Therefore the generated LO signal must have a frequency between 150 and 180 GHz at the mixer LO input. Figure 3.7 (I) shows the components used to generate this frequency a (156-180 GHz). Firstly, a signal between 13 and 15 GHz is generated by a microwave frequency synthesizer (XS-14XX, Herley-CTI) which is phase-locked using an external reference signal of 10 MHz (OCXO-S109-LF, KVG). The signal frequency is then multiplied ($\times$6) via a sextupler (RPG, DE), amplified using a W-band (75-110 GHz) power amplifier (RAL, UK), and finally, doubled to between 156-180 GHz using a Schottky diode doubler (RAL, UK). At the output of the LO module, a LO signal of 166-169 GHz with 8

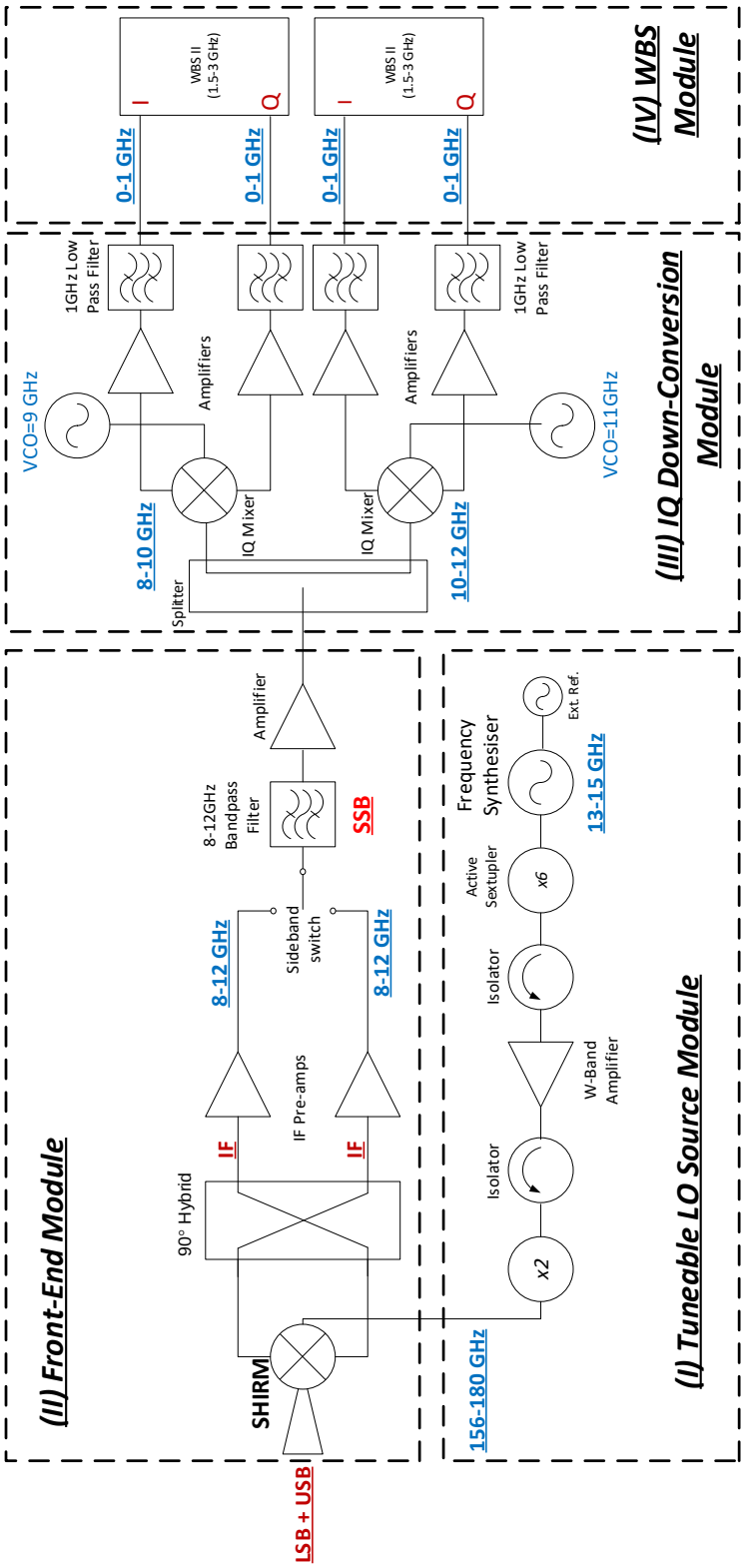


Figure 3.7: Schematic of the heterodyne spectrometer using a local oscillator and two spectrometer units. See text for details.

mW power is sent into the input port of the mixer block in the front-end module (Fig. 3.7 (I)). This power level is required at the input of the front-end mixer to obtain the best noise performance.

### 3.4.3 Front-End Module

The down-conversion of the RF takes place in the front-end module, Fig. 3.7 (II). In this radiometer, a single sideband (SSB) detection mode has been chosen to facilitate the analysis of spectral features (see Section 2.3.2). Consequently, the system is set-up to observe either the RF lower sideband (LSB) or the RF upper-sideband (USB)[276]. Briefly, the approach introduces a phase imbalance between the radio-frequency (RF) and local oscillator (LO) signals. The first element on the front-end is an ultra-Gaussian corrugated feedhorn designed by EADS-Astrium (310-360 GHz), which couples the electromagnetic radiation into a waveguide (see Section 2.4.2). This waveguide is connected to the mixer block which is the main component of this module.

This particular radiometer is using a sub-harmonically pumped image rejection Schottky diode mixer (SHIRM) manufactured at RAL and described indetail elsewhere [234] (see section 2.3.3). Te LO input signal is coupled with a 90° waveguide quadrature hybrid within the mixer block. The first advantage of this component is to double the frequency of the LO input from 166-169 GHz to 332-338 GHz. The second advantage is to produce two output signals with a phase imbalance of 90°, which are subsequently used for the rejection mechanism of the two sidebands. The LO signals are combined with the RF-radiation via two standard double sideband (DSB) Schottky diode mixers. Because of the LO imbalance combined with the RF signals, two intermediate frequency (IF) signals in two different branches are obtained: One with no additional phase compared to the RF signal and the other with a phase of +90°. A 90° quadrature hybrid coupler is then used, introducing +90° phase imbalance between the two

IF ports, producing two IFs corresponding respectively to the LSB and the USB (explained in detail in Section 2.3.3) with frequencies of 8-12 GHz. This is called side-band rejection and permits to not overlay the two side-band at the back-end of the radiometer. To select the desired sideband, an electronically controlled switch (Single-pole-double-throw: SPDT) is installed. The resulting IF signal is then filtered with a bandpass filter to reduce the noise contribution beyond the IF band (8-12 GHz), and amplified to increase the power of the restrained bandwidth signal before being sent to the next module, the IQ Down-conversion module.

### 3.4.4 IQ Down-Conversion Module

The purpose of the IQ(In-phase Quadrature) Down-Conversion Module is to generate phase quadrature signals at low frequency (0-1 GHz) as required by the WBS used at the back end of the radiometer. This module, shown Fig. 3.7 (III), splits and down-converts the IF LSB and IF USB (8-12 GHz). Initially the signal is split in two paths via a splitter which introduces 3 dB insertion loss. Then passive I/Q mixers (HMC-C042) are used to provide two outputs with relative 90° phase quadrature to each other as required by the WBS units [241]. To exploit the full IF, the LO frequency input to the IQ mixers are set at 9 GHz and 11 GHz. Those LOs are generated with wideband voltage controlled oscillators (VCOs). VCOs have been used in the past as LO source in receivers [319]. A voltage applied controls the capacitance of a varactor diode, changing the frequency of a LC-circuit oscillator [95, 259]. The purpose of this operation is to divide the IF into two equal band of 2 GHz as the WBS bandwidth is 2 GHz. Therefore the 8-10 GHz and 10-12 GHz IF branches are down converted respectively with the 9 GHz LO and the 11 GHz LO. After a further stage of amplification to ensure the correct input power to the WBS, low-pass filters are employed to eliminate aliased signals from the digitisation process within the WBS. The signals at the

input ports of the WBS units are two 0-1 GHz signals in phase quadrature (I and Q).

### 3.4.5 WideBand Spectrometer Module

The back-end spectrometers used are the WBS, made by Star Dundee Ltd [Parks] forming the WBS module, shown in Fig. 3.7 (d). They are able to perform FFT with high-spectral resolution, large instantaneous bandwidth and small acquisition time. The WBS units are digital spectrometers with two 8-bit analogue to-digital converters (ADCs). The spectrometer requires 2 inputs in phase quadrature, to be able to perform the 2048-point FFT as explained in Section 2.2.3. The 2048-point FFT is divided into two 1024-point frames operating in parallel. The powers acquired by the spectrometer have to be calibrated to be linked to brightness temperatures. The operating sampling frequency ($f_s$) corresponds to the number of samples acquired per second (sampling rate). The maximum sampling rate is 3 Gsamples/s giving 3 GHz instantaneous bandwidth per spectrometer. This is limited by the on-board crystal oscillator which defines the internal clock synthesizer working in the range 1.55 - 3.0 GHz. The entire radiometer was designed for an optimal operation at 2 GHz bandwidth. The total time that the WBS units are acquiring data and integrating the signal is defined as the integration time, $\tau$. It can be selected to be as low as 100 ms. The spectral resolution (B) is defined as the instantaneous bandwidth of the spectrometer (equal to $f_s$) divided by the 2048 frequency channels (FFT points) of the spectrometer, it varies therefore between 0.73 MHz and 1.46 MHz. These parameters have a significant impact on the experiment as they determine the sensitivity and spectral resolution of the measurement system. The sensitivity corresponds to the minimal signal intensity observable. The spectral resolution is the minimal spacing between two frequency channels defining the minimal spectral width of a signal which can be observed.

Table 3.1: Side-band frequencies of the radiometer for different sampling frequencies from the spectrometer units.

| $f_s$ (GHz) | LO (GHz) | LSB (GHz) | USB (GHz) | B(MHz) |
|---|---|---|---|---|
| 2 | 332 | 320.0 - 324.0 | 340.0 - 344.0 | 0.98 |
| 2 | 334 | 322.0 - 326.0 | 342.0 - 346.0 | 0.98 |
| 3 | 334 | 321.5 - 326.5 | 341.5 - 346.5 | 1.46 |

### 3.4.6 RF-Frequency Selection

The radiometer was designed to operate with 4 GHz total RF bandwidth by using two WBS, each with 2 GHz bandwidth. However it is possible to vary the WBS bandwidth, hence varying the total RF bandwidth as well as the IF bandwidth. The observable sidebands are defined by the choice of the sampling frequency and the LO frequency. From Equation 3.1, the LSB and USB frequency range are defined between $LSB_i$ – $LSB_f$ and $USB_i$ – $USB_f$.

$$LSB_i = LO - (11 + f_s/2) \tag{3.1a}$$

$$LSB_f = LO - (9 - f_s/2) \tag{3.1b}$$

$$USB_i = LO + (9 - f_s/2) \tag{3.1c}$$

$$USB_f = LO + (11 + f_s/2) \tag{3.1d}$$

Table 3.1 shows the LSB and USB measured using different WBS sampling frequencies and LO frequencies. For example, using $f_s$=2 GHz with a LO of 334 GHz gives either a LSB between 322 and 326 or a USB between 342 and 346 GHz with a spectral resolution of 0.98 MHz.

### 3.4.7 Summary

For the THz-DES experiment, a LO frequency of 334.5 GHz was selected in order to observe some spectral features of interest detailed in Chapters 5 and 6. A sampling frequency of 2.5 GHz was used in the WBS giving two sidebands

observable, LSB between 322.25 - 326.75 GHz and USB between 342.25 - 346.75 GHz. The spectral resolution obtained with this sampling was 1.22 MHz. This was sufficient to achieve the characterisation of faint desorption spectra with a good sensitivity, as discussed in Chapter 4. The integration time used for a THz-DES measurement was set at 500 ms. This parameter impacts significantly the sensitivity of the radiometer (see Chapter 4) and had to be small to be able to resolve with enough accuracy the desorption spectra as a function of time. Thus as the desorption mechanism is happening during less than 40 s, the signal-to-noise was sacrificed to generate more observation points. The sum-up of the THz-DES frequency down-conversion stages from the RF-frequency to the WBS input frequency is shown in Fig. 3.8.

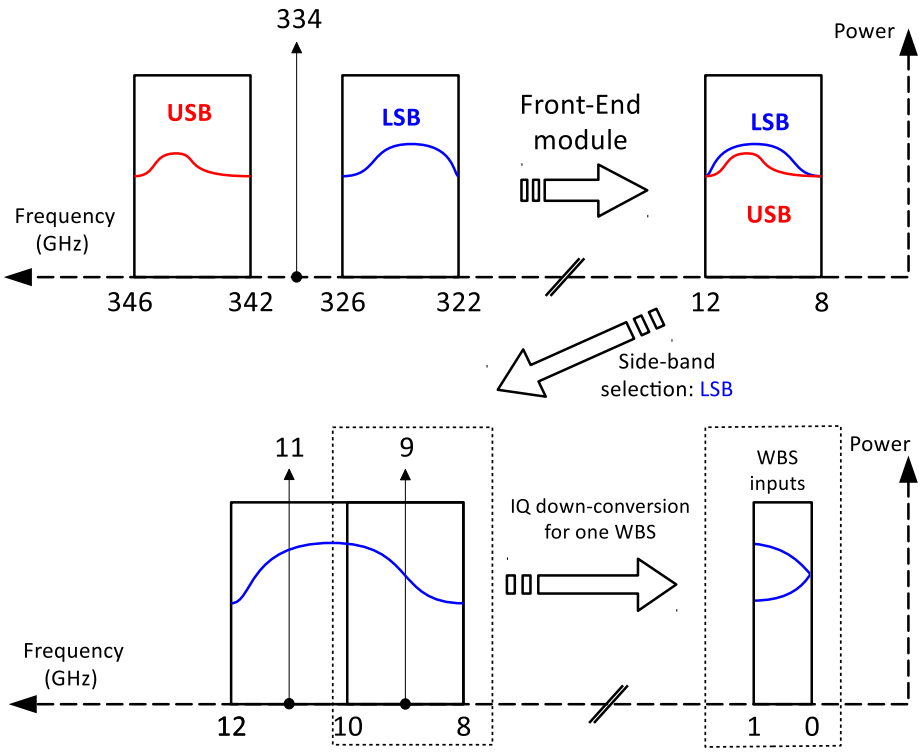


Figure 3.8: Relation between the spectrometer channels and the LSB frequency range with a sampling frequency of 2.5 GHz, LO=334 GHz.

## 3.5 The Calibration Module

Measurements performed with the radiometer must be calibrated to determine the absolute radiometric brightness temperature of the detected signal in order to retrieve the brightness temperature of spectral features from gaseous molecules. This is the role of the the calibration module (Fig. 3.1 (b)).

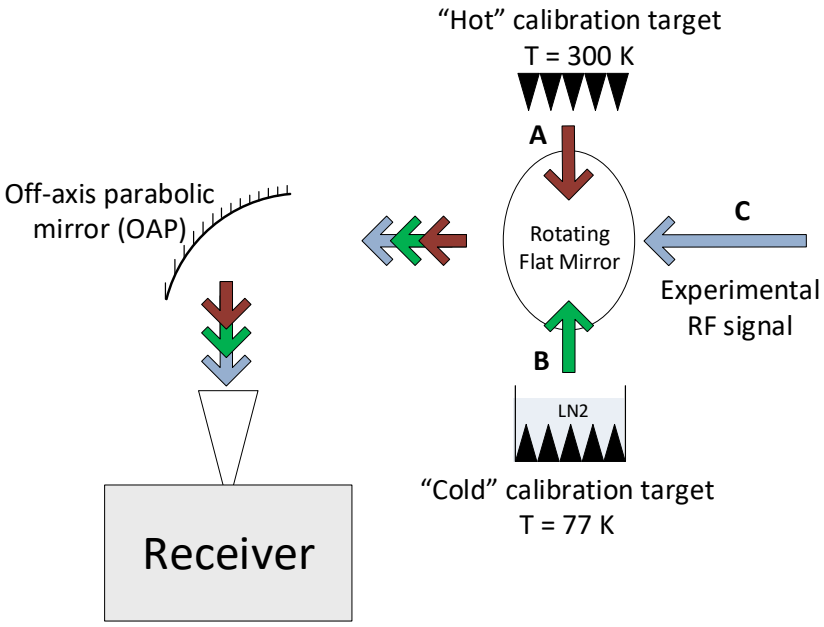


Figure 3.9: The calibration module is composed of two blackbody targets one at room temperature and one at 77 K, a rotating flat mirror and an off-axis parabolic mirror (OAP). The line of sight corresponds to signals from the desorbing molecules (C - blue arrow) is calibrated by observing the hot (A-red arrow) and cold (B-green arrow) signal by rotating the flat mirror. The OAP focusses the observed signal into the feedhorn of the radiometer.

### 3.5.1 Calibration Targets

The calibration module comprises of "hot" and "cold" blackbody calibration targets, an off-axis parabolic mirror (OAP) and a flat rotary mirror. The hot target is a pyramidal structure consisting of an aluminium base coated with ferrite-loaded epoxy absorber (Emerson and Cuming CR114)[Ecosorb.]. The physical temperature of the hot target is measured using platinum resistance temperature sensors

(PT100) mounted on the rear of the target, giving an absolute temperature measurement corresponding to the breadboard temperature (between 300-315 K). The pyramidal shape of the targets and absorber ensure that no external sources of radiation reflect from the hot target to the detector [123]. Otherwise those signals would contribute to the detected signal and decrease the experiment sensitivity, as random noise. A dewar filled with liquid nitrogen, with a base made of a pyramidal foam microwave absorber (TK RAM)[Keating], is used as the cold target with a nominal temperature of 77.3 K [117].

Both targets are considered to have an emissivity close to 1 although the corresponding power reflection coefficient is typically less than -30 dB. This implies that the resulting radiometric brightness temperature is assumed to correspond to the physical temperature[213]. In the case of the cold target, the liquid nitrogen surface reflection would increase the effective temperature of the blackbody target. The uncertainties from the targets temperature is discussed in Chapter 4.

Figure 3.9 shows a standard calibration cycle. It is defined as the measurement sequence of the signal coming from the hot target (A-red arrow), followed by the cold target (B-green arrow) and finally the acquisition of the signal coming from the experimental desorption chamber (C-blue arrow). Switching between observational views relies on the 180° rotation of a flat rotary mirror controlled by a Brushless DC-Servomotors (FAULHABER) motor. By setting the motor angle, the user defines which view the radiometer 'sees'. 0° corresponds to the "hot" target, 90° to the "cold" target and 180° to the signal coming from the desorption chamber. The rotation of the flat mirror introduces a time delay into the experiment acquisition. During that time (330 ms from A to B or B to C and 550 ms from C to A), the WBSs are switched off to change sight of view.

### 3.5.2 Quasi-Optic

The rotary mirror is an important element of the calibration module. All the optical pathways, defined by the mirror position, need to be similar for successive calibration cycle. The repeatability of the measurements for each position is essential because the mirror is not at the exact same position for a given rotation (i.e hot, cold or experimental RF signals), then an error could be introduced. The scan mirror repeatability was been studied during the design phase of the receiver. A laser was positioned in place of the feedhorn and a camera took pictures of the laser point positions on a wall at 5.75 m from the breadboard. A series of measurements for each angle were performed. The standard deviation of those results gave the measure of the mirror angle errors: $\pm 0.087°$. As the total experimental length of the THz-DES does not exceed 2 m, the deviation of the beam should be less than 3 mm.

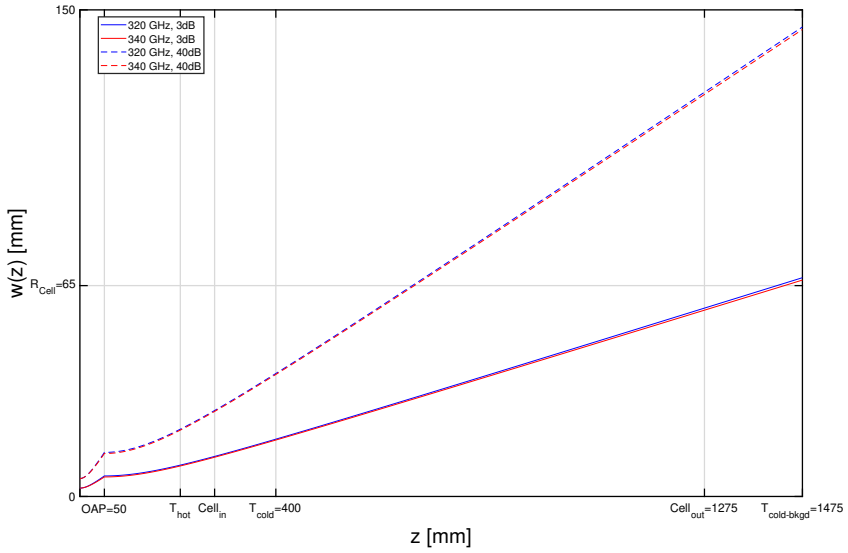


Figure 3.10: Gaussian beam radius (w(z)) as a function of the THz-DES experimental distances (z[mm]). The dashed line represents a relative power of the beam of 40 dB taper, whereas the straight line shows the relative power at 1/e, commonly used.

The RF radiation are Gaussian beam and can be calculated using the quasioptic theory (see Section 2.4) depending on frequency. Signals coming from optical

paths A, B or C, in Fig. 3.9, are each reflected on a focusing optic, an OAP, to collimate them onto the aperture of the radiometer feedhorn antenna, located in the front-end module. The role of the feedhorn is to couple the free-space signals into the waveguide used in the detectors. The focussing optic in this case is an off-axis parabolic mirror (OAP). To keep the distance between the OAP and the feedhorn short, the focal length was set at 30.621 mm, corresponding to the distance between the centre of the OAP and the feedhorn aperture.

The corrugated feedhorn used in the radiometer has an aperture radius of 4 mm and a length of 85 mm. The feedhorn beam waist is equal to $w_0(\text{mm}) = 0.644 \times r(\text{mm})$ with r the radius of the feedhorn. Figure 3.10 shows the beam radius in the experimental set up at a relative intensity of 1/e (straight lines) and at an intensity corresponding to a 40 dB Taper (dashed curves) (defined in Section 2.4). The x-axis defines the distance from each components of the calibration module to the feedhorn aperture (z[mm]). The y-axis is the Gaussian beam radius in mm. The blue and red curves are the detected Gaussian beam respectively at 320 and 340 GHz.

The beam radius at the hot and cold calibration targets, respectively called $T_{hot}$ and $T_{cold}$, are smaller than the radius of the targets which are 32.5 mm and 115 mm. Therefore there is no unwanted external contributions to those signals. Secondly, with a 40 dB edge Taper, the beam radius is bigger than the desorption chamber radius between $Cell_{in}$ and $Cell_{out}$ (straight stainless steel cylinder, see Section 3.3.1). Therefore the inside walls act as reflector for the lowest beam intensities at room temperature. Those reflections are increasing of the background brightness temperature. Finally the beams with a relative intensities of 1/e have a smaller radius than the hot, cold and background targets at their respective positions. Chamber's windows are introducing dielectric material of certain thickness within the optical path creating standing waves, as discussed in Section 4.2.2.

## 3.6 Data Acquisition and Processing

The final element of the THz-DES experiment is the data acquisition and the generation of the thermal desorption spectra (illustrated in Fig. 3.1 (d)).

### 3.6.1 Calibration Procedure

The observed brightness temperature in the scene view (view C, Fig. 3.1 (B)) is obtained by comparing it with the hot and cold views (view A and B, Fig. 3.1 (B)). To do so, a two-point calibration scheme [141, Hewison and Gaffard] is used as it presents a nominally linear receiver transfer function between those two temperature, explained in Section 2.3.6. The expression of the scene view brightness temperature (line-of-sight) is given by equation 3.2[151]. Errors on the retrieved brightness temperature from the uncertainty of the targets brightness temperature is discussed in details in Section 4.3.

$$\mathrm{BT} = \frac{\mathrm{P_{scene}} - \mathrm{I}}{\mathrm{G}} \text{with} \begin{cases} \mathrm{G} = \frac{\mathrm{P_{hot}} - \mathrm{P_{cold}}}{\mathrm{T_{hot}} - \mathrm{T_{cold}}} \\ \mathrm{I} = \mathrm{P_{cold}} - \mathrm{T_{cold}} \times \mathrm{G} \end{cases} \tag{3.2}$$

Two parameters, called the gain (G) and the integrator offset (I), are used to retrieve the brightness temperature (BT). The gain represents the amount by which an incoming signal is amplified before detection and can vary over time due to different noise contribution in the receiver. The $\mathrm{P_{hot}}$ and $\mathrm{P_{cold}}$ terms represent the spectrometer noise power output readings corresponding to the introduction of the broadband hot ($\mathrm{T_{hot}}$) and cold ($\mathrm{T_{cold}}$) reference target temperatures. The physical temperature of the hot target is monitored by two thermometers located on its aluminium metal surface at the back, with a typical value of 300 K providing its radiometric brightness temperature. The cold target has an assumed physical temperature of 77.3 K at atmospheric pressure. Variation in environmental conditions can affect the cold target bright temperature introducing an error in the radiometer calibration. However, small variations of calibration target's

brightness temperature have negligible effects due to the relatively large value of overall system noise (see Section 4.3).

Figure 3.11 shows the 'hot' (red curve) and 'cold (blue) readouts (blue and red curves) over the spectral channels during a standard calibration measurement. The y-axis is the output power, after FFT, measured by the WBS. It represents the count over the integration time over the WBS channels. The shape of the output power depends on the spectrometer sampling frequency selected and is directly linked to the IF filtering stages. Standing waves are observable as ripples over the spectrometer channels because of reflections between RF components. The spikes at channels 512, 1024, 1535 correspond to local oscillator breakthroughs at the centre of the frequency range and at half of the sampling frequency because of aliasing effects in the spectrometer units coming from the phase imbalance of the IQ module. They are later suppressed during the data processing.

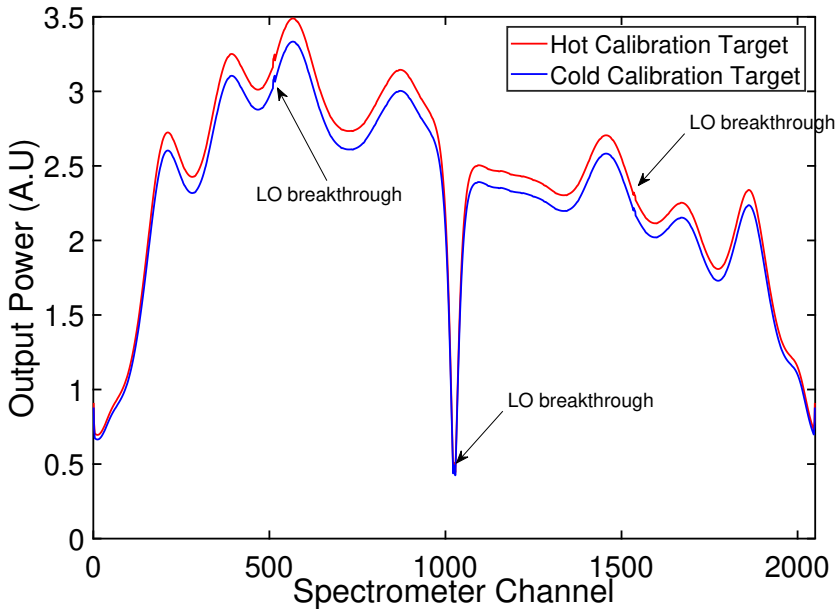


Figure 3.11: Output powers of the hot (red) and cold (blue) blackbody calibration targets are shown over the WBS frequency channel. Those powers are used to transform the RF power measured from the desorption chamber in brightness temperature.

### 3.6.2 Spectrum Generation

The system has important standing waves (see Section 4.3.2). All desorption results shown in the next chapters are presented after having proceed to a background subtraction using Matlab routines. To do so, the emitting signal under high vacuum ahead of the experiment (averaged spectra over time without molecules in the cell) is acquired and then deleted from the desorption results. This technique erases the constant standing waves patterns without affecting the desorption experimental results. Two gas phase spectrum of $8 \times 10^{-1}$ mbar of Nitrous oxide ($N_2O$), before (blue curve) and after (red curve) background subtraction are presented in Fig. 3.12. Spectral features of $N_2O$ are easily detectable and correspond to the transition $13_{0,0} - 12_{0,0}$ at 326.55 GHz with a brightness temperature of 80 K above our background temperature and $13_{-1,2} - 12_{1,2}$ at 326.68 GHz with a peak of 7 K above the background. The mean brightness temperature (baseline) over the frequency range decreased from 132.1 K to 0.3 K with a similar measurement noise floor (sensitivity) of 2 K.

### 3.6.3 THz-DES Figure Generation

To produce the THz-DES spectra, the surface temperature of the cold trap is linked to the brightness temperature measured of the desorbing gaseous molecules. The time constant of the spectrometers is set at 500 ms for each views which means that the desorption is observed every 1990 ms. The temperature data are acquired every 0.588 s, much more often than the brightness temperature after on calibration cycle. Then the acquisition time of the WBS is matched with the acquisition time of the cold trap temperature sensor. Therefore the temperature of the trap is linked to a corresponding brightness temperature over the instrument frequency range. This produces a intensity map with surface temperatures, frequencies and brightness temperatures. The first results obtained with the THz-DES experiment using nitrous oxide molecules is shown in Fig. 3.13. The y-axis

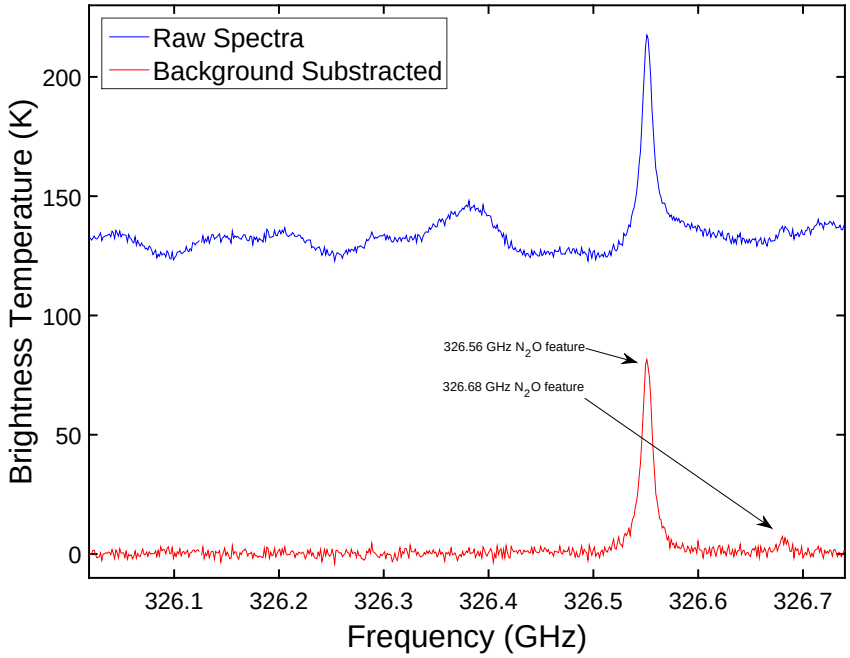


Figure 3.12: Nitrous Oxide spectra at a pressure of $8 \times 10^{-1}$ mbar before (Top) and after (Bottom) background subtraction. Two $N_2O$ spectral features are observable at 326.56 GHz and 326.68 GHz after deleted the standing waves coming from the experimental set-up.

is the cold trap surface temperature, the x-axis is the radiometer frequency range depending on the settings selected and the z-axis is the brightness temperature in Kelvins. The desorption of the molecules is observable from this figure as the brightness temperature of the spectral line is increasing. This results is explained in much more details in Section 5.4.1.

### 3.6.4 Assumptions

Some assumptions and chemistry approximations have been made in order to be able to analyse the THz-DES results:

- *Cell Vacuum*: It has been considered that operating the thermal desorption under high-vacuum instead of UVH, as a standard TPD, would be sufficient to demonstrate this proof-of-concept experiment. Background ice deposition is anticipated due to this pressure and water molecules from the cell walls may contaminate the deposited ice layers.

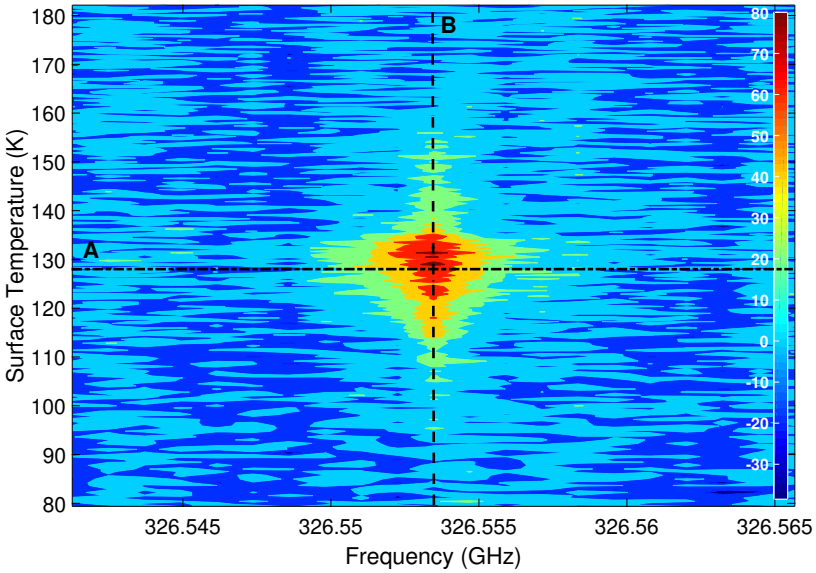


Figure 3.13: THz-DES spectra of desorbing Nitrous Oxide molecules. The brightness temperature of desorbed $N_2O$ molecules is plotted as a function of the frequency (x-axis) and the trap surface temperature (y-axis).

- *Local Thermodynamic Equilibrium (LTE)*: For gas in LTE, level of populations within the molecules follows Boltzman equations and are predetermined.[64] When the gas temperature is known, the molecular column density can be derived from a transition. The Kinetic temperature, the measure of the translational energy of molecules, will be $(3/2) \times k_B T$ with $k_B$ the Boltzman constant and T the gas temperature.

- *Molecules Temperature*: Assuming LTE, the molecules are following the Maxwell-Boltzmann distribution. Their root mean square velocity is defined as (with k the Boltzman constant ($1.38064852\ 10^{-23} m^2 kg s^{-2} K^{-1}$), T the molecules temperature and m the molecular weight):

$$V_{rms} = \sqrt{\frac{3k_B T}{m}}$$

This gives at T = 290 K: $V_{N_2O} = 405$m/s, $V_{H_2O} = 634$m/s and $V_{CH_3OH} = 475$m/s. Because of the high pressure (molecules collisions), and molecular velocity within the chamber, all desorbing molecules are considered at the

same temperature as the chamber around 290 K.

- *Ice deposition*: The deposition of the ice, although non-directional, is assumed to be homogeneous, as a first approximation.

- *Ice contamination*: Regarding the ice created on the cold surface, we consider that the ice binding energy between molecules is higher than binding energy between the molecules and the surface, only physisorption applied, no dissociative chemisorption. Molecular bonds between molecules remain and molecules are not adsorbed on the surface. Therefore the THz-DES results only correspond to the chemical properties of the ice. Moreover, the regime of thermal desorption studied corresponds to multi-layer desorption because of the amount deposited.

- *Ice Composition*: It was shown in Section 4.4.2, that water was slowly leaking into the THz-DES chamber overtime at a rate of $1.73 \times 10^{-4}$ mbar/s. Because the THz-DES experiment does not last longer than 500 - 800 s, it has been considered that the extra-$H_2O$ was not significant compared to the amount of studied molecules deposited and will not be taken into account.

- *Ice desorption*: During the desorption, we are considering that no re-adsorption of the ice is happening. This effect is likely to take place as the pumping speed to not permit to reach UHV. Because of heating ramp and the important quantity of ice desorbing, this approximation is made.

- *Desorption Energy*: The desorption mechanism is considered for all the ice studied to follow a $O^{th}$ order of reaction (see Section 2.5). As most all the ices are made of more than 1000 of monolayers ($10^{15}$ molecules/$cm^2$), their desorption is considered as multi-layered following $O^{th}$ order of reaction for the calculation of the desorption energy[50].

- *Ice Structure*: All depositions were performed at a fast rate at 77 K (see below), therefore all ices formed are assumed to be made of near crystalline

structures. For example, amorphous water ice when heated up above 135 K will crystallise[142].

## 3.7 Conclusion

The THz-DES experimental apparatus has been designed to perform gas-phase emission spectroscopy of molecules sublimating from interstellar ice analogues through thermal and non-thermal desorption mechanisms. It provides a unique way of analysing desorption mechanisms whilst producing data resembling direct astrophysical observations of molecules in star forming regions. Observing their desorption generates information about the bonding between molecules. That is, the excitation level of species evolving from the ice mantle is directly measured by the radiometer in the gas phase and could be linked to emission features observed in space by ground-based observational facilities.

The THz-DES experiment comprises a sensitive terahertz radiometer, a calibration module and a desorption chamber. Results are processed by an acquisition module giving the spectra of gas phase molecules as a function of the sample surface temperature. The present proof-of-concept system provides a measurement capability within a frequency range of 322.5-326.5 GHz to 342.5-346.5 GHz with a spectral resolution and integration time that are adjustable by the user through computer control. Spectral images can be acquired at a continuous rate that is governed by the integration period selected. Finally, ice consisting of different molecular species or different thickness can be grown in-situ using a high-vacuum cell and a cold surface where the ice is grown. The desorption mechanism studied in this thesis is only the thermal desorption. Results of the molecule's brightness temperature as a function of the cold surface temperature and the frequency are linked to give intensity map desorption figures.

The THz-DES experiment has been explained in detail in this chapter. The characterisation of its radiometric performances needs to be tested to determine

the optimum operational settings of the radiometer for the THZ-DES experiment.

# Chapter 4

# THz-DES - Radiometric Characterisation[1]

THz-DES elements have been explained as well as the operation of a THz-DES experiment. In this chapter, characterisation and optimisation studies are presented. These have been done regarding the radiometer performance and impact of the chamber on the radiometric data obtained. Measurements of gas phase molecules (Nitrous oxide $N_2O$, water $H_2O$ and methanol $CH_3OH$) are shown at the end of the chapter to characterise the spectral features observed for the different molecules before performing THz-DES measurements.

## 4.1 Introduction

The radiometer, presented in the previous Chapter, detects signals emitted from molecules and performs FFT calculations on the data in real time. This is essential to determine the noise contribution of the instrument, measure its sensitivity and ultimately quantify the sensitivity of the THz-DES experiment. Charac-

[1] Auriacombe, O. et al, Review of scientific Instruments, in prep. and published in [12]

terisation measurements are well known and have been used to test several radiometers in the past[42]. The system noise temperature ($T_{syst}$), which can be measured via the calibration targets, has the most significant impact on the receiver and depends on the technology being used. As described in Section 2.3.7, the accuracy of the measurements is inversely proportional to the system noise temperature [290]. A factor known as the 'noise equivalent differential temperature', NEδT determines the radiometric sensitivity of the brightness temperature measured by the radiometer. In addition, the stability of the various sources of radiometer noise plays an important role when carrying out experiments over an extended period of time. The parameter that describes this stability can be measured by performing an Allan variance factor [5] explained in detail in Section 2.3.8. This mathematically derived term presents noise contribution as a function of the integration time of the receiver. Knowing NEδT along with the noise stability as a function of different parameters will help to optimise the set-up for the THz-DES experiment.

Following the determination of radiometric performance, the emission brightness temperature of different gas phase molecules was acquired. Such measurements were performed to investigate the impact of spectral resolution on the features of the molecules when employing experimental configurations with varying sensitivities. For chemical interest, water, nitrous oxide and methanol molecules were selected since they present features in the LSB or USB frequency range of the THz-DES experiment.

## 4.2 Radiometric performances

The performance of the total-power radiometer sets a limit on the way that the instrument can be used during a standard THz-DES experiment. The parameters which require careful consideration are the system noise temperature, bandwidth, integration time and gain variation (explained in Section 4.2.2) since these define

both the sensitivity of the receiver and its stability. Once characterisation of the radiometer is complete, the different parameters can be carefully selected to optimise the THz-DES results.

### 4.2.1 System noise temperature

The overall noise output power of a system is proportional to the system noise temperature ($T_{syst}$) which is the sum of the noise contribution from the antenna, mixers and amplifiers (see Section 2.3.4). It is possible to determine the DSB noise temperature by carrying out a Y-factor measurement [153, 202]. This consists of measuring the power from a hot and cold calibration target and applying a proportional relation with their physical temperature to retrieve the brightness temperature of other measurements (see Section 2.3.6). The way to measure SSB noise temperature $T_{syst}$ is to mathematically compare ratios between the lower and upper IF ports in the hot and cold target view configurations. This technique is called image rejection and is well explained elsewhere in more detail [155]. The SSB system noise temperature of the instrument for one particular measurement is shown in the bottom panel of Fig. 4.1. This has been determined to be between 4000-5500 K for LSB and USB with the local oscillator tuned to a frequency of 334.5 GHz. The possibility to choose the lower or upper sideband frequency range, increases the SSB compared to a DSB receiver, by a factor known as the image rejection ratio (seen in the top panel of Fig. 4.1). This contributes to the overall system noise temperature. The red curves in Fig. 4.1 represent the lower sideband whereas the blue curves correspond to the upper sideband. The rejection ratio with the LO set to a frequency of 334.5 GHz is higher in the USB (blue curve), but the noise temperature is similar for both sidebands. The results obtained are on the order of a Schottky diode image rejection radiometer.

The noise temperature of the radiometer has an impact on the sensitivity of the instrument such that a higher noise temperature will result in an increased

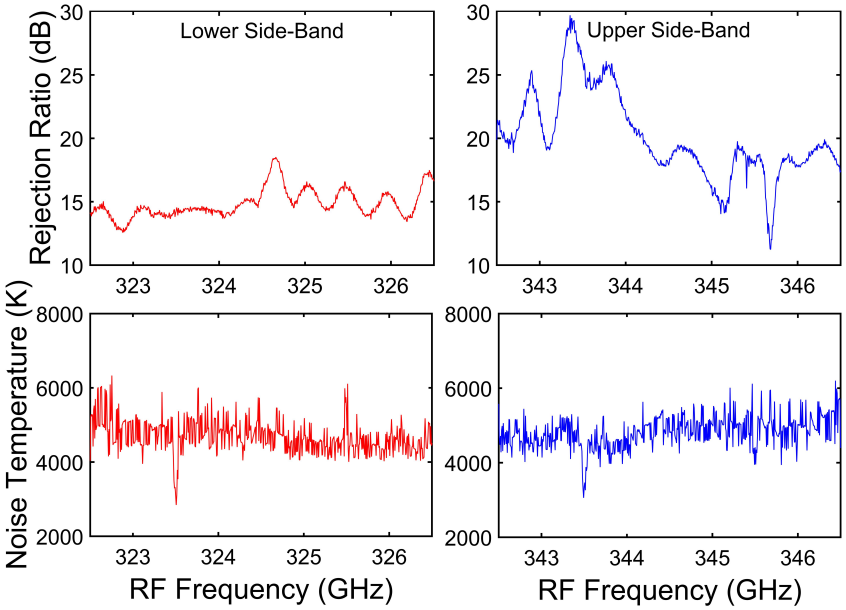


Figure 4.1: Single Sideband (SSB) image rejection coefficient (Top panel) and SSB system noise temperature $T_{syst}$ (Bottom panel) for the radiometer with a local oscillator at 334.5 GHz, $f_s = 2.0$ GHz and $\tau = 1$ s. The LSB is shown in red and the USB is shown in blue.

NE$\delta$T, a reduced instrument sensitivity. Therefore, if the instrument sensitivity decreases, the threshold for the number of molecules that can be detected by the radiometer would increase. Furthermore, if the signal intensity for a given integration time is below the instrument sensitivity then the gas signal will not be detected at all.

### 4.2.2 Sensitivity measurement

The sensitivity of the radiometer defines the feasibility of the THz-DES experiment. The radiometer settings can be changed so as to improve the sensitivity significantly accordingly to the requirements of the desorption process acquisition. For an LO frequency of 334.5 GHz and a bias voltage of -2 V, the LSB and USB noise temperatures are between 4000-5500 K as previously shown. The noise equivalent differential temperature, NE$\delta$T, defines the ability of the radiometer to distinguish changes in the observed signal [39]. It is essential to know the sensitivity of our instrument in different operating configurations (integration time,

spectral resolution) as it will give us the minimal brightness temperature of a spectral feature which can be resolved. The NEδT depends on different parameters which are: the scene temperature (Line of Sight temperature, $T_{scene}$), the spectral resolution (B), the receiver noise temperature ($T_{syst}$), the observation integration time ($\tau$), the receiver gain variation ($\Delta G/G$) which corresponds to temperature and random noise fluctuations in the overall instrument.

$$NE\delta T = (T_{syst} + T_{scene}) \times \sqrt{\frac{1}{B\tau} + (\frac{\Delta G}{G})^2 + \frac{1}{B \times N \times \tau_c}} \tag{4.1}$$

The Equation 4.1 presents the formula of the equivalent noise temperature which is the signal sensitivity [126]. In this formula, N is the amount of calibration cycle (i.e hot - cold -scene views) and $\tau_c$ is the integration time for the calibration targets. Figure 4.2 shows the simulated variation of the sensitivity based on Equation 4.1 as a function of the integration time (top left), the system noise temperature (top right), the calibration target integration time (bottom left) and the receiver bandwidth (bottom right) with different experimental configurations and the gain variance set to 0. According to the formula, NEδT decreases significantly when the integration time and the calibration integration time increase. However, as expected the noise temperature will reduce the instrument sensitivity by 1 K when it increases by approximately 1000 K.

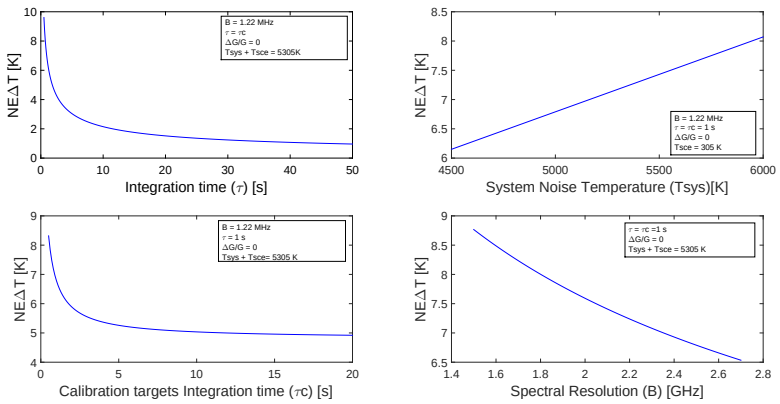


Figure 4.2: Noise equivalent temperature variation obtained by changing respectively the integration time, the system noise temperature, the calibration target integration time and the bandwidth using a gain at zero from Equation 4.1.

#### 4.2.2.1 Experimental Set-up

The first step to measure the NEδT was to acquire the brightness temperature of a temperature stabilised radiometric target in the scene view as a function of time [247]. This way, the change in measured power is directly linked to the instrument noise rather than a possible target temperature drift. A radiometric blackbody target with a pyramid shape made of aluminium and epoxy layer, shown in the image in Fig. 4.3, would be heated with a resistor and its temperature measured using a 4-wire Pt100 temperature sensor. A eurotherm controls the temperature by constantly measuring it and adjusting the heating power sent to the resistor to achieve a constant physical temperature with fluctuations below 0.1 K (at about 30 deg C). A target with a diameter of 100 mm is then placed at a total distance of 30 cm from the feedhorn aperture such that the beam is completely covered by the target as described by the optical analysis previously performed. The locations of the different targets are shown in Fig. 4.4, with one view looking down on the set-up. The feedhorn and off-axis parabolic mirror can be seen in the top left corner of the image. Once the data has been taken, NEδT is calculated as the standard deviation (Equation 4.2) for each spectrometer channel over the time or number of measurement cycles (hot-cold-scene views) which is given by N in Equation 4.1:

$$\sigma = \sqrt{\frac{1}{N}\sum_{i=1}^{N}(x_i - \mu)}; \mu = \frac{1}{N}\sum_{i=1}^{N} x_i \tag{4.2}$$

#### 4.2.2.2 Integration Time

The brightness temperature of the target when it is heated to approximately 305 K can be seen in Fig. 4.5. The presence of standing waves can be explained due to reflections between the feedhorn and the target. These waves have a period of 120 MHz for different integration times (top panel of Fig. 4.5), where the blue curve is the brightness temperature with $\tau = 0.2\,s$, the red $\tau = 1.0\,s$ and the black


Figure 4.3: View of the blackbody target, facing down, used for the NEδT experiment. The heater is placed at the back of the target as well as the 4-wire temperature sensors. The pyramidal shape of the target are seen and are connected to an aluminium plate.

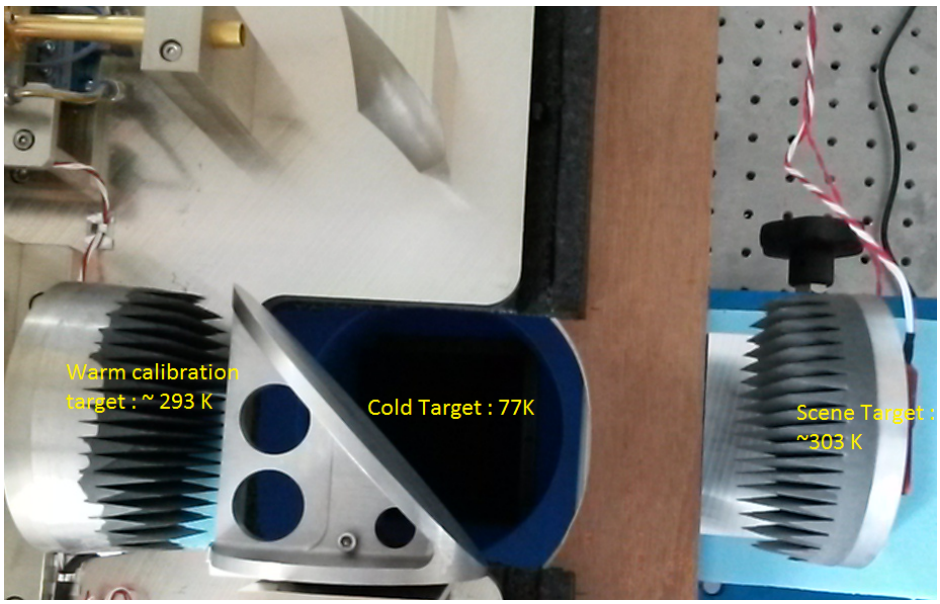


Figure 4.4: Experimental Set up for the sensitivity measurements. A scene blackbody target is placed in front of the calibration stage (on the left of the picture).

$\tau = 7.5\,\mathrm{s}$ in the LSB. In the USB with $\tau = 1\,\mathrm{s}$, the standing waves have a smaller period of 50 MHz but the same peak-to-peak brightness temperature and mean value of approximately 4 K and 306 K respectively (black curve Fig. 4.5).

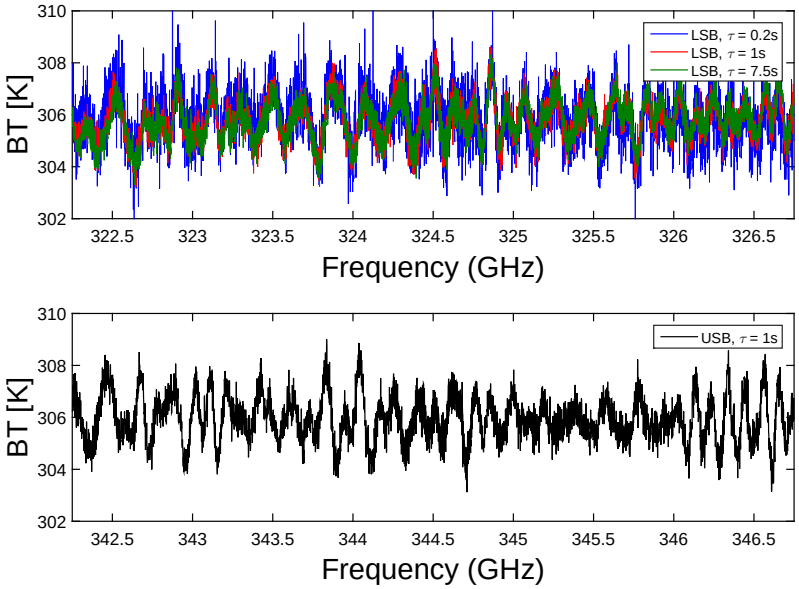


Figure 4.5: The top panel represents the brightness temperature of the warmed target in front of the radiometer in the lower side-band with different integration time $\tau$ (0.2 s in blue, 1.0 s in red, 7.5 s in green). The bottom panel shows the same brightness temperature but measured in the upper side-band with $\tau = 1.0\,\mathrm{s}$.

The results obtained are shown Fig. 4.6 for the lower sideband (top panel) and lower sideband (bottom panel) with tau = 1.0 s, $f_s$ = 2.5 GHz and LO = 334.5 GHz. Over the entire frequency range, the NE$\delta$T of the LSB is $6.89 \pm 0.16$ K and $7.37 \pm 0.24$ K for the USB. This variation is due to the fact that the system noise temperature $T_{syst}$ is not the same for each sideband. The black curves in Fig. 4.6 show NE$\delta$T using the measured $T_{syst} + T_{scene}$ and the receiver parameters in Equation 4.1 but with a gain of $\Delta G/G = 0$. The difference between the black and the blue curves gives the numerical values of the gain variation when measuring the target brightness temperature with different parameters.

Measurements for different integration times show that $\tau$ has the expected impact on NE$\delta$T, as shown in Fig. 4.7. Indeed, with $\tau = \tau_c$, the standard deviation decreases over the integration time. However, after $\tau = 7.0$s the value

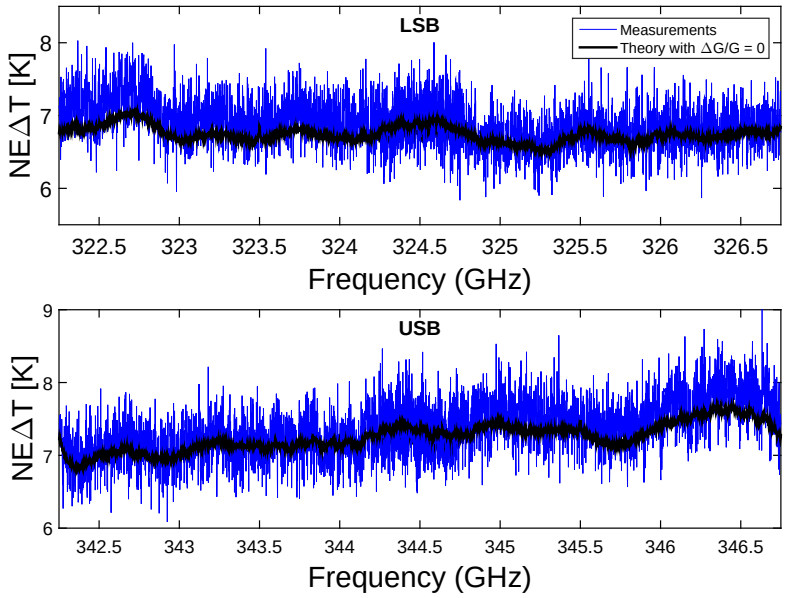


Figure 4.6: LSB (top panel) and USB (bottom panel) sensitivity with LO = 334.5 GHz,$\tau = \tau_c = 1.0$ s, fs=2.5 GHz. The blue curve is the measured sensitivity and the black curve is the calculated sensitivity based on the measured system noise temperature with a gain null ($\Delta G/G = 0$).

is stable around 3.5 K for both spectrometers. Improvement in the sensitivity is limited by the receiver gain drift ($\Delta G/G$) rising from an increase of noise within the radiometer. It is possible to calculate the gain variation using the measured NE$\delta$T for a defined integration time (Equation 4.1) by comparing the theoretical and measured NE$\delta$T. $\Delta G/G$ increases slightly over the integration time to a value of about $4 \times 10^{-4}$ (for an integration time of 50 s, a spectral resolution of 1.22 MHz, $\tau = \tau_c$, N=1, fs= 2.5 GHz, LO = 334.5 GHz.) as seen from the blue and red points in the bottom panel of Fig. 4.7.

#### 4.2.2.3 Number of Averaging Cycle

Using the data obtained for the LSB, Fig. 4.6, it is possible to determine the impact of the number of measurements or averaging cycles (N) on the sensitivity of the radiometric observations. The blue points in Fig. 4.8, are the results of different N-cycles with their respective error bars. The sensitivity achieves a constant value after about 50 cycles (within error bars) and the noise is very

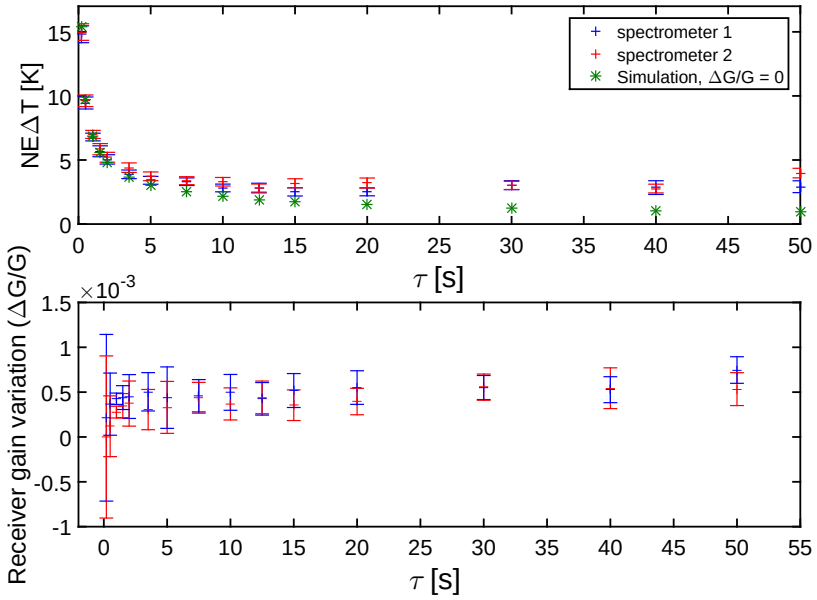


Figure 4.7: The blue and red curves on the top panel are the NEδT values for the first and second spectrometer(LSB, LO=334.5 GHz) as a function of the integration time ($\tau$). The green curve is the simulation using $\tau = \text{tau}_c$, N=1, $\Delta G/G = 0$. The bottom panel is the NEδT differences between the two spectrometer results from the top panel.

important for low N on the x-axis. Therefore, in order to decrease the uncertainty of the measurement, it is necessary to integrate the signal over a few cycles.

#### 4.2.2.4 Wideband Spectrometer Sampling Frequency

The sampling frequency of the spectrometers ($f_s$) was then changed. The WBS, detailed in Chapter 3, could perform acquisition with $f_s$ between 2.0 and 2.6 GHz which would change the spectral resolution between two FFT channels. The experimental results (blue and red points for the two spectrometers in Fig.4.9) follows the theoretical prediction (green curve, Fig. 4.9). Therefore, no clear impact on the sensitivity is seen by directly changing the experimental setting of the sampling frequency of the two spectrometer units.

Using the LSB data from Fig. 4.7, the spectral resolution was increased by integrating together different spectrometer channels using the same WBS sampling frequency. Figure 4.10 shows the results with the receiver at $f_s = 2.5\,\text{GHz}, \text{LO} =$

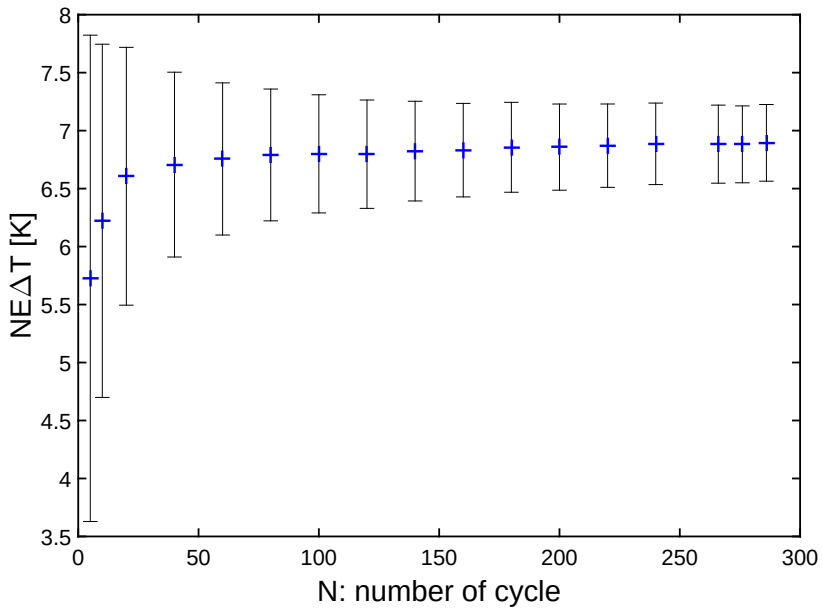


Figure 4.8: Mean value of the NEδT over the entire spectrometer's channels (in the LSB with $\tau = 1.0$s, fs = 2.5 GHz and LO = 334.5 GHz) as a function of the number of averaging cycle (hot-cold-scene views).

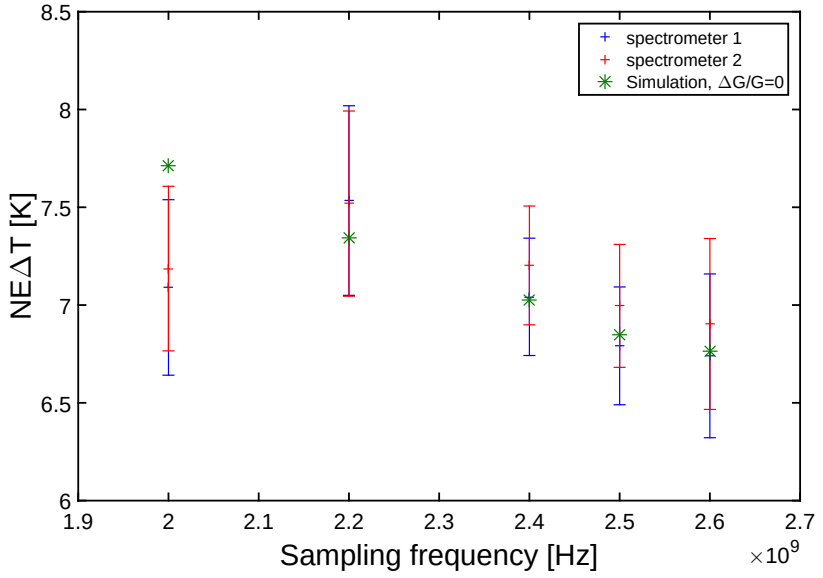


Figure 4.9: The blue and red curves on the top panel are the NEδT value for the first and second spectrometer(LSB, LO=334.5 GHz) as a function of the sampling frequency ($f_s$). The green curve is the simulation using $\tau = tau_c$, N=1, $\Delta G/G = 0$.

334.5 GHz, LSB and $\tau = 0.5$ s (blue curve), $\tau = 2.0$ s (red curve) and $\tau = 7.5$ s (green curve). When increasing the spectral resolution, the sensitivity of the radiometer improves, the NE$\delta$T reduces. This effect can be seen in the blue curve which corresponds to an integration time of 0.5 s, where NE$\delta$T is halved while the spectral resolution is doubled. However by doing this, the capacity of the radiometer to resolve faint spectral features is degraded. Furthermore, with a spectral resolution of 1.22 MHz, increasing the integration time from 0.5 s (blue point) to 7.5 s (green point) leads to a much more significant impact on NE$\delta$T, resulting in a factor of 3 reduction.

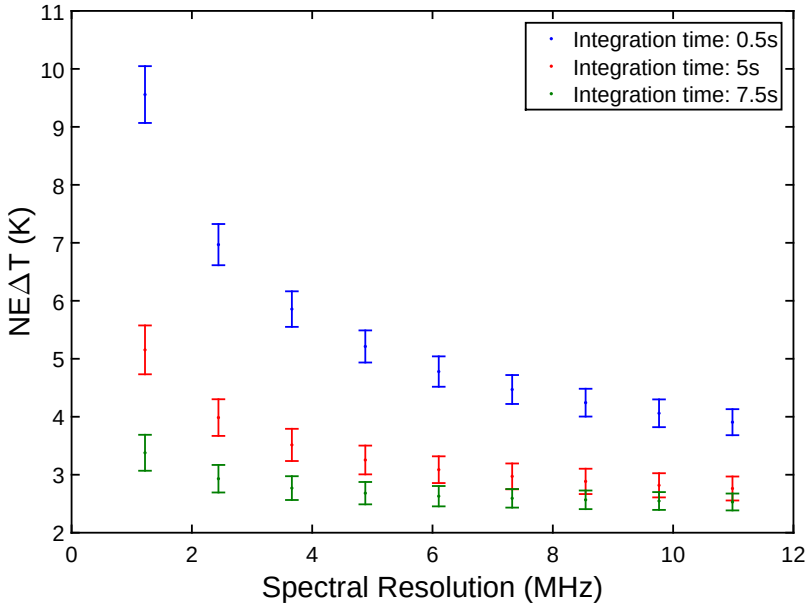


Figure 4.10: Noise equivalent differential temperature (NE$\delta$T) as a function of the spectral resolution (B) at different integration times ($\tau$). The blue curve is for an integration time of 0.5 s while the red curve shows the results for $\tau = 2.0$ s and the green curve corresponds to $\tau = 7.5$ s.

#### 4.2.2.5 Summary

Each effect from the different parameters on the radiometer sensitivity has been measured and a quantification of the gain variation of the instrument was obtained by comparing the experimental data to the theoretical simulations. First of all, increasing the spectral resolution would not be effective when trying to

observe faint narrow spectral features as these would be unseen. However, using the smallest spectral resolution (highest $f_s$) permitted by the spectrometers gives a NE$\delta$T equal to 10 K which would be the detection limit for any experiment employing the radiometer with these parameters. On the other hand, using a long integration time dramatically improves the instrument sensitivity but rapidly changing phenomena would be difficult to observe. Therefore the use of a long integration time would not be suitable for dynamic measurements, such as thermal THz-DES. The second problem with increasing the integration time is the temporal fluctuation of noise sources within the radiometer which leads to gain variation. Therefore, it is important to accurately measure the noise stability of the radiometer if reliable spectral measurements are to be achieved.

### 4.2.3 Stability Study

The noise contribution has an impact on the stability of the receiver and therefore the sensitivity of the instrument itself over time [15]. In order to establish the stability of the receiver system along with the maximum achievable integration time to maximise its sensitivity, an Allan Variance measurement was performed. The noise performance of the instrument is observable on an Allan variance diagram where a variance minimum, corresponds to the upper limit of the observation integration time before increasing the receiver gain drift ($\Delta G/G$) which affects the instrument sensitivity [254, 315]. Once the instrument is thermally stabilised, the spectrometer readout can be acquired over an extended time period by observing a radiometric target at constant temperature in the scene view. The spectral channel of the WBS readout and the corresponding blackbody target temperature are shown in the top and bottom panels in Fig. 4.11 respectively. The scene temperature can be seen to increase slightly over time as the breadboard slowly warms up due to the dissipation of energy from the spectrometer unit which is acquiring data at a fast rate. In addition, the readout power decreases as the

breadboard temperature rises. This effect does not impact the calibration mechanism with a small integration time set-up. Indeed, it is the overall scale of power which is shifted, as described in Section 4.5. The Allan Variance is then calculated from the raw data using the Overlapping Allan Variance routine [171]. Over the full spectral range and for different sampling frequencies, the system exhibits excellent stability from which an optimum integration time has been measured corresponding to the minimum of the Allan variance value.

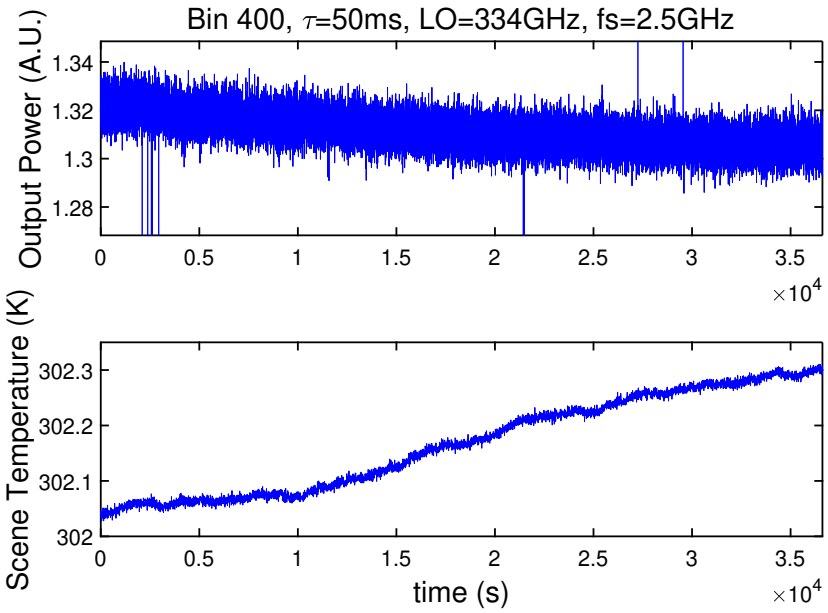


Figure 4.11: The top panel shows the measured spectrometer output power for one channel (400) as a function of the experiment time. Some error spikes are seen due to the very fast integration time used. The bottom panel corresponds to the scene temperature of the blackbody target observed as a function of the experimental time.

The results are plotted as a function of integration time used to calculate the overlapping Allan variance. This procedure has been explained in detail in Chapter 2.3.8. The typical result is shown in Fig. 4.12a for one spectrometer channel (300) in the upper-sideband with LO = 334 GHz, $f_s$ = 2.5 GHz and a measurement integration time of 50 ms. The slope obtained after calculation of the Allan variance shows different noise contributions (Fig. 4.12a). For $\tau < 80$ s, the white frequency noise is dominant. It is due to thermal noise and shot noise

(statistical fluctuations during measurements). For $80\,\mathrm{s} < \tau < 100\,\mathrm{s}$, the curve reaches a constant plateau due to the presence of flicker frequency, or 1/f, noise [294]. The integration time at the inversion point, corresponding to the lowest Allan variance value, is defined as the optimum integration time when the noise contribution is at its lowest. Finally, when $\tau > 100\,\mathrm{s}$, drift noise occurs due to changes in the experiment known as the random walk of noise and these lead to a gain variation of the instrument. Figure 4.12b shows the error bar (black points) from the previous plot. The errors on the measurements present the same trend as the overlapping Allan variance which is to be expected since the Allan variance is a measurement of the noise contributions within the receiver.

The Allan variance was measured for each channel of the two spectrometers, with the results of the first spectrometer shown in Fig. 4.13a while the results of the second spectrometer can be seen in Fig. 4.13b. The 3D-curves display the shape of the noise contribution previously discussed. Ripples, over the spectral channels, appear and come from the DC-1GHz anti-aliasing filters just before the WBS units. At channels 512, 1024 and 1536 for both spectrometers, the Allan variance curves differ because of white noise resulting from clock jitter. Furthermore, there appears to be a link between the oscillator and the sampling frequency used since at frequencies corresponding to $f_{sampling}/4$, $2 \times f_{sampling}/4$ and $3 \times f_{sampling}/4$ the noise is much higher. This appears as a spur in the Fourier frequency space and increases the noise fluctuations, seen as spikes in Fig. 4.13a and Fig. 4.13b. For these figures, maximum integration times of around 80 s have been measured across all spectrometer channels (which are shown in blue for the first spectrometer and red for the second one, Fig. 4.13c).

Finally, the optimum integration times with the same receiver parameters (LO = 334 GHz, $f_s$ = 2.5 GHz) in the lower-sideband (blue curve) and upper-sideband (red curve) for the first (Fig. 4.14a) and second (Fig. 4.14b) WBS are compared. The shape of the curves for the LSB and USB is similar and the optimum integration time is approximately 20 s for both spectrometers. The ripples

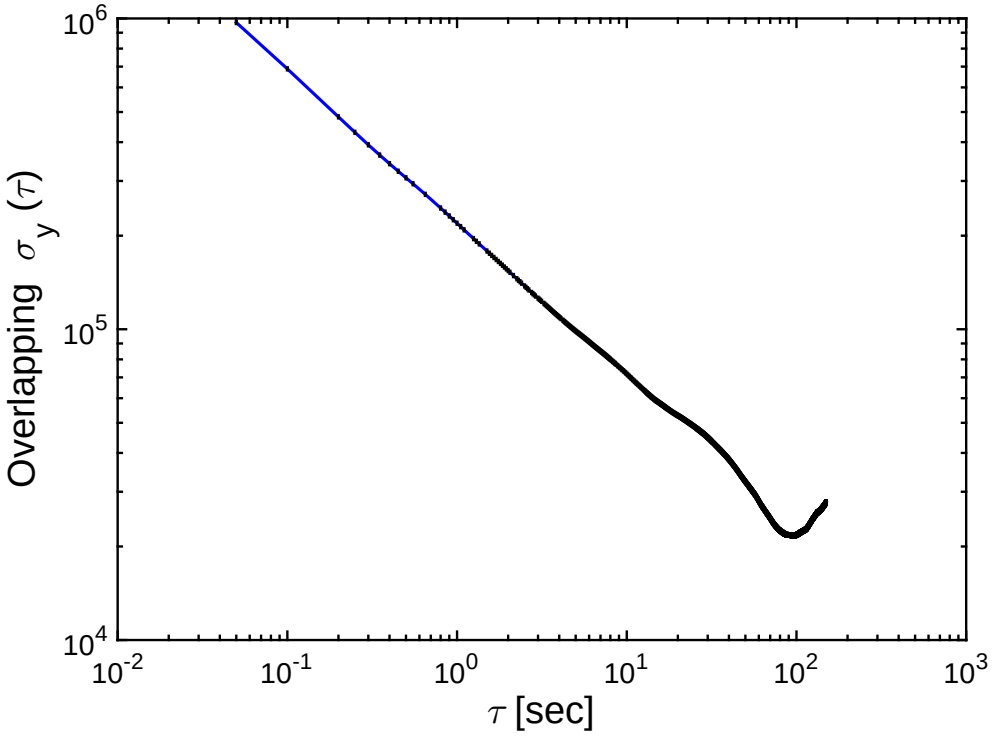


(a)

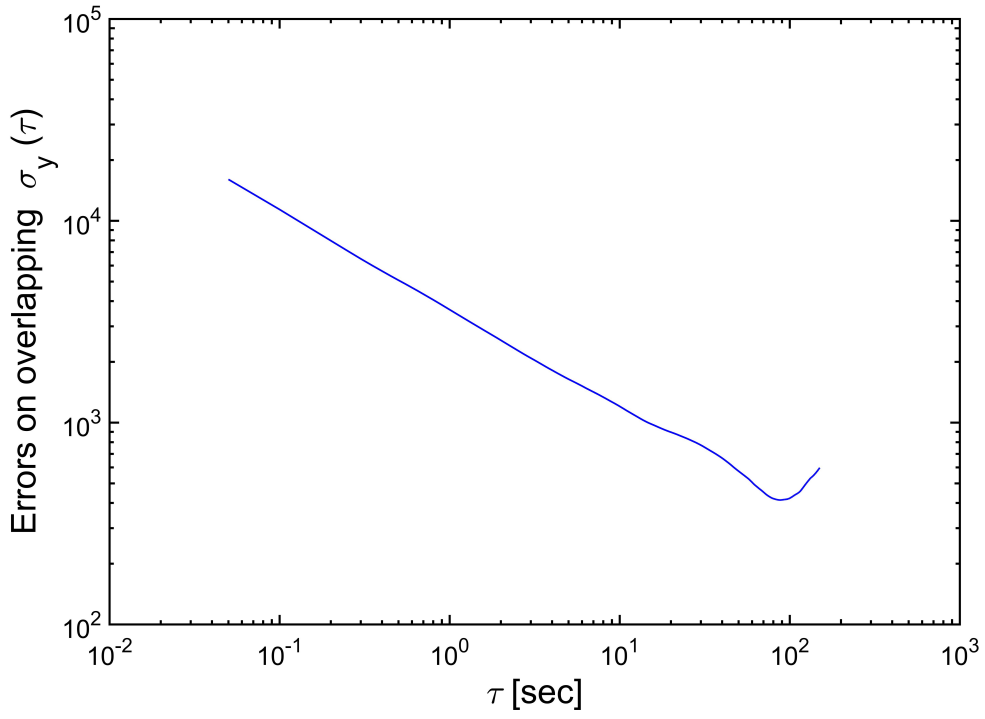


(b)

Figure 4.12: 4.12a Allan variance results for one spectrometer channel. Data has been acquired with 50 ms integration time over a long period of time. The curves present the results for one spectrometer channel (blue curve) and its related error (black bars). The optimum integration time measured (minima of the curve) is between 80 and 100 seconds over the spectral range of the spectrometers. 4.12b The error bars from the previous curve (4.12a) are shown and the trend is following the noise contributions to the receiver.

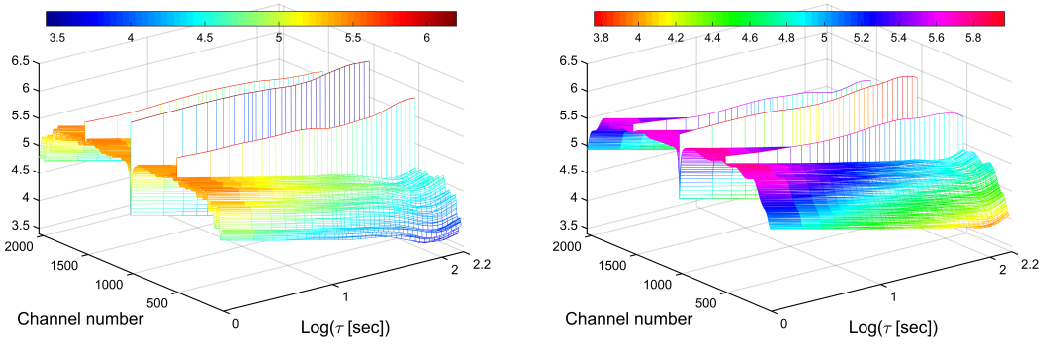


(a) (b)

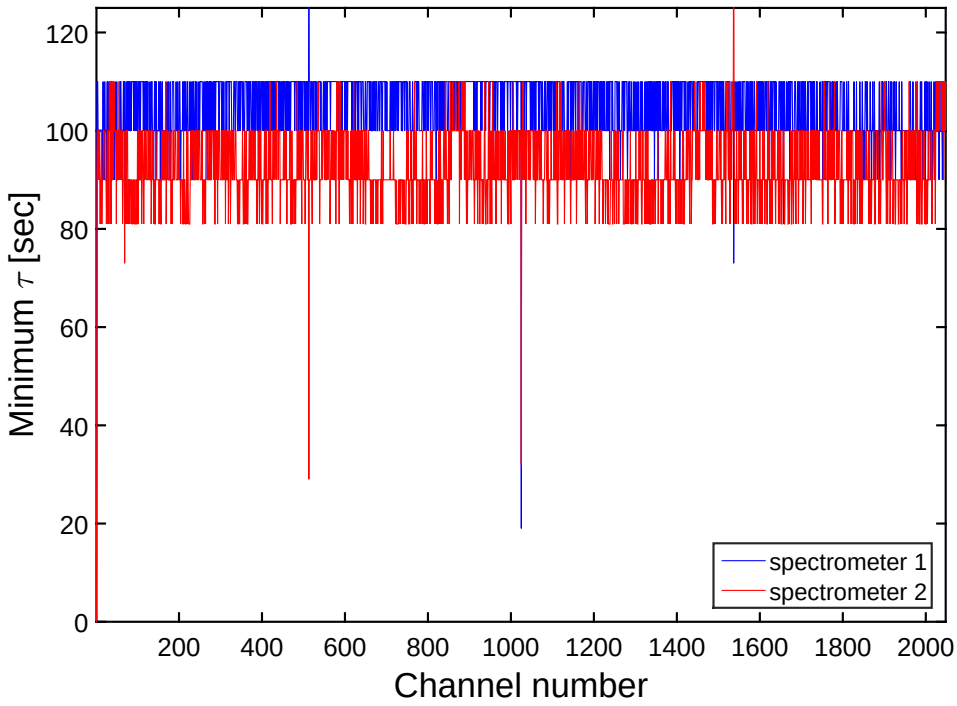


(c)

Figure 4.13: The Allan variance results with LO=334 GHz, fs=2.5 GHz and $\tau = 50$ ms from the first and second spectrometer are shown in 4.13a and (4.13b respectively. The x-axis represents the spectrometer channel number, the y-axis the natural logarithm of the integration time and the z-axis the overlapping Allan variance. 4.13c shows the optimum integration time measured (minima of the plots in 4.13a and 4.13b) for the two spectrometers (in blue and red respectively).

seen in Fig. 4.14b have previously been explained. The minimal integration time can vary significantly depending on the receiver settings but the most crucial parameters are the spectrometer response and the environmental conditions such as laboratory temperature.

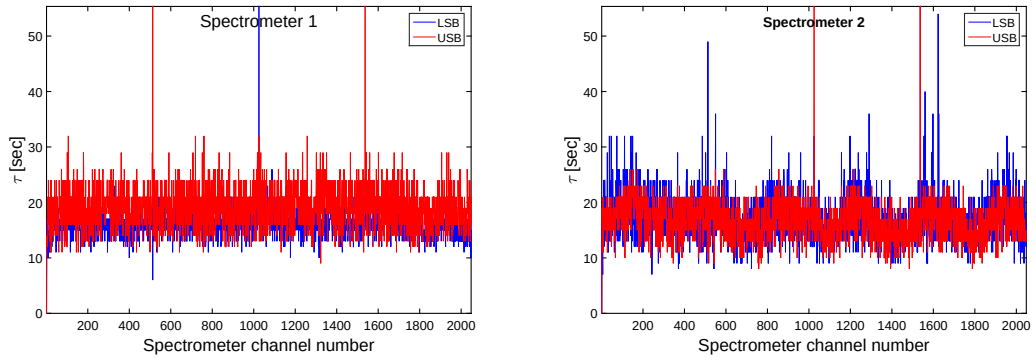


(a) (b)

Figure 4.14: Comparison between the Allan variance optimum integration time (minimum) for the first spectrometer (left panel) and the second spectrometer (right panel) in the LSB (blue curves) and USB (red curves).

To conclude, the radiometer stability was calculated via its Allan variance and an optimum integration time corresponding to the minimum in the Allan variance curve was measured. The instrument exhibits good stability with an optimal integration time of above 20 s, where the noise contribution is at its lowest value. However, since the THz-DES experiment requires fast data acquisition, this finding provides an important result for the future development of observing phenomena over extended time scales.

## 4.3 Radiometric System Optimisation

The radiometer characterisation was vital to understanding the performance of the instrument in terms of noise contribution and sensitivity. However, when integrated with the vacuum chamber other parameters such as the blackbody background temperature, standing waves due to the Mylar windows and frequency drift in the brightness temperature must be taken into account.

### 4.3.1 Cold Blackbody Calibration Target

Due to the calibration procedure, small variations in the reading of target temperatures may slightly alter the resulting brightness temperature [147, 229]. The output power is linked to the blackbody target emission temperature which is considered similar to its physical temperature. However, there is a small uncertainty which is further described in [63]. It is challenging to measure the cold target temperature due to the liquid nitrogen properties and reflection between its surface and the experiment interfaces. Using the reflection coefficient of the liquid nitrogen [180], it has been possible to approximate the temperature seen by the radiometer after reflection from room temperature sources on its surface. The power reflection coefficient is $r = (\frac{n-1}{n+1})^2$ where the refractive index of the liquid nitrogen is $n = 1.4$. The liquid nitrogen has a temperature of $T_{L.N_2} = 77.3\,K$ while the ambient room temperature is taken to be $T_{room} = 300\,K$. The liquid nitrogen transmission through the $L.N_2$ - air interface and the reflection of room temperature radiation perpendicular to the $L.N_2$ surface are considered using Equation 4.3 as a first approximation to calculate [212] the detectable cold target temperature to be $T_{cold} = 83.5\,K$. However, the effective ambient room temperature fluctuates depending on the time of the measurement.

$$T_{cold} = (1 - r) \times T_{L.N_2} + r \times T_{room} \tag{4.3}$$

A variation in the observed cold target temperature has an impact on the defined brightness temperature but does not affect the sensitivity of the instrument. Figure 4.15 (a) represents the linear curve used for the calibration with different cold temperatures. Once the cold and hot output powers have been allocated, any additional output power will correspond to the brightness temperature. A temperature variation in the cold target will slightly shift the brightness temperature curve as seen in Fig. 4.15 (a) with $T_{cold} = 77\,K$ (in blue) shifted to $T_{cold} = 83\,K$ (in black). The panel on the right (Fig. 4.15 (b)) represents the dif-

ference in brightness temperature between the curves in Fig. 4.15 (a) compared with $T_{cold} = 77$ K. For a low output power (brightness temperature below 150 K), the brightness temperature variation could be up to 6 K.

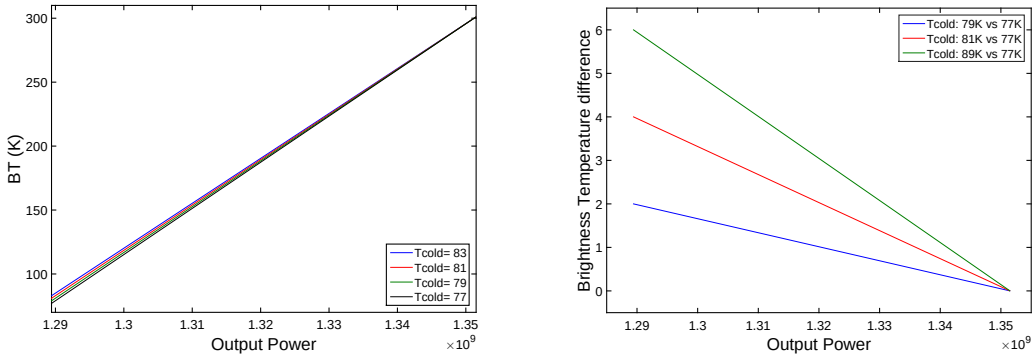


(a) (b)

Figure 4.15: (a)Calibration Curve for the SHIRM-WBS II radiometer with constant output power and varying cold calibration temperatures selected (33 K in blue, 81 K in red, 79 K in green and 77 K in black). (b)Difference between the brightness temperature with varying cold calibration temperatures and 77 K, for different scene spectrometer output powers. Blue corresponds to a cold temperature of 79 K (compared to 77 K), red represents 81 K while green is 89 K.

An experiment has been performed in order to quantify the cold target temperature with the radiometer. As previously seen, the temperature of the cold target should be between 77 K and 84 K, depending on the surface reflection. The radiometer set-up employed a local oscillator frequency of 334.5 GHz, an integration time of 1 s and an averaging time of 5 minutes. Figure 4.16 shows the brightness temperature of the observed cold target with an angle between 88 deg and 90 deg using this same one for the calibration procedure looking with an angle of 90 deg. It appeared that the median values for the different view angles are lower than 77 K on average than the selected calibration temperature. The exact same value should have been measured as the view angle is almost the same as the cold calibration view angle. Therefore, the power seen by the radiometer should be similar (Fig. 4.16). This effect is due to the slow decrease of output spectrometer power over the time that the breadboard temperature

increases. The calibrated brightness temperature will appear lower than $T_{cold}$ measured at higher output power.

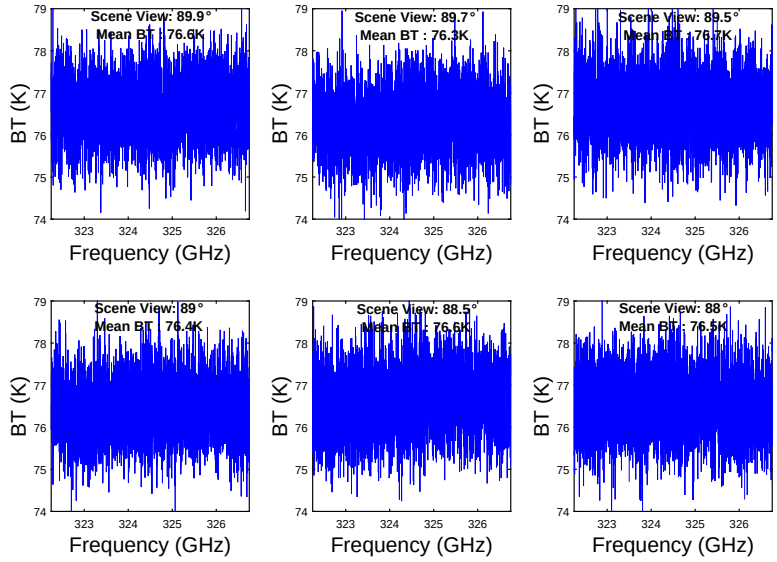


Figure 4.16: Brightness temperature of the cold calibration target measured with different cold calibration target viewing angles.

For consistency, $T_{cold}$ = 77 K has been selected for all measurements performed as it was non-trivial to define the temperature of the cold target exactly. The error in the calibrated brightness temperature is only a few kelvin as previously seen.

### 4.3.2 THz-DES Background Brightness Temperature

Once we obtain the calibrated brightness temperature, it is possible to observe the background brightness temperature of our experiment, i.e the signal from the background target (Fig. 3.1 (c)). These measurements showed that (a): the presence of standing waves appeared over the frequency range of interest; and (b): that the background temperature of the set-up was significantly higher than the expected value of 77 K.

Standing waves were observed due to the reflection of electromagnetic radiation in a Fabry Perot cavity within the system. In the final set-up configuration,

an optical resonator was created by two 50 μm Mylar windows. Part of the incident wave is reflected at the interface between different media such as the Mylar surface to air or air to liquid nitrogen surface. The transmitted electromagnetic field then depends on the length, refractive indices of the different media and the surface transmission coefficients which alter the overall transmission coefficient across the frequency range under investigation.

Every time, an electromagnetic radiation reflects on a surface, its incident electric field is multiplied by the surface's coefficient of reflection whereas it is multiplied by the transmission coefficient when passing through this surface. The wave propagating through a medium results of another multiplication factor: $\exp(-j \times k_i \times d_i)$ where $k_i$ and $d_i$ are respectively the wave vector of the medium and the distance travelled by the wave within the medium i. The wave vector, the reflection and transmission coefficients on a surface A/B are defined on Equation 4.4 where N is the frequency, c the speed of light and $n_i$ the refractive index of the medium i.

$$\begin{cases} k_i = \frac{2\pi N n_i}{c} \\ r_{ab} = \frac{n_a - n_b}{n_a + n_b} \\ t_{ab} = \frac{2 \times n_a}{n_a + n_b} \end{cases} \tag{4.4}$$

#### 4.3.2.1 Simulations

Simulations of the standing waves were performed to understand the background brightness temperature of the THz-DES experiment. Two systems were considered. The first consisted of a cavity made of [Mylar - Air (Cell) - liquid nitrogen ($L.N_2$)] and the second formed by [Mylar - air - Mylar - air - $L.N_2$], with the Mylar thickness being 50 μm in both systems. The transmittance coefficients ($t_i$) and, by extension, the overall transmittances are defined as $T_i = |t_i|^2$ for the two systems.

Therefore there are many reflections and transmissions on the different sur-

faces as shown in Fig. 4.17, for a system : L.$N_2$(1) - air(2) - mylar (3). The distance between the nitrogen and mylar was 1.5 m ($d_1$), the mylar has a thickness of $d_2 = 50\ \mu$ m.

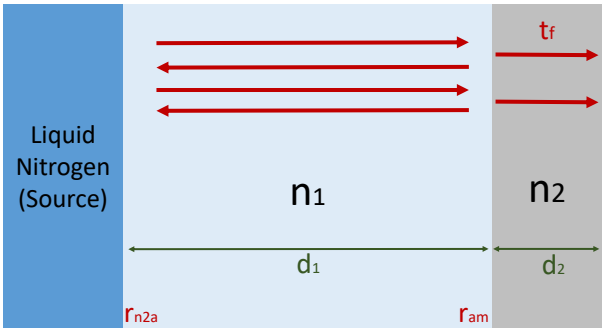


Figure 4.17: Schematic of the standing waves set-up considering two medium , Air and Mylar. [107]

The equation obtained is presented below where $t_{12}$ and $r_{12}$ are the coefficients for an air-mylar surface, $t_{21}$ and $r_{21}$ for a mylar-air surface and $r_{s1}$ the reflection L.$N_2$-air.

$$t_1 = \frac{t_{12}t_{21}\exp(-jd_2k_2)}{(1-r_{12}r_{21}\exp(-jd_2k_2))(1-r_{12}r_{s1}\exp(-jd_1k_1))} \tag{4.5}$$

Results for a system made of two mylar windows separated by a distance $d_3 = 1$ m : L.$N_2$(1) - air(2) - mylar (3) - air (4) - mylar (5), are shown on Equation 4.6.

$$t_2 = \frac{(t_{12}t_{12}\exp(-jd_2k_2))\times(t_{21}t_{21}\exp(-jd_3k_3)\exp(-jd_4k_4))}{(1-r_{12}r_{21}\exp(-jd_2k_2))(1-r_{12}r_{s1}\exp(-jd_1k_1))(1-r_{12}r_{21}\exp(-jd_3k_3))(1-r_{12}r_{21}\exp(-jd_4k_4))} \tag{4.6}$$

Then the transmittance and reflectance are given by :

$$\begin{cases} T_i = |t_i|^2 \\ R_i = 1 - T_i \end{cases} \tag{4.7}$$

Finally, the calculated background temperature is given by Equation 4.8,

where $BT_{77K}$ is the $L.N_2$ source and $BT_{293K}$ is an extra radiative source at room temperature which arises due to reflections within the vacuum cell.

$$BT_{final} = BT_{293K} \times (1 - T_i) + BT_{77K} \times T_i \tag{4.8}$$

Figure 4.18 shows simulation results performed using the previously described experimental configuration to model the standing waves for an ideal system. The blue curves represent the set-up with 2 Mylar windows, while the red and green curves respectively correspond to a system with just one Mylar window placed at the entrance of the chamber and one at the rear of the chamber, in front of the background target. The frequency of the standing waves decreased when the window was moved away from the $L.N_2$ background target, changing from 600 MHz at 0.5 m (red curve) to 200 MHz at 1.5 m (green curve). In the single window configurations, the mean value of 116 K was similar for the red and green curves with a peak-to-peak value of 30 K. These values increase when a second Mylar window is added. Indeed the mean brightness temperature when modelling the set-up with two windows (blue curve) is 147.6 K with a peak-to-peak intensity of approximately 40 K.

#### 4.3.2.2 Measurements

Spectroscopic measurements were performed to obtain a comparison to the simulations described in the previous subsection and these results can be seen in Fig. 4.19. The blue curve represents the vacuum cell with two Mylar windows under high vacuum ($8 \times 10^{-3}$mbar). The mean brightness temperature is about 135 K but with a peak-to-peak value of 16 K. The red curve corresponds to the results of a similar experiment but instead of using high vacuum, air was introduced into the system until atmospheric pressure was reached. These results show that the mean value does not change at 138 K but the peak-to-peak value reduces down to 11 K. The peak-to-peak value observed when the cell is under vacuum is due to the

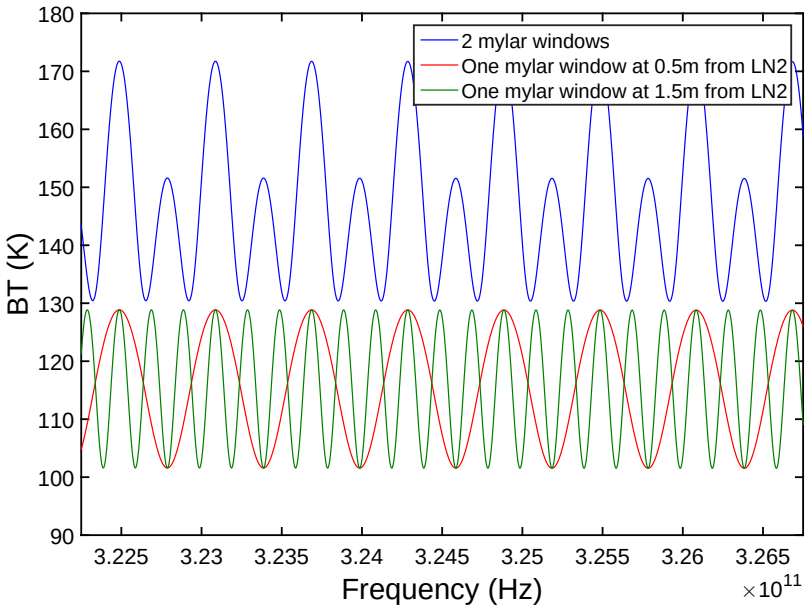


Figure 4.18: Standing wave simulations of a cell employing 2 Mylar windows (blue curve), one Mylar window 0.5 m from the liquid nitrogen dewar (red curve) and one Mylar window 1.5 m from the dewar (green curve).

deformation of the Mylar windows. Indeed, the flexing of the Mylar films significantly increases the reflection inside the chamber, adding room temperature RF contributions to the background temperature and thus increasing the measured peak-to-peak value. The mean values of the observed background temperature with the Mylar windows agree with the simulated results (blue curve, Fig. 4.18), although the peak-to-peak values are different. This discrepancy arises from the complexity of simulating all of the RF signal contributions in the experiment.

The green curve in Fig. 4.19 corresponds to a Mylar configuration located at 1.5 m from the L.$N_2$ source. It has a mean of 118 K, a peak-to-peak value of 20 K and a frequency period of 200 MHz. When compared to the simulation result (green curve, Fig. 4.18), the frequency period and the mean value are similar but once again the peak-to-peak value differs for the same reasons as previously described.

The final configuration measured was the background temperature without the presence of any windows in the optical path (black curve). The mean brightness temperature observed was 97.8 K, with a peak-to-peak value of 4 K and a

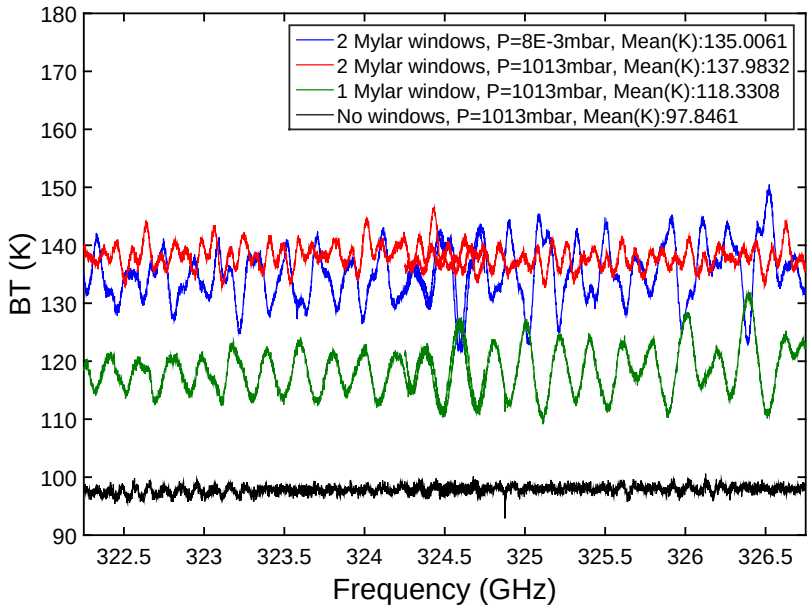


Figure 4.19: Background temperature measured in the THz-DES experiment. The blue and red curves show the background temperature with the cell closed by 2 Mylar windows and pumped down to $8 \times 10^{-3}$ mbar and under atmospheric pressure. The green curve shows the results with only one Mylar window at 1.5 m from the nitrogen dewar. The black curve is the background temperature through the cell without any windows present.

frequency period of 100 MHz. In an ideal system, a background temperature of 77 K should be measured. In this case, the measured results were 20 K higher and also contained some very small standing waves. Both of these effects could enhance reflections with the wall of the chamber which has already been confirmed with the optical analysis previously described.

#### 4.3.2.3 Conclusion

The THz-DES experiment is a very complex system where reflections and RF signals can contribute to the background temperature (2 Mylar windows, chamber wall RF contributions, flat mirror, liquid nitrogen dewar). Moreover, the Mylar windows used flex and deform when the vacuum cell is pumped down to its lowest pressure. Therefore, the Mylar contributions do not act as a simple, flat window element but rather behave as a lens, with the ability to focus the optical beam. This makes the system challenging to simulate accurately and predict

its behaviour. The measured mean brightness temperature across the tested frequency range appears much higher than the 'ideal' value of 77 K from the cold background target, with a period between 150 and 300 MHz. However, at atmospheric pressure the curvature of the Mylar windows does not change significantly and the shape of the standing waves remains the same but with a lower peak-to-peak value.

### 4.3.3 Voltage Controlled Crystal Oscillators

As explained in Section 3.4.6, using a sampling frequency higher than 2 GHz creates a frequency overlap between the two WBS units. However, the background brightness temperature did not overlap while measuring the cell with a pressure of about $10^{-5}$ mbar and the local oscillator set to 2.5 GHz. A frequency offset of 15 MHz was measured between the two spectrometers. This shift can be seen in the blue curve of Fig. 4.20 (a). It results from the fact that at 9 and 11 GHz (which correspond to the local oscillator frequencies of the IQ down conversion module (Section 3.4.4)), the Voltage Controlled Crystal Oscillators (VCOs) are highly dependent on their operating temperature. Indeed the frequency of the VCOs can vary by about 0.8 MHz per Kelvin. Given that they are attached to the baseplate of the spectrometers, their physical temperature increases while acquiring data due to the increase in the radiometer temperature over the duration of the measurement. As a result, the observed water molecule spectral feature was shifted by 5.3 MHz when compared to the HITRAN molecular database. The gas phase spectrum of water is explained in detail in Section 4.4.2.

A simple set-up has been installed for characterising the drift of the VCOs. We connected the VCOs to a switch that enabled either the 9 or 11 GHz VCO to be selected. In addition, an 8 dB attenuator was used before the switch to minimise reflection into the waveguide. A spectrum analyser was then used to measure the frequency peak delivered by each of the VCOs. The tuning was done once

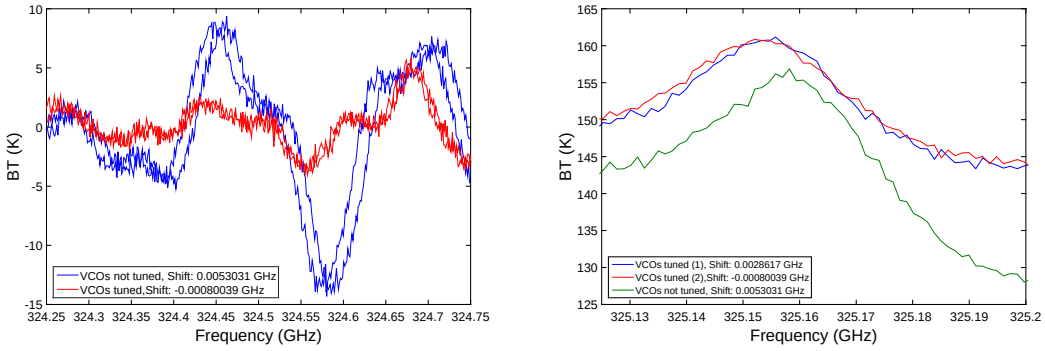


(a) (b)

Figure 4.20: (a) Frequency shift observed between the two spectrometers due to a VCO offset before (blue curve) and after correction (red curve). (b) Impact of tuning the VCOs to the peak of the observed water molecule feature compared to the database value before (red) and after correction (blue and red).

the breadboard baseplate temperature reached a plateau i.e when a temperature balance was achieved between the radiometer baseplate and the heatsink of the WBS units. This occurred at around 33.4°C. The temperature rise decreases the output frequency of the VCOs. By using the water emission line at 325.153 GHz and the brightness temperature overlap, it is possible to verify that the water feature is located at the correct frequency and the overlap occurs between the WBS units. The red curve in Fig. 4.20 (a), shows a good match between the WBS brightness temperatures. The green curve in Fig. 4.20 (b) shows the water feature without tuning compared to the blue and red curves, which correspond to the 2 WBS brightness temperatures after tuning.

## 4.4 Gas Phase Emission Spectroscopy

Using the THz-DES set-up, preliminary gas phase spectra are presented for a selection of molecules in order to determine the observable features and to present the standard FFT obtained from the THz-DES instrument. The spectral features observed are based on the theory of spectroscopy detailed in Chapter 2.

### 4.4.1 Nitrous Oxide

Nitrous Oxide contains various rotational transitions in the terahertz frequency range. Figure 4.21 shows simulated $N_2O$ transitions obtained using the Reference Forward Model (RFM), which was developed by Dr. Dudhia at Oxford University [66, 67]. It is a line-by-line radiative transfer model based on HITRAN 2016 [110] (explained in detail in Chapter 5). This simulation shows the brightness temperature of $N_2O$ under 1 mbar of pressure between 0 and 400 GHz in a 1 m vacuum cell.

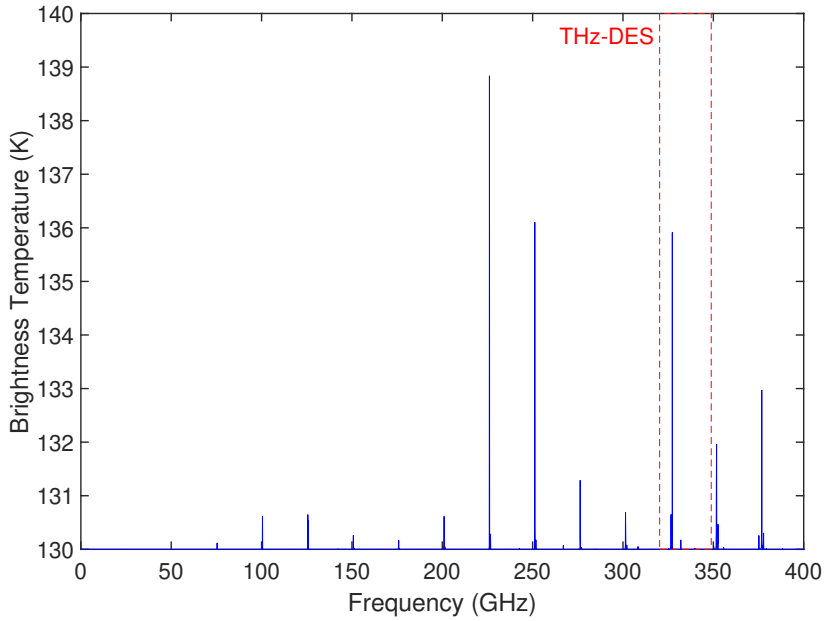


Figure 4.21: The simulated $N_2O$ brightness temperature in a 1 m vacuum cell under 1 mbar of pressure. The THz-DES frequency range is shown in red.

Nitrous oxide was the first molecule introduced into the cell via a lecture bottle connected to a regulator. A vacuum pressure of $8 \times 10^{-3}$ mbar was established within the 1 m cell before $N_2O$ gas was pumped into the chamber up to a pressure of 15 mbar. Two peaks were expected with $J = 13_{0,0} - 12_{0,0}$ at 326.556 GHz and a low intensity one for $J = 13_{-1,2} - 12_{1,2}$ at 326.691 GHz. Figure 4.22 presents the spectra of $N_2O$ across a frequency range of 326.50 – 326.75 GHz and a chamber pressure between 0.2 mbar to 15 mbar (respectively grey and blue curves on Fig 4.22). The radiometer was set up in its LSB configuration with a local oscillator

frequency of 334.5 GHz, an integration time of 1 s and a sampling frequency of 2.5 GHz. The spectral resolution of the spectrometer is high enough to detect low intensity lines with a narrow Full-Width-at-Half-Maximum (FWHM). As previously seen, the presence of standing waves is especially apparent in the blue curve (at 15 mbar) when pressure broadening plays a significant role. Once the pressure begins to decrease, the smallest intensity lines at 326.691 GHz are resolved. This effect begins to emerge at approximately 8 mbar (dark green curve).

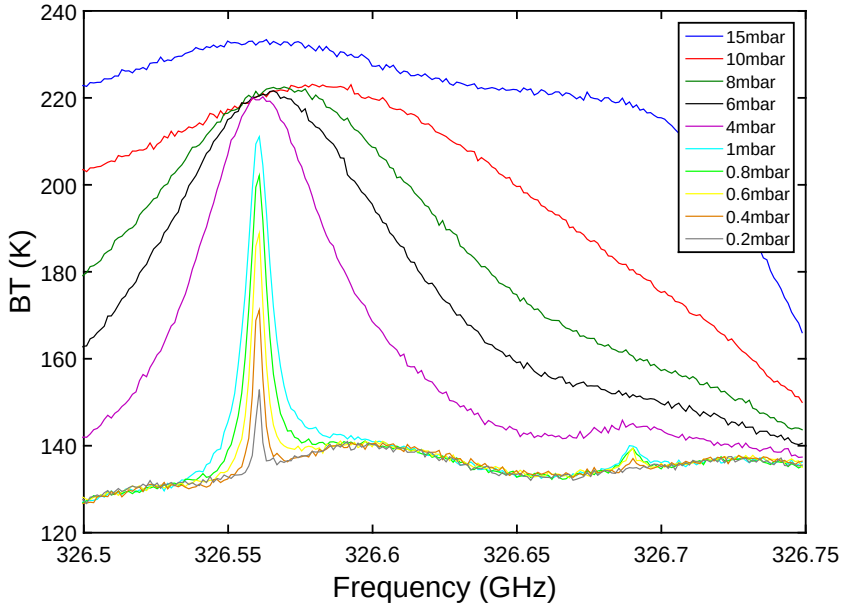


Figure 4.22: Brightness temperature of gas phase $N_2O$ in the LSB with LO = 334.5 GHz, $\tau = 1$ s and $f_s = 2$ GHz from 15 mbar (blue curve) to 0.2 mbar (grey curve).

### 4.4.2 Water Vapour

To begin with, the brightness emission temperature of water vapour was measured. $H_2O$ molecules present a para-transition with quantum numbers: $5_{1,5}$–$4_{2,2}$ at 325.15 GHz. A known amount of water is introduced into the vacuum chamber. Next, the brightness temperature corresponding to different pressures for a constant optical path is acquired. Figure 4.23 shows the simulated spectra using

the RFM model for frequencies between 0 and 400 GHz. Only one transition which is detectable in the THz-DES range appears in the simulation and this seems to be considerably weaker than the line at 375 GHz.

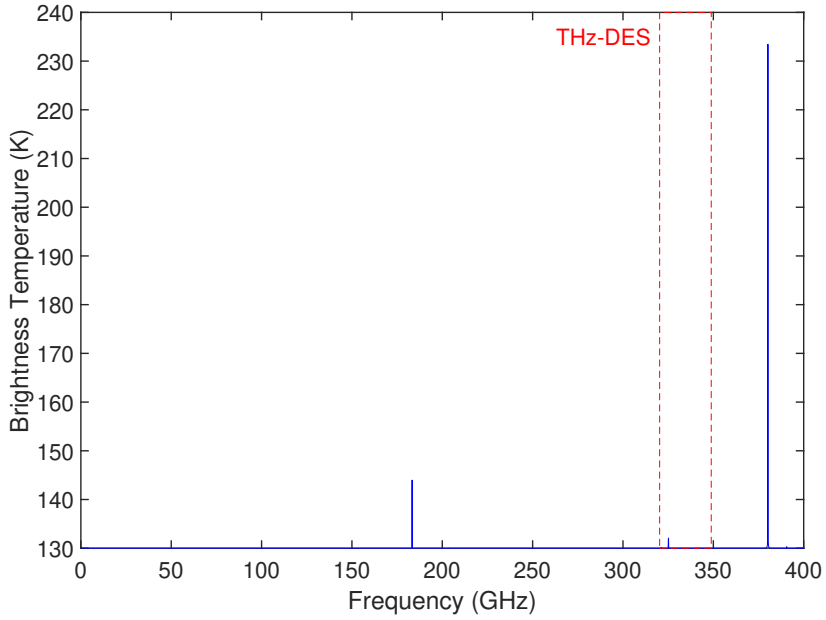


Figure 4.23: Simulated $H_2O$ brightness temperature in a 1 m vacuum cell with 1 mbar of $H_2O$. The THz-DES frequency range is shown in red.

The water vapour is produced by a freeze-pump-thaw cycle. A sample cylinder at atmospheric pressure contains air and liquid water. In order to pump the air out of the cylinder, it was frozen with liquid nitrogen. This meant that the ice formed inside the cylinder was at a temperature of 77 K. Next, the cylinder was pumped down to a pressure of $8 \times 10^{-3}$ mbar. Any molecules that do not freeze at 77 K are pumped away, thus purifying the $H_2O$ ice. Once the water begins to sublimate, the valve connected to the pump is closed off and a liquid-gas equilibrium is created inside the cylinder. This operation is repeated three times in order to eliminate any residual air that was trapped in the ice. Finally, pure water vapour was obtained and sent through the dosing line into the chamber. The initial results, shown in Fig. 4.24, were measured with a total pressure inside the chamber of $8 \times 10^{-1}$ mbar. As expected, a water feature can be seen at 325.15 GHz with a brightness temperature of 20 K above the background standing waves

(138 K).

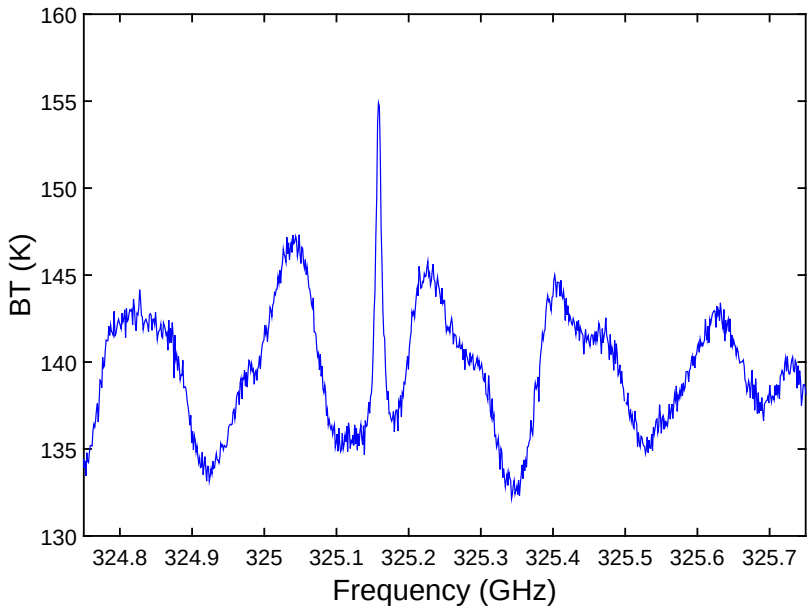


Figure 4.24: Spectroscopic water vapour feature at 325.15 GHz observed with the SHIRM-WBS II breadboard at a pressure of $8 \times 10^{-1}$ mbar inside the gas cell.

**Vacuum Cell Adsorption.**

While performing spectroscopic measurements with this set-up, a spectral feature began to appear if the chamber was left under vacuum for an extended period of time (less than 30 min). This line was located at 325.15 GHz, the exact frequency of the $5_{1,5} \rightarrow 4_{2,2}$ water transition. To investigate the possibility of a vacuum leak in more detail, the chamber was pumped down to the lowest attainable pressure, below $10^{-4}$ mbar. All of the valves were then closed off to allow any leaking material to enter the chamber while the emission brightness temperature was measured in the lower sideband. The leak rate was found to be around $1.73 \times 10^{-4}$ mbar/s when not pumping (Fig. 4.25 (a)). Spectral measurements provided confirmation that the primary molecule in the leak was water due to the presence of a line at 325.153 GHz, as shown in the results in Fig. 4.25 (b). The feature begins to appear at a pressure of $2 \times 10^{-2}$ mbar (red curve). The signal intensity reached a peak at around 156 K, with pressure broadening clearly visible in the magenta curve in Fig. 4.25.

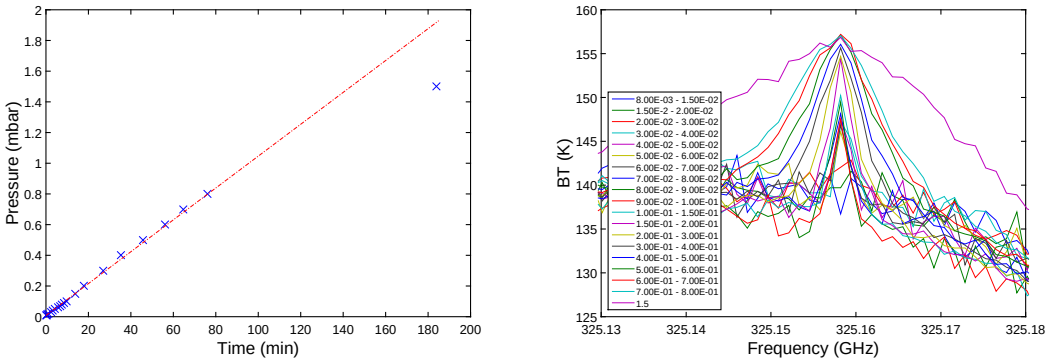


(a) (b)

Figure 4.25: (a) shows the pressure inside the cell as a function of time once the chamber is hermetically sealed. The dashed red curve is a linear fit to the data which covers the range from t = 0 to t = 80 min. (b) represents the brightness temperature of the gas leakage inside the cell from $8 \times 10^{-3}$ mbar (blue curve) to 1.5 mbar after 3 h and 4 minutes (purple curve).

A straightforward experiment was carried out to check whether the leak into the chamber consisted mainly of water vapour or some other combination of gases. The test involved checking for the presence of the measured, 325.15 GHz feature with the chamber at a pressure of 1.5 mbar while exposed to flowing air, static air or the suspected pure water vapour gas. The results of this experiment are shown in Fig. 4.26. The 325.15 GHz water line only appears when the chamber is exposed to the pure water vapour gas (blue curve) whereas under the same pressure conditions, neither the flowing (red curve) nor static (green curve) atmospheric gas produces the feature. Therefore, it is possible to conclude that the leak does not consist of the usual ratio of atmospheric gases but is instead mostly made up of water molecules, corresponding to the Mylar characteristic. Furthermore, the line at 1.5 mbar agrees with the one observed when pure water vapour is introduced.

In conclusion, the possible reasons for water leaking into the chamber over an extended period of time when the system is not connected to a vacuum pump could include residual water in the lines, valves and walls which transformed into the gas phase inside the cell. However, the main source of leakage is due to the low rate absorption of atmospheric water vapour through the Mylar windows.

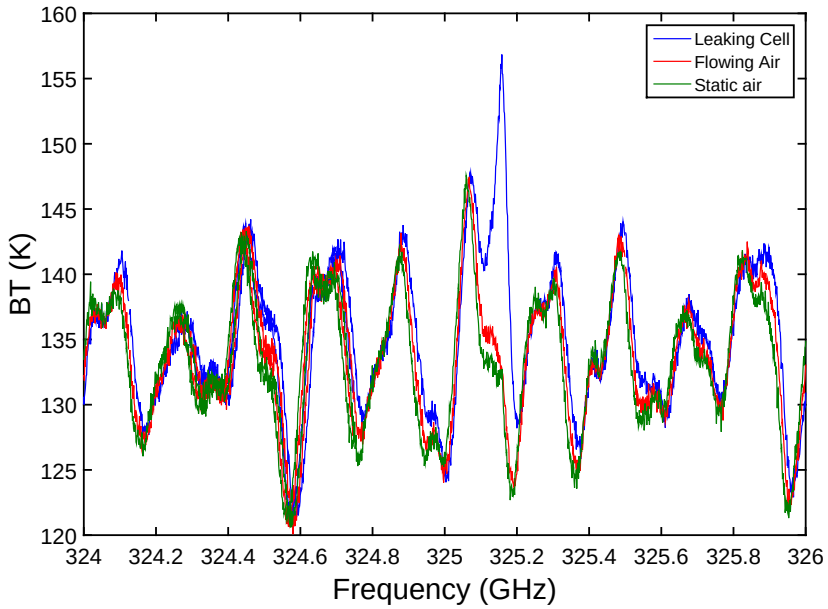


Figure 4.26: Comparison of the emission brightness temperature for different gas combinations leaking into the cell. Pure water vapour (blue curve) produces a feature at 325.15 GHz, while neither flowing (red curve) nor static (green curve) air at the same pressure lead to the presence of the line.

### 4.4.3 Methanol

The last molecule analysed in the gas phase was methanol ($CH_3OH$). In the THz, it contains a very rich spectrum in its ro-vibrational transition levels. Indeed many ro-vibrational lines are observable. Figure 4.27 shows the simulated brightness temperature of $CH_3OH$ from 0 to 400 GHz using the RFM radiative transfer model described in Chapter 5. The THz-DES frequency range is shown in red. The different spectral features observed using the THz-DES instrument are shown in Table 4.1.

Table 4.1: $CH_3OH$ THz-DES spectral features with their spectroscopic characteristics [219].

| Molecule | Frequency (GHz) | Quantum Numbers | Transition |
|---|---|---|---|
| $CH_3OH$ | 326.631 | $10_{1-}/10_{0+}$ | A |
| $CH_3OH$ | 342.730 | $13_{1-}/13_{0+}$ | A |
| $CH_3OH$ | 344.109 | $18_2/17_3$ | E |
| $CH_3OH$ | 344.312 | $10_2/11_3$ | E |
| $CH_3OH$ | 344.443 | $19_{1+}/18_{2+}$ | A |
| $CH_3OH$ | 345.904 | $16_{1-}/15_{2-}$ | A |

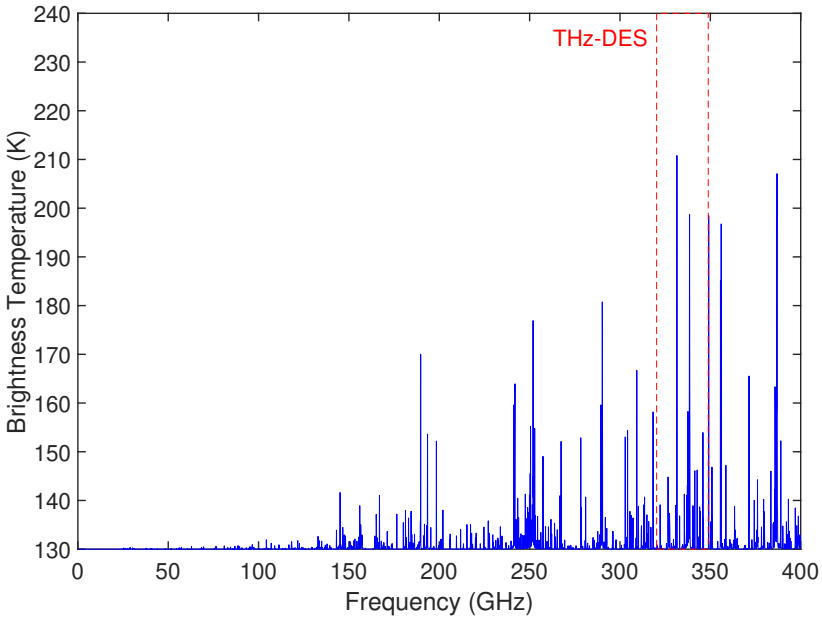


Figure 4.27: Simulated $CH_3OH$ brightness temperature in a 1 m vacuum cell with 1 mbar of $CH_3OH$. The THz-DES frequency range is shown in red.

To obtain the results in Fig. 4.28, different local oscillator settings were used for the lower and upper sidebands while the chamber was under 2.5 mbar of pressure. The frequency range over which no data was acquired, represents the local oscillator gap of about 8 GHz. The blue curve in Fig. 4.28 corresponds to the lower sideband of the instrument. The red, green and black curves are the emission features of methanol observed in the upper sideband with an LO frequency of 329.0, 330.0 and 334.5 GHz.

## 4.5 Brightness temperature calibration procedure

The calibration procedure detailed in Section 3.6.1 describes the standard method to obtain the brightness temperature from an RF signal by measuring the output power of a hot and cold calibration target. In this section, an alternative calibration technique has been explored for the THz-DES experiment and its possible future iterations. This method consists of performing the calibration procedure

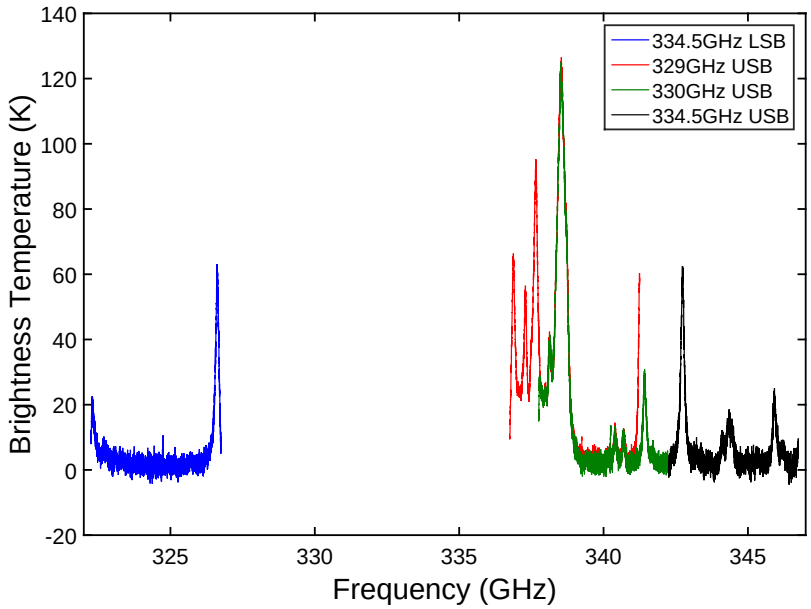


Figure 4.28: Gas phase Spectra in the LSB and USB of 2.5 mbar of $CH_3OH$ taken with different local oscillator settings: 334.5 GHz LSB (blue curve) and USB (black curve), 329.0 GHz (Red curve), 330.0 GHz (green curve).

only before or after the desorption measurements so the acquisition speed is not limited by the use of a rotary mirror.

Instead of constantly rotating and acquiring the output power from three different sources which usually defines one calibration cycle, each source is observed for an extended period of time before moving on to the next one. Figure 4.29 shows the way that such acquisition was done. For a specified integration time (1 s), the same target is observed over an extended averaging time period. The dark blue curve represents the scene view power emanating from the cell when it is filled with 13 mbar of gaseous water. The flat mirror then rotates to observe the cold target (red curve) before the signal from the hot target (dark green curve) is acquired. The slope of each power curve decreases with the number of acquisition cycles performed (time of total observation). A linear fit can then be applied to these output powers to obtain a constant power over time value for the three sources while keeping the absolute difference in power. The light blue, magenta and light green curves correspond to the scene, cold and hot target views respectively.

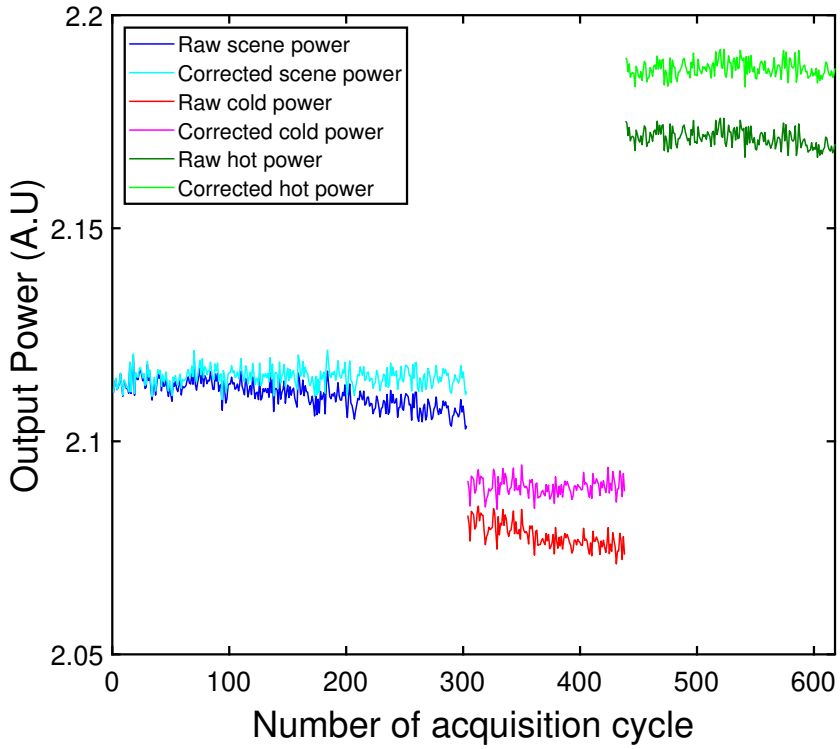


Figure 4.29: Acquisition of the scene power (blue line), cold target power (red line) and hot target power (dark green line) in succession. The light blue, magenta and light green curves show the corrected power obtained when taking into account the instrument gain variations for the scene, cold and hot target power respectively.

To better understand the fitting mechanism, only the hot target has been considered in Fig. 4.30. The top panel shows the raw data for the hot target temperature (blue curve) and data which has been corrected (red curve) using a linear fit (black curve). The bottom panel of Fig. 4.30 shows a similar operation on the hot target power. An increase in the target temperature should imply a decrease in the observed power. This is due to a gain drop defined by the stability and the gain variation intrinsic to the radiometer. Therefore, the measured temperature and measured power must be readjusted based on the first acquisition cycle. The curve used to fit the data was of the form $y = a \times x + b$. The same mathematical expression was used for the power of the other targets with the cold calibration target at a temperature of 77 K. The different coefficients are shown in Table 4.2. Once the "flat", corrected signals were obtained (light curves in Fig.

4.29), two offsets were added to the cold and hot power signals. It is necessary to add these offsets to maintain the difference between the three target views, in a manner equivalent to the offsets measured in the raw data during the cycle when the mirror rotates. Indeed for that cycle, no gain variation has yet occurred in the instrument and it can therefore be taken as a reference for future acquisition cycles. The first offset was taken to be $8.1 \times 10^6$ while the second as $5.6 \times 10^7$. These correspond to the cold and hot power curves respectively.

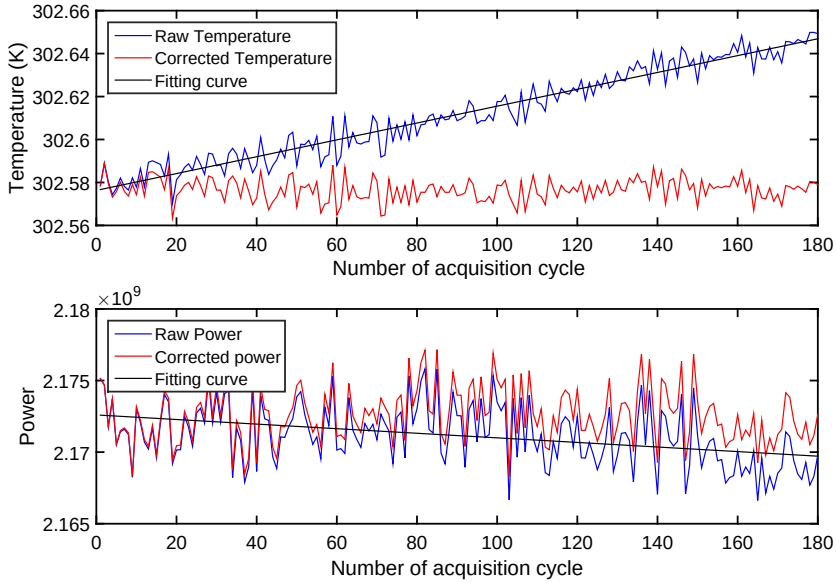


Figure 4.30: The top panel shows the hot target temperature fluctuations over a number of acquisition cycles and the fitting procedure used to obtain a constant temperature value (blue to red curves). The bottom panel displays a fit to the raw, hot target power data (blue curve) to achieve the corrected value (red curve).

Table 4.2: Fitting coefficients for the hot target temperature, scene, cold and hot views applying $y = a \times x + b$, where y is either the temperature or the power and x is the number of acquisition cycles.

| **Name** | **a** | **b** |
|---|---|---|
| Hot target temperature | $3.9 \times 10^{-4}$ | $3.0 \times 10^2$ |
| Hot target power | $-1.2 \times 10^4$ | $1.2 \times 10^9$ |
| Cold target power | $-3.1 \times 10^4$ | $1.2 \times 10^9$ |
| Scene view power | $-1.7 \times 10^4$ | $1.2 \times 10^9$ |

Once the corrected power for each of the views is determined, it is possible to proceed to the mathematical procedure which is explained in Section 3.6.1.

The new brightness temperature of gaseous water molecules is calculated. Before applying the equation to obtain the brightness temperature, the power for each target is averaged over the number of acquisition cycles. The results are shown in Fig. 4.31. The standard calibration brightness temperature procedure is shown in blue. As expected, standing waves due to the Mylar windows can be observed along with a broad spectral feature at 325.15 GHz. The red curve shows the brightness temperature using the raw data but with an added offset of –14 K to each point in order to match the mean value of 140.77 K that was obtained using the standard calibration brightness temperature process (blue curve). Although there is a difference of 14 K in the mean value, the trend in the red curve is similar to that in the blue curve, with similar standing waves and water features present. However, at around 324.3 GHz and after 326.4 GHz the edge brightness temperature values for one of the spectrometers do not match very well. Finally, by applying the correction (green curve), an excellent match is achieved when compared to the standard calibration brightness temperature process, without any of the edge effects observed in the red curve.

To compare the standard and corrected calibration brightness temperatures, the difference between the blue and green curves in Fig. 4.31 was calculated. The result highlights small brightness temperature variations between the two methods. The mean value of the brightness temperature difference was 2.25 K across the frequency range for which data was obtained. This is shown by the blue curve in Fig. 4.32.

The new calibration procedure fits the results obtained using the standard calibration process. However, due to two reasons the technique is not suitable for this proof-of-concept THz-DES experiment. Firstly, the radiometer temperature is not constant over time. Indeed depending on the environmental temperature, as well as the consistent operation of the spectrometers, its temperature will fluctuate (often in a non predictable manner) thus adding a gain variation to the acquired power. Therefore, it is challenging to fit the measured power with a lin-

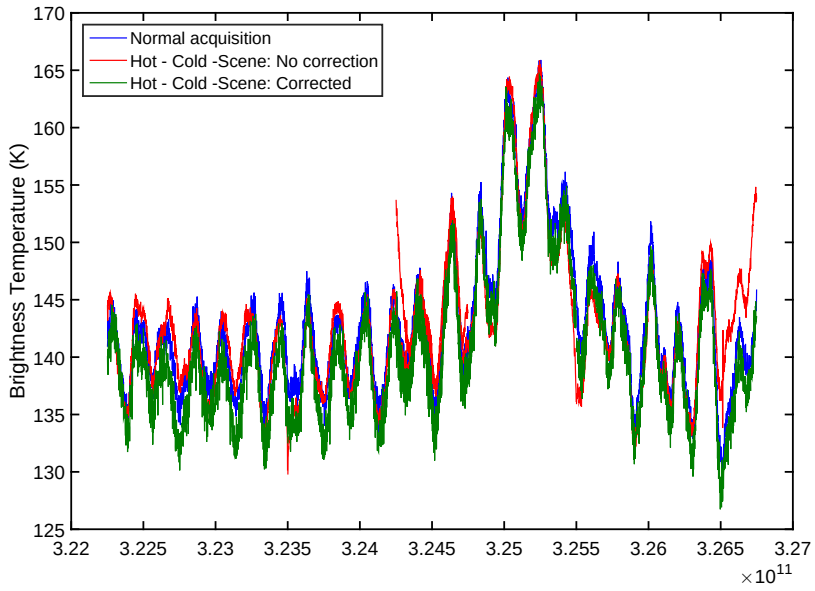


Figure 4.31: Comparison of brightness temperature for a standard acquisition process of 13 mbar of $H_2O$ (blue curve) with the uncorrected long-averaging acquisition procedure that has been manually shifted by –14 K (red curve) and the corrected long-averaging procedure (green curve) for the same amount of water.

ear curve as shown in the example in Fig. 4.30. In addition, the variation could be different for the three views. Nonetheless, this technique would potentially be more applicable to the current set-up if the thermal stability of the radiometer could be controlled in a more reliable manner. The second issue with this procedure arises from the fact that when the signal observed in the scene view changes due to the amount of emitting molecules, the output power will vary.

This technique for calibrating radiometric signals has previously been used for pure gas phase spectroscopy [307] and is a very promising approach for a future iteration of the THz-DES experiment. The fast acquisition of spectra without introducing an observational time delay would be highly beneficial to desorption analysis. In a future THz-DES experiment upgrade, it may even be possible to integrate the calibration module inside the desorption chamber and proceed to the THz-DES experiment ahead of the calibration stages. The advantages of this would include having a compact set-up and the ability to use just one cold

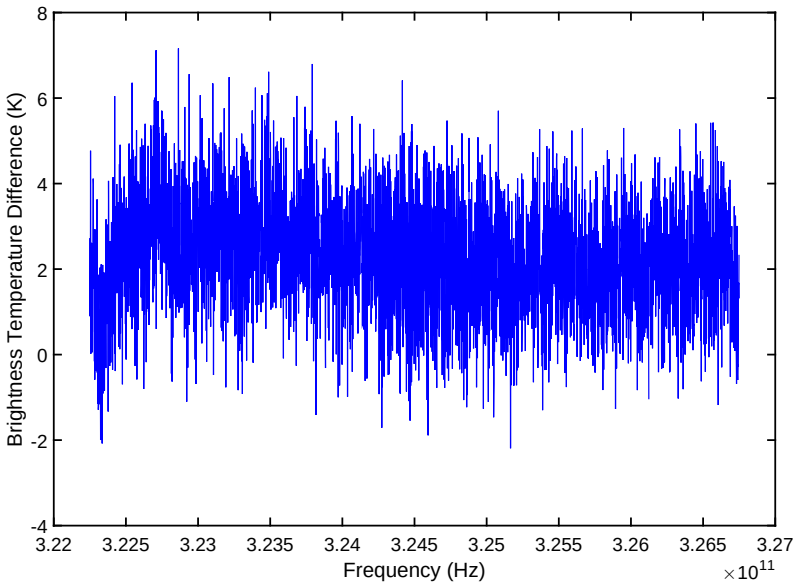


Figure 4.32: Brightness temperature difference between the standard acquisition and the corrected long-averaging procedure over the available frequency channels.

blackbody background target as the experimental background source and the cold calibration target.

## 4.6 Conclusion

This Chapter presented the characterisation of the THz-DES radiometer performance. Different parameters such as the LO frequency range, the spectral resolution (controlled via the sampling frequency) and the observational time (or integration time, $\tau$) are presented in Table 4.3 and can be changed to define the performance of the radiometer. The integration time, $\tau$, is one of the key parameters and represents the period of time over which the signal is integrated by the spectrometers. Increasing the integration time will significantly increase the sensitivity of the instrument. However, the stability study has shown that this parameter should not exceed 20 s as sources of noise affect the performance of the experiment and are challenging to constrain will appear within the radiometer after such time scales.

Spectra of gas phase molecules have been measured using the THz-DES ex-

Table 4.3: Key radiometer parameters which directly impact the frequency range, spectral resolution or sensitivity of the experiment.

| Name | Symbol | Settings | Impact |
|---|---|---|---|
| LO frequency | LO (GHz) | 334.5 GHz | Frequency Range |
| Sampling Frequency | $f_s$ (GHz) | 2.5 GHz | Spectral resolution-Bandwidth-Sensitivity |
| Integration time | $\tau$ (s) | 500 ms | Observation time-Sensitivity-Stability |

periment. LSB and USB data acquisition for the same molecular sample can be performed in succession for different chamber pressures. The selected spectroscopic features for nitrous oxide, water and methanol are shown in the Table 4.4.

Table 4.4: Selected spectral transitions of $N_2O$, $H_2O$ and $CH_3OH$ for the THz-DES experiment with their corresponding quantum numbers from the JPL catalogue[219].

| Molecule | Frequency (GHz) | Quantum Numbers |
|---|---|---|
| $N_2O$ | 326.556 | $13_{0,0}/12_{0,0}$ |
| $H_2O$ | 325.153 | $5_{1,5}/4_{2,2}$ : Para |
| $CH_3OH$ | 326.631 | $10_{1-}/10_{0+}$ : A |
| $CH_3OH$ | 342.730 | $13_{1-}/13_{0+}$ : A |
| $CH_3OH$ | 344.109 | $18_2/17_3$ : E |
| $CH_3OH$ | 344.312 | $10_2/11_3$ : E |
| $CH_3OH$ | 344.443 | $19_{1+}/18_{2+}$ : A |
| $CH_3OH$ | 345.904 | $16_{1-}/15_{2-}$ : A |

THz-DES experiments in Chapter 5 and 6 have slightly different settings, as shown in Table 4.3. These settings limit the types of experiments that the user can perform with the THz-DES system. A short integration time would permit the observation of dynamic processes while static mechanisms would benefit, in term of sensitivity, from setting a high integration time. In this proof-of-concept experiment, as the desorption mechanism has never been observed through the developed desorption chamber, the signal-to-noise was sacrificed to operate fast measurements with high-spectral resolution. The beginning of the desorption mechanisms is key to retrieve parameters such as the desorption energy, as explained in the next Chapter. For $N_20$, it occurs over 40 s. Considering the

calibration mechanism, only a third of this time could be used to observed the desorbing signal. Therefore, to measure more data points, the integration time was set to 500 ms, for all THz-DES measurements presented in the following Chapters. This generates a measurement sensitivity of 9 K. As a low volume of molecules are expected to desorb inside the vacuum chamber, the broadening of the spectral lines would be minimal and only very faint features would be emitted. The sampling frequency of the radiometer was set at 2.5 GHz, giving 1.2 MHz spectral resolution without decreasing the 9 K sensitivity.

# Chapter 5

# First THz-DES Results[1]

In this chapter, the first THz-DES results are presented with nitrous oxide ($N_2O$), water ($H_2O$) and methanol ($CH_3OH$) molecules. Pure ice desorption experiments for different thicknesses were performed on selected molecules. $N_2O$ was selected because of the bright feature observable in the THz-DES frequency range and as it is widely used in Earth observation and planetary science. $H_2O$ and $CH_3OH$ ices are key molecules in dense regions of the interstellar medium where stars form. Understanding the sublimation behaviour of these ices is vital to explain the chemistry observed in star formation regions. The qualitative and quantitative approaches presented in this chapter successfully describes the thermal desorption effect and its impact on the spectroscopic lines.

## 5.1 Introduction

Three molecules were selected for the first THz-DES experiments. These molecules, $N_2O$, $H_2O$ and $CH_3OH$, have been widely studied, are key molecules in the ISM, and present spectral transitions observable with THz-DES. Spectroscopic measurements of these molecules have been presented in Section 4.4. The features studied in this chapter are shown in Table 5.1 with their corresponding quantum

[1] Auriacombe, O. et al, Review of scientific Instruments, in prep. and presented in [11]

Table 5.1: Selected spectral transitions of $N_2O$, $H_2O$ and $CH_3OH$ for the THz-DES experiment with their corresponding quantum numbers from the JPL catalogue[219].

| Molecule | Frequency (GHz) | Quantum Numbers |
|---|---|---|
| $N_2O$ | 326.556 | $13_{0,0} - 12_{0,0}$ |
| $H_2O$ | 325.153 | $5_{1,5} - 4_{2,2}$ : Para |
| $CH_3OH$ | 326.631 | $10_{1-} - 10_{0+}$ : A |

numbers[219].

Another advantage of investigating $N_2O$, $H_2O$ and $CH_3OH$ is that these molecules have sublimation temperatures corresponding to the THz-DES surface temperature range. Sublimation temperatures of $N_2O$ have been measured for various pressure values[91, 314]. For a THz-DES pressure valuebetween $10^{-5}$ and $10^{-3}$ mbar, the thermal desorption is found to be between 100 and 115 K, as seen in Fig. 5.1. In THz-DES, water desorbs between 195 and 210 K [88, 173, 178], and $CH_3OH$ sublimates from 170 to 190 K [173, 225]. Standard TPD (see Section 1.3.2) has been used intensively on these three molecules to retrieve the desorption energy temperature. This is explained in Chapter 6.

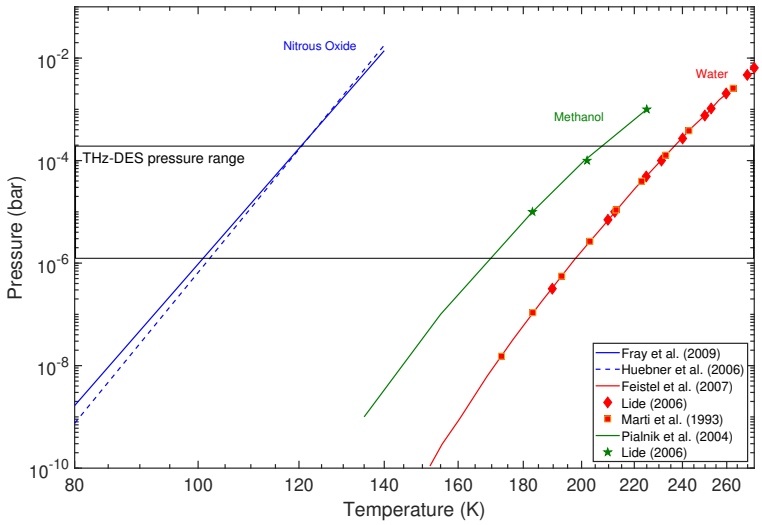


Figure 5.1: Sublimation Temperatures of $N_2O$, $H_2O$ and $CH_3OH$ as a function of the pressure.

### 5.1.1 Nitrous Oxide

Nitrous oxide has been observed for Earth observation and astrophysical purposes. $N_2O$ was detected in space for the first time in 1994 by Ziurys et al.[323], using the Arizona Radio Observatory (ARO) telescope. The transitions observed were at 75 (J=3-2), 100 (J=4-3), 125 (J=5-4), and 150 GHz (J=6-5). More recently, it has also been detected within the Sagittarius cold molecular cloud by observing the J=6-5 transitions (150 GHz)[115]. $N_2O$ contains an N-O bond, making it a strong indicator of the presence of N-O chemistry involved in the ISM, similar to nitric oxide[324] and nitroxyl[273]. N-bearing molecules are expected to freeze out onto grain mantles[40]. Chemical reactions with other molecular species occurs within the ice. For example, the nitrous oxide abundance in the interstellar medium can be explained by surface interactions between oxygen-bearing components like NO[115] (or electrically excited O[139]) and $N_2$ ice formed on dust particles. When ice sublimates, the nitrous oxide is then released into the gas phase, making it detectable by telescopes.

A laboratory study from Zheng et al.[321] showed that $N_2O$ is formed within an ice mixture of $H_2O/N_2$ using energetic electron irradiation. This mechanism has been observed on surface ice on Triton, Neptune's largest moon[139]. The chemistry involving N-bearing and O-bearing species, observed in the ISM, operates similarly on Triton but at higher pressures[57]. There is still limited knowledge on $N_2$ in the ISM as $N_2$ is inactive in the microwave and infrared spectral regions. $N_2O$ can therefore be used as a tracer for the abundance of the parent molecule, $N_2$[7]. Similarly, $N_2O$ has been detected desorbing from comets, and can be used to deduce the abundance of $H_2$ ice[252]. Moreover, $N_2O$ is also a key molecule in atmospheric science, as it is an ozone-depleting substance. It has been seen that nitrous oxide is trapped in Arctic sea ice and when it sublimates, it is released into the atmosphere and subsequently into the ozone layer[230]. Moreover, from an experimental point of view, $N_2O$ is easy to manipulate as it

can be stored in a gaseous lecture bottle with no freeze-pump-thaw cycle required for further purification.

### 5.1.2 Water

Water is a fundamental species in molecular astrophysics. $H_2O$ was detected for the first time in the Orion Nebula in 1969. This first observations were made by observing microwave radiation at 22 GHz[46], and later, the water line studied in this chapter at 325.15 GHz, was detected in Orion-KL[191], followed by many detections, for example with ALMA band 7 [236]. The *WISH* programme of the Herschel space telescope made significant observations in pre-stellar cores and star forming regions of gas-phase water and molecules related to its chemistry. From observations, $H_2O$ was found to be the most abundant molecule in interstellar icy mantles[105]. In dense cold regions of the ISM, only water formed on dust grains can explain its abundance. Tielens and Hagen[289] discussed the mechanism of water ice formation on dust grains, and their results, now supported by experimental evidence [68, 168], showed that water is formed via three mechanisms which are the hydrogenation of O, $O_2$ and $O_3$. $H_2O$ ice molecules would then interact with other atoms and/or molecules leading to the formation of more complex molecules. When the dust temperatures rose above 100 K[89, 244], water and trapped complex organic molecules sublimate into the gas phase. During this lapse, the gas phase abundance of water appears similar to the ice abundance. Laboratory studies on water ice are necessary to understand the chemistry involved within the ice depend on reactants, temperature, and thickness (See van Dishoeck et al. [300]) and the formation of $H_2O$ ice via a controlled environment using TPD techniques (see Section 1.3.2).

A constraint on the ortho/para ratio of water in the gas has been detected in space due to the spectroscopic peculiarity of water (see Section 4.4.2). For example, Hogerheijde et al.[129] observed two microwave radiation bands at 557

GHz (ortho-$H_2O$) and 1113 GHz (para-$H_2O$) using the Herschel-HIFI instrument. They found out that the ortho/para ratio in the protoplanetary disk studied (TW Hya) was much lower than the range of ratios measured for Solar System comets[26], 0.77 vs 2 to 3. Cold water would have a ratio below 1 whilst hot water regions would have a ratio of the order of 3 [76]. Some studies have concluded that the ortho/para ratios do retain history of the formation temperature, a pure para-$H_2O$ shows ortho/para ratio upon sublimation[266]. Some questions remain, such as would photodesorption water present the same ortho/para ratio and what are the processes leading to ortho/para ratio equilibration.

Studying $H_2O$ with the THz-DES experiment is a significant step in astrochemistry laboratory experiments, to further understand the evolution of the ortho-para ratio observed in the THz.

### 5.1.3 Methanol

Methanol is another very important interstellar molecule. It has been observed in its gaseous phase, for example at 96.7 GHz in dark clouds [92] but also in its solid phase as interstellar ice at 2.2 μm [27]. By observing the abundance of methanol in the ISM and comparing it to astrochemical models results [101] as well as gas-phase laboratory formation experiments [104], it has been found that $CH_3OH$ is predominantly formed via solid state reactions on dust grains, especially on CO-rich ices[97, 227].

The first main benefit of studying methanol ice desorption is that methanol is a key player in chemical reactions on ice dust grains [103]. Therefore, knowing how methanol ice evolves as a function of temperature is fundamental to the analysis of chemical reactions, which may happen within this ice.

The second benefit is that it can be used to help to determine the molecular deuteration ratio, which is a very powerful tool to retrieve physical conditions and the history of interstellar gas[240]. Various observations of rotational transi-

tions have given measurements of the deuteration ratios of methanol, for example in proto-stars looking at $CH_2DOH/CH_3OD$ (larger than 3) [111] or in hot cores (around 1.5) [44]. Comparison of models [112] and laboratory data [227] can potentially provide a full story of the methanol chemistry. Therefore, observations of methanol ice from the THz-DES experiment, using varying experimental conditions may provide valuable laboratory-based data on the deuteration ratio to be compared to observations.

The final benefit is that methanol presents interesting spectroscopic properties. Because it is an asymmetric molecule, it presents many spectral transitions between A- and E- symmetry energy levels, as explained in 2.2.1. For example, Mendoza et al. measured methanol emissions between 292-356 GHz using the APEX telescope to determine the A/E ratios for $CH_3OH$ and $CH_3ON$ to derive the abundance and trace chemistry activities [190]. Therefore, the observations and analysis of THz A- and E- transitions and the comparison of their ratio would give insight of any preferred desorption-energetic transitions depending on the temperature or molecular interactions or maybe the ice structure. This is investigated in more detail in Chapter 6.

### 5.1.4 Desorption Activation Energy

Most of our knowledge on interstellar and cometary ice is a combination of observations and laboratory experiments that simulate physical mechanism under similar environmental conditions. Previous analyses have been made on the thermal desorption of pure and binary ices [52, 89, 161, 197, 201]. A review of the literature in term of desorption activation energy for $N_2O$, $H_2O$ and $CH_3OH$ is given here.

The formation of $N_2O$ within the ice was studied using TPD[132] or non-thermal mechanisms such as photon irradiation sources[251]. Table 5.2 shows the values taken by the desorption energy for $N_2O$ ices between 18 and 25 kJ/mol.

Lian et al.[172] found a value of 22.19 kJ/mol at a wavelength of 2236 $cm^{-1}$ and 28.95 kJ/mol at 2270 $cm^{-1}$ on an MgO substrate. The amount of nitrous oxide in this study was lower than 3 monolayers. In this case, the purpose was to understand the interaction between $N_2O$ and its MgO substrate during a TPD experiment.

As explained in Chapter 5, water is an essential component of interstellar ices. From the literature review, values of desorption energy for water vary from 40 up to around 50 kJ/mol depending on substrate, ice structure and coverage. Methanol presents a desorption energy between 30 and 46 kJ/mol.

Table 5.2: Desorption activation energy of $N_2O$, $H_2O$ and $CH_3OH$ (in kJ/mol) from various TPD experiments in the literature.

| **References** | **Desorption Energy (kJ/mol)** | **Notes** |
|---|---|---|
| | $N_2O$ | |
| Toker et al.[291] | 17.99 | Photoinduced, PsI |
| Cornish et al.[56] | 21.9 | Pt(111), 50 Multilayer |
| Kiss et al.[158] | 21.9 | Pt(111), 50 Multilayer |
| Lian et al.[172] | 22.19<br>28.95 | 2236 $cm^{-1}$, MgO(001)<br>2270 $cm^{-1}$, MgO(001) |
| Sawabe et al.[250] | 23.4-25.3 | 0.44 ML, (90 - 100 K) |
| Black et al.[22] | 23.6 | (103 - 123 K) |
| Blue and Giauque[23] | 24.6 | (148 - 182 K) |
| Bryson et al.[35] | 25.1 | (68 - 80 K) |
| | $H_2O$ | |
| Bolina [24] | 39.9 | |
| Sandford et al. [246] | 40.0334<br>42.154 | Un-annealed pure<br>Annealed pure |
| Sandford et al.[245] | 42.154 | CSI substrate, $1^{st}$ order |
| Sack et al.[243] | 42.454 | |
| Smith et al.[270] | 46.4<br>47.7 | Multi-Layer amorphous, Pt(111)<br>Multi-Layer crystalline, Pt(111) |
| Bryson et al.[36] | 47.278 | Polycrystalline structure |
| Fraser et al.[89] | 47.999 | Au substrate |
| Speedy et al.[277] | 48.249 | Ru(001)/Au(111) substrate |
| Haynes et al.[120] | 49.795 | Sapphire substrate |
| | $CH_3OH$ | |
| Christmann et al.[47] | 29.932 | Pd(100) |
| Sandford et al.[246] | 35.17 | CsI |
| Martin-domenech et al.[179] | 36.209 | KBr |
| Bolina et al.[25] | 40.741 | HOPG (Leading edge) |
| Brown et al. [33] | 40.8 | HOPG (Leading edge) |
| Smith et al. [270] | 44.6 | multilayer, Pt(111) |
| Burke et al. [37] | 46 | HOPG $1^{st}$ order |
| Nishimura et al. [200] | 46.394<br>44.815 | Al2O3(0001)<br>Hsub for bulk crystalline |
| Green et al. [113] | 43.235<br>44.07<br>43.235<br>45.438<br>45.48 | Au<br>Silica<br>Silica (leading edge)<br>Silica (simulation)<br>HOPG (Simulation) |

## 5.2 Experimental methodology

The experiment has been explained in details in Chapter 3 and the assumptions made regarding the analysis of the THz-DES data (see Section 3.6.4) applies in this chapter.

### 5.2.1 Ice deposition procedure

The ices formed in this chapter is composed of single kind of molecules, respectively $N_2O$, $H_2O$ and $CH_3OH$. This ice is called pure ice. Molecules are firstly stored in the dosing line, which has a certain constant volume. They are then introduced into the vacuum chamber once the cold trap has been cooled down to its lowest temperature (77 K). The deposition mechanism of the ice has been introduced in Section 3.3.2 and is briefly summarized.

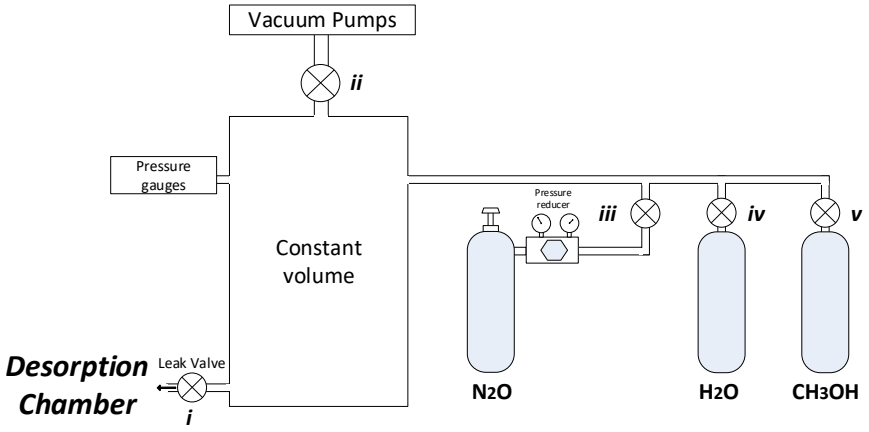


Figure 5.2: THz-DES dosing line configuration for nitrous oxide, water or methanol molecules, pure ice deposition.

The standard procedure is composed of few steps and is referred to as 1 exposure time deposition.

- Introduce 25 mbar of gaseous molecules in the constant volume: valves *i and ii* close; opening valve *iii* for $N_2O$ or freeze-pump-thaw cycle via valve *iv or v* for $H_2O$ or $CH_3OH$.

- Cool down the cold finger temperature to 77 K while still pumping on the desorption chamber: valves *i and ii* close.
- Once the surface temperature reached 77 K, isolate the desorption from its pumping system and open valve *i*.
- Keep valve *i* open until the pressure in the dosing valve reaches $1.10^{-2}$ mbar. Then close valve *i*.
- Wait until the pressure in the desorption chamber reaches $1.10^{-3}$ mbar. Open valve *ii* so as to clean the dosing line.
- Connect the pumping system to the desorption chamber to reach $10^{-5}$ mbar.

For multiple exposure times deposition, the same procedure is applied as for one deposition, but it is repeated the number of times required. For example, at the beginning of the new deposition, the desorption chamber is under vacuum and the valve *ii* is closed in order to introduce 25 mbar of molecules in the dosing line.

### 5.2.2 Experimental settings

For all the experiments presented in this chapter, the local oscillator of the receiver was set at 334.5 GHz. Each WBS is set with 2.5 GHz sampling frequency in order to be able to detect the spectral features listed in table 5.1. With those settings, the THz-DES frequency range became 322.25 - 326.75 GHz in the LSB and 342.25 - 346.75 GHz in the USB with a spectral resolution of 1.22 MHz. The transitions studied in this chapter appeared to be all in the LSB. The integration time used to acquire the spectroscopic data was set at 500 ms, to give the best sensitivity for a small observation cycle time.

A measurement of the NEδT as a function of the integration time has been presented on Fig. 4.7 (Section 4.2.2), shown as the red curve on Fig. 5.3. From this result, it appears that by increasing the integration time from 0.5 s to 5 s, the NEδT is divided by a factor two, doubling the sensitivity of the instrument.

Figure 5.3 shows the interval of time that the mirror is taking to switch between two identical views (one calibration cycle), for example between the view corresponding to the observation of the signal from the THz-DES chamber. One calibration cycle is completed in 2.67 s with an integration time ($\tau$) of 0.5 s. By setting the integration time to 5 s, the instrument will observe the brightness temperature from the THz-DES chamber only every 16 s. By comparing Fig. 3.6 and Fig. 5.6, it can be seen that the leading edge of the $N_2O$ desorption occurs over a period of 160 s. The respective number of points when $\tau$ is 0.5 s and 5 s are 60 points and 10 points only. Therefore to have more points to define the desorption curve, a fast but noisier measurement was used rather than a slow and lower noise measurement. A slower heating would permit to have high signal to noise ratio and low rate of change but was not achievable in this stage of the THz-DES experiment.

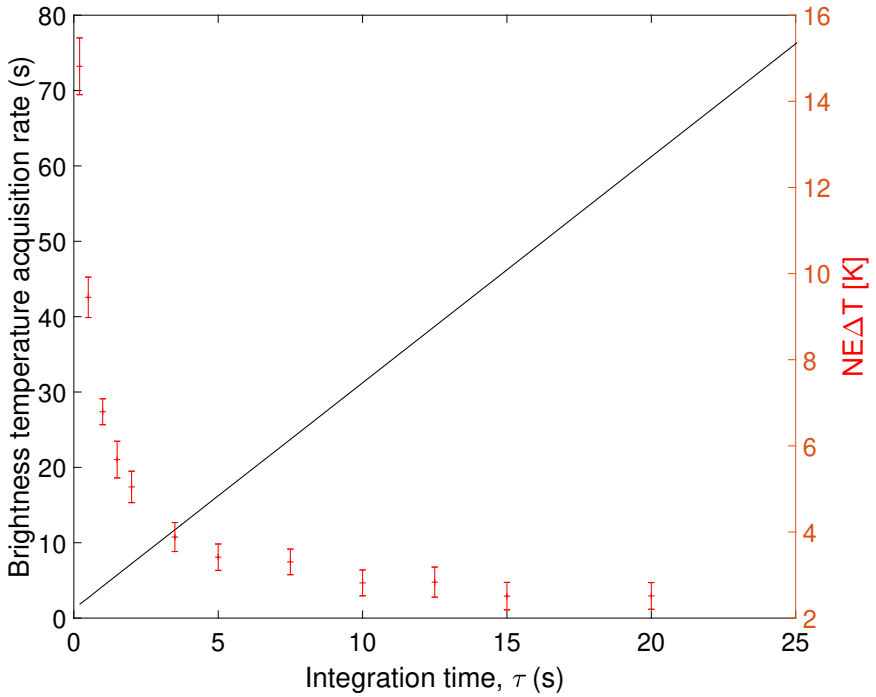


Figure 5.3: Brightness temperature acquisition rate and instrument sensitivity as a function of the integration time. It corresponds the period of time taken by the rotary mirror to acquire the same angle view i.e. after one calibration cycle.

The THz-DES acquisition starts once all the $LN_2$ had boiled off from the

cold trap. The thermal desorption is enhanced with the use of heaters at their maximal capacity with the Eurotherm (see Section 3.3.1). Surface temperatures and brightness temperatures data are recorded simultaneously and linked via their computer clocks. Then data are processed using MATLAB routines, as explained in Chapter 3.

## 5.3 Nitrous Oxide THz-DES

### 5.3.1 One exposure time

The first THz-DES spectra of the desorption phenomena in emission spectroscopy is presented in Fig. 5.4. The results come from the desorption of a layer of $N_2O$ grown with one deposition time. This shows the measured brightness temperature (BT) of desorbed $N_2O$ as a function of the frequency (y-axis) and trap surface temperature, noted $T_{surface}$ (x-axis). The blue contours (BT between -10 and 10 K) are the experimental noise from the radiometer, about 10K. The $N_2O$ feature J = 13 - 12 is measured at 326.553 GHz. It is 3 MHz away from the CDMS value 5.1. This does not affect the detection as the centre frequency is consistent over the THz-DES experiment. It is because of a small VCOs offset, as explained in Section 4.3.3. $N_2O$ molecules, observed via their central frequency, start to desorb at approximatively 100 K at a pressure of about $10^{-5}$ mbar. The observed feature is very weak with a BT rising to 20 K for a surface temperature of 110 K. Then the spectral line becomes wider (yellow, green surface contours). The number of molecules, into the optical path of the radiometer, increases significantly as desorption occurs and line broadening is happening as gas-phase molecules collide in the desorption chamber. The opposite effect is seen from $T_{surface}$ = 135 to 160 K, molecules are being pumped away. Desorption stopped and the pumping rate dominates. Finally, after $T_{surface}$ = 160 K, all molecules have been pumped out of the chamber, BT reaches the noise floor for all frequencies (the green

contour disappeared). At the central frequency signal, Bt is 80 K above the background at a trap temperature of $T_{surface}$ = 130 K (dark red contour). To retrieve qualitative trends on the desorption from the BT acquired, two ways of observing the THz-DES results are possible. They are shown as A and B in Fig. 5.4.

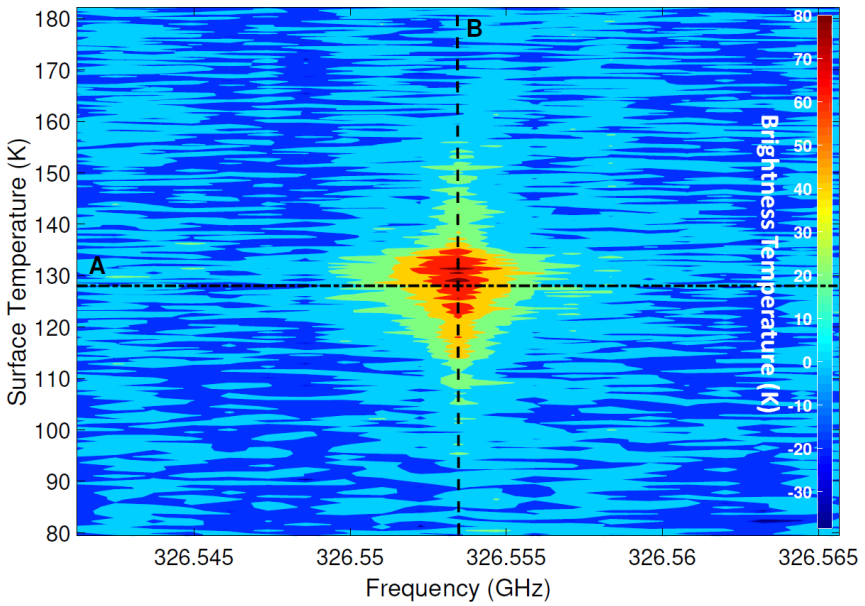


Figure 5.4: $N_2O$ THz-DES Result for one exposure time deposition. The contour figure of the brightness temperature of desorbed $N_2O$ molecules is plotted as a function of the frequency (x-axis), the trap physical temperature (y-axis).

### A - Frequency Domain

The first way to analyse the THz-DES results is in the frequency domain. It consists of plotting the BT as a function of the frequency for various surface temperature, as shown by the dashed line noted A in Fig. 5.4. This dashed line (A) corresponds to a $T_{surface}$ = 129.0 K. The BT for different surface temperatures is shown in Fig. 5.5. Brightness temperatures for $T_{surface}$ of 94.8 K (blue curve), 115.3 K (red curve), 129.0 K (green curve and previous A-dashed line) and 141.5 K (black curve) are shown from 326.545 GHz to 326.565 GHz.

At $T_{surface}$ = 94.8 K, no $N_2O$ is desorbing, resulting in a flat intensity, within the noise floor. Then desorption starts as the temperature increases. The bright-

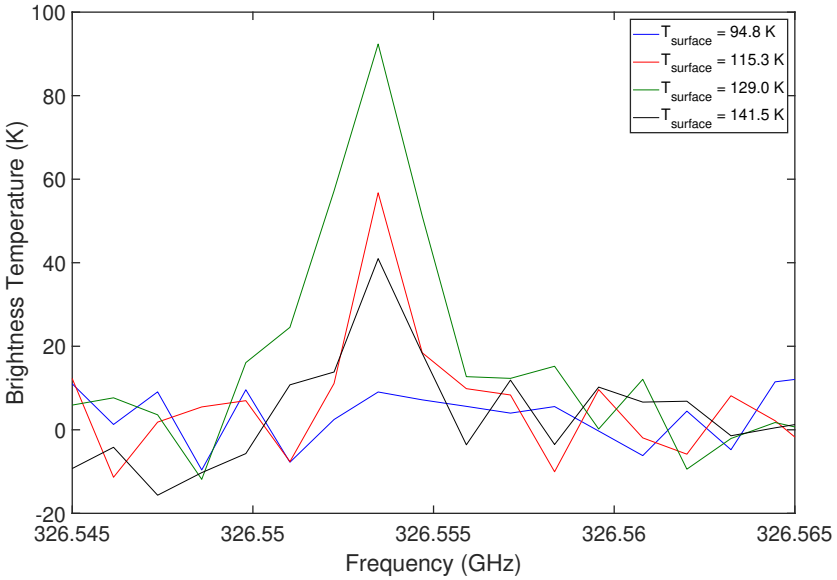


Figure 5.5: Brightness temperature for spectral feature of $N_2O$ molecules as a function of the frequency at different trap physical temperature, respectively 94.8 K (blue curve), 115.3 K (red curve), 129.0 K (gree curve) and 141.5 K (black curve).

ness temperature is increasing at the frequency of $N_2O$ feature (356.553 GHz) and away from this central frequency no radiations are detected. As the number of molecules emitted increases, the value of the brightness temperature rises from 56.74 K to 92.36 K when the surface temperature increases from 115.3 K to 129 K. Then all the ice desorbs and molecules are pumped away. The brightness temperature decreases (40.98 K at $T_{surface}$ = 141.5 K) and eventually reaches the THz-DES noise floor.

The line broadening is observable in the frequency domain. Adjacent spectrometer channels to the centre line frequency, 326.553 GHz for $N_2O$, are tracers of this pressure broadening effect (see Section 2.2.2). Molecule collisions within the chamber reduce the lifetime of their upper state which impact the width. This is a quantum effect dependent on the pressure and the temperature of the molecules. As seen in Fig. 5.5, the spectral line intensifies and becomes wider over frequency. The line intensity increased until the molecular density in the beam path reaches a value where self-broadening is important, leading to a higher full-

width at half-maximum (FWHM).

### B - Surface Temperature

The second method to analyse the THz-DES results is closer to standard TPD curves. Instead of spectroscopically observing the emissions, only the one channel corresponding to the central feature frequency is selected. The brightness temperature at this frequency is then plotted over the surface temperatures. This corresponds to the B-dashed line in Fig. 5.4. Figure 5.6 shows the spectra from Fig. 5.4 at four frequencies corresponding to the central frequency line channel (blue curve and previous B-dashed line), 1 channel (red curve), 2 channels (green curve) and 5 channels (black curve) away from the central channel. The maximum intensity is measured at 326.5535 GHz.

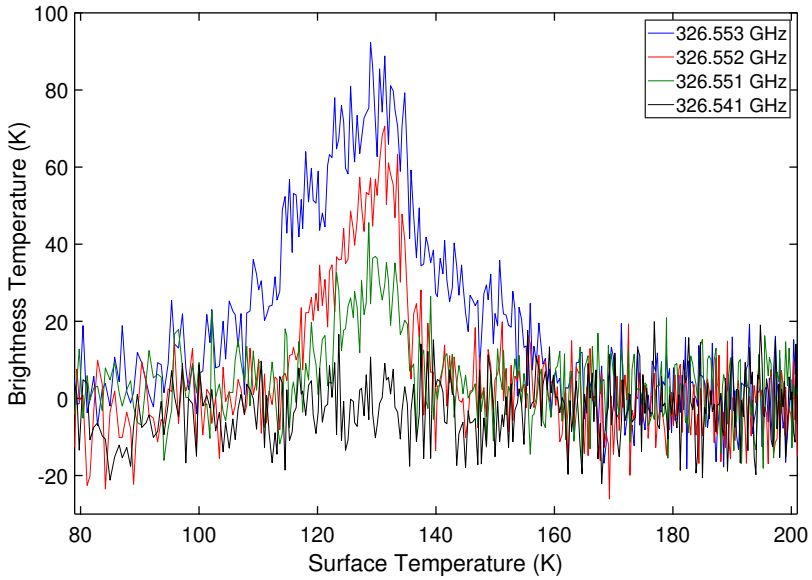


Figure 5.6: Brightness temperature for spectral feature of $N_2O$ molecules for its peak frequency (blue curves) and the 'wings' which are the nearest spectrometer channels (red, green and black curves).

By analysing the central frequency, $N_2O$ desorption starts around 100 K when the intensity from the blue curve becomes higher than the noise floor (around 10 K). This corresponds to the literature value from Fig. 5.1[91]. From $T_{surface}$ = 95 - 135 K, the BT increases to reach a maximum value around BT = 80 K.

More $N_2O$ ice is sublimated into the desorption chamber. The newly gaseous molecules emit with more intensity as their amount increases. The BT give a direct measurement of this phenomena. From $T_{surface}$ = 130 - 160 K, the pumping rate becomes higher than the desorption rate. The number of molecules in the chamber drops, as observed from the BT. After 160 K, no radiation is detected. All icy molecules have desorbed and been pumped away.

Looking at the 'spectral wings'(red and green curves), their BT rises above the noise floor at $T_{surface}$ = 115 K and 120 K, respectively. The BT trends are following the one of the central frequency from $T_{surface}$ of 115K to 140K. Then no signals are detected. Those 'spectral wings' corresponds to the width of the features as seen in Fig. 5.5 and are indicators of the pressure broadening described above.

**Summary**

As expected $N_2O$ sublimates at around 100 K for a pressure below $10^{-5}$ mbar. THz-DES Spectroscopic results give real emission intensity and can be analysed depending on the surface temperature and the frequency. TPD-like curves corresponding to the brightness temperature of the central frequency line as a function of the surface temperature is best suited in order to describe and quantify the thermal desorption mechanism. This first result from the THz-DES experiment gave insight on the power offered by the THz-DES spectrum. It demonstrates that sublimation data depends on the pressure and it can be acquired with accuracy. The impact of pressure broadening has been seen as the number of molecules in the gas phase increases.

### 5.3.2 Spectral Line fitting

As explained in Section 2.2.2, line broadening plays an important role on atmospheric Earth and exoplanetary or space spectroscopy. It gives insight on absorption cross sections, abundances[121] via pressure broadening[194] or thermal

broadening[30]. In the THz-DES, as the number of molecules is low, the natural broadening occurs firstly linked to the lifetime of the excited level according to the Heisenberg uncertainty principle as explained in Section 2.2.1. Then molecular collisions occur in the gas phase. The pressure broadening is due to the increase of the uncertainty in the excited energy level as a colliding molecule will disrupt the emitting molecule [41]. Those two mechanisms involved here present a Lorentzian line profile.

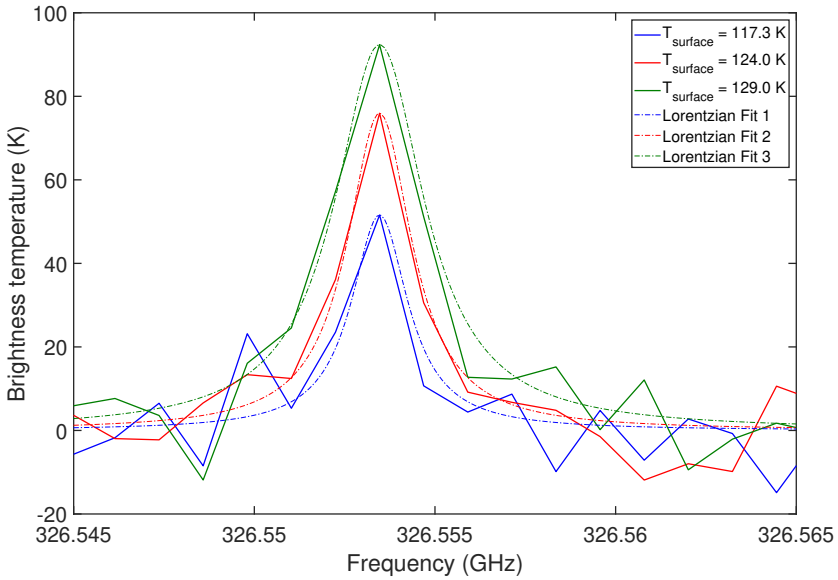


Figure 5.7: $N_2O$ brightness temperature for one deposition at 117.3 K (blue curve), 124.0 K (red curve) and 129.0 K (green curve). The dashed curves are the brightness temperature obtained using a Lorentzian fitting function.

The brightness temperatures measured as a function of the frequency, as explained in Fig. 5.5, were used to fit the data using a Lorentzian function. Figure 5.7 shows the measured BT with its corresponding fit (dashed line) for the surface temperature of 117.3 K (blue curves), 124.0 K (red curve) and 129.0 K (green curve) were fitted using a Lorentzian function. The fitting function is applied on the data by matching their FWHMs. The FWHM is increasing as the line gets brighter, respectively at 1.9 MHz, 2.2 MHz and 3.0 MHz at $T_{surface}$ of 117.3 K, 124.0 K and 129.0 K.

### 5.3.3 Multiple exposure times

According to TPD literature (see Section 1.3.2), the thickness of the ice grown should not impact the desorption rate. This means that for two ices with different deposition amounts, the sublimation point should be identical and the BT's slope at the beginning of the desorption similar[90]. The thickness dependence of nitrous oxide desorption has been studied with 1, 3 and 6 exposure times. Figure 5.8 shows the brightness temperatures measured at 356.553 GHz for 1 exposure time (blue curve), 3 exposure times (red curve) and 6 exposure times (green curve).

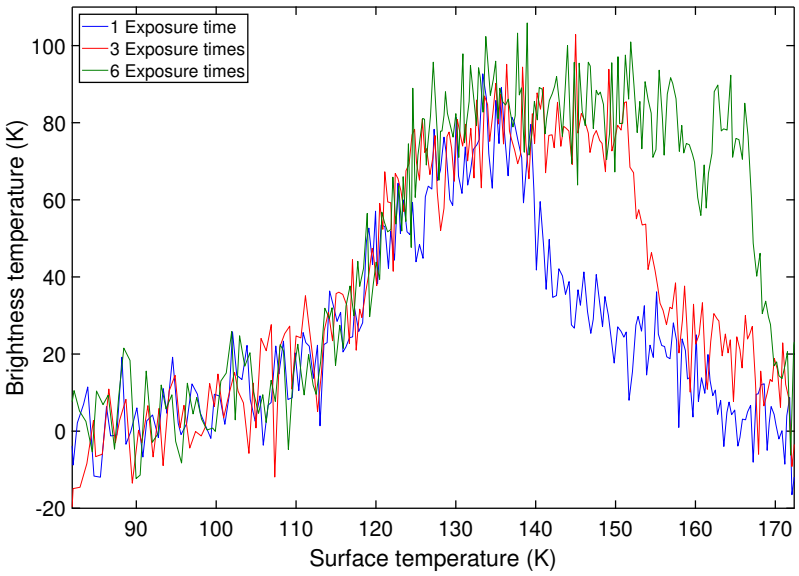


Figure 5.8: Brightness temperature versus surface temperature as a function of the ice thickness grown for $N_2O$. The blue curve is related to the brightness temperature for an ice made via 1 exposure time deposition whereas in the case of the red curves, 3 times more $N_2O$ has been deposited and for the green curve 6 times more.

From $T_{surface}$ = 77 K to 140 K, BTs from all thickness's desorptions are perfectly matching. The sublimation point and desorption rate are the same for those three ices. At $T_{surface}$ = 140 K, the blue BT starts decreasing as the desorption mechanism stopped and the pumping rate is dominant. However, the red and green BT are retain the same value of about 80 K up. At $T_{surface}$

= 155 K, the pumping rate for 3 exposure times ice becomes predominant in the cell resulting a decrease of the red BT. However $N_2O$ from the 6 exposure times deposition is still sublimating as the green BT is at 80 K. A momentary decrease in its BT to 60 K appears at $T_{surface}$ = 160 K. Then the brightness temperature returns to the plateau value of 80 K. This effect is due to a quick decrease of the number of molecules desorbing. The explanation could be due to the non-homogeneity of the thick ice grown. Because the ice grown is very thick and not deposited directionally on the cold area, area with ice further away from the heater would desorb slightly later in time, therefore at a higher surface temperature. This effect lasts only 3 s. Then the green BT return to 80 K. At $T_{surface}$ = 170 K, all ice on the trap desorbed and the decreasing slope is observed as expected.

It appears from those experiments that the thickness of the ice does not impact on the thermal desorption process, confirming previous TPD-findings. The BT curves match perfectly until the number of molecules is more important for thicker ice, where the desorption lasts longer while the cold surface is heating up to higher temperature.

### 5.3.4 Discussion

This first THz-DES agrees with TPD experiments displaying a glimpse of its performance. Indeed the sublimation point measured was within the range of the desorption chamber pressure, 100 K at around $10^{-5}$ mbar. The thickness of the ice does not perturb the desorption rate as seen by observing the THz-DES results for various ices. This highlights the practicability of this experiment.

Typical THz-DES curves can be split into 5 parts, as shown in Fig. 5.9. The brightness temperature is 0 K while ice is on the cold surface of the trap. At $T_{surface} = T_{des}$, $T_{surface}$ reached the sublimation point ($T_{des}$) of the studied molecule. Then the positive slope of BT corresponds to the thermal desorption

of the ice molecules. A plateau may be reached when the thickness of the ice is important enough, corresponding to the equilibrium of the desorption and pumping rate in the chamber. Then a decreasing slope is seen corresponding to the pumping rate. Molecules are pumped out of the desorption chamber. Finally, all the ice has desorbed and all gaseous molecules pumped away leaving a BT at 0 K.

Lorentzian line profiles can be fitted to the THz-DES results. The natural and pressure broadening occurs with the THz-DES as the pressure within the desorption chamber is higher than $10^{-6}$ mbar.

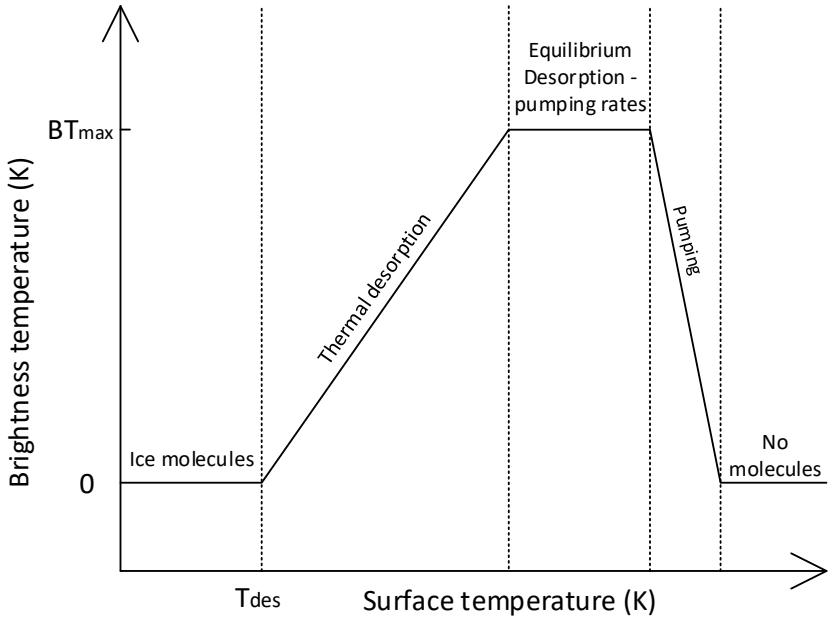


Figure 5.9: The 5 phases of the thermal-desorption in the THz-DES proof-of-concept experiment. Icy molecules sublimate and are observed in their gaseous forms. A plateau of their emission brightness temperature may be rich depending on the thickness of the ice grown. Then once the desorption stopped, molecules are pumped out of the chamber.

A first limitation was observed for thick ice configuration. A quick decrease of the number of molecules desorbing was observed. The fact that the BT increased again means that icy molecules desorbed at apparent higher surface temperature. This was linked to the non-homogeneity of the ice deposition due to the

experiment configuration. Re-adsorption could potentially be another reason. Molecules desorbing first could be re-adsorbed on the warming up surfaces. However, because of the fast heating rate applied on the experiment, this should not be significant here.

## 5.4 Pure Ices THz-DES

This section presents the THz-DES results for $H_2O$ and $CH_3OH$.

### 5.4.1 Water THz-DES

After demonstrating the capacity of the THz-DES experiment with N2O, $H_2O$ was deposited on the cold trap surface following the liquid deposition procedure explained in Section 5.2.1. In a similar way, only the central frequency, 325.153 GHz for para-$H_2O$ ($5_{1,5} - 4_{2,2}$, Table 5.1) is used for desorption analysis and the impact of the thickness is characterised.

#### 5.4.1.1 One exposure time

The THz-DES results obtained for 1 exposure time of water molecules is shown in Fig. 5.10. The blue curve represents the central frequency at 325.148 GHz whereas the red, green and black curves are showing other spectrometer channels at 325.150 GHz, 325.151 GHz and 325.157 GHz. Because of the low intensity of this water feature, all BT curves have been smoothed to make the THz-DES results more readable as the noise is half the maximum BT, 12 K. The more intense brightness temperature is measured at 325.148 GHz which is about 4 MHz away from the database value (Table 5.1) as observed for $N_2O$.

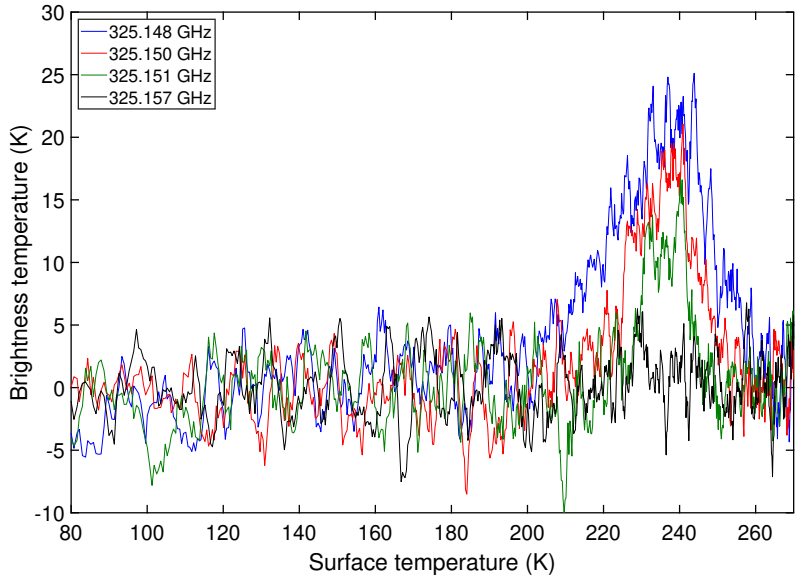


Figure 5.10: Brightness temperature of desorbed $H_2O$ molecules as a function of the physical temperature. The blue curve is the raw data of the central frequency channel and the black line is the smoothed data. is showing the desorption results for different frequency channels at 325.148 GHz (blue line), 325.150 GHz (red curve), 325.151 GHz (black curve) and 325.157 GHz (black curve).

The sublimation temperature in the THz-DES pres range($10^{-5}$ -$10^{-3}$ mbar) was $T_{surface}$ = 200 K. Between $T_{surface}$ = 210 - 240 K, thermal desorption occurs as described in Section 5.3.4, reaching a maximum brightness temperature of 21 K. From $T_{surface}$ = 140 K to 260 K, all $H_2O$ ice sublimated and remaining gas phase molecules are pumped away. After 260 K $H2_O$ disappeared from the desorption chamber completely.

Similarly to $N_2O$, the pressure broadening effect is well observable by comparing the central frequency with other channels. From $T_{surface}$ = 220 K - 230 K, the intensity at 2 MHz from the central line (red curve) rises from 0 K to 15 K. At $T_{surface}$ = 230 K, the signal at 325.151 GHz starts to increase. This means that the spectrum is widening over the frequency. The black curve corresponding to a channel at 9 MHz from the central frequency remains within the noise floor.

#### 5.4.1.2 Multiple exposure times

Similarly to Section 5.3.3, THz-DES experiments were performed for different water ice thickness. The results are shown in Fig. 5.11 with 1 exposure time in blue and 3 exposure times in red. The smooth brightness temperatures for each experiment at the central frequency (325.148 GHz) are plotted.

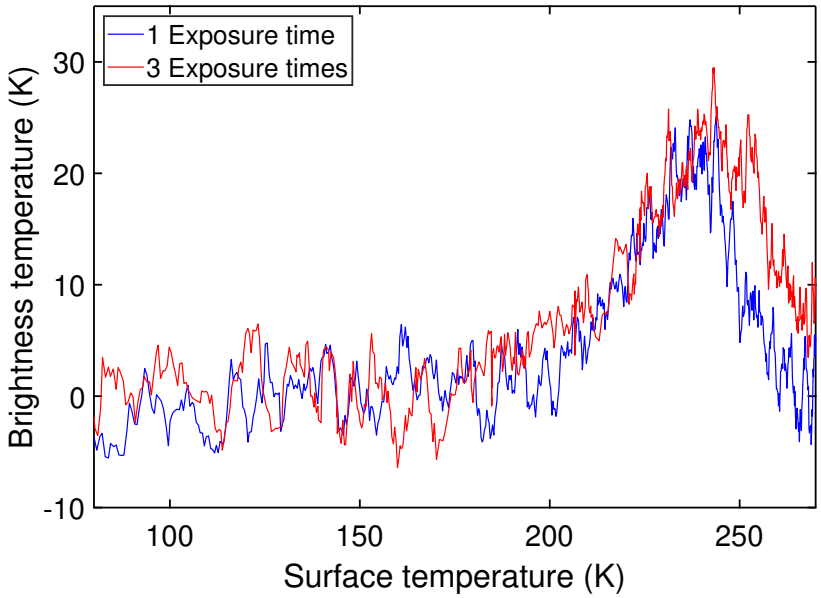


Figure 5.11: Brightness temperature versus Surface Temperature as a function of the ice thickness grown for $H_2O$. The blue curve is related to the brightness temperature for an ice made via 1 deposition whereas in the case of the red curves, 3 times more $H_2O$ has been deposited.

Exactly the same trend as observed for $N_2O$ is seen when increasing the amount of ice deposited onto the surface of the cold trap. Thermal desorption takes place normally for both ices up to $T_{surface}$ = 245 K. After this point, the blue curves BT decreases to the noise floor while red curves BT decreases only at $T_{surface}$ = 255 K. The desorption for thicker ice is lasting longer being the BT at the noise floor 10 K further in term of surface temperature than for the 1 exposure time deposition ice.

As seen for $N_2O$, the thickness of the ice for $H_2O$ does not impact the sublimation mechanism in term of desorption temperature and rate. However, the brightness temperature for a thick ice has a maximum intensity plateau spreading

over a wider range of surface temperatures. Indeed, the amount of ice will take longer to desorb and be pumped away from the desorption chamber.

### 5.4.2 Methanol THz-DES

The last molecule studied here is $CH_3OH$. Its THz-DES spectra is measured for the centre frequency 326.631 GHz, A-$CH_3OH$ ($10_{1,9-} - 10_{0,10+}$), with various ice thickness. THz-DES spectrum are especially required for binary ice configuration explained in Chapter 6. Methanol is contained in the dosing in its liquid phase. Therefore its deposition followed the same procedure as for water.

#### 5.4.2.1 One exposure time

The thermal desorption of pure $CH_3OH$ ice with 1 exposure time was performed and the THz-DES results are shown in Fig. 5.12. The highest brightness temperature of the J= $10_{1,9-} - 10_{0,10+}$ methanol $A_{\pm}$-transition was measured at 326.630 GHz. As seen for $N_2O$ and $H_2O$, the offset is about 3.3 MHz away from the literature value (Table 5.1). The red, green and black curves are the brightness temperature acquired at 1.2 MHz, 2.4 MHz and 7.3 MHz away from the central frequency.

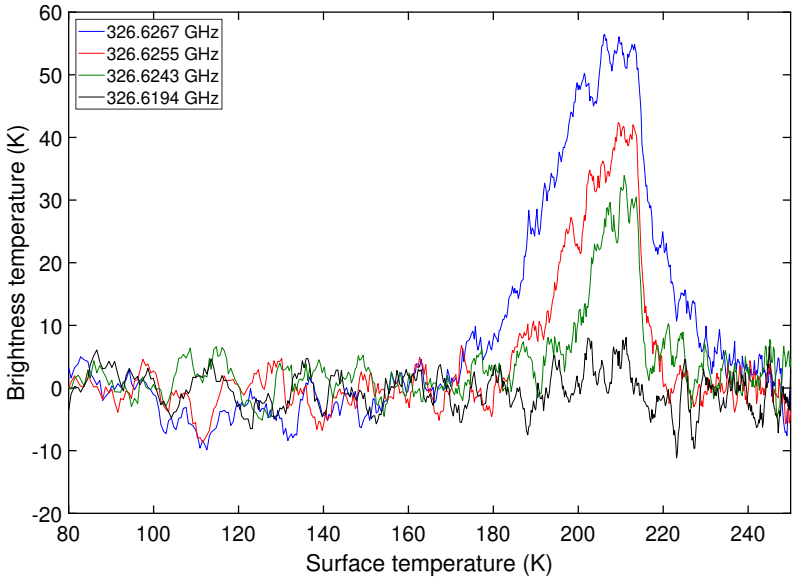


Figure 5.12: THz-DES brightness temperature for one deposition of $CH_3OH$ molecules at its peak frequency in the LSB (blue curve). The width of the line is shown via the "wing" which are the nearest spectrometer's channels (red, green and black curves).

From $T_{surface}$ = 80 K to 170 K, all BTs have values within the noise floor and are within the noise of about 7 K. The sublimation temperature for methanol is $T_{surface}$ = 170 K. Between $T_{surface}$ = 170 - 205 K, desorption is happening. The ice sublimates into the chamber and is detected by the radiometer resulting in the increase of the measured BT up to 55 K. At $T_{surface}$ = 182 K and 195 K respectively, BTs measured at 326.626 GHz and 326.624 GHz rise above the noise floor as a result of the broadening of the spectral feature in the frequency domain (as seen for $N_2O$ and $H_2O$). From $T_{surface}$ = 205 K to 215 K, constant BT values of 55 K (blue curve), 40 K (red curve) and 30 K (green curve) are observed. From $T_{surface}$ = 215 K to 230 K, the pumping rate becomes higher than the desorption rate, signals decrease before turning into the noise floor range.

#### 5.4.2.2 Multiple exposure times

A 3 exposure times ice was created and sublimated. Results, shown in Fig. 5.13, are consistent with the findings on $N_2O$ and $H_2O$. The blue curve is the BT from

the THz-DES of 1 exposure time ice and the red curve for 3 exposure times. The THz-DES is similar up to a surface temperature of 205 K, as expected as the thickness should not affect the desorption rate.

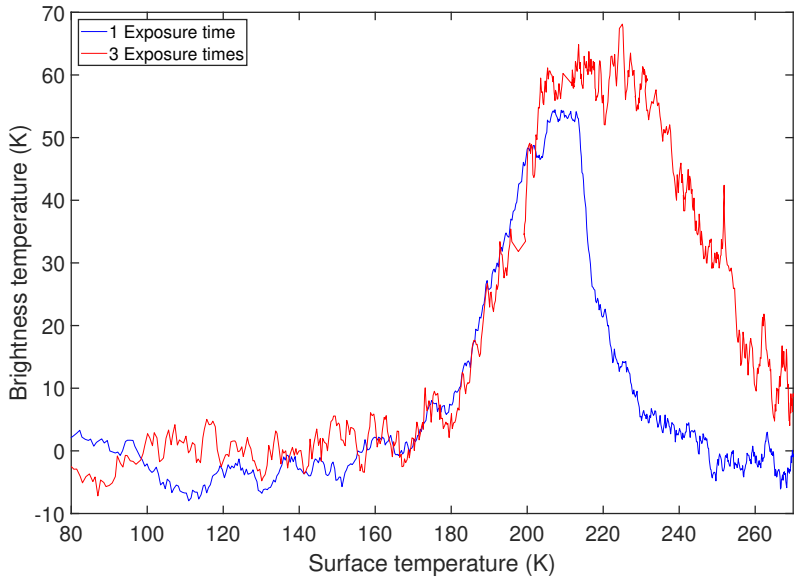


Figure 5.13: Comparison of the THz-DES results at the central line frequency of methanol between one (blue curve) and three depositions (red curve).

From $T_{surface}$ = 77 K to 170 K, the blue curve presents a plateau of BT = 55 K whereas the red curve's plateau is BT = 60 K. The BT for 3 exposure time stays at 60 K for a wider temperature range, up to 235 K. As seen earlier, the intensity plateau represents the period of time when pressure equilibrium is reached. This is observed as the amount of methanol sublimating is more important for thicker ice. As pumping rates are similar for both experiments, but the number of molecules emitting higher for the red curve, the spectral line intensity will increase until the equilibrium between desorbing molecules and pumping them out of the chamber. Finally, it appears that the pumping slope corresponding to the decrease of the BT is less steep for the red curve than for the blue one. This could be explained because the ice has been formed on a higher surface area of the trap than for one exposure, which would warm up more slowly than the bottom of the trap. The spike at $T_{surface}$ = 245 K, is an example of this effect when lot of remaining ice further from the heater finally sublimates.

The surface coverage of methanol does not impact the desorption mechanism observed using the THz-DES experiment. The difference between THz-DES results is observed due to the limitations of the current proof-of-concept experiment not performing in UHV.

### 5.4.3 Discussion

First THz-DES results have been shown to match to literature values in terms of sublimation temperature, and to TPD results in terms of laboratory thermal desorption. The first information retrieved was the spectral information. Expected transitions as stated in Table 5.1 were observed with a small offset between 3 - 4 MHz and a noise floor of 10 K. This corresponds to the VCO offset explained in Section 4.3.3 but it does not impact the spectral observations. Because of the increase in the number of molecules emitted whilst the desorption is occurring, the brightness temperatures at the line frequencies increased and self- and pressure broadening was observed in the frequency domain. The real line shapes observed reflect the LTE conditions and were fitted to a Lorentzian function. The advantages of using Schottky diodes (within the THz-DES radiometer) as detectors are that it gives the absolute calibrated intensity with a large instantaneous bandwidth at room temperature.

Table 5.3 sums up the phase properties derived from the desorption of pure $N_2O$, $H_2O$ and $CH_3OH$ ice at around $10^{-5}$ mbar. The analysed $N_2O$ $13_{0,0} - 12_{0,0}$ at 326.556 GHz has a sublimation temperature of 100 K with a maximum brightness temperature of 80 K. A-$CH_3OH$ $10_{1,9-} - 10_{0,10+}$ at 326.631 GHz has a sublimation and brightness temperature of 170 K and 55 K respectively. Finally, the highest sublimation temperature and lowest emission brightness temperature were measured for para-$H_2O$ $5_{1,5} - 4_{2,2}$ at 325.153 GHz, 200 K with a BT of 24 K.

THz-DES thermal desorption starts from the sublimation temperature of the

Table 5.3: Selected spectral transitions of $N_2O$, $H_2O$ and $CH_3OH$ for the THz-DES experiment pure ice

| **Molecule** | **Frequency (GHz)** | $T_{des}$ | $BT_{max}$ |
|---|---|---|---|
| $N_2O$ | 326.553 | 100 K | 80 K |
| $H_2O$ | 325.148 | 200 K | 24 K |
| $CH_3OH$ | 326.627 | 170 K | 55 K |

studied molecules. The brightness temperature will steadily increase to reach a maximum intensity. Then depending on the amount deposited on the surface and because the use of only a high vacuum, a plateau may appear at the maximal BT value corresponding to the desorption - pumping equilibrium. Once all ice molecules have sublimated, they are pumped away, leading to the decrease of the brightness temperature to the noise floor of the experiment.

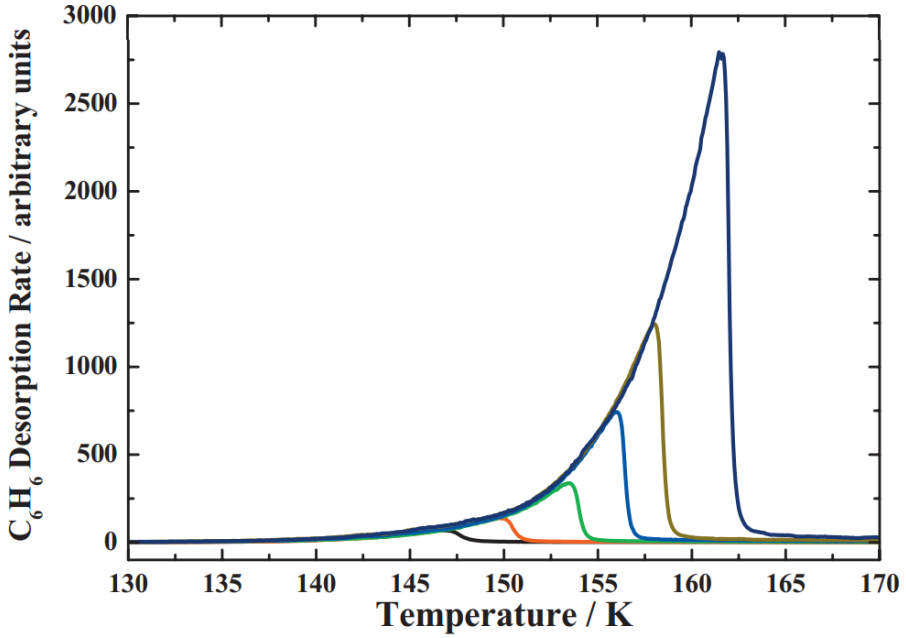


Figure 5.14: Experimental TPD traces for the desorption of 10, 20, 50, 100, 200, and 500 L exposures of $C_6H_6$ from the amorphous SiO2 substrate. [288]

The impact of the thickness in THz-DES results on the thermal desorption, for $N_2O$, $H_2O$ and $CH_3OH$, corresponds to the TPD studies with zero-order desorption kinetics [270] (explained in Section 2.5). The comparison between the THz-DES results for $N_2O$ with 1, 3 and exposure times (Figures 5.13) is com-

pared to the desorption rate of $C_6H_6$ ice formed of various 10, 20, 50, 100, 200 and 500 layers [288]. It is clear in Fig. 5.14 that the desorption rate (derivative of the signal intensity over the desorption time) is similar for all ices of different thicknesses. This is also observed on the THz-DES brightness temperatures between $T_{surface}$ = 77 K and 130 K, as the signals are matching their derivative as well.

## 5.5 Desorption Activation Energy Procedure

This section will present the mechanism to determine the desorption energy for methanol applied to the methanol feature measured in the LSB at 326.63 GHz presented in Section 5.4.2.

### 5.5.1 Reference Forward Model

The surface coverage, used in the Polanyi-Wigner Equation 2.46, is directly proportional to the number of molecules desorbing as the surface temperature increases. The number can be retrieved using spectroscopic level population based on the transitions lifetime for the spectral features observed[110]. The brightness temperature can then be linked to a number of molecules. A line-by-line radiative transfer model was used due to the complexity and the high number of transitions in the Terahertz (see Section 4.4).

The Reference Forward Model (RFM) has been developed by Dr. Dudhia at University of Oxford[67]. Although this model is predominantly used for atmospheric simulations, it was possible to use it for the THz-DES benefits. The RFM provides basic parameters for each transition (such as wavenumber, intensity, Lorentz half-width) based on HITRAN 2016[110]. The radiance for any spectral lines is internally calculated and converted into brightness temperature using the inverse of the Planck function (see Section 2.5). A homogeneous volume of 1 m path length was considered for the simulation, filled with one type

of molecule ($10^6$, mixing ratio in parts per million volume (ppmv)) at a temperature $T_{RFM}$, background temperature of $T_{bkg}$ and pressure P varying from $5.10^{-5}$ to 0.25 mbar. To simulate the methanol feature at 326.63 GHz, the RFM was set with a frequency range between 326.5 and 326.75 GHz, $T_{bkg}$ = 130 K corresponding to the noise floor temperature of the raw THz-DES data at the feature frequency.

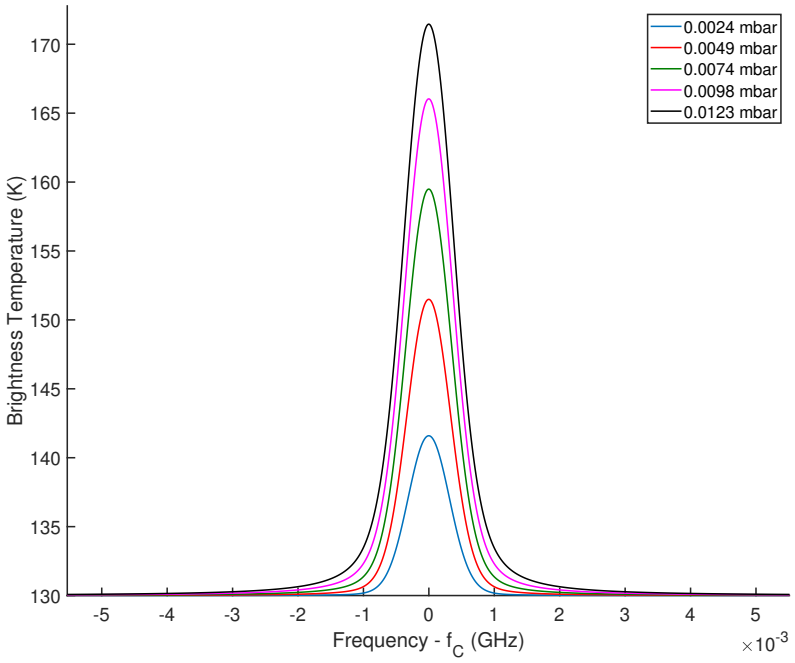


Figure 5.15: Simulation of the brightness temperature using the Reference Forward Model (RFM) for the methanol line at 326.63 GHz as a function of the partial pressure of methanol in a 1 m vacuum chamber with a background temperature of 130 K.

Figure 5.15 shows the simulated brightness temperature for a methanol gas at 293 K with a pressure range from 0.0024 mbar (blue curve) to 0.0123 mbar (black curve). The spectral line is plotted in the frequency domain after subtracting the central line transition ($f_c$). As the pressure increases, BT increases and is broadened because of the same effect as described in Section 2.2.2. The brightness temperature reaches 171 K at 0.0123 mbar, 41 K above the background temperature.

It is possible to plot BT peaks for each pressure. Figure 5.16 shows BT peaks

with $T_{RFM}$ = 193 K (blue curve), 243 K (red curve) and 293 K (green curve). As expected, peak intensities do not follow linear trends for the 3 gases temperature, for example at 0.018 mbar the methanol feature will be stronger for molecules at 243 K than at 293 K or 193 K. The RMS speed of molecules of methanol is about 364 m/s at 170 K using $v_{RMS} = \sqrt{3RT/M}$ with R, the molecular gas constant and M the molecular mass (0.032 kg/mol for $CH_3OH$) (see Section 3.6.4). In the THz-DES, the distance between the chamber walls and the cold trap is small, less than 30cm. Because of the high vacuum conditions, methanol molecules interact with the chamber within a fraction of a second. Therefore, their temperature is considered to be similar to the chamber at 293 K. The rest of the simulations follow this assumption.

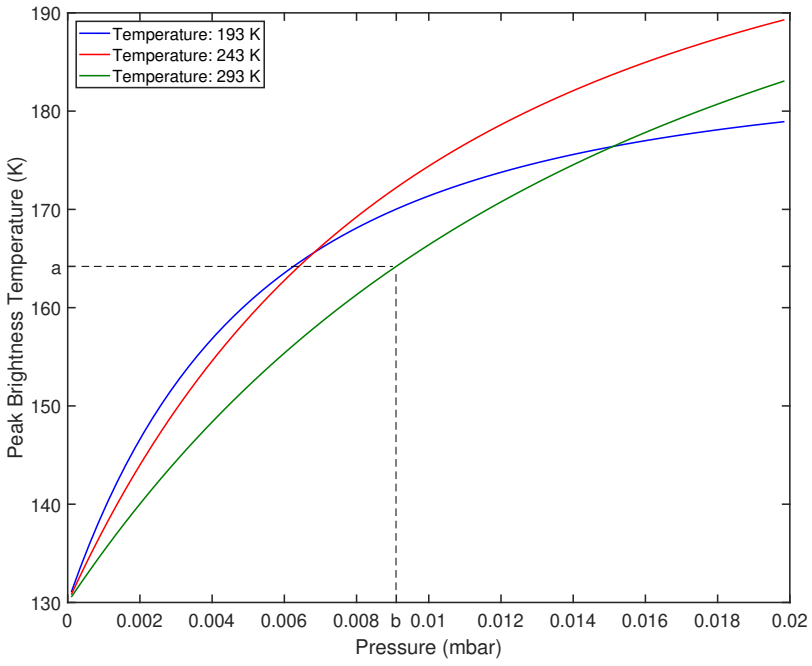


Figure 5.16: Maximum brightness temperature at the central line frequency of methanol as a function of its partial pressure within the 1 m THz-DES chamber. The temperature of the molecules emitted was set at 193 K (blue curve), 243 K (red curve) and 293 K (green curve).

To process the THz-DES data obtained, BT measured in TPD-like curves (see Section 5.3.1) is transformed into pressure using the RFM simulations. The green curve in Fig. 5.16 is used to determine the observed pressure by correlating it

to the BT peak observed. For example, with a measured brightness temperature at the feature frequency equal to a value of "a" [K], this value corresponds to a pressure "b" [mbar] such that a = $f_{RFM}$(b) with f standing for the function represented by the green curve. Only brightness temperatures above the noise floor of $T_{kbg}$ = 130 K can be characterised using the RFM as values below the noise floor would correspond to negative pressures.

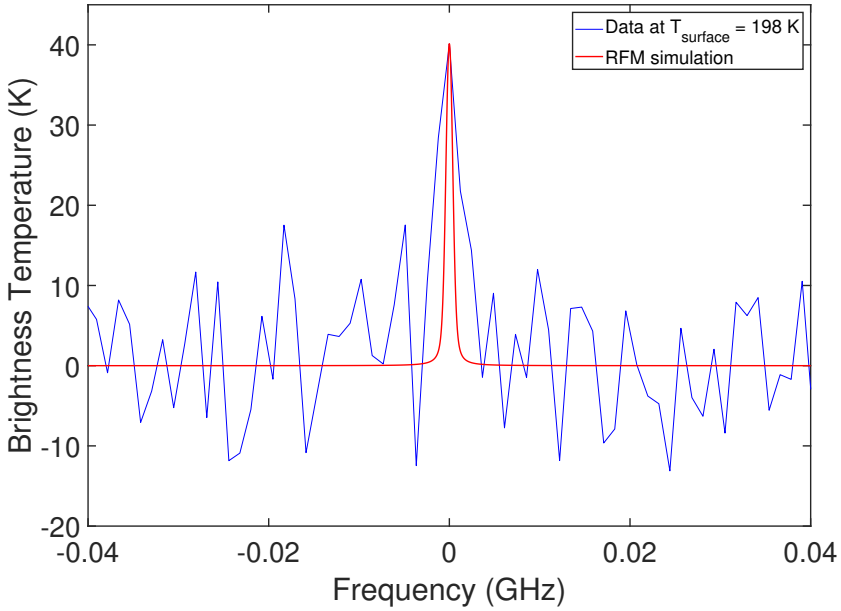


Figure 5.17: Methanol features measured by via THz-DES at $T_{surface}$ = 198 K (blue curve) and the RFM (red curve) showing a peak brightness temperature of 40 K.

Finally, the brightness temperature obtained with the RFM model is compared with the THz-DES data for $T_{surface}$ of 198 K, which has the same brightness intensity peak measured (40.11 K). The THz-DES data is shown in blue and the RFM BT's corresponds to the red curve in Fig. 5.17. It appears that the FWHM of the THz-DES data is 2.5 times higher than the simulated lines. This is due to the combination of a high noise within the THz-DES and the spectral resolution of the detector not being small enough. Moreover, it is likely that other molecules such as $N_2$ or $H_2O$ are present in the chamber in a very small and undetectable amount, as stated in Section 4.4.2.

### 5.5.2 Number of molecules desorbing

Once the THz-DES pressure is determined over the experimental time, the number of molecules desorbing can be calculated using the Ideal Gas Law. Because methanol is considered as a classical gas or Maxwell Boltzmann gas, N number of molecules is calculated using the equation 5.1.

$$N = \frac{P \times V \times N_a}{R \times T} \tag{5.1}$$

with V the chamber volume ($0.0133 m^3$),P the pressure (mbar), R = $8.314 \times 10^{-5} m^3.bar.K^{-1}.mol^{-1}$ the gas constant, T the gas temperature (=$T_{RFM}$) and $N_a$ the Avogadro constant($6.022 \times 10^{23} mol^{-1}$). Figure 5.18 shows the number of molecules from the THz-DES data (blue curve) and the smoothed data (red curve). Because of the noise presented on the data, the smoothed curve is used for calculating the derivative. As expected, the desorption trend does not change using this method. The total amount of $CH_3OH$ desorbing over the experiment corresponds to the integer under the curve and represents the experimental coverage: $2.29 \times 10^{21}$ molecules of methanol.

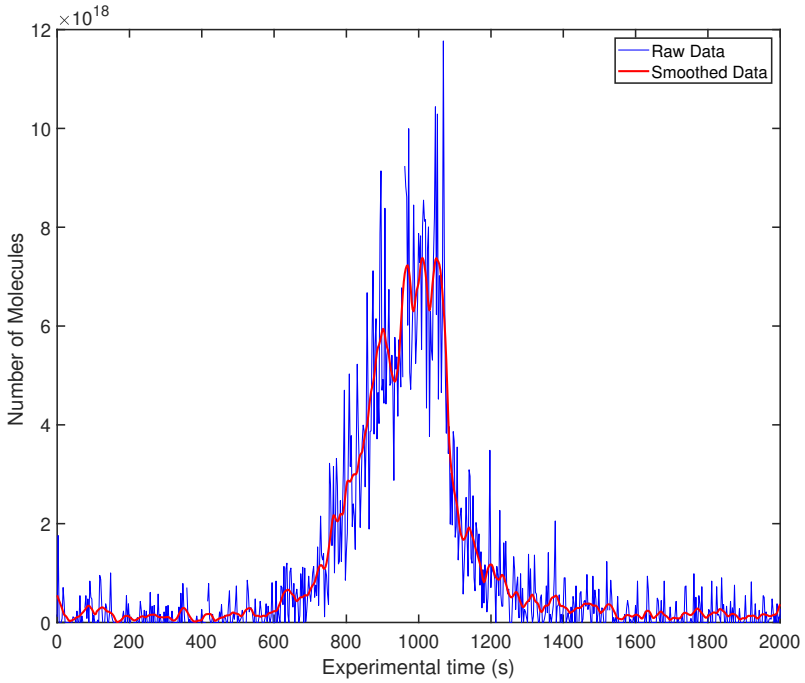


Figure 5.18: Amount of $CH_3OH$ desorbing during the THz-DES. The pressure from BT using the RFM is shown in blue while the red curve is the smoothed function applied.

### 5.5.3 Uncertainty in the number of molecules

Because of the use of the smooth pressure curve, it is important to characterise the uncertainty on pressure from the experimental THz-DES uncertainty. The standard deviation (std) of the brightness temperature at the feature frequency was measured at 7.8 K, this value is rounded to nearest integer 8 K. Then using the RFM transformation defined by the green curve from Fig. 5.16, an error bar on each BT can be obtained by adding or deleting half of the rounded standard deviation (±4K). Higher and lower pressure curves are obtained and shown in Fig. 5.19. The red curve corresponds to the standard transformation using the RFM of the BT into pressure (P(BT)). The blue curve is the pressure positive uncertainty (P(BT+std(BT)/2)) and the green curve is the negative pressure uncertainty(P(BT-std(BT)/2)). In other words, the area between the blue and the green curves is the pressure uncertainty obtained using the RF at different

BT. The final uncertainty is selected as the maximal pressure difference between the red curve and the blue or green curves.

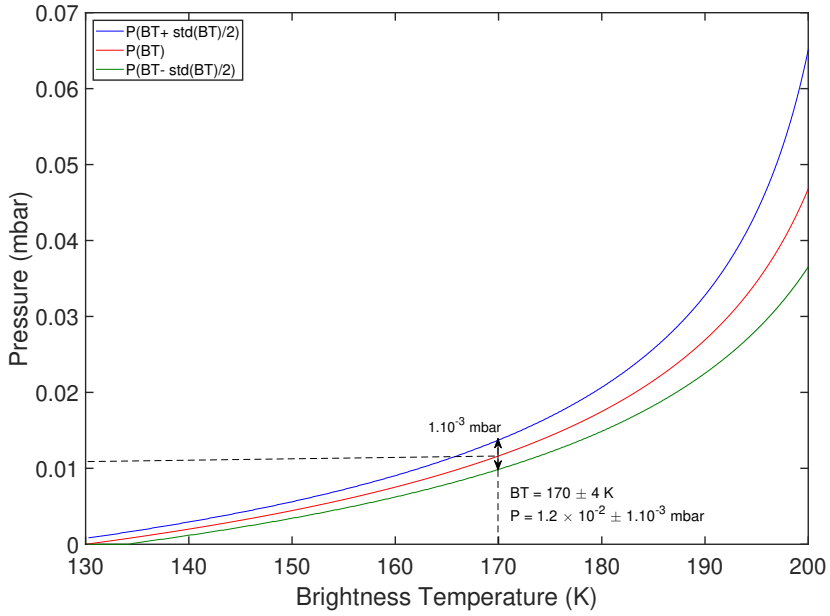


Figure 5.19: Uncertainty on the THz-DES pressure using the standard deviation of the measured BT using the RFM simulation. The red curve is the pressure from the smoothed BT while the blue and green curve are respectively the higher and lower pressure using BT uncertainty.

For example, at BT = 170 ± 4K, the nominal pressure (red curve) is 0.01165 mbar. Using the RFM, the pressure at BT + std(BT)/2 = 170 + 4 K is 0.01375 mbar. This value corresponds to the positive uncertainty at BT = 170 K. Similarly, the pressure at BT - std(BT)/2 = 170 - 4 K is 0.0099 mbar. Therefore the final pressure for BT = 170 ± 4K is P = $1.2 \times 10^{-2} \pm 1 \times 10^{-3}$mbar.

The corresponding uncertainty on the number of molecules was then calculated using equation 5.1 and is shown either as a function of the experimental time (Fig. 5.20a) or the surface temperature (5.20b). As expected from Fig. 5.19, the uncertainty is higher for higher values of BT because of the non-linearity between pressure and BT. This data is used to retrieve the desorption energy.

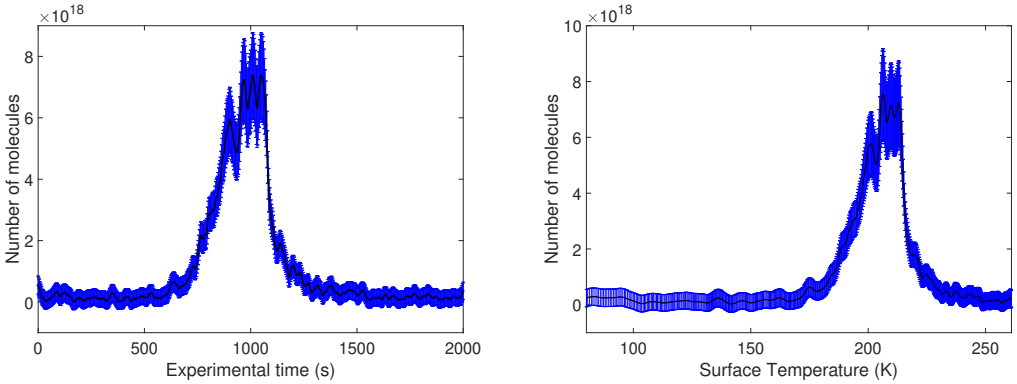


(a) (b)

Figure 5.20: Number of molecules desorbing (N) during the THz-DES as a function of the experimental time (a) (5.20a and the surface temperature (b)(5.20b).

### 5.5.4 Polanyi-Wigner Equation

The standard temperature programmed desorption (TPD) commonly uses quadrupole mass spectrometers, monitoring the amount of adsorbate molecules released into gas phase as a function of the temperature. The activation energy for desorption for the studied molecule is retrievable by using equation 5.2 (from Equation 2.46). It appears that $r_t$ is a function of 1/T.

$$r_t = -\frac{dN}{dt} = \nu \times \exp\left(-\frac{E_{des}}{RT}\right) \tag{5.2}$$

The desorption rate appears to be the derivative over time of the desorbing number of molecules, or the derivative of N over the temperature divided by the heating rate (dT/dt). The first challenge in this proof-of-concept experiment is that the heating rate is not linear. Secondly, the noise within the data makes it difficult to calculate the derivative of N as a function of time. Figure 5.21 shows the direct derivative of N(t) without (blue curve) or with (black curve) smoothing. Slope changes due to the noise will give a calculated derivative either positive or negative, undermining any characteristic slope needed to calculate the rate of desorption according to equation 5.2. Various techniques are presented here and

in the annexe to calculate the desorption activation energy of pure methanol.

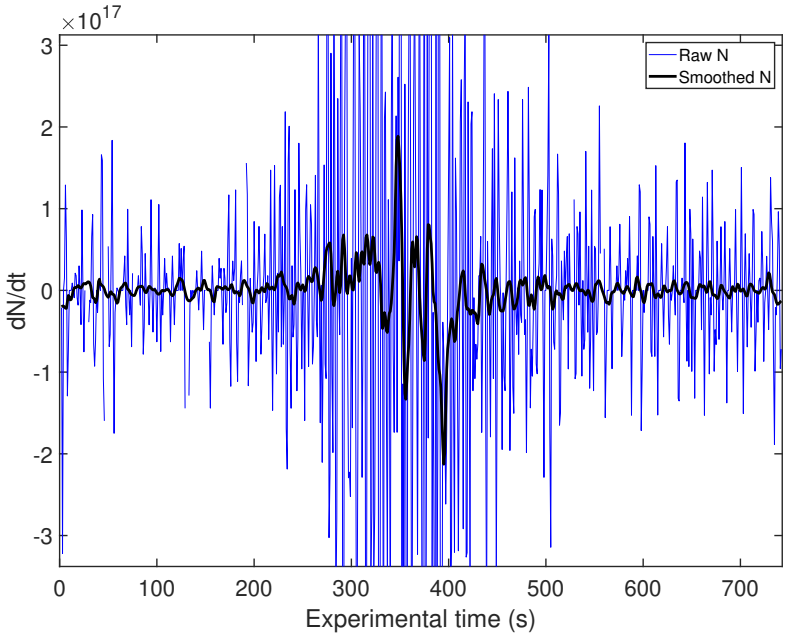


Figure 5.21: Calculated derivative of the number of molecules desorbing using the 'raw' N data (blue) and the smooth data corresponding to the red curve in Fig. 5.19.

### 5.5.5 Method

A quantitative study of the pure-ice THz-DES results for $N_2O$, $H_2O$ and $CH_3OH$ was carried in order to retrieve the desorption energy of those molecules within the THz-DES experimental set-up. A method was determined which could be applied on most data-set obtained. All ways to calculate the desorption energy have studied and are presented in the Appendix A, the current method is the number 2. It is based on the correlation of simulations and data and presents the following steps:

1. Calculate the RFM maximal brightness temperature (RFM BT) for each frequency features as a function of the pressure.
2. Correlate the RFM BT with the THz-DES BT (at the central frequency).
3. Retrieve the corresponding THz-DES pressure.

4. Calculate the THz-DES number of molecules desorbing using the Ideal Gas Law.
5. Smooth the number of molecules as a function of the experimental time (17 points).
6. Select the desorption range: From experimental time = 0 s up to the first number of molecule peak.
7. Apply Gaussian Fit Functions ($N_{Gauss}$) with uncertainty of $R_N^2$.
8. Derive the Gaussian Fit Functions over the experimental time ($dN_{Gauss}/dt$).
9. Plot $dN_{Gauss}/dt$ as a function of 1/T.
10. Fit $dN_{Gauss}/dt(1/T)$ using an exponential function.
11. Calculate the desorption Energy as a function of the exponential factor (b), R the Avogadro constant: $E_{des} = -b \times R$.

The desorption energy calculated via this method does not take into account the uncertainty in brightness temperature from the measurements due to the 2 fitting mechanisms used. An error due to the last fitting process is calculated. This final exponential fitting is also performed over a range of temperatures from the beginning of the desorption to a temperature which presents a BT equals to half BT's maximum. This is the case in order to obtain better accuracy of the desorption energy when desorption occurs as it should have an exponential form (section 2.2.4). Moreover, to characterise the impact of the BT uncertainty on the final desorption energy retrieved, the NEDT (sensitivity, see Section 4.2.2) is applied to the smoothed BT at the central line frequency: $BT_{err} = BT \pm NE\delta T$. Figures 5.22a and 5.22b show the nominal brightness temperature and number of molecules desorbing of methanol in blue, BT–NEδT and BT+NEδT, respectively, the red and green curves. As expected the higher is the brightness temperature (BT + NEδT) the higher the retrieved number of molecules desorbing will be.

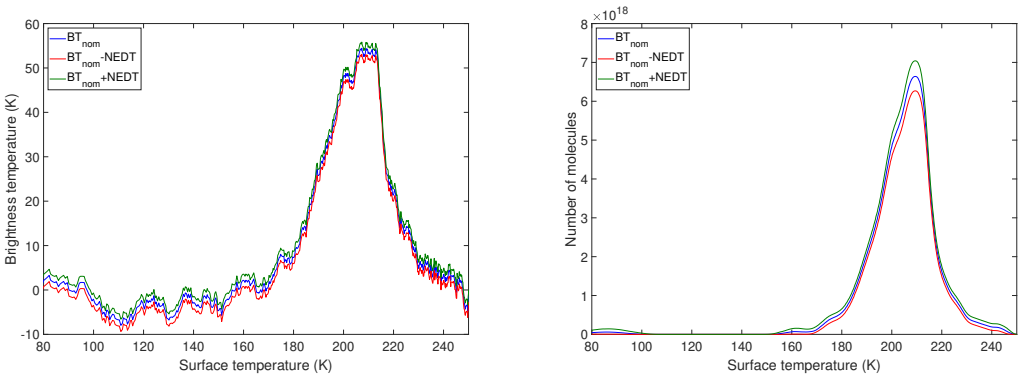


(a) (b) N=f(temperature)

Figure 5.22: (a)THz-DES results for methanol (blue curve) and corresponding BT with offset which is the value of the NEDT (red, green curves). (b)Number of molecule desorbing (N) during the THz-DES as a function of the experimental time for the three curves from Fig. 5.22a.

Then by applying this method to both curves, three curves representing the desorption energies calculated for various desorption temperatures are obtained. Those curves are shown for methanol in Fig. 5.23. The blue curve corresponds to the desorption energy derived from the nominal (measured) THz-DES brightness temperature($BT_{nom}$). The desorption energies for $BT_{nom} - NE\delta T$ and $BT_{nom} + NE\delta T$ are shown via the red and green curves. From 5.23, it appears that the desorption energies vary slightly depending on the measured BT. Indeed the exponential fitting will be shifted when offsetting the $BT_{nom}$ by the measured $NE\delta T$. Secondly, the desorption energies slightly decrease from a temperature of 185 K. At this temperature, a small change of slope is observe in Fig. 5.22b. The exponential fitting factors are impacted by those changes making the desorption energies decrease.

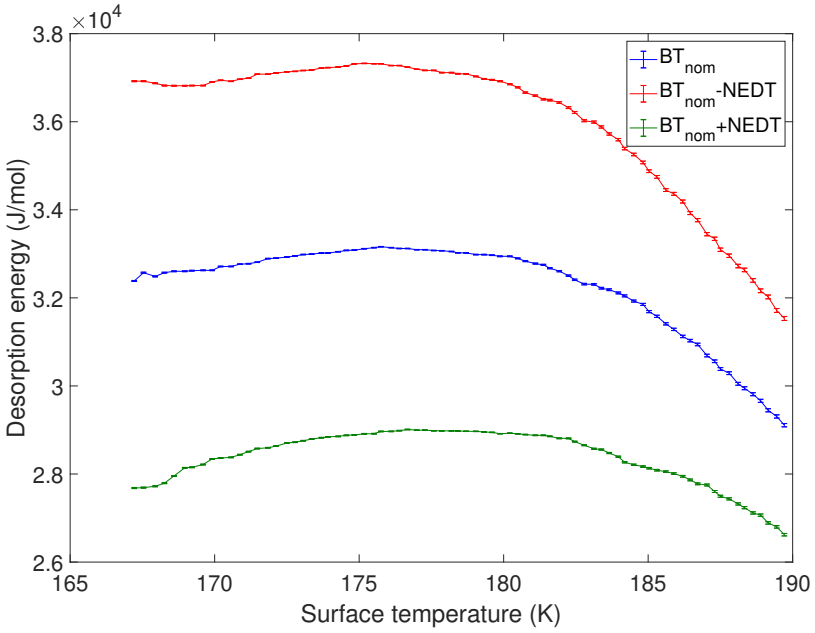


Figure 5.23: Calculated methanol desorption energies using the 'raw' N data (blue) and the smooth data corresponding to the red and green curves in Fig. 5.22b.

All presented THz-DES results show the nominal desorption activation energy ($E_{nom}$) and their uncertainties over the fitted desorption temperature range. $E_{nom}$ is calculated as the mean value of the energy (blue curve) and the uncertainty as the standard deviation of the data point within this curve. Another energy term is provided, which is called the mean desorption activation energy ($E_{av}$) and is calculated from $E^{BT}_{nom}, E_{BT_{nom}-NE\delta T}, E_{BT_{nom}+NE\delta T}$ and its uncertainty corresponding to the standard deviation between them. Finally, the amount of molecules is calculated as the area below the N-curves with the uncertainty corresponding to the standard deviation with the N curves for $BT_{err} = BT \pm NE\delta T$.

## 5.6 THz-DES Desorption Energy Results

The desorption activation energies calculated by the method presented in the previous section have been calculated for all THz-DES results for $N_2O$, $H_2O$ and $CH_3OH$ in this chapter.

The desorption energy of $N_2O$ was measured between 10 and 14 kJ/mol,

Table 5.4: Desorption activation energy for $N_2O$, $H_2O$ and $CH_3OH$ THz-DES results in kJ/mol for various deposition exposure time (Exp. time).

| **Mol.** | **Exp. time** | $E_{nom}$ (kJ/mol) | $E_{av}$ (kJ/mol) | $R_N^2$ | **N** |
|---|---|---|---|---|---|
| $N_2O$ | 1 | $13.4 \pm 3.3$ | $13.4 \pm 3.2$ | 0.9993 | $5.0 \times 10^{21} (\pm 1 \times 10^{21})$ |
| | 3 | $10.9 \pm 0.1$ | $10.9 \pm 0.3$ | 0.9976 | $10 \times 10^{21} (\pm 1 \times 10^{22})$ |
| | 6 | $13.7 \pm 2.6$ | $13.9 \pm 2.5$ | 0.9977 | $19 \times 10^{21} (\pm 6 \times 10^{21})$ |
| $H_2O$ | 1 | $32.9 \pm 1.4$ | $31.7 \pm 9.5$ | 0.9867 | $12 \times 10^{21} (\pm 2 \times 10^{21})$ |
| | 3 | $29.2 \pm 3.2$ | $29.3 \pm 5.5$ | 0.9988 | $25 \times 10^{21} (\pm 2 \times 10^{21})$ |
| $CH_3OH$ | 1 | $32.2 \pm 1.1$ | $32.2 \pm 3.3$ | 0.9992 | $2 \times 10^{21} (\pm 2 \times 10^{20})$ |
| | 3 | $32.0 \pm 1.5$ | $31.9 \pm 3.0$ | 0.9960 | $6 \times 10^{21} (\pm 6 \times 10^{20})$ |

depending on the thickness of the ice, whereas literature values are set between 17 and 25 kJ/mol. Similar effects was observed for $H_2O$ with measured values between 29 - 33 kJ/mol against 39 - 50 kJ/mol in the literature. Energy values for $CH_3OH$ seems to match the lower end of the values from the literature, 31 - 33 kJ/mol vs 29 - 47 kJ/mol. For all measured molecules, as expected, thickness of ice does not impact the desorption energy measured.

The THz-DES desorption activation results calculated by the developed method on the first terahertz spectroscopic measurements of desorbing ices with this proof-of-concept experiment are extremely interesting and encouraging for the future use of THz-DES techniques. They are within the order of magnitude or even matching the literature values to a certain extent. Discrepancies observed rises from limitations on both the data analysis and the experimental set-up.

Firstly, it is very probable that the measured desorption energies are correct and differ from the literature value because it is not the total amount of molecules desorbing which is measured but the amount of molecules having the specific observed energy state transitions. We could imagine that other desorbing molecules are desorbing in another rotational state and therefore not been detected by the THz-DES. However ideally combining the amount of those molecules in all their rotational states would most likely rise to the amount of molecules detected with other techniques in literature experiments.

Secondly, the ices grown are not mono-layer thick ices ($10^{15}$ molecules/cm$^2$) as often in literature. Ices presented here are very thick ices made of $10^{21}$ molecules. Therefore it is more than probable that a difference exist between thin and thick ices as molecules are not bonding strongly with the surface. Only a small amount of them bond with the surface and would present literature desorption energy values binding with the substrate. It is possible that this effect explains the discrepancy observed.

The pressure within the THz-DES is order of magnitude higher than ultra-high vacuum conditions. Therefore, sublimation occurs at a higher temperature and the formed ice may be contaminated with low levels of other compounds leaking through the desorption chamber. Those molecules may slightly disrupt the sublimation of the so-called pure ices. Moreover, it is also likely that re-adsorption of the molecules desorbing first on the cold surface occur. The real number of molecules desorbing around the sublimation point should be higher than observed. This would affect the desorption rate. It would become higher if all molecules were detected and the desorption energy would have higher values.

The surface of the cold trap where molecules are deposited is not made of one single material but of plain stainless steel with Kapton and aluminium tapes in order to maintain the temperature sensors in thermal contact with the trap. As seen in literature, the desorption energy does vary depending on what kind of ice is deposited but more importantly, the kind of surface it is deposited on. This, although it should be a minor factor for the aforementioned reasons on ice thickness, could at least partially explain some of the discrepancy between literature and THz-DES results for $N_2O$.

Although observing the spectral signatures of molecules would aid understanding of the spectroscopic characteristics of molecules desorbing and the potential interaction they have within their ice, the standard TPD analysis is challenging to apply. The number of molecules desorbing is calculated using the reference forward model to correlate the number of molecules to the molecular brightness

temperature at the feature frequency. The THz-DES has around 10 K standard deviation in the current setting, which impacts the calculation of the number of molecules. Another uncertainty in the calculation of the desorption energy is due to the non-linear heating rate. Because of this, the Polanyi-Wigner equation has to be accounted for over the experimental time to calculate the desorption rate. The use of fit function on N and dN/dt adds another step of uncertainty, as only the mean values are accounted.

## 5.7 Conclusion

In this chapter, experimental results and analysis probe that spectroscopic measurements of desorbing ice are matching the thermal dynamics for pure ice configuration as observed in the literature with TPD techniques. THz-DES is capable to observe spectrally weak and strong transitions features at ALMA band 7 frequencies (around 325 GHz). The THz-DES results provide spectroscopic information of the spectral line and TPD-like curves. The spectral lines are observed through their real emission intensities, which are proportional to the total amount of molecules desorbing but representing those only in the particular transitions state observed. The thermal evolution of the ice is characterised by increasing the surface temperature of the ice. A broad THz-DES study over a wide frequency range, i.e. detecting many different energy state transitions, would be required to fully analyse the population distribution of transition states of the desorbing species.

In THz-DES experiments, TPD like curves for the observed transition are plotted as the radiometric brightness temperature against the surface temperature. From those two main parameters, the desorption temperature and the desorption activation energy are derived. THz-DES data show matching desorption energy for the three molecules ($N_2O$, $H_2O$ and $CH_3OH$) characterised. The desorption energy was estimated by postulating a leading edge analyses (details

in the appendix A). Values from the literature differ from the THz-DES for $N_2O$, $H_2O$ being lower but not totally for $CH_3OH$ depending on the reference as seen in Table 5.5. Few reasons that can explain the discrepancy between THz-DES experiments and literature data have been explained in Section 5.6, going from experimental limitations to analysis approximations.

Table 5.5: Comparison of the desorption energy (kJ/mol) between literature values and the THz-DES results for pure ice.

| **Molecule** | **Transitions** | $E_{literature}$ (kJ/mol) | $E_{THz-DES}$(kJ/mol) |
|---|---|---|---|
| $N_2O$ | $13_{0,0} - 12_{0,0}$ | 17 - 25 | 10 - 14 |
| $H_2O$ | $5_{1,5} - 4_{2,2}$ : Para | 39 - 50 | 20 - 40 |
| $CH_3OH$ | $10_{1-} - 10_{0+}$ : A | 29 - 47 | 28 - 36 |

A likely and possible reason would be that the desorption energy depends on the transitions observed. This means that the amount of molecules in a particular state differs from the total amount of molecules leaving the icy surface. Desorption would appears spectroscopically dependant. A hint of this was introduced by Lian et al.[172], where they combined FT-IR data with standard TPD data to state that the $N_2O$ desorption energy was measured at 22.19 kJ/mol at 2236 $cm^{-1}$ and 28.95 kJ/mol at 2270 $cm^{-1}$. However it has not been detected directly. THz-DES permits a direct measurement of this characteristic. The veracity of those THz-DES results would be an important step forward in laboratory astrochemistry and for the astronomers community in general.

The fact that desorption is a rational energy selective mechanism has interesting impact on the physic of molecular cloud and nebulae. Firstly, if species desorb with a specific transition population, the latter would be preserved in the gas phase because gas-phase interactions among different molecules are usually quite rare. This is a key information for radio astronomer who are deducting abundances, ratios and amount of molecules the same way as THz-DES does. However, this rises new questions: -Why desorption is a spectroscopic preferential

mechanism? -How does this impact the chemistry happening on grain surface? -Would the population levels change when molecules are interacting with other kind of molecules in binary systems? To reply to the last question, the THz-DES was set-up in a binary ice configuration operation as described in the Chapter 6.

# Chapter 6

# Binary Ice System

# THz-DES Results[1]

## 6.1 Introduction

Chapter 5 presented the first THz-DES results of pure ice thermal desorption composed either of nitrous oxide, water or methanol. Pure ice TPD permits to characterise the binding energy between a material (the substrate) and few monolayer ($10^{15}$mol/cm$^2$) of material, for example using a material as a catalysist of certain molecular species[65]. A very important factor is the structure of which the ice is formed as explained in Section 1.3.2. Amorphous ice, the most abundant in space is formed below 120 K, at low deposition speed [253] and it is a key factor in thermal desorption. The desorption may be the witness of structural change within the ice [51, 54]. Many studies determined the desorption energy and TPD behaviour of molecules such as $N_2$[208], CO[208], $O_2$[2], $H_2O$[90] or $CH_3OH$[113]. In the ISM, as explained in Chapter 2, interstellar ices forming the mantle of dust grain are not homogeneous. They could be formed of many molecular species, which can potentially interact. The presence of many species within the ice with

[1] Auriacombe, O. et al, A&A, in prep. and presented in [11]

different sublimation temperature makes the desorption mechanism more complex to understand and to model[305]. Therefore, it is very important to study simple binary system ice configurations in order to characterise the binding energies between the molecules and the desorption behaviour between two molecules before simulating complicated ice systems.

Collings et al.[50] defined three categories depending on their desorption behaviours. The first category, the CO-like species ($CH_4$, CO, $O_2$) presents a double peak in their pure ice TPD configuration due to the desorption of multilayer and monolayer (surface bound) molecules. In layered configuration with porous water, CO will diffuse through the water layer [53]. As temperature increases, multilayer desorption is observed when amorphous water crystallises, releasing trapped molecules of CO into the gas phase (volcano desorption[268, 269]). A signal is also produced at water sublimation temperature, CO molecules are desorbing alongside the water molecules (co-desorption)[85]. Ayotte et al. [13] measured via their TPD experiment, layered configuration of $O_2$ on top of $H_2O$. The results showed that no co-desorption was detected if the water ice was a dense non-porous film of water. However co-desorption was measured when the water layer was in an amorphous structure. The second category are the water-like molecules, such as HCOOH or $CH_3OH$. $CH_3OH$ pure ice TPD have a multilayer peak meaning that molecules are strongly bond with each other. When forming binary systems with water, $CH_3OH$ will present this multilayer feature but also a peak at the same surface temperature as the water sublimation. The ability for methanol to bind to water ($H_2O$) is commonly known. Finally, the third category corresponds to the intermediate species. Molecules such as $CO_2$[87], $SO_2$ or OCS, exhibit desorption characteristics between the categories 1 and 2. Category 3 molecules will desorb via volcano effect and co-desorption. They will diffuse within the water ice, and possibly be trapped within the ice only sublimating when water desorbs.

Water and methanol are very important molecules in star formation regions. Many laboratories studies analysed the TPD behaviour of binary systems made of

water and methanol[34, 179, 316]. A TPD spectra from Wolff et al.[316] is shown in Fig. 6.1. In Fig. 6.1, the signals detected are proportional to the amount of methanol molecules desorbing from ice configurations comprising methanol as the top layer and water as the bottom layer. The Mass 31 is measured as it corresponds to the amount of the dominant ion produced by the ionisation of methanol through a QMS. Indeed the ionisation process forced the loss of one proton producing $CH_3O^+$ which has a mass of 31. Two peaks are observed, the first has the same temperature of pure methanol ice. The second peak is assigned to the trapping of $CH_3OH$ within the $H_2O$ ice and happens at the sublimation temperature of the water ice layer. A shift in the sublimation peak in layered configuration shows that the bonding between the two molecules is stronger than between molecules of a same kind. In this study, the authors showed that thicker water ice layers trap more $CH_3OH$. This increased volume of trapped $CH_3OH$ results in the temperature shift of the first peak detected.

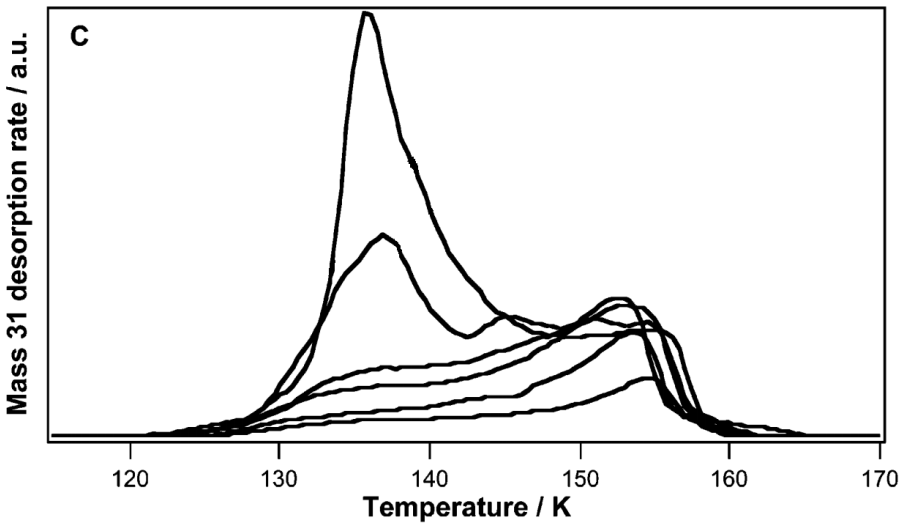


Figure 6.1: TPD spectra of methanol for ice configurations made of 3, 5, 7, 10, 15 and 20 layers of $CH_3OH$ above 50 L of water. Credit [316]

Studies looking at molecule-surface potential energy and molecular dynamics of desorption mechanism have revealed that possible energy partitioning of the internal (vibrational and rotational) state may happen during desorption.

Restriction of the rotational/vibrational degree of freedom of the ice molecules can occur when they are desorbing. Jacobs et al. published in 1988[138] the first measurements of rotational alignment in desorption. They showed that molecules desorbing with different angular momentum (J) will rotate with a preferential direction either with a helicopter-like motion or cartwheel-like motion. This effect will populate differently the rotational energy states with preference to rotating in a plane perpendicular to the surface (cartwheel). Combining laboratory data with complex molecular simulation software allows for the analysis of how molecules adsorb on various surfaces and helps defining what the binding structures are. For example, nitrous oxide has been found to weakly bind with palladium (111) with its O atom pointing towards the surface[163] at low coverage. All the techniques used to characterise the rotational dynamics are based on the reflection or transmission of incident beams of photons or electrons on the surface and detected afterwards by means of infrared reflection-absorption spectroscopy [166]. THz-DES is one of the first technique to observe molecule-surface interactions and the rotational dynamics of desorption from the direct emission of the icy molecules adsorbed onto the surface.

THz-DES results are expected to present the same TPD behaviour as obtained within the literature for nitrous oxide, water and methanol. Moreover the desorption energy calculated with the method explained in Section 5.5 should correspond to the list from Table 1.1 in Chapter 5. The aim of this chapter is to start gathering information on preferential energy state distribution during thermal desorption by looking at A- and E- transitions of methanol.

## 6.2 Experimental methodology

The assumptions used here to study the desorption of binary ice configurations are similar to the ones used for pure ice and are explained in detail in Section 3.6.4.

#### 6.2.0.1 Ice deposition procedure

Three main ice configurations are going to be compared in this section. The first one is the layered ice. The notation for layered ices is: X/Y – a/b, where X is the top layer molecular specie, Y the bottom layer specie and a, b are the respective amounts in terms of deposition exposure time. The other configuration possible is the mixed ice: X : Y – a : b. The schematic in Fig. 6.2 shows the three configurations previously explained. (a) corresponds to X/Y – a/b, (b) to Y/X – b/a and (c) to X : Y – a : b.

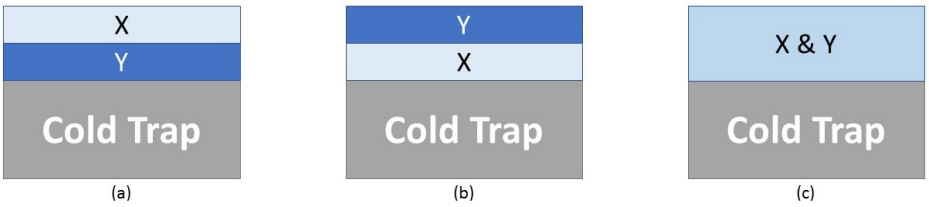


Figure 6.2: Schematic of the ices experiments configurations. X and Y are the two molecular species used during the THz-DES experiments. (a) and (b) are the layered configurations where X is either on top or below Y. (c) represents the mixed configurations. The amount of X and Y is the same in all case (a), (b) or (c).

The standard procedure of 1 deposition exposure time is described in details in Section 5.2.1. To form a layered ice configuration, two standard procedures are used with additional steps. Considering two molecular species, X and Y, with respective deposition exposure time of 'a' and 'b', respectively. The procedure for layered ice X/Y – a/b is:

- Perform 1 deposition exposure time standard procedure of Y.
- Close the deposition valve *i*.
- Repeat deposition exposure time standard procedure of Y, 'b-1' times.
- Close the valve *i*.
- Perform 1 deposition exposure time standard procedure of X, 'a' times.
- Close the valve *i*.
- Wait until the pressure in the desorption chamber reaches $1.10^{-3}$ mbar. Open the valve *ii* so as to clean the dosing line.

- Connect the pumping system to the desorption chamber to reach $10^{-5}$ mbar.

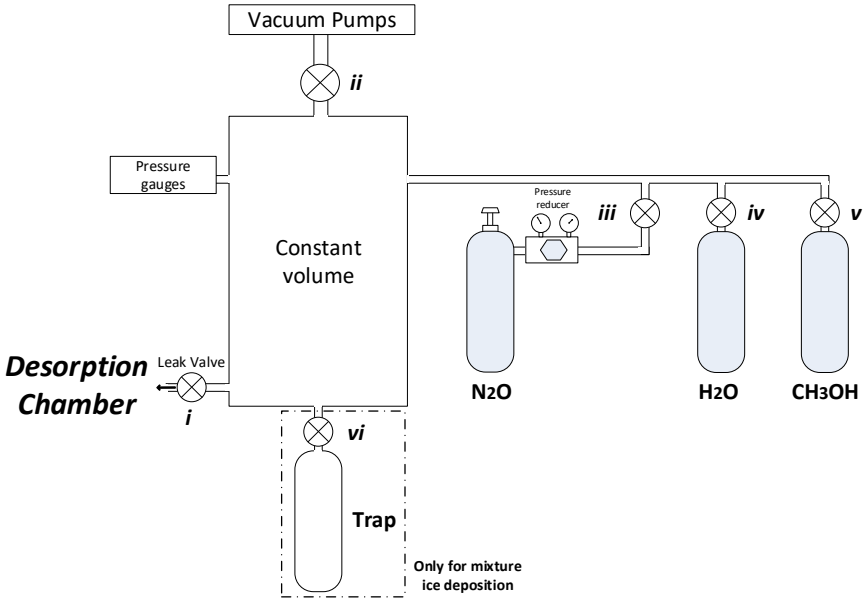


Figure 6.3: THz-DES dosing line configuration for nitrous oxide, water or methanol molecules for layered and mixed ice configurations.

For mixed ice deposition, a lecture bottle (valve 'vi' in Fig. 6.3) is needed for mixing the gaseous molecular species before forming the ice in the vacuum chamber. The procedure to create the mixed ice configuration X : Y – a : b on the cold trap is as follows:

- Introduce 25 mbar of gaseous molecules X in the constant volume: valves *i and ii* close; opening valve *iii, iv or v and vi.*
- Close valves *iii, iv or v*, *vi* open.
- Cool down 'Trap' to 77 K monitoring the dosing lie pressure. Once it reaches less than $1.10^{-2}$ mbar, all molecules of X are considered frozen on the cold wall of the trap.
- Close valve *vi.* This corresponds to the pre-selection of 1 deposition exposure time. Repeat from the first step with X, 'a' times.
- Open valve *ii* to 'clean' the dosing line.
- Introduce 25 mbar of gaseous molecules Y in the constant volume: valves *i and ii* close; opening valve *iii, iv or v and vi.*

- Close *iii, iv or v*, *vi* open.
- Cool down 'Trap' to 77 K. All molecule of Y will freeze on the cold wall of the trap.
- Close valve *vi*. This corresponds to the pre-selection of 1 deposition exposure time. Repeat from the first step using Y, 'b' number of times.
- Open valve *ii* to 'clean' the control volume. Warm up 'Trap' to sublimate all mixed molecules in the dosing line.
- Cool down the cold finger temperature to 77 K while still pumping on the desorption chamber: valves *i and ii* close.
- Once the surface temperature reached 77 K, isolate the desorption from its pumping system and open valve *i*.
- Keep valve *i* open until the pressure in the dosing valve reaches $1.10^{-2}$ mbar. Then close valve *i*.
- Wait until the pressure in the desorption chamber reaches $1.10^{-3}$ mbar. Open valve *ii* so as to clean the dosing line.
- Connect the pumping system to the desorption chamber to reach $10^{-5}$ mbar.

Those standard deposition procedures for layered and mixed ice configurations have been used to study of the water, nitrous oxide and methanol configurations.

#### 6.2.0.2 Experimental settings

For all the experiments presented in this chapter, the local oscillator of the receiver was set at 334.5 GHz, 2.5 GHz sampling frequency, a spectral resolution of 1.22 MHz and an integration time of 500 ms. THz-DES results in Section 6.3 and 6.4 have frequency range in the LSB: 322.25 - 326.75 GHz. Those in Section 6.5 have a frequency range in the USB 342.25 - 346.75 GHz. All the spectral lines observed within this chapter are listed in Table 6.1.

Table 6.1: Selected spectral transitions of $N_2O$, $H_2O$ and $CH_3OH$ for the THz-DES experiment with their corresponding quantum numbers from the JPL catalogue[219].

| Molecule | Frequency (GHz) | Quantum Numbers |
|---|---|---|
| $N_2O$ | 326.556 | $13_{0,0}/12_{0,0}$ |
| $H_2O$ | 325.153 | $5_{1,5}/4_{2,2}$ : Para |
| $CH_3OH$ | 326.631 | $10_{1-}/10_{0+}$ : A |
| $CH_3OH$ | 342.730 | $13_{1-}/13_{0+}$ : A |
| $CH_3OH$ | 344.109 | $18_2/17_3$ : E |
| $CH_3OH$ | 344.312 | $10_2/11_3$ : E |
| $CH_3OH$ | 344.443 | $19_{1+}/18_{2+}$ : A |
| $CH_3OH$ | 345.904 | $16_{1-}/15_{2-}$ : A |

Similarly to the previous chapter, the THz-DES acquisition starts once all the $LN_2$ boiled off from the cold trap. Surface temperatures and emission brightness temperatures data are recorded simultaneously and linked via their computer acquisition time. Data are then processed using Matlab routines, as explained in Chapter 3.

## 6.3 $H_2O - N_2O$ Configurations

### 6.3.1 1-1 configurations

As explained in Chapter 5, THz-DES results have two main components. Frequency information is obtained by detecting specific molecular energy level transitions. Desorption information is obtained by plotting the brightness temperature as a function of the surface temperature of the warming ice. In this section, nitrous oxide and water molecules are studied in various ice configurations. The THz-DES full dataset obtained for the desorption of $H_2O/N_2O$ – 1/1 is plotted in Fig. 6.4. The peak intensity on the right is the nitrous oxide spectral line. This line intensifies as the surface temperature increases provoking the $N_2O$ desorption. The water line seen near 325 GHz is much weaker and can be observed

at higher temperature as the sublimation temperature of water is around 250 K. The rest of this section will present cross sectional figures corresponding to a single frequency channel, where the brightest intensity of those two lines was measured.

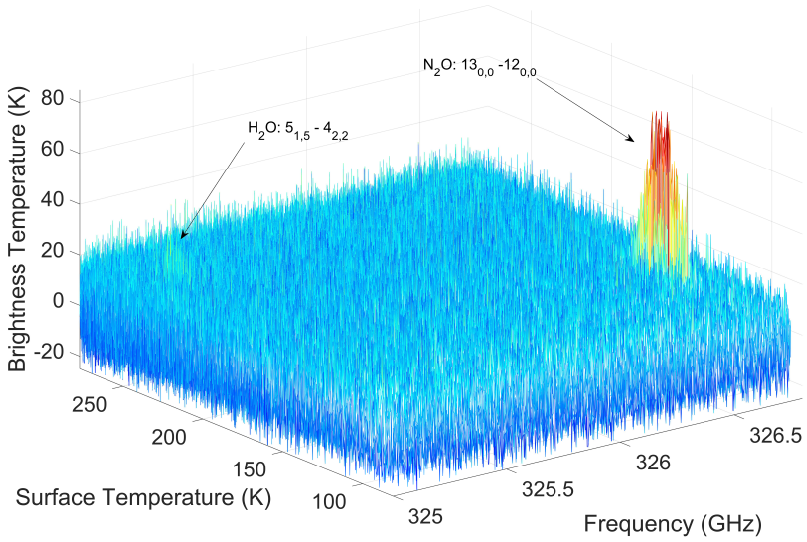


Figure 6.4: Surface temperature of the cold trap as a function of the THz-DES brightness temperature and frequency. This intensity map shows the THz-DES results of the $H_2O/N_2O - 1/1$ ice configuration.

Results for three experiments with nitrous oxide and water are shown in Figs. 6.5a and 6.5b. The configurations are $H_2O/N_2O$–1/1 (red curves), $N_2O/H_2O$–1/1 (green curve) and $H_2O : N_2O - 1 : 1$ (black curve). The blue curves on those plots represent the desorption of pure nitrous oxide in Fig. 6.5a and water in Fig. 6.5b. The amount of each molecular components corresponds to one deposition exposure time in order to compare them with the pure ice THz-DES.

From $T_{surface}$ = 77 K to 100 K, no signals are observed in both figures. The desorption is only starting at a surface temperature of 100 K in Fig. 6.5a corresponding to $N_2O$. From $T_{surface}$ = 100 K to 130 K, the trends for all ice's configurations are exactly the same. Their $N_2O$ brightness temperatures increase from the noise floor (0 K) to 75 K intensity. Therefore, there is no apparent difference in their sublimation temperature regardless of the $N_2O$ orientation;

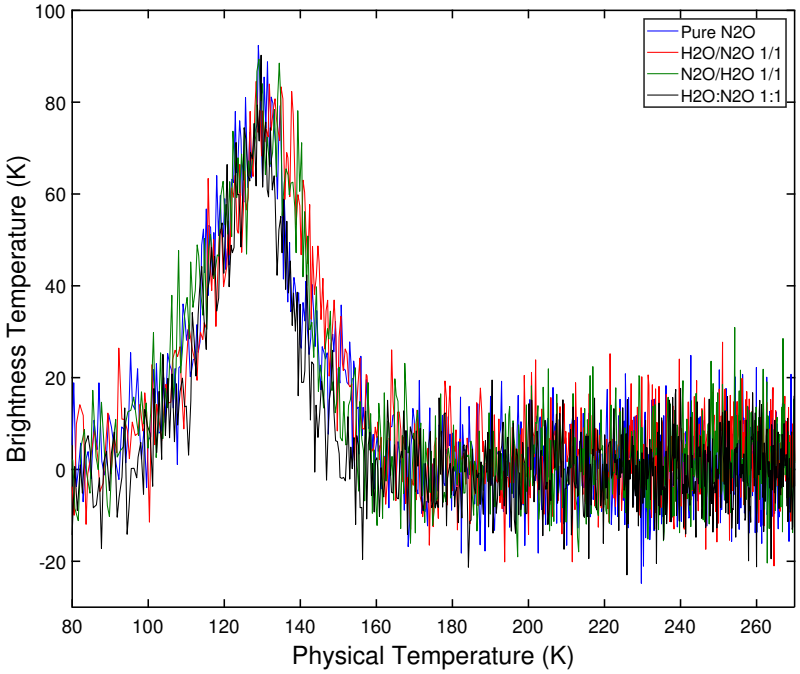


(a)

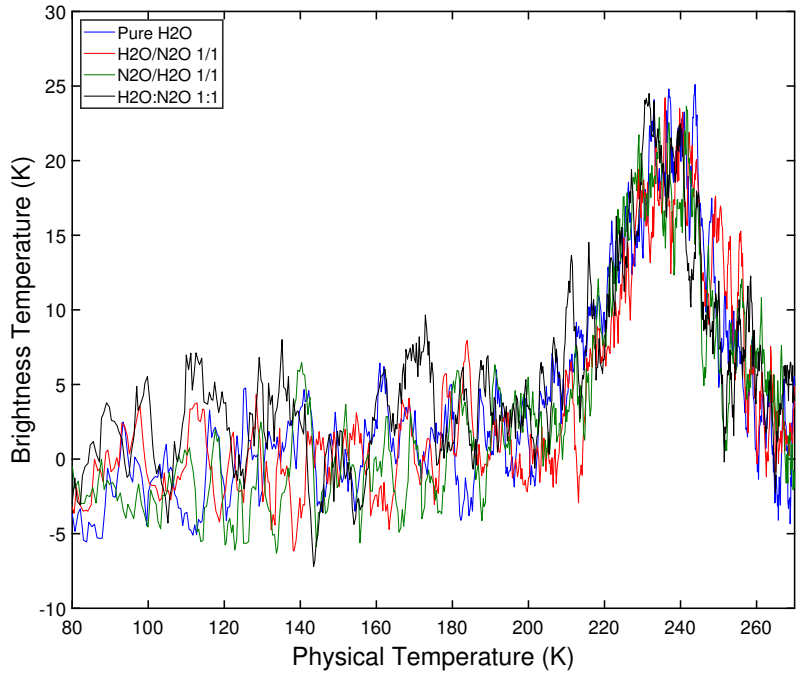


(b)

Figure 6.5: Comparison of the different layered configuration THz-DES results. The blue curves are the brightness temperature of the pure desorbed molecule, the red curves is the results for $H_2O/N_2O-1/1$, the green curves for $N_2O/H_2O-1/1$ and the black curves for $H_2O:N_2O-1:1$. 6.5a shows the results for nitrous oxide whereas 6.5b shows the BT of the water features when desorbing from the icy layers.

Table 6.2: Desorption activation energy for $N_2O$-$H_2O$ ice configurations in kJ/mol.

| **Mol.** | **Exp. time** | $E_{nom}$ (kJ/mol) | $E_{av}$ (kJ/mol) | $R_N^2$ | **N** |
|---|---|---|---|---|---|
| $N_2O$ | | | | | |
| $N_2O$ | 1 | $13.4 \pm 3.3$ | $13.4 \pm 3.2$ | 0.9993 | $5.0 \times 10^{21} (\pm 1 \times 10^{21})$ |
| $H_2O/N_2O$ | 1/1 | $11.5 \pm 0.9$ | $11.1 \pm 2.5$ | 0.9998 | $4.7 \times 10^{21} (\pm 4 \times 10^{21})$ |
| $N_2O/H_2O$ | 1/1 | $14.7 \pm 2.5$ | $14.3 \pm 2.9$ | 0.9996 | $4.1 \times 10^{21} (\pm 3 \times 10^{21})$ |
| $H_2O : N_2O$ | 1:1 | $16.0 \pm 2.3$ | $16.0 \pm 2.0$ | 0.9997 | $3.0 \times 10^{21} (\pm 2 \times 10^{21})$ |
| $H_2O$ | | | | | |
| $H_2O$ | 1 | $32.9 \pm 1.4$ | $31.7 \pm 9.5$ | 0.9867 | $12 \times 10^{21} (\pm 2 \times 10^{21})$ |
| $H_2O/N_2O$ | 1/1 | $45.7 \pm 1.1$ | $47.0 \pm 7.7$ | 0.9835 | $7.5 \times 10^{21} (\pm 4 \times 10^{21})$ |
| $N_2O/H_2O$ | 1/1 | $45.0 \pm 2.3$ | $52.9 \pm 11$ | 0.9906 | $9.6 \times 10^{21} (\pm 5 \times 10^{21})$ |
| $H_2O : N_2O$ | 1:1 | $56.3 \pm 5.5$ | $53.3 \pm 7.3$ | 0.9014 | $5.5 \times 10^{21} (\pm 1 \times 10^{21})$ |

either forming the bottom layer, upper layer or mixed with water. From $T_{surface}$ = 130 K to 160 K, the BTs are diverging. Indeed, the BTs from pure nitrous oxide and mixed ice (blue and black curves) are decreasing with a surface temperature 6 K lower than the signals from the layer ices (red and green curves). However the decreasing rate is similar for all measurements corresponding to the pumping rate of the THz-DES experiment. A reason of this discrepancy could be explained by a larger amount of nitrous oxide within the ice for $H_2O/N_2O$ and $N_2O/H_2O$. Another reason could come from the ice configuration itself. A slight increase in molecular deposition could have occurred during layered configuration.

Figure 6.5b shows the smoothed brightness temperature observed from water desorption in pure (blue), layered (red and green) and mixed (black) configurations. Between $T_{surface}$ = 77 K and 200 K, the brightness temperatures measured for the water line are within the experimental noise floor (10 K). Between $T_{surface}$ = 200 K and 230 K, all intensities have similar increasing trends for layered, mixed or pure ice experiments. The intensity reaches about 23 K. At 240 K, water ice from all the experiments have desorbed and $H_2O$ molecules are pumped away at a similar pumping rate.

With the method presented in Section 5.5, the desorption energies for $N_2O$

and $H_2O$ were calculated and results are shown in Table 6.2. Firstly, the number of molecules calculated for $N_2O$ are within the same order of magnitude for all ice configurations. It is important to notice that the uncertainty on the number of molecules may not be relevant for some results as the measured NEδT used in the method in Section 5.5 may be too high. Therefore, the THz-DES brightness temperature difference observed must come from a configuration effect, where molecules desorb faster in mixed ice than in a layered configuration. Interaction of $N_2O$ with $H_2O$ would be more important within layered ice and may retain molecules in the solid phase for a longer period. Another possibility could come from the non-linearity of the temperature curve as seen in Section 5.3.1. Therefore a small quick temperature step would sublimate slightly more molecules than a steady ramp. The desorption energies ($E_{nom}$ or $E_{av}$) are similar to pure ice for $N_2O$.

An interesting effect is seen with water. In pure ice configuration, the desorption energy calculated was around 30 kJ/mol, slightly lower than literature values. However, in layered configuration, water has a higher desorption energy within the literature, between 45 and 50 kJ/mol. Therefore, water molecules need more energy to sublimate when interacting with the nitrous oxide molecules in any configuration. Moreover, no difference is seen whether $H_2O$ is the top layer, bottom layer, or mixed.

A very important result when comparing Figs. 6.5a and 6.5b is that nitrous oxide and water desorption are independent from each other regardless the orientation; layered or mixed. Figure 6.5a shows that the brightness temperatures for all configurations stay within the noise floor at the surface temperature when water desorbs, i.e. from 200K to 260 K. Similarly, in Figure 6.5b, no signs of water desorption are observed for any configuration between 100 K and 160 K. This means that for $H_2O/N_2O-1/1$, when $N_2O$ is forming the bottom layer, the $N_2O$ molecules diffuse through the interstitial layers with the water ice above it (without sublimation of water ice molecules). Equivalently, in the $N_2O/H_2O-1/1$ ,the

$H_2O$ molecules diffuse through the interstitial layers the nitrous oxide ice above it. This mechanism is similar to a $CO_2$-type desorption as studied in other TPD experiments [134]. However our calculations on the desorption energies show that water molecules require slightly higher energy in order to sublimate, whereas nitrous oxide are not affected. This effect might come from the low binding energy of $N_2O$ and high binding energy of $H_2O$.

### 6.3.2 $H_2O/N_2O$ - Ice Thickness impact

For the 1-1 THz-DES results, the configuration $H_2O/N_2O$ was selected as the top layer having a higher sublimation temperature than the bottom layer. Therefore, the behaviour of the molecular specie desorbing first provides information about the molecular interactions present in the ice.

The impact of the amount of molecules forming the top layer (water) and bottom layer (nitrous oxide) has been analysed via THz-DES. Figure 6.6a and 6.6b show a comparison between pure ices (blue curves), $H_2O/N_2O$ 1/1 (red curves), $H_2O/N_2O$ 1/2 (green curves) and $H_2O/N_2O$ 4/1 (black curves).

When there is more $N_2O$ forming the bottom layer (green curve), the desorption occurs at $T_{surface}$ = 90 K and last over a bigger temperature range ($T_{surface}$ = 190K). The difference with the pure (blue) or the 1/1 layered configuration (red) comes directly from the deposition of a higher number of $N_2O$. $N_2O$ molecules would desorb in higher quantities at the sublimation temperature. This is the reason why the green BT increases from $T_{surface}$ = 90 K. The number of molecules desorbing in the two exposure time deposition is three times higher than for pure ice, about $15 \times 10^{21} \pm 1 \times 10^{22}$ due to calculation's artefacts (Table 6.3). From $T_{surface}$ = 95 K to 150 K, $N_2O$ is desorbing as a standard THz-DES. The difference appears between $T_{surface}$ = 150 K and 190 K. The brightness temperature is reduced by half of its maximal value reaching a second intensity plateau at 40 K. This is due to the late sublimation of nitrous oxide trapped

below the icy layer of water. The slope is still slowly decreasing meaning that the number of molecules desorbing is higher than the pumping rate. No nitrous oxide is detected where water desorption starts at 210 K. From Figure 6.6b, the $H_2O$ brightness temperature measured is similar between the $H_2O/N_2O$ 1/2 or 1/1 and pure $H_2O$. This means that the amount of nitrous oxide forming the bottom layer do not impact the water top layer desorption. Moreover while desorbing, $N_2O$ is not carrying away $H_2O$ ice.

By increasing the amount of water forming the top layer in a $H_2O/N_2O$ 4/1 configuration, the black curves were obtained. $N_2O$ THz-DES for $H_2O/N_2O$ 4/1 and $H_2O/N_2O$ 1/1 are identical and no water desorption is observed at $N_2O$ sublimation temperature. However, a change is observed for the water desorption as expected. In Figure 6.6b, water is still desorbing from 240 K to 260 K for the 4/1 configuration whereas it stops at 240 K in the 1/1 and pure ice system. This is due to the higher amount of $H_2O$ forming the 4/1 layer of ice. From Table 6.3, the number of molecules is three times higher for 2 deposition exposure times than for one. The amount of water molecules is multiply by a factor 5 - 6.

Table 6.3: Desorption activation energy for $N_2O/H_2O$ ice configurations at various thickness.

| **Mol.** | **Exp. time** | $E_{nom}$ (kJ/mol) | $E_{av}$ (kJ/mol) | $R_N^2$ | **N** |
|---|---|---|---|---|---|
| $N_2O$ | | | | | |
| $N_2O$ | 1 | $13.4 \pm 3.3$ | $13.4 \pm 3.2$ | 0.9993 | $5.0 \times 10^{21}(\pm 1 \times 10^{21})$ |
| $H_2O/N_2O$ | 1/1 | $11.5 \pm 0.9$ | $11.1 \pm 2.5$ | 0.9998 | $4.7 \times 10^{21}(\pm 4 \times 10^{21})$ |
| $H_2O/N_2O$ | 1/2 | $12.2 \pm 1.6$ | $13.2 \pm 2.1$ | 0.9998 | $15 \times 10^{21}(\pm 1 \times 10^{22})$ |
| $H_2O/N_2O$ | 4/1 | $14.4 \pm 4.6$ | $13.7 \pm 4.7$ | 0.9988 | $4.7 \times 10^{21}(\pm 4 \times 10^{22})$ |
| $H_2O$ | | | | | |
| $H_2O$ | 1 | $29.2 \pm 1.1$ | $29.0 \pm 3.5$ | 0.9873 | $12 \times 10^{21}(\pm 2 \times 10^{21})$ |
| $H_2O/N_2O$ | 1/1 | $45.7 \pm 1.1$ | $47.0 \pm 7.7$ | 0.9835 | $7.5 \times 10^{21}(\pm 4 \times 10^{21})$ |
| $H_2O/N_2O$ | 1/2 | $29.4 \pm 0.1$ | $31.4 \pm 9.8$ | 0.9756 | $5.0 \times 10^{21}(\pm 4 \times 10^{21})$ |
| $H_2O/N_2O$ | 4/1 | $24.5 \pm 4.0$ | $24.3 \pm 6.4$ | 0.9139 | $34 \times 10^{21}(\pm 0.4 \times 10^{21})$ |

The desorption energies (Table 6.3) are very similar for $N_2O$ and $H_2O$ when varying the quantity of ice. However, higher energy for $H_2O$ in 1/1 configurations

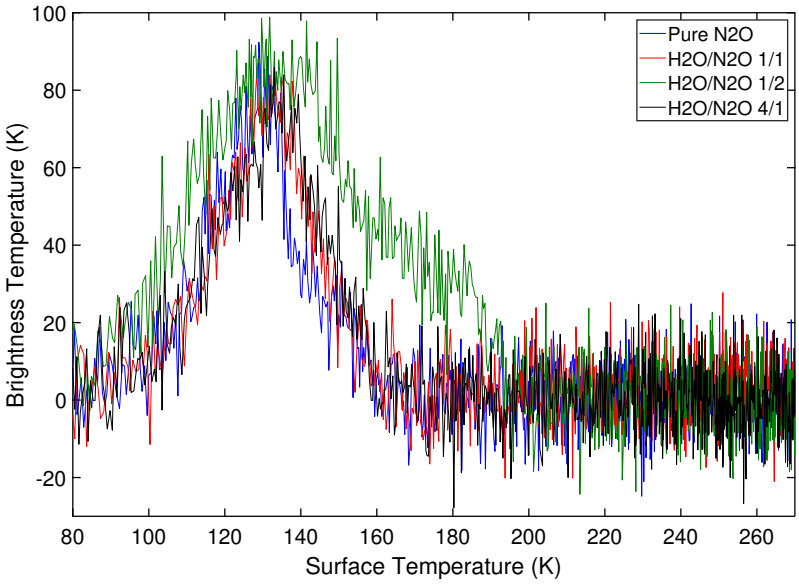


(a)

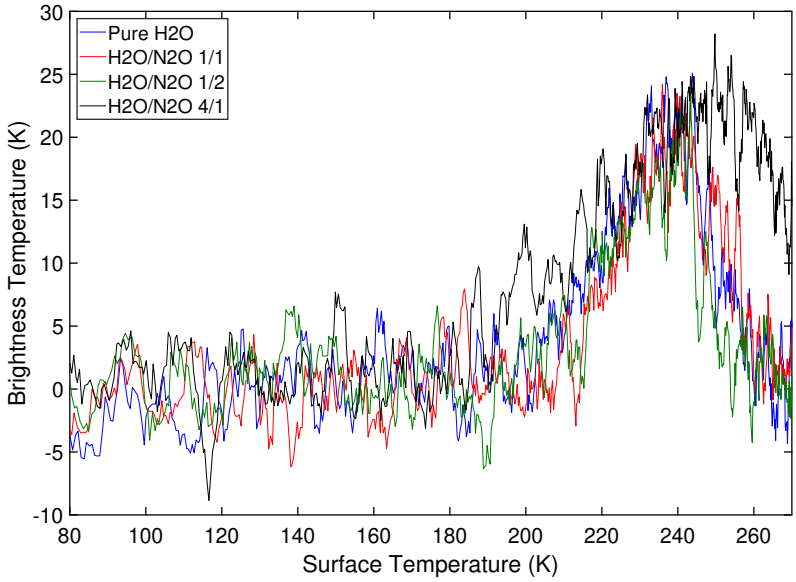


(b)

Figure 6.6: Impact of the thickness of the water ice in $H_2O/N_2O$ configuration compared with pure desorbed molecules (blue curves). The red lines shows the brightness temperature (BT) for a ratio 1/1 and the black lines a ratio 4/1 for the nitrous oxide feature (panel (a)) and the water feature (panel (b)).

is measured. The water feature is a weak line and the method to retrieve the desorption can be affected by important random noise during a measurement. $E_{av}$ results have an uncertainty of 7.7 kJ/mol. This provides a high NE$\delta$T identification. The analysis of water desorption energies will be considered limited by the weak signature of its spectral line.

Results displayed in Table 6.3 proves the amount of water forming the top layer do not impact the desorption of the bottom layer for a $H_2O/N_2O$ system. Reciprocally the amount of nitrous oxide forming the bottom layer does not impact the thermal desorption of water. Similar desorption energies were retrieved meaning that $N_2O$ and $H_2O$ are not interacting within each other in the solid phase. However, the desorption of $N_2O$ can seem delayed in term of surface temperature either because it is constrained by the top water ice layer or for sensitivity reasons. THz-DES is able to characterise the solid phase properties of the ice by looking at the gaseous materials coming out of it.

## 6.4 $H_2O - CH_3OH$: Lower Sideband

After characterising the THz-DES interactions of $H_2O$ and $N_2O$, water and methanol ice configurations were studied due to their respective importance in star forming regions as described in Chapter 5. The various ice configurations analysed were $CH_3OH/H_2O$, $CH_3OH : H_2O$, $H_2O/CH_3OH$ of varying thickness.

### 6.4.1 1-1 configurations

Figure 6.7 presents the full THz-DES dataset for $H_2O/CH_3OH$–1/1 in a intensity map format. The features at the right corresponds to methanol whereas the faint line around 325 GHz is the signal from desorbing water molecules. Similarly to the previous section, only cross section will be presented.

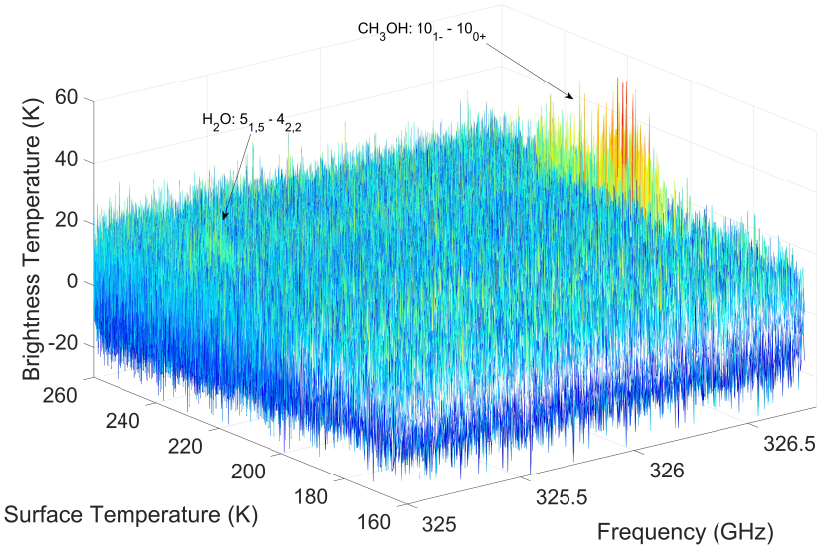


Figure 6.7: Surface temperature of the cold trap as a function of the THz-DES brightness temperature and frequency. This intensity map shows the THz-DES results of the $H_2O/CH_3OH$ – 1/1 ice configuration.

Figure 6.8 shows the surface temperature as a function of the experimental time for $CH_3OH/H_2O$ 1/1 (blue curve), $CH_3OH$ : $H_2O$ 1 : 1 (red curve), $H_2O/CH_3OH$ 1/1 (green curve) and pure water and methanol (black dashed curves). All curves follow the same trend over the time. The surface trap temperature is non-linearly going from 77 K to 270 K. This implies that the THz-DES spectra can be compared as the same desorption rate is applied for the different configurations.

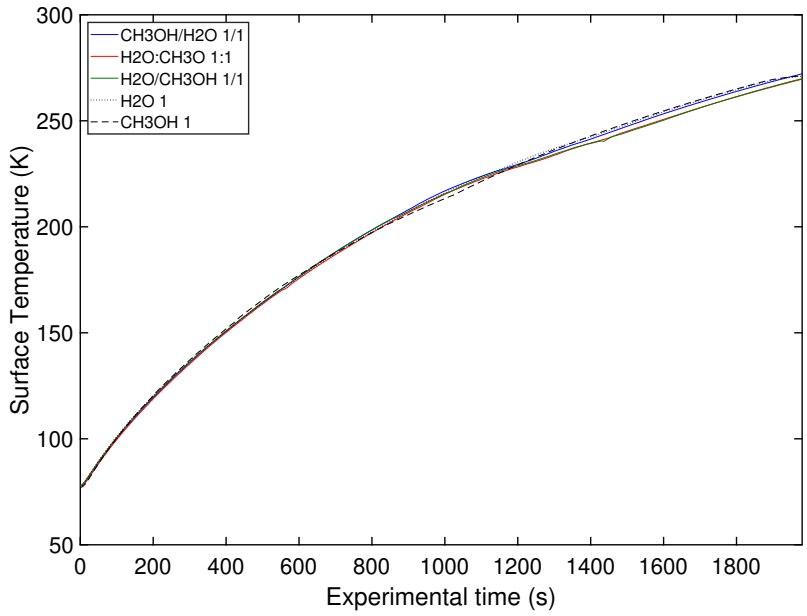


Figure 6.8: Physical surface temperature of the cold trap as a function of the THz-DES experimental time for layers. The blue, red and black curves are respectively the $CH_3OH/H_2O$ 1/1, $CH_3OH$ : $H_2O$ 1:1, $H_2O/CH_3OH$ 1/1. The two black dashed line are the THZ-DES temperature for $CH_3OH$ and $H_2O$ one deposition.

The THz-DES results are shown for the central line frequency of methanol (Fig. 6.9a) and water (Fig. 6.9b) as a function of the trap surface temperature. For each figures, the blue represents the pure ice configuration, the red curve is the $CH_3OH/H_2O$ 1/1 configuration, the green curve is the $CH_3OH$ : $H_2O$ 1:1 and the black curve $H_2O/CH_3OH$ 1/1. The different curves presented are smoothed for clarity.

Figure 6.9a shows the methanol THz-DES results for the various configurations. The red, green and black curves have the same trend for all surface temperature range. From $T_{surface}$ = 77 K to 170 K, no signal is detected as the sublimation temperature is not reached. For $T_{surface}$ = 170 K to 185 K, the brightness temperature is slightly increased to reach about 10 K, the point at which a small amount of icy $CH_3OH$ started to desorb. The intensities measured show the black curve to be higher than the green and red higher than black. This means that when $CH_3OH$ is forming the top-layer, higher quantities are likely to

desorb than when below $H_2O$. Mixed ice has the apparent slowest desorption. At 185 K, the three curves present a steep increase to reach a maximum brightness temperature of 40 K at a surface temperature of 205 K. Although methanol is forming the bottom layer of the $H_2O/CH_3OH$ (black curve), almost the same amount is desorbing as when it is mixed or forming the top layer as shown in Table 6.4. The difference in intensity indicates that less methanol is desorbing. From $T_{surface}$ = 205 K to 245 K, the brightness temperature decreases from 40 K to 20 K, with some variation between the ice configurations. The red curve has the highest peak (45 K) of the three configurations. This means that methanol is sublimating with a slightly higher rate. From $T_{surface}$ = 245 K to 252 K, the brightness temperatures sharply decrease to reach the noise floor. For $T_{surface}$ > 252 K, no more signal is detected by the radiometer. The variation in the gradual decline of brightness temperature between 205 K and 245 K is due to the ice configurations and to the experimental set-up. This will be explained after describing the signals observed by the water ice.

Figure 6.9b shows the water THz-DES results for the same configurations. The desorption of water starts at a trap surface temperature of 210 K. From $T_{surface}$ = 210 K to 230 K, the brightness temperature for all configurations (red, green and black curves), similar desorbing trends are observed. From $T_{surface}$ = 230 K to 240 K, a plateau is reached at 18 K but signals detected are weak because of the transition observed. From $T_{surface}$ = 240 K to 255 K, the pumping rate is higher than the desorption rate and decreasing slopes are measured for each experiment. After 255 K, all the water ice has sublimated from the cold trap and no signals are detected. No differences are seen for water desorption, in Fig. 6.9b, when comparing the pure and binary ice spectra. Water sublimation begins at 210 K and follows the same trend over the entire range of surface temperature.

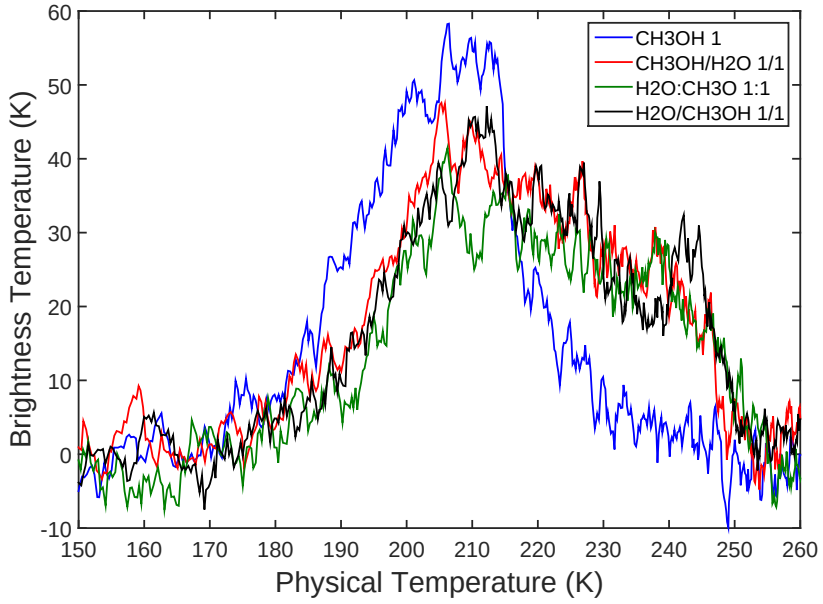


(a)

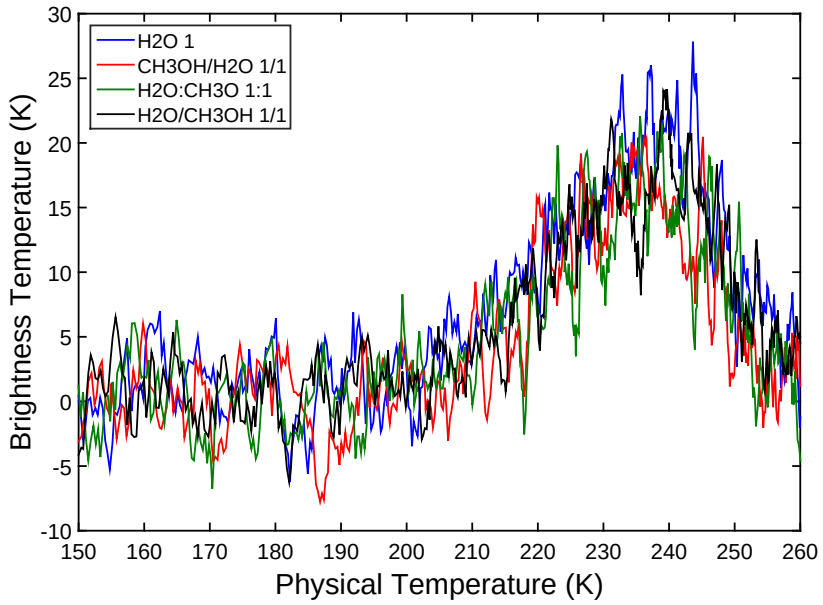


(b)

Figure 6.9: THz-DES smoothed BT results for $CH_3OH$ - $H_2O$ results. The top panel (a) is the methanol BT measured for $CH_3OH1$ (blue), $CH_3OH/H_2O$ 1/1 (red), $CH_3OH : H_2O$ 1:1 (green) and $H_2O/CH_3OH$ 1/1 (black). Panel (b) is the water BT measured for $CH3_OH1$ (blue), $CH_3OH/H_2O$ 1/1 (red), $CH_3OH : H_2O$ 1:1 (green) and $H_2O/CH_3OH$ 1/1 (black).

Table 6.4: Desorption activation energy for $CH_3OH$-$H_2O$ ice configurations in kJ/mol.

| **Mol.** | **Exp. time** | $E_{nom}$ (kJ/mol) | $E_{av}$ (kJ/mol) | $R_N^2$ | **N** |
|---|---|---|---|---|---|
| $CH_3OH$ | | | | | |
| $CH_3OH$ | 1 | $32.2 \pm 1.1$ | $32.2 \pm 3.3$ | 0.9992 | $2 \times 10^{21}(\pm 2 \times 10^{20})$ |
| $CH_3OH/H_2O$ | 1/1 | $31.0 \pm 1.1$ | $31.3 \pm 17.0$ | 0.9976 | $2.1 \times 10^{21}(\pm 5 \times 10^{20})$ |
| $H_2O : CH_3OH$ | 1:1 | $43.2 \pm 2.4$ | $44.0 \pm 7.5$ | 0.9940 | $1.7 \times 10^{21}(\pm 2 \times 10^{20})$ |
| $H_2O/CH_3OH$ | 1/1 | $39.0 \pm 1.1$ | $39.0 \pm 3.6$ | 0.9983 | $2.1 \times 10^{21}(\pm 5 \times 10^{20})$ |
| $H_2O$ | | | | | |
| $H_2O$ | 1 | $32.9 \pm 1.4$ | $31.7 \pm 9.5$ | 0.9867 | $12 \times 10^{21}(\pm 2 \times 10^{21})$ |
| $CH_3OH/H_2O$ | 1/1 | $46.9 \pm 2.6$ | $51.4 \pm 24$ | 0.9663 | $4.4 \times 10^{21}(\pm 8 \times 10^{21})$ |
| $H_2O : CH_3OH$ | 1:1 | $29.0 \pm 4.2$ | $29.1 \pm 6.0$ | 0.9465 | $5.3 \times 10^{21}(\pm 1 \times 10^{21})$ |
| $H_2O/CH_3OH$ | 1/1 | $39.0 \pm 0.9$ | $40.3 \pm 1.5$ | 0.9781 | $7.0 \times 10^{21}(\pm 2 \times 10^{21})$ |

Desorption energies for methanol are higher by 5-10 kJ/mol when it is mixed or is deposited below water as shown in Table 6.4. The highest values are observed for mixed ices. This means that the $CH_3OH$ bonding is stronger when methanol is mixed with the $H_2O$ molecules. The desorption energy of water is at its highest when forming the bottom layer followed by when forming the top layer. Surprisingly, the water desorption energy when it is mixed with methanol has the same value as for pure ice. This is not the case for methanol. Methanol bonding with water has an increased impact on the desorption as they are trapped within the ice. The uncertainty on $E_{av}$ for $H_2O$ and $CH_3OH$ in $CH_3OH/H_2O$ is very high meaning that the BT standard deviation for this experiment is high and would impact the retrieval of the desorption energy. Therefore the calculated $E_{des}$ may not be representative.

From Section 6.3, it has been shown via THz-DES that molecules with different sublimation temperatures could desorb without interacting within each other. However this is not the case for the methanol and water binary systems. First of all, methanol desorption is delayed compared to pure $CH_3OH$ desorption. When methanol is desorbing from 170 K to 205 K, no water signal is observed in Fig. 6.9b. Water is not co-desorbing with methanol below 210 K. The delay in

methanol desorption means that methanol molecules are interacting with water molecules for all the configurations. Methanol molecules are strongly bound to their neighbouring molecules, $H_2O$. Intermolecular hydrogen bonds form $CH_3OH$ and $H_2O$ clusters which change the sublimation point of the methanol molecules. At 210 K, the methanol signature is still observed although it should have completely desorbed at this temperature. This temperature exactly coincides with the sublimation temperature of water. By comparing Figure 6.9a and Figure 6.9b, the signal observed from 205 to 245 K is due to the desorption of methanol trapped in the water ice layers. As the surface temperature increases the number of trapped methanol molecules released in the chamber decreases, therefore the decreasing intensity observed in Fig. 6.9a. The trapping behaviour of methanol with the ice layer is especially noticeable for the $H_2O/CH_3OH1/1$ (black). In Figure 6.9b, at 240 K a peak of intensity from $H_2O$ appears at the same temperature as the brightness temperature of $CH_3OH$; this peak rises from 20 to 30 K. This desorption event shows remaining $CH_3OH$ molecules trapped within water are co-desorbed with $H_2O$ molecules. The trend is also observed within the desorption energy. When water is layered with methanol ($H_2O/CH_3OH$), desorption energies of methanol and water are higher than for their respective pure ice configuration. This is the evidence of H-bonding interaction between water and methanol especially seen for mixed ice .

### 6.4.2 $H_2O/CH_3OH$ - Water Thickness Impact

The bonding was significantly observed in $H_2O/CH_3OH$ configuration. Therefore that type of ice was selected to analyse the impact of the quantity of water ice on the desorption phenomena. This could be used to determine if molecules of methanol are more trapped within a thicker water ice layer resulting in a more delayed sublimation or if the volcano effect is more clearly observable. Figure 6.10a and Figure 6.10b are showing the THz-DES results respectively for methanol and

water at their central line frequency. The blue curves are the brightness temperature measured for the configuration $H_2O/CH_3OH - 1/1$. It is compared to the red curves, $H_2O/CH_3OH - 3/1$.

In Figure 6.10a, the blue and red curves have similar trends up to 205 K surface temperature at the maximal desorption rate. Methanol molecules are starting to desorb at similar surface temperature even with a thicker layer of water above the sublimating methanol ice. From $T_{surface}$ = 205 K and 245 K, the same trend is observed for both experiments with a decreasing slope up to 235 K and an increase of desorbing molecule after 235 K. However the red curve is lower than the blue curve by 5 K in intensity. This means that less methanol is desorbing from the ice over that period of time. The red curves show a delayed end of desorption and some volcano effects at 259 K and 263 K corresponding to a peak in the brightness temperature. This means that the methanol desorption is slowed down while the thick water layers desorb and that some trapped methanol sublimates at higher temperature than previously seen.

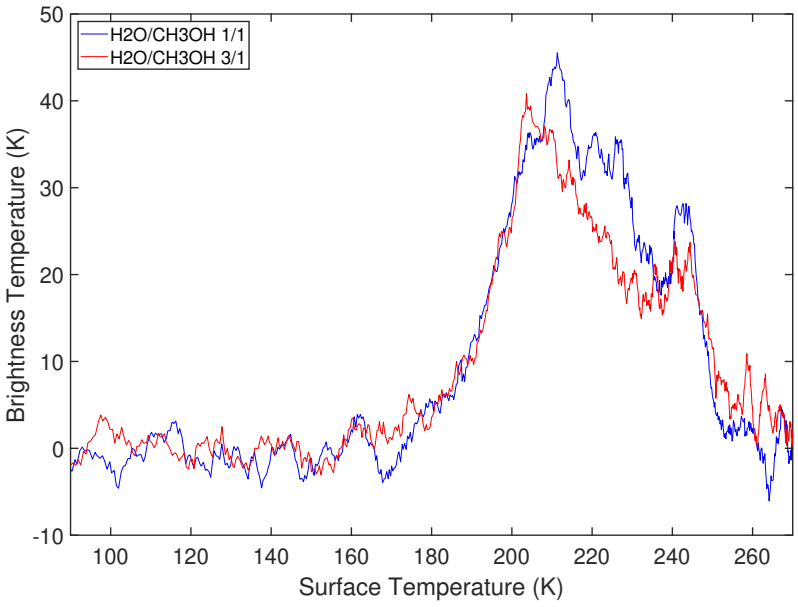


(a)

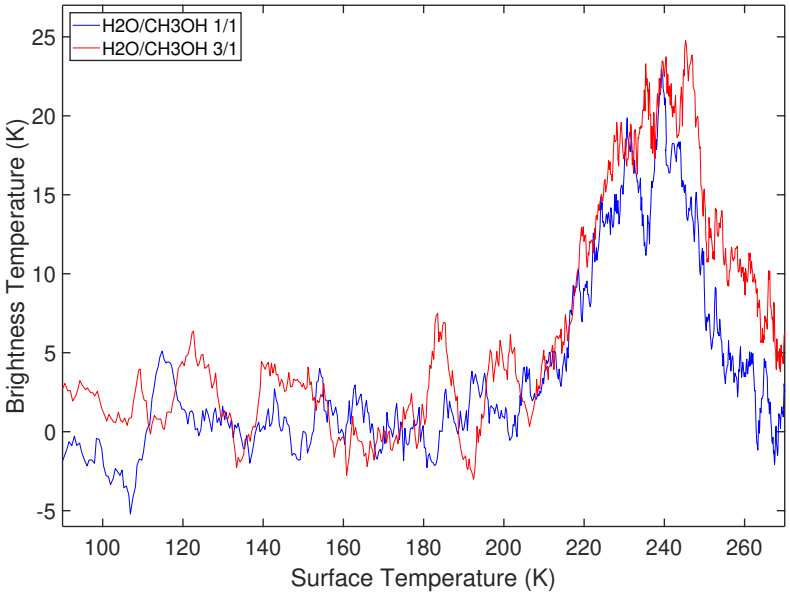


(b)

Figure 6.10: Impact of the top water thickness in $H_2O/CH_3OH$ layered configuration: 1/1, blue curves and 3/1 red curves compared with pure methanol and water (black curves). Panel (a) is the smoothed methanol THz-DES BT and panel (b) the results for the water spectral line.

In Figure 6.10b, both curves overlap up to 230 K. Thermal desorption is occurring at the same temperature with the same rate for both configurations. As there are more water molecules forming the top layer (red curve), the sublima-

tion of the water molecules last over a longer time, i.e. over a higher range of surface temperature (between 230 K and 247 K). For the $H_2O/CH_3OH$ – 3/1 configuration, a sharp decrease of the brightness temperature, from 24 to 12 K, is observed between 247 K and 251 K. A linear slow decrease of the brightness temperature is seen from 251 K to 267 K (red curve). At 251 K, most of the water from 1 deposition is desorbed. For the 3 deposition exposure time case, remaining water molecules due to the thickness of ice are still desorbing but in a smallest quantity. The observed methanol peak intensities at 259 and 263 K corresponds to desorption of the water ice where $CH_3OH$ molecules were trapped. The measured water peak detected at 266 K is likely to be due to the sublimation of water molecules deposited on the cold trap far from the bottom surface where the heater is located. Therefore, the actual desorption temperature would not correspond to the measured temperature. A temperature gradient must exist with the trap itself.

Table 6.5: Desorption activation energy for $CH_3OH$-$H_2O$ ice configurations at various thickness.

| **Mol.** | **Exp. time** | $E_{nom}$ (kJ/mol) | $E_{av}$ (kJ/mol) | $R_N^2$ | **N** |
|---|---|---|---|---|---|
| $CH_3OH$ | | | | | |
| $H_2O/CH_3OH$ | 1/1 | $39.0 \pm 1.1$ | $39.0 \pm 3.6$ | 0.9983 | $2.1 \times 10^{21}(\pm 5 \times 10^{20})$ |
| $H_2O/CH_3OH$ | 3/1 | $25.2 \pm 1.3$ | $25.2 \pm 2.5$ | 0.9971 | $1.8 \times 10^{21}(\pm 0.6 \times 10^{20})$ |
| $H_2O$ | | | | | |
| $H_2O/CH_3OH$ | 1/1 | $39.0 \pm 0.9$ | $40.3 \pm 1.5$ | 0.9781 | $7.0 \times 10^{21}(\pm 2 \times 10^{21})$ |
| $H_2O/CH_3OH$ | 3/1 | $37.3 \pm 1.1$ | $41.6 \pm 6.9$ | 0.9586 | $17 \times 10^{21}(\pm 5 \times 10^{21})$ |

$CH_3OH$ desorption energies between $H_2O/CH_3OH$ 1/1 and 3/1 are slightly different, respectively $39.0 \pm 3.6$ kJ/mol and $25.2 \pm 2.5$ kJ/mol, from Table 6.5. In Figure 6.10a, the BT curves have similar trends. However between 160 K and 185 K, the red curve present a small plateau. This could be due to a continuous desorption in small quantity which is not seen in the 1/1 configuration. This plateau made the desorption rate flatter and therefore the desorption energy

lower than the 1/1 configuration. It could be due to a non-uniform deposition where for example some methanol ice was not perfectly covered by water ice or a gap within the deposited amorphous water ice was releasing a constant amount of desorbing methanol from the bottom layer. On the other hand water desorption energies stay constant whether it is made of three deposition exposure time or one, about 40 kJ/mol.

Only methanol desorption is impacted by the presence of the water molecules forming the top layer. It appears that the amount of ice forming the top layer has no significant impact regarding the co-desorption of methanol. No significant shift were observed for thicker ice and desorption energies were similar.

### 6.4.3 $H_2O/CH_3OH$ - Heating rate impact

Using the configuration $H_2O/CH_3OH$ 1/1, the heating rate applied on the surface of the cold trap was changed in order to analyse its impact on the THz-DES curves. Four $H_2O/CH_3OH$ 1/1 ices were studied applying various heating ramp conditions. Figure 6.11 shows the surface temperature of the trap as a function of the experimental time when no heating was applied on the ice (blue curve), 25 % (red curve), 50 % (red curve) and 100 % (black curve) heating rate applied. The percentage listed are representing the setting on the heaters controller. 0% means that no voltage is applied to the heaters. The convection of 293 K atmosphere outside the trap is warming the trap's walls slowly. 100 % applied means that full power is applied on the cold trap heater. All heating ramps are not linear in the THz-DES proof of concept experiment. When no heaters are used, it takes about 5000 s to go from 77 K to 273 K. When the heater is used at full power (100 %), it takes only 2000 s for the trap to warm up.

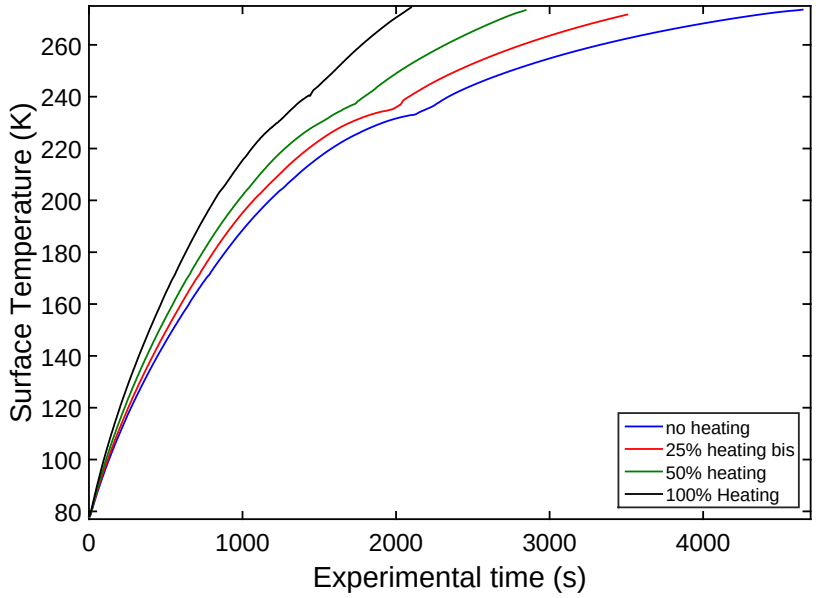


Figure 6.11: Physical surface temperature of the cold trap during a $H_2O/CH_3OH$ 1/1 THz-DES experiment with no heating power (blue curve), 25% heating power (red curve), 50% heating power and 100% heating power.

Figure 6.9a and Figure 6.9b shows the THz-DES results for methanol and water respectively. As for the previous figure, the heating rates applied are shown in different colours: 0 % (blue), 25 % (red curve), 50 % (red) and 100 % (black). The trend of all the THz-DES corresponds to a standard $H_2O/CH_3OH$ 1/1 desorption as explained in Section 6.4.1.

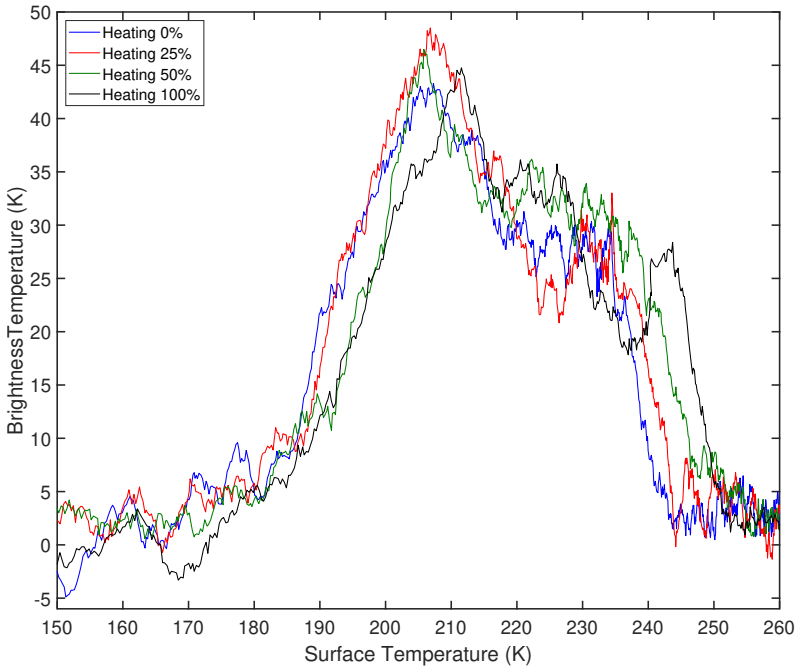


(a)

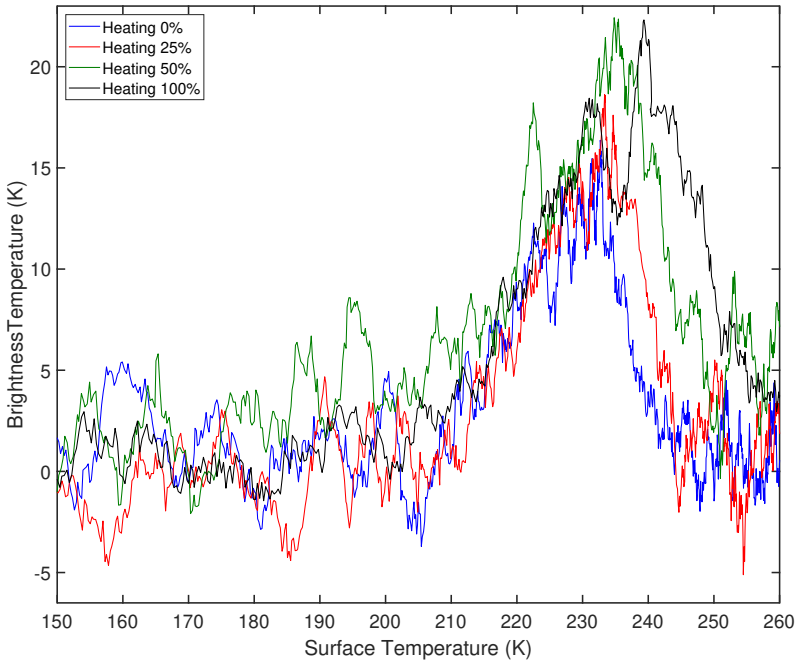


(b)

Figure 6.12: THz-DES smoothed BT for methanol (a) and water (b) in $H_2O/CH_3OH$ 1/1 THz-DES layer experiment with no heating power (blue curve), 25% heating power (red curve), 50% heating power and 100% heating power.

The impact of the heating rate on methanol desorption is shown in Fig. 6.12a.

Firstly the steep slope occurring from 190 K is different depending on the heating ramp. The blue (0%) and red (25 %) curves are following the same trend from 185 K with a peak intensity reached at $T_{surface}$ = 205 K. The green (50 %) and black (100 %) curves have parallel slopes with about 4 K offset. In the case of 50% heating (green curve), the peak intensity is reached at 205 K whereas for the black curve (100 %) it appears only at 215 K. Secondly, the main difference in Fig. 6.12a occurs at the end of the methanol thermal desorption. The end of THz-DES curve is shifted as the surface temperature increases. For methanol, the pumping rate is higher than the desorption rate (sharp decreasing slope) at 235 K for 0 % heating, 238 K for 25 %, 240 K for 50 % and 243 for 100 %. A similar pattern is seen for the water desorption in Fig. 6.12b as methanol and water co-desorb at those temperatures. This means that the desorption when occurring at higher speeds is delayed in terms of measured surface temperature. When the cold surface is slowly heated, the overall desorbing time is higher than for a 'fast' desorption. This is why a shift of the surface temperature is seen on both THz-DES curves. High heating rate induces a desorption over a short period of time and the temperature reading is seen higher than when the sublimation is spread over a long time as all molecule will eventually desorb before reaching the same high temperature.

Table 6.6: Desorption activation energy for $H_2O/CH_3OH$ ice configurations at various heating rate.

| **Heating Rate** | $E_{nom}$ (kJ/mol) | $E_{av}$ (kJ/mol) | $R_N^2$ | **N** |
|---|---|---|---|---|
| $CH_3OH$ | | | | |
| 0 % | $30.8 \pm 0.5$ | $30.7 \pm 2.2$ | 0.9947 | $3.5 \times 10^{21}(\pm 0.8 \times 10^{20})$ |
| 25 % | $32.0 \pm 1.0$ | $32.0 \pm 5.8$ | 0.9938 | $3.3 \times 10^{21}(\pm 2.4 \times 10^{20})$ |
| 50 % | $26.5 \pm 3.6$ | $26.4 \pm 5.8$ | 0.9883 | $2.9 \times 10^{21}(\pm 2.7 \times 10^{20})$ |
| 100 % | $38.1 \pm 1.7$ | $38.0 \pm 2.9$ | 0.9989 | $1.4 \times 10^{21}(\pm 1.7 \times 10^{20})$ |
| $H_2O$ | | | | |
| 0 % | $44.7 \pm 1.5$ | $48.2 \pm 32$ | 0.8078 | $4.6 \times 10^{21}(\pm 1.0 \times 10^{21})$ |
| 25 % | $54.3 \pm 3.9$ | $52.9 \pm 21$ | 0.9921 | $5.4 \times 10^{21}(\pm 2 \times 10^{21})$ |
| 50 % | $31.6 \pm 3.7$ | $31.7 \pm 4.3$ | 0.8736 | $6.9 \times 10^{21}(\pm 0.2 \times 10^{21})$ |
| 100 % | $35.8 \pm 0.3$ | $39.7 \pm 12$ | 0.9759 | $7.3 \times 10^{21}(\pm 2 \times 10^{21})$ |

The desorption energies calculated are within the order of magnitude of the one caculated for pure ices desorption, around 35 kJ/mol, Table 6.6. For $CH_3OH$, the calculated desorption energy is higher with 100 % heating than with 0 %. The same effect is observed for water although more noisy data were measured for the first two results (0 % and 50 %). As explained above, the reason for this effect could be that the trap surface temperature increase exceeds the desorption rate. Molecules desorb at a measured temperature higher than the surface temperature at which the real desorption happens. The heating rate changes the speed of diffusion though the ice layer [50].

## 6.5 $H_2O - CH_3OH$: Upper Sideband

The THz-DES experiment permits the observation of different frequencies, the RF-lower and RF-upper sideband of the radiometer, corresponding to various molecular rational transitions. In this section, THz-DES was used to show the possibility it offers toward the analysis of any spectral thermal desorption predilection for transitions such as ortho-, para- for water or A-, E- for methanol. Methanol has various spectral lines in the USB of THz-DES as shown in Table

6.7, with the frequency, logarithmic relative intensity, quantum numbers and the kind of transition. The assignment (I to V) of the observable spectral lines of methanol within 342.25 GHz to 346.75 GHz is listed and A- and E- transitions (see Section 4.4.3) are simultaneously observable in the USB.

Table 6.7: Assignment to the USB spectral lines of methanol shown in Fig. 6.13.

| **Symbol** | **Frequency (GHz)** | **Log(INT)** | **QN'** | **QN"** | **Species** |
|---|---|---|---|---|---|
| I | 342.730 | -3.3146 | 13(1)- | 13(0)+ | A |
| II | 344.109 | -3.9498 | 18(2) | 17(3) | E |
| III | 344.312 | -3.8865 | 10(2) | 11(3) | E |
| VI | 344.443 | -3.8355 | 19(1)+ | 18(2)+ | A |
| V | 345.904 | -3.7535 | 16(1)- | 15(2)- | A |

### 6.5.1 A- and E- THz-DES

Two ice configurations are studied in this section: $H_2O/CH_3OH$ 1/6 compared with $CH_3OH$ 6. The deposition exposure time was selected at a value of 6 as very weak lines were aimed to be observed. THz-DES results from previous sections on methanol-water ice configurations showed that the methanol desorption is delayed in terms of surface temperature compared to pure methanol ice desorption. Methanol is co-desorbing and some volcano effect appears after the sublimation temperature of water is reached. The desorption energy measured for $H_2O/CH_3OH$ was found higher than the one calculated for pure ice.

Figure 6.13 shows full dataset acquired and post-processed of the $CH_3OH$ 6 ice. The x-axis is the frequency range (GHz), the y-axis is the surface temperature (K) and the brightness temperature corresponds to the colour map. As expected, the brightness intensity detected was for the feature noted I at 342.73 GHz. The second stronger line was observed at 345.9 GHz.

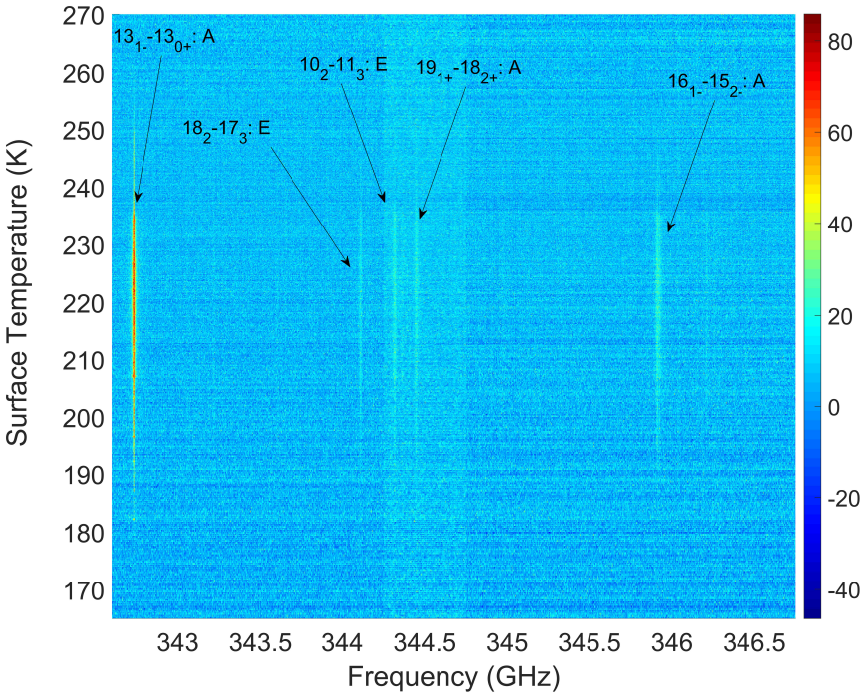


Figure 6.13: Surface temperature of the cold trap as a function of the THz-DES brightness temperature and frequency. This intensity map shows the THz-DES results of the $CH_3OH-6$ ice configuration detected in the USB of the instrument.

Fig 6.14 shows the desorption profile of the upper sideband $CH_3OH$ transitions in pure and a $H_2O/CH_3OH$ 1/6 mixture, plotted as brightness temperature versus surface temperature. The blue curves in Fig. 6.14 are the THz-DES results for the 6 deposition exposure time ice whereas the red curves are the results for the binary configuration $H_2O/CH_3OH$ 1/6. The brightness temperatures for the two experiments are listed accordingly to Table 6.7. Offset are used in order to compare the shape of the observed features. Until the surface temperature reached 170 K (dashed black vertical), no signals are observed above the noise floor for pure or binary ices. It is immediately apparent that the five $CH_3OH$ transitions used to extract this desorption data are less intense than those on the lower sideband, used to generate Fig. 6.9a and Fig. 6.9b. Consequently the S/N ratio is lower, and the desorption profile is harder to observe.

As seen in Section 6.4.1, and described in the literature [316], the desorption of $CH_3OH$ ice is delayed in binary systems when compared to pure $CH_3OH$

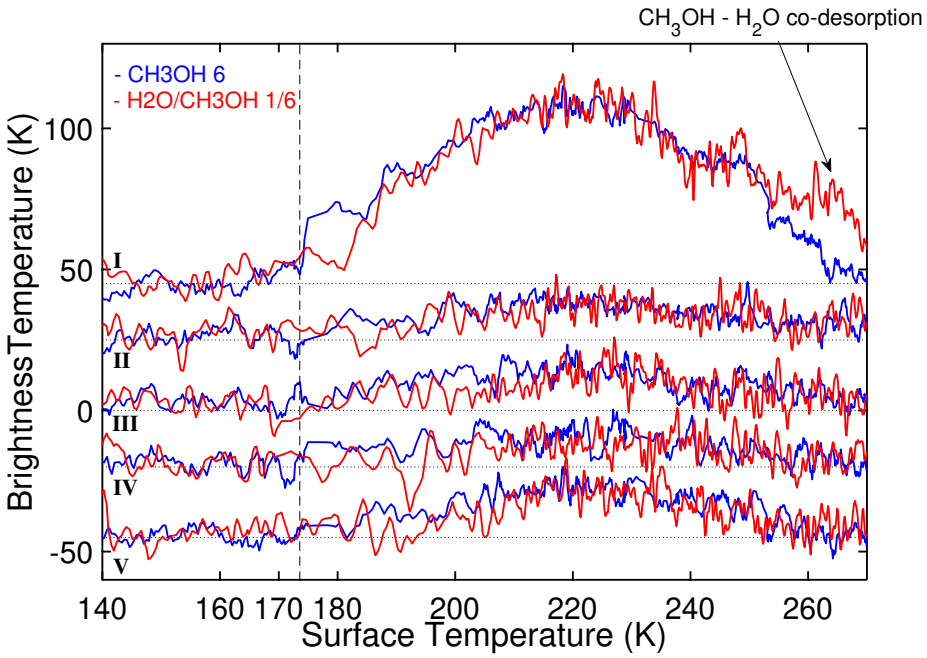


Figure 6.14: Comparison of the THz-DES results between the desorption of pure $CH_3OH$ with 6 depositions (blue curves) and $H_2O/CH_3OH$ 1/6 ice (red curves) in the USB. The baseline of the five features listed in Table 6.7 are offset for clarity.

ice alone. This is indicative that the methanol is not any longer present as an over-layer in the ice structure but either trapped or intermixed with the water component. This is best observed in Figure 6.9a, where, whilst water desorption matches irrespective of the pure or binary nature of the ice studied, the leading desorption edge in $CH_3OH$ mixed ice is significantly impacted in water. The difference that manifests at our heating temperature in a lag of around 10 K is related to the diffusion lengths and kinetics between methanol and water within the ice. Since the temperatures exceed the desorption energy of methanol when methanol molecules reach the vacuum interface they will desorb. This is entirely consistent with the literature and know behaviour of such systems.

The leading edge is vital to qualitatively and quantitatively understand desorption processes. In the brightest upper sideband trace in Fig. 6.14, there is an indication which is inclusive that this same effect is seen. Simply looking at the trace labelled I, it seems the onset of $CH_3OH$ desorption may be delayed in the water binary ice system, although certainly co-desorption of $CH_3OH$ with the

water is indicated at the higher temperatures. However, it is difficult to conclude this with the low statics (S/N) in the data. Of the remaining 4 transitions, 2 are from A states and 2 E states of methanol. The desorption can be seen in all cases, though with even lower intensity, the details of the desorption are difficult to ascertain. Nevertheless traces II, III, IV, all have a desorption peak with at least 4 sigma certainty, so desorption is observed. It is also clear that even within the limits of the S/N the shape of the desorption curves is not the same for every transition but these cannot easily be associated with A or E transitions specifically. Likewise, at the very low detection levels, it is not possible to see any discernible difference in the $CH_3OH$ desorption from pure or mixed ices. This may mean weaker transitions or certain energy state are less populated during desorption (this has been observed elsewhere in surface dynamics [172]) or could simply be a limitation of the S/N and low intensity transitions. It is therefore necessary to do a full leading edge and initial peak analysis to extract the desorption information. Likewise, data beyond this point should be treated with caution since it related to potential pressure and self-broadening of the weaker lines.

Table 6.8: Desorption activation energy for $CH_3OH$-$H_2O$ ice configurations in the USB.

| **Mol.** | **Exp. time** | $E_{nom}$ (kJ/mol) | $E_{av}$ (kJ/mol) | $R_N^2$ | **N** |
|---|---|---|---|---|---|
| I: $13_{1-}/13_{0+}$: A | | | | | |
| $CH_3OH$ | 6 | $45.8 \pm 0.5$ | $45.8 \pm 2.0$ | 0.9987 | $7.4 \times 10^{21}(\pm 5.2 \times 10^{20})$ |
| $H_2O/CH_3OH$ | 1/6 | $46.8 \pm 0.4$ | $46.8 \pm 3.1$ | 0.9966 | $8.1 \times 10^{21}(\pm 6.4 \times 10^{20})$ |
| II :$18_2/17_3$: E | | | | | |
| $CH_3OH$ | 6 | $20.6 \pm 0.3$ | $20.0 \pm 7.6$ | 0.9638 | $8.4 \times 10^{20}(\pm 7 \times 10^{19})$ |
| $H_2O/CH_3OH$ | 1/6 | $9.7 \pm 0.7$ | $9.6 \pm 0.8$ | 0.9954 | $7.2 \times 10^{20}(\pm 2 \times 10^{19})$ |
| III :$10_2/11_3$: E | | | | | |
| $CH_3OH$ | 6 | $27.1 \pm 1.9$ | $37.2 \pm 20.3$ | 0.9540 | $13.2 \times 10^{21}(\pm 5 \times 10^{21})$ |
| $H_2O/CH_3OH$ | 1/6 | $15.0 \pm 0.7$ | $14.8 \pm 3.5$ | 0.9481 | $8.3 \times 10^{21}(\pm 2.8 \times 10^{21})$ |
| IV :$19_{1+}/18_{2+}$: A | | | | | |
| $CH_3OH$ | 6 | $25.4 \pm 2.4$ | $26.1 \pm 4.0$ | 0.9760 | $13.5 \times 10^{21}(\pm 0.2 \times 10^{21})$ |
| $H_2O/CH_3OH$ | 1/6 | $21.6 \pm 1.5$ | $21.7 \pm 4.1$ | 0.9552 | $6.5 \times 10^{21}(\pm 1.4 \times 10^{21})$ |
| V :$16_{1-}/15_{2-}$: A | | | | | |
| $CH_3OH$ | 6 | $36.3 \pm 1.4$ | $34.5 \pm 14.8$ | 0.9873 | $10.6 \times 10^{21}(\pm 6 \times 10^{21})$ |
| $H_2O/CH_3OH$ | 1/6 | $20.1 \pm 3.6$ | $19.3 \pm 5.3$ | 0.9611 | $10.2 \times 10^{21}(\pm 5 \times 10^{21})$ |
| LSB: $10_{1-}/10_{0+}$: A | | | | | |
| $H_2O/CH_3OH$ | 1/6 | $39.0 \pm 0.4$ | $38.8 \pm 3.3$ | 0.9897 | $8.0 \times 10^{21}(\pm 6 \times 10^{21})$ |

Calculation of the desorption energies were performed on the spectral lines observed in the USB and the obtained energies are displayed in Table 6.8. Line I presents equivalent energies for $H_2O/CH_3OH$ 1/6 and $CH_3OH$ 6 of about 45 kJ/mol which corresponds to the literature TPD value. The energies for the other lines is lower between 20 and 35 kJ/mol. Line IV has a desorption energy of 36 kJ/mol for pure ice but drops to 20 kJ/mol for layered ice. This is the opposite of what was observed at the frequency of 326.6 GHz in the LSB where $E_{des}$ was measured of 39 kJ/mol in layered ice and 32 kJ/mol in pure methanol. This is proven by calculating the desorption of the LSB methanol feature for a $H_2O/CH_3OH$ 1/6 configuration. The result was a desorption energy of $38.8 \pm 3.3$ kJ/mol, identical to the value obtained in the LSB 1/1 configuration. Finally, A- transitions have for pure ice equivalent or higher desorption energies. A very interesting effect is seen when water is added. The desorption energy for the E- transitions drop significantly, from 27 kJ/mol to 15 kJ/mol for line III. This

is also seen for line IV. It indicates that methanol molecules bonding with the water molecules causes preferential desorption regarding the rotational energy transitions. It might be the case that A- transitions are the favourite desorption transition levels when $CH_3OH$ is in contact with $H_2O$.

### 6.5.2 A- and E- Ratios

Following the THz-DES results on the A- and E- transitions, a ratio analysis was carried out so as to determine any behaviour characteristics to A or E transitions. As stated by Table 6.7, lines I, IV, V are A spectroscopic level whereas lines II and III are E. By plotting the ratio between the desorption of a A-line and the other A- or E-lines, it is possible to determine if the desorption mechanism has preferential energetic transitions. Indeed by comparing the measured ratios of different spectral lines in different ice configurations, it is possible to evaluate if the ratio between A-/E- transitions is changing between pure methanol ice or binary ice desorption. The ratio between A-/E- and E-/E- lines for $CH_3OH$ and $H_2O/CH_3OH$ ice are shown respectively in Figs. 6.15a and 6.15b. The A-/E- and E-/E- ratios are calculated by dividing the brightness temperature measured for the feature III (A-) and IV (E-) by the brightness temperature observed for the line I (A-). The results from desorption of pure $CH_3OH$ ice (blue curves) and binary ice (red curves) are plotted for each ratios.

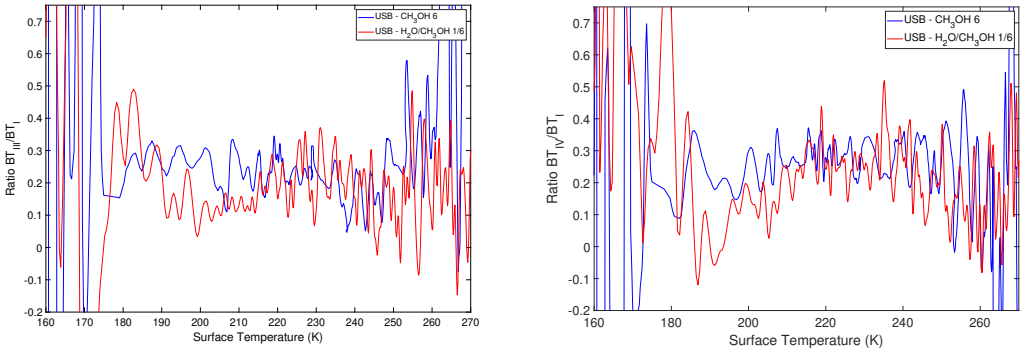


(a) (b)

Figure 6.15: Ratio calculated between line III and I (6.15a) and line IV and I (6.15b) for $CH_3OH6$ THz-DES (blue curve) and $H_2O/CH_3OH1/6$ (red curve) experiments in the USB.

For pure methanol (blue curves), the ratios for A-/E- and E-/E- (from Fig. 6.15a and Fig. 6.15b) present similar variations as the surface temperature increases. The transitions ratios are between 0.2 - 0.3 over the desorption process from 170 K to 250 K. After 250 K, no intensity are measured for line III and IV, resulting to undetermined ratios. Up to 190 K, ratios for $H_2O/CH_3OH$ 1/6 configuration (red curves) are noisy and undetermined. This is due to the fact that desorption of methanol did not yet occur for a binary system. This is confirmed via the results analysed in Fig. 6.14, their brightness temperatures are within the noise floor. In Figure 6.15a the A-/E- ratio appears lower in the binary configuration than for pure ice between 185 to 215 K, 0.1 against 0.25 for pure ice. Between 215 and 240 K, the ratio goes from 0.1 to 0.25 for binary configuration, same as calculated for pure ice. In Figure 6.15b the binary ratios (red curve) increase from 0 to 0.2 between 185 and 215 K. This is due to an observed desorption delay compared to pure ice at this frequency. Between 215 and 240, pure and binary ices present the same E-/E- ratios. Surface temperatures between 240 K to 265 K correspond to the first part of the methanol co-desorption with water. After 260 K, although the co-desorption is still happening, the signal observed at lines III and IV are too weak and undetectable resulting in undefined ratios. Due to the noise measured for low intensity spectral features, it is difficult to determine

the preference of A- or E- transitions.

## 6.6 Conclusion

Two binary systems configurations were deposited, thermally desorbed and analysed with the THz-DES experiment. The first one was nitrous oxide combined with water, the second one methanol with water. These two binary systems configurations were studied either in a configuration of layers or mixed together before deposition. The main conclusions are as follows:

- THz-DES is able to analyse molecular interactions within the ice by observing their signals in the Terahertz frequency range while sublimating.
- THz-DES is able to observe weak or strong spectral lines of any molecules provided they are within the experiment's spectral range.
- The amount of molecules deposited during 'one deposition exposure time' is around $5.10^{21}$ molecules, $10.10^{21}$ molecules and $2.10^{21}$ molecules respectively of $N_2O$, $H_2O$ and $CH_3OH$.
- $N_2O$ - $H_2O$ results:
    1. $N_2O$ and $H_2O$ do not interact in the solid phase. Only their multilayer desorption signals are observed for both molecular types at their respective sublimation temperature.
    2. The thickness of water ice forming $N_2O/H_2O$ layer has no impact on the desorption characteristic.
    3. Desorption activation energies for layers and mixed configurations are within the errors corresponding the values measured for pure ice desorption in Chapter 5.
- $CH_3OH$ - $H_2O$ results:
    1. Thermal desorption of $CH_3OH$ - $H_2O$ presented the same trends and characteristics as TPD measurements from the literature [34, 316].

Methanol, with a lower sublimation temperature than water, diffuses through the water ice. $CH_3OH$ are trapped within the solid $H_2O$ and H-bonds between $CH_3OH$ and $H_2O$ appear stronger than the binding of $CH_3OH$-$CH_3OH$. The impact on the THz-DES curve is that remaining methanol molecules are co-desorbing with water at a higher surface temperature than that of pure methanol ice.

2. Ice thickness does not impact the desorption of the molecules. The increasing trend observed in the brightness temperature are similar for $CH_3OH$ and $H_2O$ for any ice thickness.
3. The heating rate on the surface of the trap was changed. Its impact on the desorption was observed with THz-DES. Only the THz-DES spectra, desorbing at high-surface temperature, were shifted due to a high amount measured in the gas phase while the temperature increased. Heating did not change the desorption energy but it did affect the speed of diffusion of molecules though ice layers.

- Spectroscopic results:

1. THz-DES of A- and E- spectral lines were compared for pure $CH_3OH$ 6 and $H_2O/CH_3OH$ 1/6. Co-desorption was observed even if water features is not directly detected.
2. Comparison of A-/E- ratios and E-/E- ratios for pure and layered configurations could bring information about the preferentially rotational transitions during the thermal desorption. Moreover, some variation may also appear within the same spectroscopic group A- or E-.

Desorption activation energies could be calculated on the different observed transitions, giving an estimated value of the apparent desorption energy for the corresponding experiment. The number of molecules corresponds to the overall amount of molecules desorbing from the surface, emitting the measured brightness temperature at a specific frequency. Comparing the calculated N values between

spectral line may give an approximation of the differences of populations observed in a non-LTE environment. Care should be taken when analysing weak lines or with high noise floor around the desorption temperature. The uncertainty is coming from:

1. Weak spectral line observed.
2. Noise within the measurement around the desorption temperature and fitting errors on the corresponding curves($\delta E_{av}$).
3. First fit: Gaussian ($R_N^2$).
4. Second fit: Exponential ($\delta E_{nom}$).

THz-DES offers a unique way to analyse the thermal desorption of binary ice systems. It has demonstrated its capacity to reproduce well determined TPD results through the TPD-like trends and the calculation of the desorption activation energy. It appears that THz-DES is a promising technique which can detect a variety of spectral features, such as the ALMA telescope. This enables the observation of molecular species which would have formed within the ice providing these new components have their spectral features within the frequency range of the instrument. The spectral ratios information, in this Chapter methanol A- and E- lines, can be characterised to determine if the desorption and/or the molecular interactions within the ice have an impact of the desorption rate of various rotational transitions. Finally, a comparison of those ratios can be carried out for different ice configurations, or desorption mechanisms, for example, to increase our knowledge on various ratios observed in space. The instantaneous observable bandwidth is the key for the final two points as it permits the observation of various spectral features simultaneously. Therefore, it appears that the next step in the development of the THz-DES is to increase the frequency capability of the experiment by developing a new channel, which is presented in Chapter 7.

# Chapter 7

# Conclusions and Future Work

The aim of this thesis was to address the following question:

*Can we design, build and exploit an experiment to emulate the way astronomers detect the gas-phase behaviour of molecules desorbing from interstellar ices, to better understand the gas-ice synergy in interstellar regions? In other words can we build an "ALMA in the Lab"?*

The very existence of this thesis proves that a simple answer to this question is *'Yes'*. The first major challenge, in this work, was to design and build the experiment. The second challenge was to obtain proof-of-concept data, and the third, undertaking a complete data analysis such that the spectroscopic and thermodynamic data obtained could be benchmarked against the existing literature, and show that THz-DES is a viable laboratory astrophysics technique to address questions of astronomical relevance in the future. In this thesis, I have designed and built the THz-DES experiment, combining heterodyne techniques operating in the Terahertz frequency range with laboratory gas-phase spectroscopy and ice-desorption techniques, such that I have indeed realised an 'ALMA in the Lab' during my PhD.

## 7.1 Detailed Conclusions

This section presents some significant findings which relate to the engineering and science undertaken in the course of this PhD. The work presented in Chapter 3 of this thesis demonstrated that it was feasible to combine known radiometric detection techniques with the known experimental procedures for thermally desorbing solid-state materials, to produce gas phase molecules whose spectra could be detected. The transitions studied during this thesis are listed in Table 7.1.

The final THz-DES system I built was composed of 3 main elements:

- a vacuum chamber
- a THz radiometer
- Data acquisition and Processing system

Table 7.1: Selected spectral transitions of $N_2O$, $H_2O$ and $CH_3OH$ for the THz-DES experiment with their corresponding quantum numbers from the JPL catalogue[219].

| **Molecule** | **Frequency (GHz)** | **Quantum Numbers** |
|---|---|---|
| $N_2O$ | 326.556 | $13_{0,0}/12_{0,0}$ |
| $H_2O$ | 325.153 | $5_{1,5}/4_{2,2}$ : Para |
| $CH_3OH$ | 326.631 | $10_{1-}/10_{0+}$ : A |
| $CH_3OH$ | 342.730 | $13_{1-}/13_{0+}$ : A |
| $CH_3OH$ | 344.109 | $18_2/17_3$ : E |
| $CH_3OH$ | 344.312 | $10_2/11_3$ : E |
| $CH_3OH$ | 344.443 | $19_{1+}/18_{2+}$ : A |
| $CH_3OH$ | 345.904 | $16_{1-}/15_{2-}$ : A |

As Chapter 3 demonstrated, spectra were observed replicating the predicted spectral features of the test molecule $N_2O$ in terms of line position, intensity and even pressure-related self-broadening effects on the line-widths. This was a key benchmark going forward to the remainder of the thesis, because the THz-DES experiments rely on accurately 'observing' these spectral parameters from molecules in the gas-phase. The development work undertaken also demonstrated

that the experiment was operational, and proved that emission spectra from gas-phase molecules desorbed from a condensed phase ice could be observed in "real time" during the thermal warm-up of that ice, and spectra plotted as a function of frequency, intensity and 'effective surface temperature' of the ice.

The work in Chapter 4 therefore built on this success, and focused on only gas-phase spectroscopy, with the purpose of characterising the radiometer, specifically (when applied in the THz-DES technique), to demonstrate that the system was sensitive enough to observe molecules desorbing from interstellar ice analogues. The main aim of the work undertaken was to optimise the experimental parameters and understand the noise-limiting and sensitivity issues with the THZ-DES technique. Specifically the work identified four key parameters that were optimised for the largest THz-DES signal in the applications discussed in this thesis:

- *The sampling frequency, LO frequency and Sideband Selection*:

  Typically, the sampling frequency was set at 2.5 GHz. This defined the instantaneous bandwidth over which the molecules could be 'observed' during an experiment (4.5 GHz). However, the sampling frequency was intrinsically linked to the spectral resolution and for faint (or weak) spectroscopic features, low sampling frequency was required. The data with $N_2O$ gas-phase work indicated that the real lineshape of spectral features directly reflected the population of molecules in the observed energy state. This enabled other physical parameters to be determined from the spectral data, such as line broadening effects, line frequencies and desorption energies (as shown in later chapters). The THZ-DES currently was set at a LO frequency of 334.5 GHz. Combined with a sampling frequency of 2.5 GHz, two sidebands are observable LSB = 322.25 - 326.75 GHz used in Chapters 5 and 6 and USB = 342.25 - 346.75 GHz used in Chapter 6. LSB or USB was chosen to detect the spectral features listed in Table 7.1. In this thesis, where well known transitions were exploited, spectral accuracy was

not so important. As indicated later in this Chapter, when THZ-DES is subsequently applied to the search e.g. COM formation, spectral features may not be well known. In those cases, the spectral line positons may be more relevant to identifying chemical processes. Since bandwidth and resolution act in opposition to each other, this suggests that in future experiments where a transition is to be studied for thermodynamic purposes, bandwidth could be sacrificed for resolution and better line profiling. On the other hand, if new species are generated, resolution may be sacrificed for bandwidth in the first instance.

- *The integration time*:

  This parameter defined the amount of averaging on the incoming signal and affected the signal-to-noise ratio. The averaging time is not independent of the heating rate of the ice sample: if the heating of the ice sample occurs too rapidly combined with a long averaging period, thermal or temporal resolution in a dynamic experiment would be decreased significantly. The THz-DES experiment performed in this thesis were all set with 500 ms to generate information to characterise the desorption as a function of the surface temperature with sufficient sensitivity. In the future, it would be possible to conduct experiments observing the desorption in a 'static' mode, as explained in Section 7.3. Phenomena could be set as seen as static over a long period, for example desorbing constantly the same amount of material over time either with photo-desorption or at a constant temperature would permit to increase the integration time. This could be applied to the analysis of desorption plumes, photo-desorption mechanisms or the products of chemical reactions in the solid phase.

- *The Calibration module*:

  An advantage of using a total-power radiometer is its ability to measure the absolute brightness temperature of gas phase molecular species. This

is possible by integrating the instrument with a calibration module made of known blackbody sources. The absolute measurement of the intensity is a very important step for laboratory astrochemistry as the results gathered could be compared directly with radio-telescopes observations. It gives a direct comparison of the amount of molecules, the molecular temperature and the composition percentage from the spectral lines observed.

After describing and characterising the developed experiment, the first THz-DES results were obtained by observing thermal desorption from pure ices of nitrous oxide, water and methanol in Chapter 5. This Chapter demonstrated that the THz-DES retrieved the correct desorption trends of pure ices as studied by the literature. A new approach using spectroscopic features was presented allowing desorption activation energies to be derived from THz-DES data and these results compare well with values in existing literature. The first part of Chapter 6 compared values in the literature to the THz-DES results from combinations of the previously studied molecules (nitrous oxide, water and methanol) in layered or mixed ices. THz-DES results for pure, layered and mixed ices agreed with with values identified in the literature reviewed. This was an important step to follow after designing the experiment as it proves that THz-DES is observing real scientific phenomena and can retrieve corresponding values before new possibilities are explored. The main comparisons were as follows:

- *Pure ice*: $N_2O$, $H_2O$ and $CH_3OH$ were desorbed from ice formed of respectively $5.0 \times 10^{21}$, $12 \times 10^{21}$ and $2 \times 10^{21}$ molecules in a one deposition exposure time procedure. Their sublimation temperature correspond to the literature for a base pressure of $10^{-5}$ mbar, respectively 100 K, 200 K and 170 K. A similar trend to TPD-curves were observed, with the brightness signals increasing as the molecules desorbed and decreasing when desorption ended. The pumping rate became greater than the desorption rate. Once all of the ice sublimated, the brightness temperature measured reached the

noise floor.

- *Desorption activation energy*: A method based on a radiative forward model and the leading edge analysis method permitted to retrieve desorption activation energy. The results obtained were within the order of magnitude of the literature values. For pure ice, the THz-DES values were for 10-14 kJ/mol, 29-33 kJ/mol and 31-33 kJ/mol for $N_2O$, $H_2O$ and $CH_3OH$ compared to values identified in the literature of 17-25, 39-50 and 29-47 kJ/mol. This discrepancy may be explained by the important amount of ice desorbing, limitations on the experimental sensitivity for weak lines like water and/or the retrieval methods uncertainty.

- *$N_2O$- $H_2O$*: Nitrous oxide desorption appears not to be affected by the presence of water molecules in its ice. $N_2O$ diffuse through the ice without being trapped and a single peak was observed at the pure ice sublimation temperature.

- *$H_2O$- $CH_3OH$*: Another result from the literature has been confirmed via the THz-DES experiment. Water and methanol molecules are co-desorbing from layered and mixed ices. This effect is also observed via the THz-DES results.

- *Ice Thickness*: The thickness of the pure ices was increased. THz-DES results showed good agreement to a $0^{\text{th}}$ reaction. This was expected because the desorption trend and desorption energy did not vary with the thickness.

- *Heating Rate*: Although no changes were to expect by changing the heating rate in accordance with the literature. The trend observed corresponded to the literature but a variation was observed when the heating power into the THz-DES cold trap was altered. Although the desorption energies retrieved for methanol were identical, higher values were calculated for higher heating rate. The current proof-of-concept experiment does not have an adequate

heating system to accurately measure the heating rate impact on the desorption. A future upgrade of the experiment would be able to confirm or refute the results obtained.

In the second part of Chapter 6, discrepancies between energy level populations of desorbing species were investigated - predominantly in the A- and E-transitions of methanol. In some cases, there is tenuous evidence to suggests that certain energy levels are under-populated relative to the population expected in LTE (local thermodynamic equilibrium) conditions. It appears that desorption energies may vary between energy states or spin states of molecules. Indeed, observations of methanol A- and E- transitions were obtained investigating pure methanol ice and an ice formed of water and methanol layers. It appeared that when water and methanol were interacting, the desorption energy of A- transitions remained constant and the E- lines calculated energies decreased. A surface interaction constraint can be generated by the interaction of molecules in the ice. The dynamics and internal energy of desorbing molecules has been studied extensively in the past for limited metal surface-adsorbate systems but not in star forming regions.

## 7.2 Future Work: THz-DES Development

Although the main purpose of the thesis has been achieved, the current proof-of-concept experiment has a number of limitations that ideally would be fully addressed before the experiment is used to study further astronomical processes such as non-thermal desorption, ortho-para ratios, A-E ratios in desorbing molecules, formation of complex organic molecules (COMS) and kinetics of complex molecule formation as a function of surface distances[298]. To achieve all these long-term experimental aims, my PhD has highlighted that some significant experimental changes would be required. Here I have detailed those associated with the experimental chamber, sensitivity of the THZ-DES method, specifically the calibration

targets and background signal. Although these changes have not all yet been implemented, significant design and development work have to be considered.

### 7.2.1 THz-DES in UHV

The chamber used for the THz-DES proof-of-concept could be significantly upgraded and make the THz-DES a state-of-the-art astrochemistry experiment. For instance, the current chamber operates at nominal vacuum of $10^{-5}$ mbar and the background pressure contains molecules from either the permeation from the Mylar windows,the chamber walls or the rubber o-ring (see Section 4.4.2). Those molecules (mainly water) would potentially freeze with/onto the ice while its deposition on the cold trap during a THz-DES experiment. Because of this, the purity of the measured ice is not of 100%. Whilst the quantity of molecules is extremely low, it could still impact the sensitive chemistry associate with ice formation or during desorption. The very high pumping speed would prevent any re-adsorption of the desorbing molecules on the icy sample mirroring current TPD experiments (see Section 1.3.2) where desorbed species are pumped away before they are re-adsorbed by the cold surface. Another impact of those background levels would be to broaden the spectral lines of the molecules. Having a system performing under UHV would bring the experimental pressure closer to the one in the dense cloud environment. Depending on the flow rate and temperature of deposition on the cold surface, amorphous ice (ASW) could be grown and its desorption difference with crystalline ice could be analyse in the Terahertz frequency range (see Section 1.2.2).

Figure 7.1 lists the different modifications to be made to obtain a next generation UHV THz-DES chamber. Firstly (a), the rubber o-rings and seals would be change using either vacuum baked O-rings (Fluro or Butyl O-rings) or gasket copper flanges. Their leak rate[59] depends on the permeation rate and out-gassing rate, the lowest the better (as shown in table 7.2). The copper gasket are oxygen

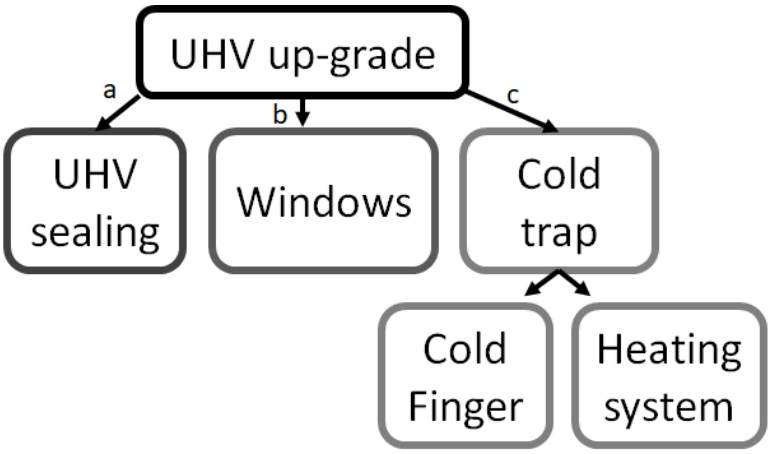


Figure 7.1: Modifications on the THz-DES system in order to have a UHV chamber with increased performances.

Table 7.2: Key parameters of the radiometer which would have a direct impact on the frequency range, spectral resolution or sensitivity of the experiment.

| Material | Permeation Rate $H_2O$tL/sec/lin.cm, 23°C, 50%R.H. | Out-gassing tL/sec/lin.cm, 23°C |
|---|---|---|
| Butyl | $5 \times 10^{-9}$ | $1 \times 10^{-5}$ |
| Nitrile | $1 \times 10^{-7}$ | $1 \times 10^{-6}$ |
| Flouro | $6 \times 10^{-9}$ | $3 \times 10^{-8}$ |

free with leak below $10^{-9}$ mbar l/s. Ideally, these o-rings should be vacuum baked at high temperature to reduce the water out-gassing by an order of magnitude.

Windows (b) are currently made of 50 μm thick Mylar (Section 3.3.1) and leak mainly water inside the chamber (Section 4.4.2) which impact directly the ice formed on the cold trap. Under low pressure they deform and this is observed to increase the amplitude of the standing waves in the background signal (Section 4.3.2). A change in window to an alternative high-transmittance material, for example, .crystal quartz (75%), TPX (95%), HDPE (90 %) or PTFE (95 %) [TYDEX optics], can be considered. Best is coated crystal quartz or coated sapphire windows [Thomas Keating] with good vacuum properties and transmission coefficients, though these are relatively thick and certainly very costly. The best way would be to even remove any front window of the chamber by including the feedhorn of the radiometer inside it. This is described in next Section. In this configuration, vacuum will be UHV and the standing waves will be eliminated or

significantly decreased in intensity.

The last possible upgrade on the THz-DES chamber is to improve the cold trap (c). At the moment, the cold trap (described in Section 3.3.1) is a stainless steel cylinder filled with liquid nitrogen at 77 K, which is the lowest temperature achievable. Once all the nitrogen has evaporated, the temperature rises at an uncontrolled rate to room temperature (see Section 3.3.5) and currently there is no ability to maintain a constant temperature. This limits the desorption experiment. A commercial cold finger system would resolve this issue. The ST-400 Ultra High Vacuum cryostat (from JANIS, Ltd.) could be installed with a temperature range from 2 - 500 K and a nominal temperature stability of 50 mK. It has Si diode temperature sensors and tantalum foil heater. Such systems are commonly used in ice studies or TPD experiments[90] and allow deposition of the molecules at low temperature achieving either amorphous or crystalline ices (see Section 1.2.2). A typical proportional-integrate-derivative (PID) temperature controller can achieve a set-point accuracy of order 0.1 K and a linear ramp or step ramp can be applied to achieve different temperature levels. This will allow observation of the ice desorption at a constant temperature over time and determining with high accuracy the sublimation point.

### 7.2.2 Experiment Sensitivity

Not using a chamber's front window will permits UHV operation and decrease the background temperature. The radiometer feedhorn could be placed inside the chamber, by placing the all front-end receiver inside the cryostat. Vacuum feedthroughs would be used to connect the system power and the IF output to the back-end spectrometer.

Calibration of the radiometer is an important aspect of the experiment arrangement. Although the desorption process can be observed with an uncalibrated instrument, a lack of calibration means no real intensities are measured.

The proof-of-concept system utilised a relatively simple approach as described in Section 3.5 and this is affected by the presence of the vacuum interface windows. The new way was described in Section 4.5 and would permit to have only one cold blackbody target. Desorbed molecules before being pumped away might be seen in the optical path of the hot and cold calibration targets. Therefore not the spectral line would be calibrated out and nothing would be detected. To find a solution to this problem either a double chamber configuration could be used or a more complicated chamber configuration using off-axis parabolic mirrors after the calibration modules. An option is shown in Figure 7.2. The feedhorn located inside the chamber is facing a rotary mirror which can be switch to the cold, hot or scene views as in current THz-DES. In the scene view a parabolic or ellipsoidal mirror can be used to focus the beam above the desorption area with a background target at the rear of the new chamber.

A second method could use an active hot and cold load connected directly to the mixer block. This configuration is known as Dicke-principle[61]. The Dicke method reduces system gain variations. Active cold and hot load can be set at temperature of 120 K and 240 K using high-electron-mobility transistor (HEMT)[310] or monolithic microwave integrated circuit (MMIC)[311] technology. This kind of radiometer presents many advantages and should be seriously considered for the future upgrade. It has the main advantages to be compact as it includes the calibration modules with its first components. There is no risk of having desorbing molecules in the calibration optical path.

A third improvement to boost the sensitivity of the measurement is to include a RF LNA just after the feedhorn and before the mixer block. As explained in Section 2.3.4, the gain of the first components in a mutli-stage systems will have the biggest contributions in the total noise. Therefore having a high gain LNA will significantly decrease the system noise temperature of the receiver. This approach is been used in various radiometric instrument that are currently developed such as the Microwave Sounder (MWS)[232] and the Microwave Imager [160]. The

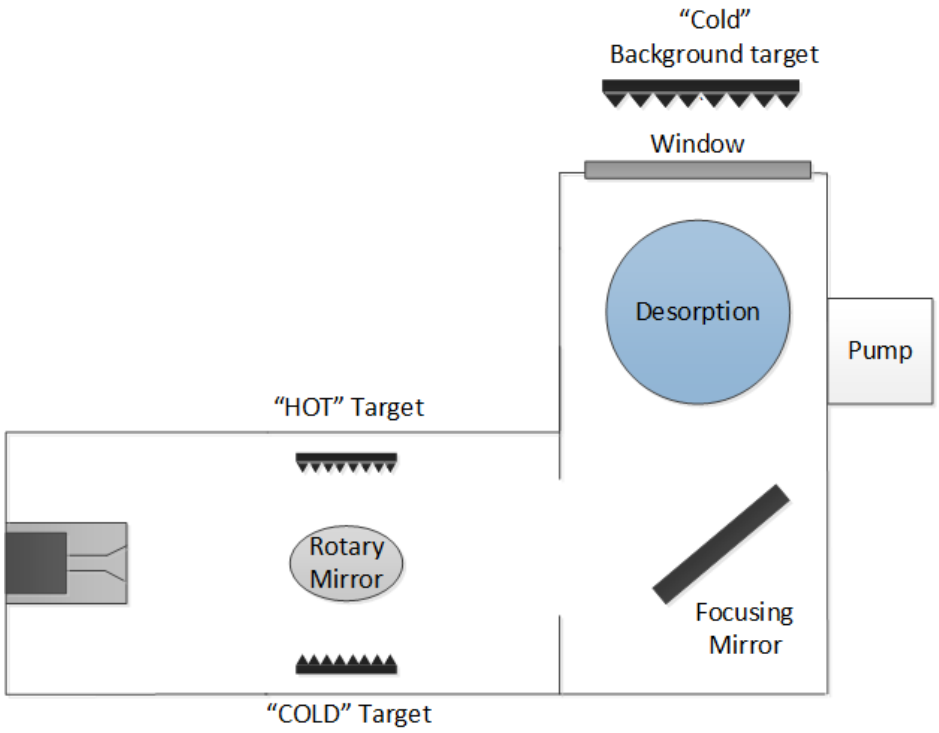


Figure 7.2: One possible configuration of the new chamber when the radiometer feedhorn is located inside the vacuum chamber. The calibration module is also inside the chamber.

sensitivity of the instrument will be improved (Section 4.2.2) which will permit to observe weak lines. To proceed with this change, a significant amount of development in the Terahertz technology side is required. However it would be possible to change the Schottky-barrier mixer with a SIS mixer which has higher sensitivity. SIS mixers have to be cooled to low temperatures. Therefore the design and configuration of the radiometer will be much more complicated.

Finally, measuring the amount of ice desorbing with accuracy is vital. The amount of ice formed for each experiment is necessary for scientific analysis. Two ways could be considered. The first one would be to connect a quadrupole mass spectrometer (QMS) to measure the number of desorbing molecule. This method is commonly used in TPD experiments [50, 53, 90]. Secondly a laser can be set up in order to measure the ice thickness on the cold finger to characterise the ice layer before desorption. The spatial interference of the laser radiation is measured after its reflection on the ice surface giving a measure of the ice thickness [62].

Moreover to have a full understanding of the desorption mechanism, the addition of a quadrupole mass spectrometer as seen in TPD experiments would be useful since this would show what species are inside the chamber.

Those technical improvements on the chamber and radiometer to remove the front-window of the chamber, increase the radiometer sensitivity and measure with accuracy the amount of deposited ice are necessary to optimise the THz-DES experiment. However, the chamber also possesses a rear window which would need to be removed for the same reason as the front window.

### 7.2.3 THz-DES Frequency Range

The main transitions observable in the terahertz region are created from transitions between pure rotational levels of light molecules, higher excited rotational states of complex organic molecules (COMs)[258], low ro-vibrational modes of carbon chain molecules and between energy levels of large molecules [106]. This range of molecular sizes detectable in the terahertz is a key advantage. Small molecules would either be detectable from the interstellar medium where star forms whereas heavy molecules would give insight of hot cores and their surroundings. As explained in Chapter 2, molecules such as $H_2O$, CO, $H_2$, HCN or $CH_2$ will react under various environmental conditions within the ice on dust grains to form more complex molecules. Gas phase molecular composition of hot core reflects the evaporation of these ices by desorption processes. As the chemistry occurring on interstellar grains at low temperature cannot be analysed directly with observations, gas phase molecular tracers are studied to retrieve how molecules have been formed, at which temperature and following which reactions. Deuterated molecules are the perfect candidates for this application. The amount of deuterated species is higher in the cold interstellar medium than the cosmic H/D ratio[184]. This ratio is directly linked to the chemical reactions which happened in the solid phase [238]. Therefore, the deuterated molecules

are the best tracers of dense and cold gas of the densest regions[318]. Molecules such as $N_2D^+/NH_2D$[75], $NH^+/ND$[195] or more recently $c-C_3HD/c-C_3H_2$ [43] or DCN/HCN[131], are a few examples of detectable molecules in the terahertz frequency range by ALMA or SOFIA. For example, the $N_2D^+$ (3-2) was observed at 231.32 GHz [164] and the $N_2H^+$ (4-3) detected with JCMT at 372.72 GHz in two early stage cores to find the dynamics and history of those cores. Another interesting molecule is the hydrogen cyanide, detected for the first time at 88.6 GHz (1-0) in 1971 [272]. Its deuterated molecule, DCN, has been found in higher quantity in the ISM than the H/D cosmic ratio. The H/D ratio is dependent on chemical reaction network [238] occurring in cold, dense interstellar cores. The observation of HCN at high rotational transitions would provide the physical conditions of dust formation region[80]. Finally, the combined detection of molecules could bring more information about ice within proto-planetary disks and solar nebulas. For example, $N_2H^+$ (4-3) is used to determine the CO snow line radius of solar like nebula, as its emission is a tracer of CO depletion[228].

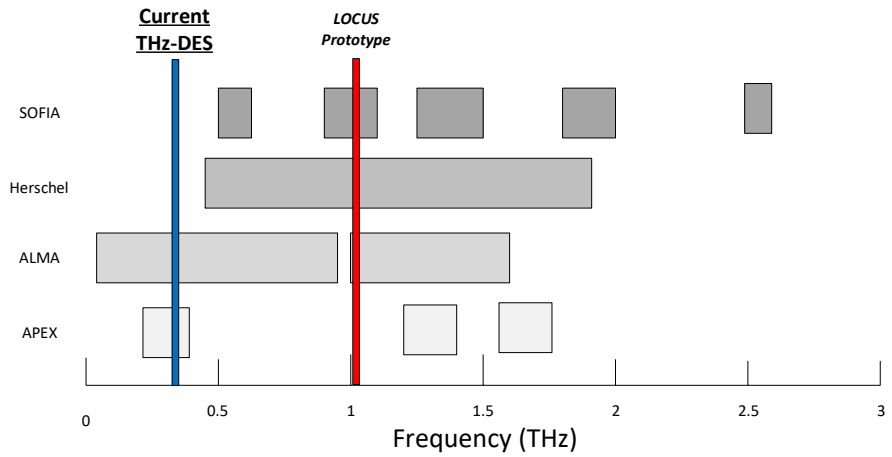


Figure 7.3: Frequency range of various instruments: GREAT, ALMA, SAFARI compared with the THz-DES frequency range and the new radiometer prototype developed at RAL (LOCUS).

Observations in submillimetre wavelengths and terahertz frequencies are now possible from technical developments in radio astronomy for the past decades. With current capabilities, many more molecular rotational transitions can be ob-

served. Some examples of ground based radio telescopes operating in the millimetre and submilimetre wavelength range are ALMA[109] and its pathfinder experiment APEX, the SubMM Array (SMA) and the James Clerk Maxwell Telescope (JCMT). Examples of air-borne and satellite missions are Stratospheric Observatory for Infrared Astronomy (SOFIA), Herschel[218] and SPICA[136, 137]. Future missions such as the Far Infrared Spectroscopic Explorer (FIRSPEX)[237] with 4 frequencies bands (460, 809, 1900, 4700 GHz) or the HERO instrument proposed for the NASA Origins Space Telescope, would bring state-of-the-art sensitivity and spectral resolution dedicated to the observation of multi-phase ISM in the universe as never before. The proof-of-concept THz-DES experiment currently encompasses a fraction of the ALMA band 7 (275 - 370 GHz) from 320 GHz to 350 GHz. Its frequency coverage is shown in Fig. 7.3 and compared to that of major radio-telescopes. With radio-telescope facilities planned, or relatively recently commissioned e.g. ALMA, there is a need to provide a complementary laboratory measurement capability. It is therefore important to extend the frequency range of the THz-DES experiment. The ideal would be the possibility to cover the entire ALMA frequency range but also frequencies above 1 THz where more rotational features are accessible. This would allow, for instance, the H/D ratio within the ice desorption to be studied along with the preferential transitions during desorption, as observed in the previous Chapter, and thus application to higher rotational quantum numbers.

As a step towards achieving the above, a prototype receiver is under development that operates at 1.15 THz for a mission concept called 'LOCUS' [280]. Possessing a similar architecture to the radiometer used in the current THz-DES proof of concept, this new instrument will allow observation of molecules of astronomical interest[204] such as Diazenylium ($N_2H^+$ at 1.117 THz), heavy water (1.158 THz), NO(1.153 THz), HCN(1.151 THz), DCN(1.157 THz) or COMs. A picture of the instrument is shown in Fig. 7.4. It is composed of a local oscillator chain pumping a sub-harmonic mixer at a LO frequency of 573 GHz.

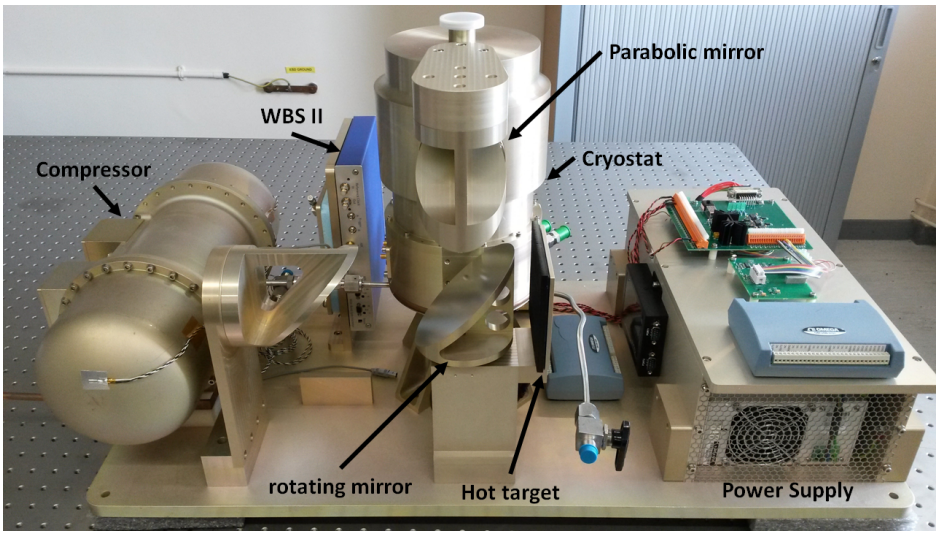


Figure 7.4: Picture of the LOCUS breadboard instrument. Various parts of the radiometer can be seen such as the WBS unit, power supply and cryostat used to cool down the front-end.

The front-end module is cooled down to 60 K inside a cryostat in order to increase its radiometric performances. A similar WBS spectrometer will be used to characterise the radiometer and perform spectroscopic measurements. The development of this prototype is ongoing and will not be discussed within this PhD thesis. More information about the LOCUS prototype instrument could be found in the following articles [74, 116, 231, 249, 281, 295, Zafar et al.].

In the future, a multi-channel radiometer covering a broad frequency range would provide the ideal instrument as it will allow characterisation of gaseous mechanisms and comparison with a wider range of spectral lines of a molecular species. This would allow identification of unknown features observed during desorption with their corresponding molecular origins.

### 7.2.4 Background Signal

The THz-DES background source is composed of a blackbody target placed in a liquid $N_2$ dewar (77 K) (described in Section 3.3). Having this kind of background source with very easy set-up, presents two main disadvantages. The first one is that the liquid nitrogen will boil over a period of time and a lengthy experiment

would be affected. Second problem is its location outside the chamber. A rear window is needed to keep the chamber isolated from the environment. The chamber windows introduce standing wave, described in Section 4.3.2, and increases the background temperature from 77 K to about 130 K. It is interesting to try to minimize the use of windows by integrating the background source inside the desorption chamber.

### 7.2.5 Upgraded THz-DES experiment

Finally, to complete the upgraded THz-DES chamber, a UV-Lamp could be added. This UV-Lamp would be used for non-thermal desorption study (see Section 1.3). Thermal and non-thermal desorption of the same ice configurations would be compared. A schematic of a possible THz-DES is shown in Figure 7.5.

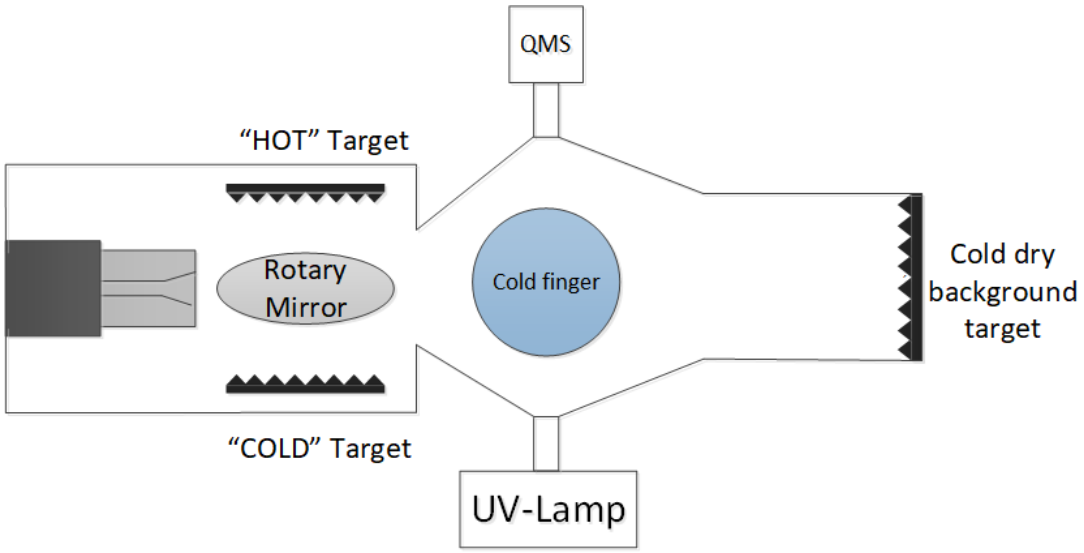


Figure 7.5: Possible schematic of a possible configuration of the new THz-DES experiment. The first difference is the inclusion of the feedhorn and calibration module inside the chamber. Then a QMS is added along with a photo-desorption source. Finally the dry cold load (background signal) is attached to the desorption chamber.

The radiometer, at 350 GHz or above 1 THz, has its feedhorn inside the chamber. The calibration targets can be seen via a rotary mirror. This configuration will need to be carefully designed not to have any desorbing molecules in the calibration path. A commercial cold finger is used to cool down the temperature

of the surface where the ice is grown. The temperature of growth can be controlled with accuracy, lower than the current 77 K. During the heating up, two methods can be selected: linear ramp or stages. A QMS should be installed to know exactly how many molecules are desorbing (depending on the molecules) and therefore how much was deposited on the surface. The background source is a dry cold target placed at the rear of the cell such that the radiometer sees desorbing molecules against that source. Extensive design work is required on the optics and the exact positions of all the components regarding the experiment sensitivity performance and the experiments required to best analyse desorption processes.

## 7.3 Astrophysical Implications

The THz-DES is the first laboratory experiment to observe direct spectroscopic emission of desorbed species in the Terahertz region. The aim of this thesis was to develop, benchmark and calibrate the THz-DES technique with known literature data. upgrade on the current proof-of-concept would help the astronomer community in many ways as THz-DES brings unique and novel observations of spectral features from desorbing molecules. Future THz-DES experiments would generate multiple astrophysical implications.

Firstly, thermal desorption can be analysed from a new perspective. THz-DES could be used alongside the TPD method to compare thermal desorption activation energies to standard method. The desorption activation energy for all spectral features for pure and mixed ices should be measured and characterised with accuracy. Any difference between measurements would allow insight into the preferential behaviours of specific energy states of molecules and the mechanism by which two molecular species interacting in the solid phase impacts those transitions states. New questions could be answered in terms of surface science, such as; do bonding sites preferential energy states during surface dynamics impact

gas phase? How is the ortho-para ratio changing during desorption for various features. How is the ortho-para is evolving in different ices configurations? Similarly, these questions could also apply to the H-/D- ratio or A-/E- ratios and answered with the THz-DES. The results would increase understanding about the origin of the ratios observed in space and which parameters (surface temperature, molecular interactions and rotational preferences) have the greatest impact.

Non-thermal desorption should also be observed using the same mechanism to investigate thermal and non-thermal mechanisms. Implications on the spectroscopic differences between thermal and non-thermal mechanisms could be considerable. Photo-desorption has a very important role in cold star forming regions. The quantification through spectral measurements will benefit the modellers community as it could allow adjustment of desorption energy for numerous species and for various spectral lines. It would be beneficial for astronomers as they could compare their observations with laboratory-based results where parameters are well defined.

THz-DES is able to observe spectral lines over a broad frequency range. Therefore, any unknown molecules can be determined by comparing its signature to spectroscopic databases. With a sensitive experiment, it would be possible to trace the chemical reactions and determine if the chemical product was formed in/on the ice or largely in the gas phase after the desorption mechanism. This is of crucial importance to define how and where complex organic molecules, already observed in the gas phase, are formed.

THz-DES could also be used in order to investigate desorption dynamics. The spectral information observed from desorbing plumes would characterise with high accuracy where any molecules are desorbing. For example, from a mixed ice. It would generate knowledge about the way those molecules spatially desorb and their preferential rotational state. This is important for astronomers as the non-LTE may be directly observed from those experiments and this can be compared with their observations.

The upgrade of the technique in terms of frequency range and sensitivity would bring new insights into the THz-DES results and implications as discussed above. Low intensity signals would be detectable and variation of features intensities determined with greater accuracy. The impact would be the detection of very low numbers of molecules and observation of monolayer ices. Monolayers ices have different properties compared to multilayer ice as monolayer molecules predominantly bond with the substrate. Moreover, in space, due to the low density of molecules, monolayers ices are believed to be found in larger quantity than thick ices. A broad frequency range covering the entire Terahertz spectrum would be ideal as no limitation of the atmospheric attenuation exists. However, it is not possible to combine all the observations at all frequencies in a single radiometer. The advantages of this extension would be the characterisation of all previous experiments (thermal, non-thermal desorption, spectroscopic preferential behaviour studies, chemical reactions in ices or desorbing plumes shapes) at all frequency for many molecular species. Those information would be useful for careful comparison with observations of similar phenomena happening in space.

## 7.4 Concluding Remarks

This work has produced the first laboratory based experiment observing the thermal desorption process via emission spectroscopy in the Terahertz frequency range. Our instrument uses a heterodyne radiometer operating between 320-350 GHz in single sideband detection mode, in combination with a vacuum desorption chamber, dosing line and cold trap to freeze and then thermally desorb molecules from the solid to the gas phase. The instrument acquires, with high spectral resolution, the absolute intensity emitted by the rotational energy transitions of those molecules. The results obtained via our proof-of-concept apparatus illustrate the capability of the THz-DES technique. Nitrous oxide, water and methanol thermal desorption described in this thesis have shown a good agreement with values

in the literature. The next steps will involve increasing the frequency range of the instrument to allow observation of more spectral features from different molecules observed in space and upgrade the entire system to transition from a proof-of-concept experiment to cutting-edge laboratory experiments. The THz-DES experiment offers a unique way to observe the desorption mechanism. Many experiments based on the work from this thesis can be considered for future development. For example, applying THz-DES to thermal and non-thermal desorption processes, characterising the desorption energies for all available transitions for more molecules and releasing a THz-DES catalogue based on those results. Finally, it would be possible to characterise desorption plumes as molecules are spatially desorbing from the surface and by measuring spectral signals to determine if COMs are formed within the ice before desorption or as they come out of the icy surface. This thesis represents a first and important step towards the development of the THz-DES technique, and its unique capability to understand desorption mechanism from a spectroscopic perspective.

# Appendix A

# Desorption Energy Analytical Methods

## A.1 Method 1

This first method consists of retrieving the derivative of $N_t$, the number of molecules (N) plotted against the experimental time by fitting the curve when desorption occurs with an exponential fit. The result is then plotted over 1/T and another exponential fit is applied in order to retrieve the desorption energy such as $\frac{dN}{dt}(1/T) = A \times \exp(B/T)$, with $B = -E_{des}/R$.

Firstly, $N_t$ is fitted with an exponential function over the experimental time when desorption starts, such that $N_t(t) = a_t \times \exp(b_t \times t)$. The red curve in Figure A.1 is the fit applied from a surface temperature of $T_s = 78.2$ K at 68 s up to $T_i = 198$ K at 870 s. A full range of fitting over the desorption time was studied to characterise the impact of the fitting process on the desorption energy, by keeping the starting point fixed and changing the end-of-fit point from $T_{f1} = 180$ K to $T_{f2} = 210$ K. The fitting functions obtained ($N_{fit} = a_t \times \exp(b_t \times t)$) were derived to obtain $dN_{fit}/dt$ which was then plotted as a function of 1/T (Equation 5.21) and fitted with another exponential function : $\frac{dN_{fit}}{dt}(1/T) = A \times \exp(B/T)$,

giving $E_{des} = -B \times R$.

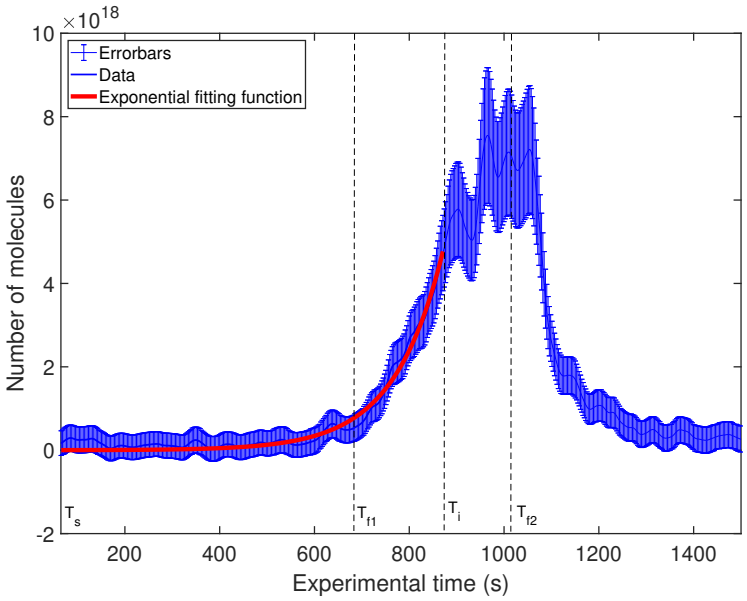


Figure A.1: Fitting of N=f(time). The number of molecules, N, (blue curve) is fitted with an exponential function (red curve). Many fit functions were studied by varying the end-of-fit $T_i$ between $T_{f1}$ and $T_{f2}$.

Figure A.2 shows the desorption energy for methanol, with Method 1, as a function of the maximum temperature used for the fitting procedure ($T_{f1}$ = 180 to $T_{f2}$ = 210 K). The desorption energy increases from 5 to 30 kJ/mol between $T_i$ = 180 to $T_1$ = 190 K. The number of molecules desorbing between those surface temperatures was very low. The fitting of N is not well matched impacting the coefficient in the exponential, and by consequence the desorption energy calculated. Between $T_1$ = 189.5 K and $T_2$ = 201 K, the desorption activation energy is $29.8 \pm 0.7$ kJ/mol. After $T_2$ = 201 K, the desorption rate decreases because BT reaches a plateau. Therefore, a mismatch between the fitting curve and the data is observed causing the decrease of the exponential slope, or the desorption energy.

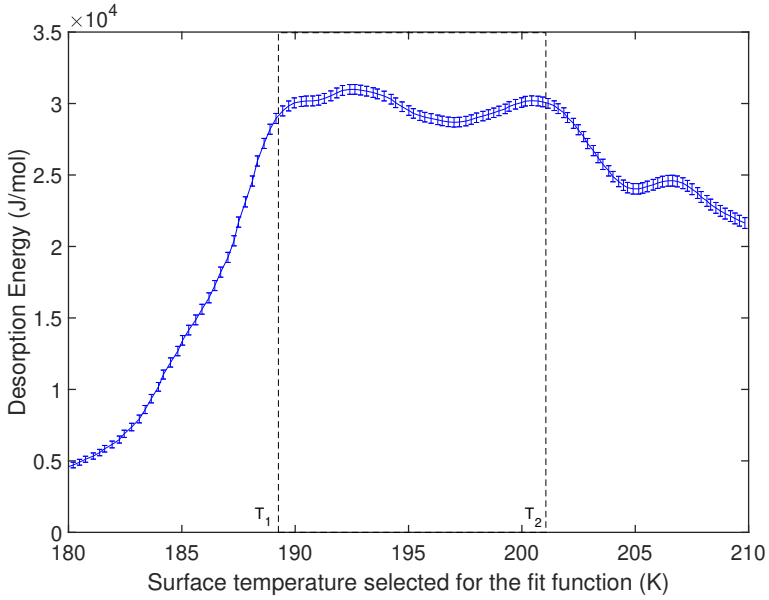


Figure A.2: Desorption energy calculated by deriving the exponential fitting function, plotting it over 1/T and applying a second exponential fit. The x-axis represents the range of surface temperatures over which the fitting process was applied ($T_{f1}$ to $T_{f2}$).

The first exponential fit of N(t) could be selected for a range of surface temperature up to 201 K with a correlation coefficient of 0.9709. This new function is then plotted over 1/T and fitted with another exponential using a fitting range from 77 K to 180 - 196 K. The mean correlation coefficient for those fits is $R^2 = 0.9960 \pm 9.10^{-4}$, giving a desorption energy of $E_{des} = 24.5 \pm 2.6 \times 10^{-3}$ kJ/mol.

Method 1 has the advantage of being able to fit mathematically to the Polanyi equation using exponential fitting functions. The main disadvantage is the propagation of the uncertainty using a 2-steps fitting mechanism. Moreover, it appeared that N(t) does not correlate perfectly with the exponential trend over its complete desorption.

## A.2 Method 2

Method 2 is based on a double fitting mechanism, as seen for Method 1, but using other fitting functions. The first step in this method is to apply a Gaussian

function to the THz-DES number of molecule. The Gaussian function $N_{gaussian}(t)$ used is shown in Equation A.1 with a, b, c the fitting parameters, and t the experimental time (s).

$$N_{gaussian}(t) = a \times \exp\left(-\left(\frac{t-b}{c}\right)^2\right) \tag{A.1}$$

Ngaussian(t) is then derived to mirror the desorption rate according to the Polanyi-Wigner Equation 5.2. The calculated $\frac{dNgaussian(t)}{dt}$ is plotted as a function of $\frac{1}{T_{surface}}$ and an exponential fitting function is applied in order to retrieve the desorption activation energy as seen previously.

Figure A.3a shows the Gaussian fit (red curve) applied to N(t) (blue curve). The fitting coefficients, from Equation A.1, are $a = 1.943 \times 10^{19}$, $b = 1152$, $c = 227.8$ with a correlation coefficient of $R^2 = 0.9927$. A value of $R^2 = 1$ would explain all the variability of the data around its mean values. $\frac{dNgaussian(t)}{dt}$ plotted as a function of 1/T is shown in Figure A.3b. The fitting range was selected from 80 K to the final fitting temperature ($T_f$) from $T_1 = 176.7$ K to $T_2 = 200.9$ K. The red curve in Figure A.3b is the exponential fitting function applied on dN/dt(1/T) so as to calculate the desorption energy.

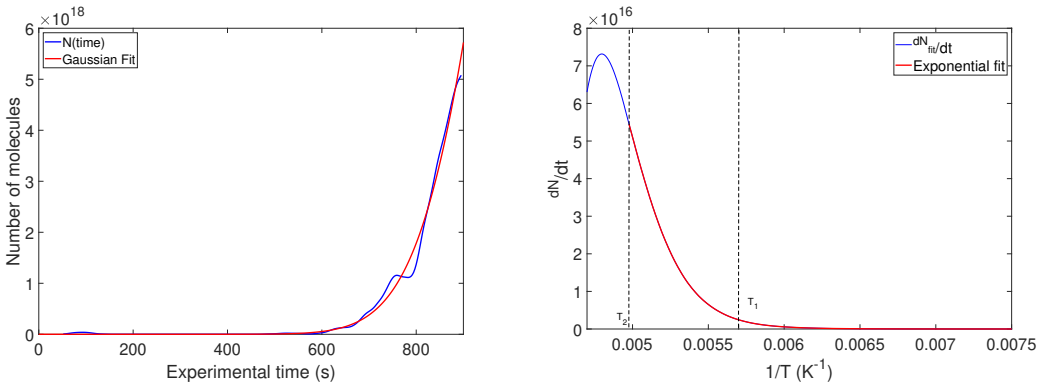


(a) N=f(time) (b) dN/dt=f(1/T)

Figure A.3: Figure A.3a shows the number of molecules fitted with a Gaussian function. In Figure A.3b, the derivative of the fit dN/dt is then plotted as a function of 1/T (blue curve) and fitted with an exponential function (red curve) between two end-of-fit temperature: $T_1$ and $T_2$.

The desorption activation energy of methanol using this method is plotted in

Figure A.4. The x-axis represents the temperature range used when applying the exponential fit. For $T_f$ higher than 182 K, $R^2$ starts to decrease, errorbars increase which means that the exponential function applied does not correlate well to the data. The maximal $R^2$ was found at $T_{surface} = 177.0$ K with a value of $R^2 = 0.999956$. The desorption energy at that point is $E_{des} = 32.4 \pm 0.05$kJ/mol. It is possible to calculate the desorption mean value for $T_f$ is between 177.3 and 193.9 K giving a desorption energy is $32.2 \pm 1.1$ kJ/mol with a $R^2 = 0.9992 \pm 1.1 \times 10^{-4}$. When averaging with the brightness temperature sensitivity, the desorption energy becomes $32.2 \pm 3.3$ kJ/mol.

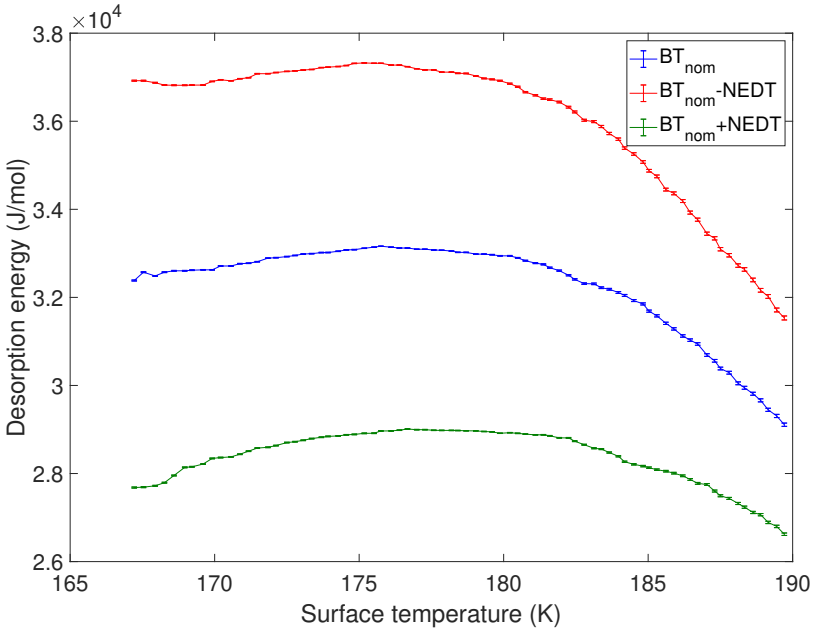


Figure A.4: Calculated methanol desorption energies using the 'raw' N data (blue) and the smooth data corresponding to the red and green curves which corresponds to the number of molecules plus (green) or minus (red) the BT sensitivity.

Although this method do not propagate the error from the measurement of the number of molecules, the Gaussian functions do match the desorption curve. The Polanyi-Wigner Equation is followed so as to calculate the desorption rate and the exponential fits have good correlation coefficients. This makes Method 2 a strong candidate to apply because of its simplicity and efficiency to calculate the desorption energy.

## A.3 Method 3

Method 3 was introduced because Method 1 was using a succession of fit propagating fitting errors impacting the determination of the desorption energy, and minimising the impact of the fit on N. For this method, the number of molecules is defined by Equation A.2, as a function of $g(t) = \frac{1}{T(t)}$.

$$N(t) = A_t \times \exp(B_t \times g(t)) \tag{A.2}$$

The derivative of N(t), $\frac{dN(t)}{dt}$, is calculated as shown on Equation A.3. Then replacing g(t), plotting $\frac{dN}{dt}$ as a function of 1/T and fitting it with an exponential corresponding to Equation 5.2, gives the desorption energy.

$$\frac{dN(t)}{dt} = A_t \times B_t \times \frac{dg(t)}{dt} \times \exp(B_t \times g(t)) = B_t \times \frac{dg(t)}{dt} \times N(t) \tag{A.3}$$

The first step was to calculate $\frac{dg(t)}{dt} = \frac{d1/T)}{dt}$. Figure A.5a and A.5b correspond respectively to $g(t) = \frac{1}{T(t)}$ and $\frac{dg(t)}{dt}$. As the surface temperature increases over time, it is expected to observe a downward slope as soon as the desorption starts at 75 s. Figure A.5b shows the derivative of $g(t) = \frac{1}{T(t)}$, the term $\frac{dg(t)}{dt}$ from Equation A.3. g(t) is decreasing over time as the surface temperature increases.. Moreover, the absolute values of $\frac{dg(t)}{dt}$ decrease over time as the slope of 1/T is steeper at the beginning of the experiment.

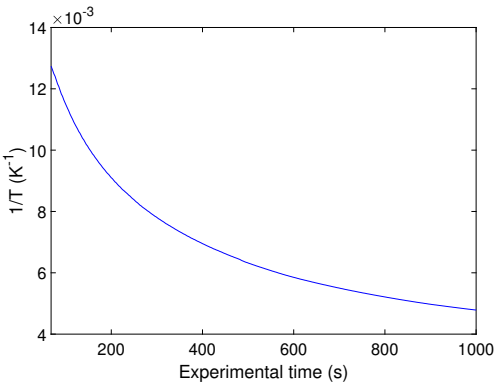


(a) 1/T = g(t)

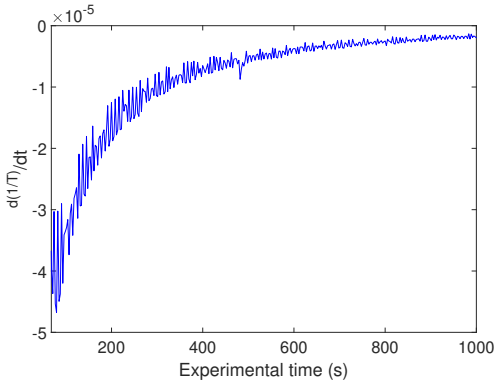


(b) d(1/T)/dt = $\frac{dg(t)}{dt}$

Figure A.5: The inverse of the surface temperature g(t) = 1/T as function of the experimental time is shown in Figure A.5a. Its derivative is caculated ($\frac{dg(t)}{dt}$) and plotted in Figure A.5b.

The second step was to multiply the obtained $\frac{dg(t)}{dt}$ by N and the constant $B_t$ from Equation A.3. $B_t$ is the exponential factor in N(t) and $B_t$ values were taken from the first fit (N as a function of time) of Method 1. Between $T_1$ = 189.5 K and $T_2$ = 201 K, the mean value of $B_t$ is $-3.70 \times 10^{-3} \pm 3.10^{-2}$. The results of dN/dt(1/T) over 1/T are shown in Figure A.6. An exponential fit is then applied to retrieve the negative exponential factor corresponding to $E_{des} = -B \times R$.

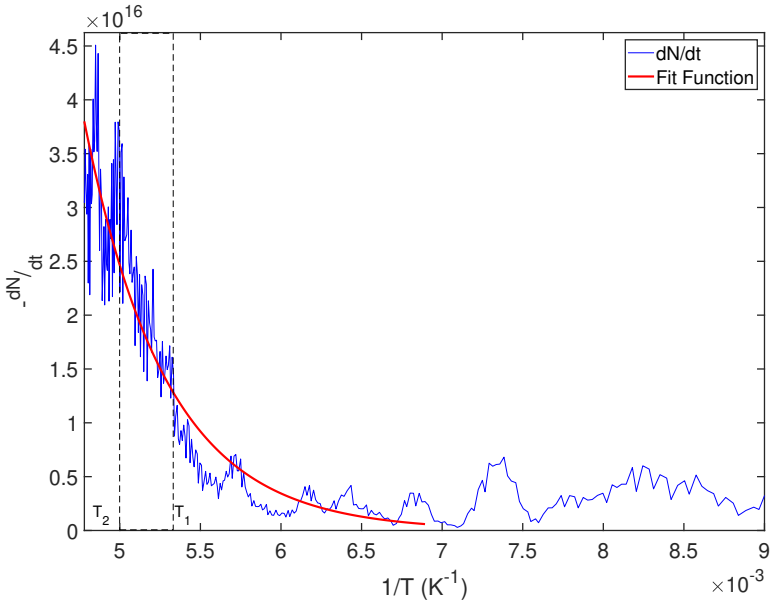


Figure A.6: dN/dt has been calculated by a fitting exponential factor ($B_t$) from N(time), the number of molecules (N) and $\frac{dg(t)}{dt}$ from Figure A.5a as a function of 1/T . The red curve is the exponential fit used to calculated $E_{des}$.

Another way is to apply a logarithmic function to the calculated dN/dt(1/T), as shown in Figure A.6. This is similar to the leading edge analysis characterised by Equation 2.47. In this case, a linear curve should be observed and the slope B (in Equation A.4) should be equal to $B = -E_{des}/R$.

$$\ln(-dN/dt) = \ln(\nu) - \frac{E_{des}}{RT} = A - B \times \frac{1}{T} \tag{A.4}$$

Figure A.7 shows ln(-dN/dt) as a function of 1/T. The linear fit applied was calculated using the weight (error bar) at each point. The end temperature selected to apply the fitting function (red curve) was increased from $T_1 = 189.5$ K to $T_2 = 201$ K with a starting temperature of $T_{start} = 165$ K.

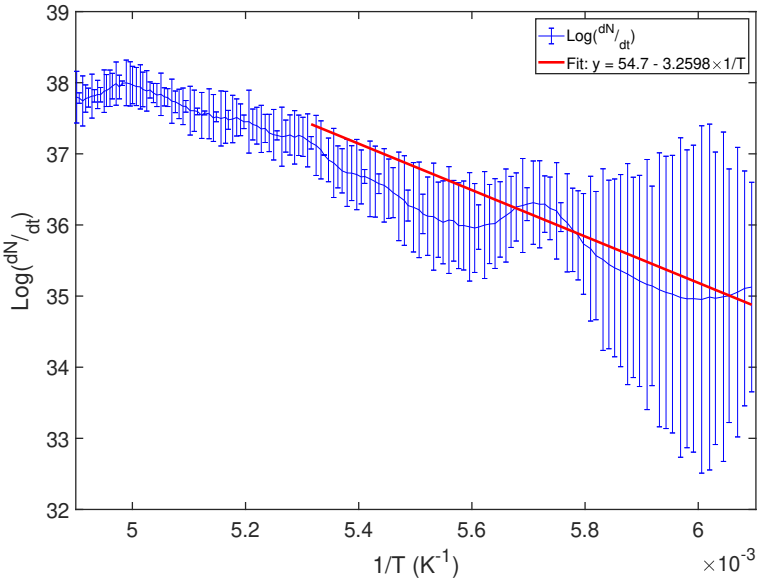


Figure A.7: Leading edge analysis calculation fitting Log(dN/dt)(blue curve) with a linear curve (red) such that Log(dN/dt) = a/T + b.

The results of the desorption activation energy using the exponential (blue curve) and the leading edge (red curve) fittings are shown in Figure A.8. For increasing the fitting range from $T_1 = 189.5$ K to $T_2 = 201$ K does not impact the desorption energy significantly. The exponential fitting gives a desorption activation energy of $23.2 \pm 2.6$ kJ/mol which is the mean value of the calculated desorption energy between 189.5 and 201 K. The leading edge fitting for this

method presents a desorption energy of $23.3 \pm 1.6$ kJ/mol.

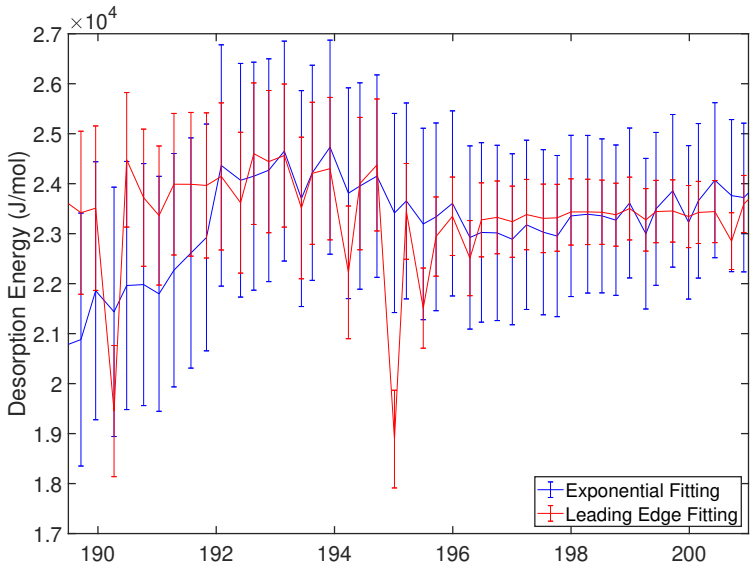


Figure A.8: $E_{des}$ calculated using Method 3 with exponential fit (blue curve) or the leading edge analysis (red curve). $E_{des}$ was calculated between 18 and 27 kJ/mol.

This method is the best mathematically in terms of the calculation of dN/dt using the heating rate data. The uncertainty due to the fit process occurs only at the last stage. The disadvantage of this method is the noise observed at low surface temperatures (high 1/T) in Figure A.6. This makes the fitting process complicated and not very reliable. even using the leading edge analysis.

## A.4 Method 4

This method was based on the approximation of a linear heating rate applied on the exponential properties of the desorption rate from the Polyani-Wigner Equation 5.2. The function N(1/T) and dN/dt(1/T) will have the same exponential coefficient. Therefore, by fitting N(1/T) with the function $f(1/T) = A \times \exp(B \times 1/T)$, the coefficient B is obtained and the desorption energy is calculated such that $B = -E_{des}/R$. Similar to Method 2, it is possible to perform the analysis using the exponential fitting function on N(1/T) or applying

the leading edge process and fitting ln(N(1/T)). The slope of the leading edge is $B = -E_{des}/R$.

Figure A.9 shows the exponential fitting mechanism on retrieved number of molecules, N (blue curve). The red curves is the fitting function for a certain temperature ranges. $T_1$ and $T_2$ represent respectively the temperature when desorption just started and when desorption reached the plateau described in Section 5.3.4. The corresponding desorption energy is around 32 kJ/mol for the red curve and 21 kJ/mol for the black curve.

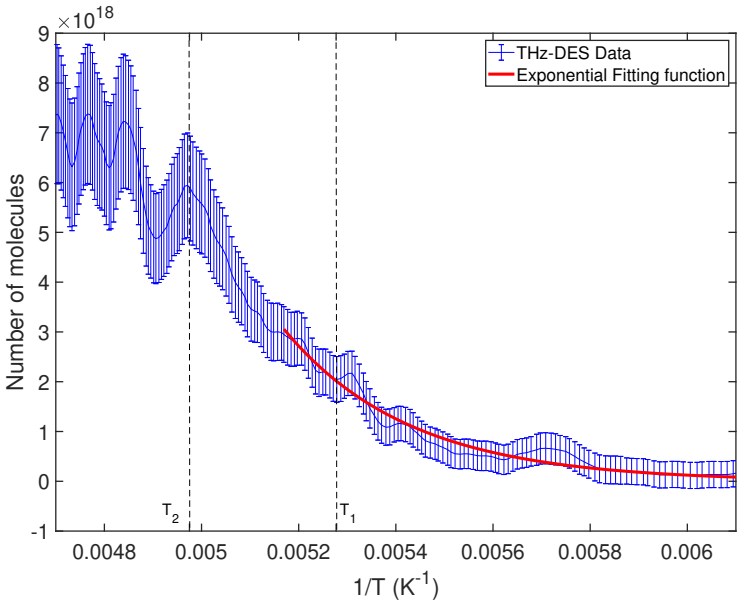


Figure A.9: Number of molecules as a function of 1/T (blue curve) with an exponential fitting function (red curve). The end-of-fit was selected between $T_1$ and $T_2$.

The desorption energies for both mechanisms are shown in Figure A.10. The mean value for the exponential fitting approach is $30.8 \pm 1.1$ kJ/mol whereas it is $26.6 \pm 5.5$ kJ/mol when using the leading edge analysis. The main disadvantage of this method is that it does not account for the non-linear regime of the temperature as a function of the experimental time. Moreover, the difference in results between the exponential fitting process and the leading edge analysis suggests that the fitting mechanism is not ideal.

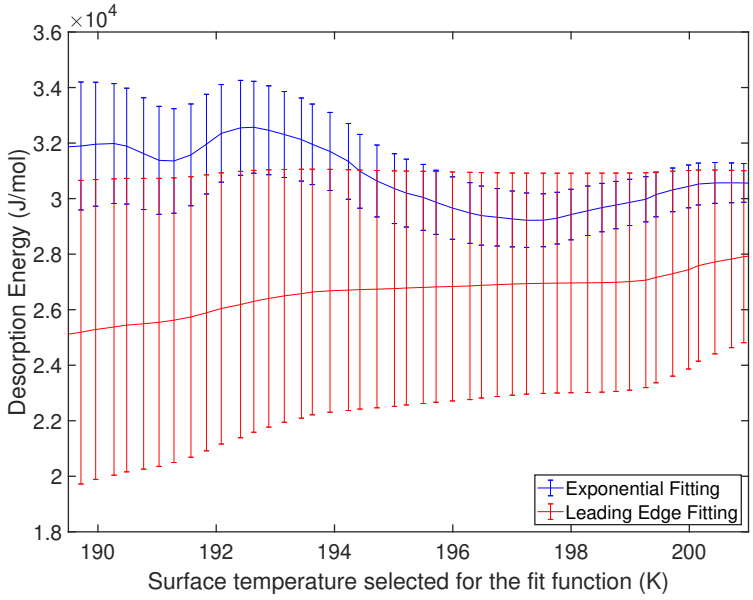


Figure A.10: $E_{des}$ calculated using Method 4 with exponential fit (blue curve) or the leading edge analysis (red curve). $E_{des}$ was calculated between 18 and 36 kJ/mol.

## A.5 Method 5

The last method tested to calculate the desorption energy of methanol using the THz-DES data is based on the Clausius-Clapeyron analysis. During a sublimation process, the vapour pressure increases as a function of the ice surface temperature following the exponential variation. This variation corresponds to the Clausius-Clapeyron equation (Equation A.5), where P is the pressure, A the pre-exponential factor, R the gas constant, T the temperature and $\Delta H_{sub}$ the enthalpy of sublimation. Following the same principle as the leading edge analysis, a linear fit was applied such as log(P)=A-B/T.

$$P = A \times \exp(-\Delta H_{sub}/RT) \tag{A.5}$$

Figure A.11 shows the enthalpy of sublimation calculated using different temperature ranges to apply the fit. For this measurement, $\Delta H_{sub}$ varies between 17 and 31 kJ/mol. The value at 200 K is taken as a reference. The mean value over

the fitting temperature range is $E_{des} = 26 \pm 6$ kJ/mol.

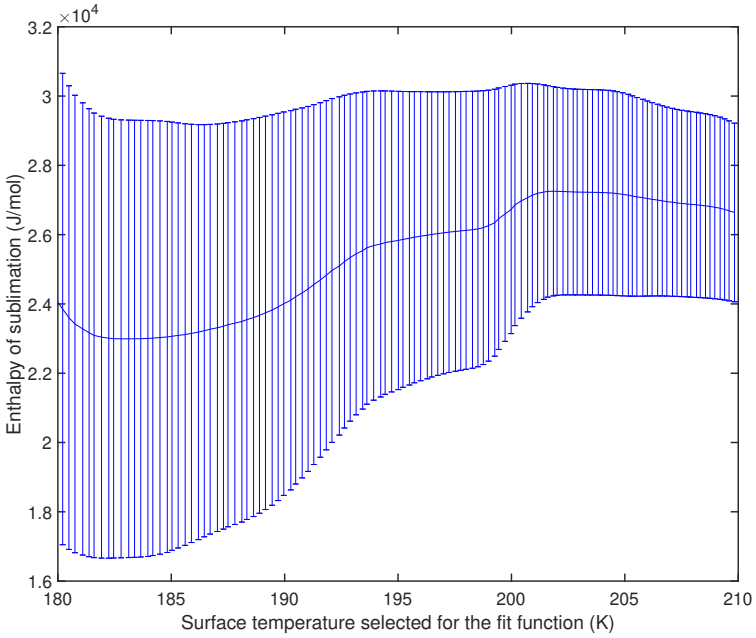


Figure A.11: $E_{des}$ calculated using method 5 with the Clausius-Clapeyron analysis. $E_{des}$ was calculated between 16 and 32 kJ/mol.

This method is using the pressure values instead of analysing the number of molecules desorbing. Therefore one less approximation is taken while calculating the desorption energy. It gives a good estimate of the sublimation enthalpy but the analysis via the desorption rate is more effective and accurate at low pressures.

## A.6 Method Comparison

The desorption activation energy of methanol was calculated using different methods based on the fitting of the desorption rate (-dN/dt) from the Polanyi-Wigner Equation. Five methods were characterised with their advantages and limitations. A summary of the retrieved desorption energy is shown in Table A.1. The range of desorption energies observed on the THz-DES experiment for methanol was measured between 23 and 40 kJ/mol depending on the analytical method selected.

Table A.1: Comparison of the desorption activation energy for $CH_3OH$, one exposure time deposition, using the five methods. $E_{des}$ varies between 26 to 41 kJ/mol depending on the selected method.

| **Method** | **Desorption Energy (kJ/mol)** | **Comments** |
|---|---|---|
| 1 | $29.8 \pm 0.7$ | Exponential Fit |
| 2 | $32.4 \pm 0.05$<br>$32.2 \pm 1.1$ | Max($R^2$)<br>Mean($R^2$ ) |
| 3 | $23.2 \pm 2.6$<br>$23.3 \pm 1.6$ | Exponential Fit<br>Leading Edge |
| 4 | $30.8 \pm 1.1$<br>$26.6 \pm 5.5$ | Exponential Fit<br>Leading Edge |
| 5 | $26 \pm 6$ | $\Delta H_{sub}$ |

All methods have advantages and limitations. For the analysis of all THz-DES data, Method 2 was selected not only because it gives the desorption energy closest to its literature value, but also because of its good correlation coefficient during the fitting process and its ease of use in the data processing routines. Method 2 is applying a Gaussian fit on the converted THz-DES BT in number of molecules. This fitting function is then derived over the time and plotted over 1/T. An exponential fit is then used on the final curves by varying the end of the fitting range. The desorption energy is either calculated from the maximum correlation coefficient or over a range of temperature where desorption occurs.

# Bibliography

[1] Acharyya, K. (2014). Laboratory study of sticking and desorption of $H_2$ and its significance in the chemical evolution of dense interstellar medium. *Monthly Notices of the RAS*, 443:1301–1309.

[2] Acharyya, K., W. Fuchs, G., J. Fraser, H., F. van Dishoeck, E., and Linnartz, H. (2018). Desorption of co and $o_2$ interstellar ice analogs. *http://dx.doi.org/10.1051/0004-6361:20066272*.

[3] Allamandola, L., Sandford, S., and Valero, G. (1988). Photochemical and thermal evolution of interstellar/precometary ice analogs. *Icarus*, 76(2):225 – 252.

[4] Allan, D. (1966a). Statistics of atomic frequency standards. *Proceedings of the Institute of Electrical and Electronics Engineers*, 54(2):221–&.

[5] Allan, D. W. (1966b). Statistics of atomic frequency standards. *Proceedings of the IEEE*, 54(2):221–230.

[ALMA] ALMA. Atacama large millimeter/submillimeter array.

[7] Almeida, G. C., Pilling, S., de Barros, A. L. F., da Costa, C. A. P., Pereira, R. C., and da Silveira, E. F. (2017). Processing of n2o ice by fast ions: implications on nitrogen chemistry in cold astrophysical environments. *Monthly Notices of the Royal Astronomical Society*, 471(2):1330–1340.

[8] Andersson, S., Al-Halabi, A., Kroes, G.-J., and van Dishoeck, E. F. (2006). Molecular-dynamics study of photodissociation of water in crystalline and amorphous ices. *Journal of Chemical Physics*, 124:064715–064715.

[9] Apker, L. R. (1948). Surface phenemona useful in vacuum technique. *Industrial & Engineering Chemistry*, 40(5):846–847.

[10] Arndt, F., Sieverding, T., and Anders, P. (1990). Optimum field theory design of broad-band e-plane branch guide phase shifters and 180 degrees couplers. *IEEE Transactions on Microwave Theory and Techniques*, 38(12):1854–1861.

[11] Auriacombe, O., Fraser, H., Ellison, B., Ioppolo, S., and Rea, S. (2016). Terahertz desorption emission spectroscopy (thz des) - alma in the lab. In *American Astronomical Society Meeting Abstracts #228*, volume 228 of *American Astronomical Society Meeting Abstracts*, page 104.03.

[12] Auriacombe, O., Fraser, H., Ellison, B., and Rea, S. (2015). Desorption emission spectroscopy using thz radiometry (thz des). In *IET Colloquium on Millimetre-Wave and Terahertz Engineering Technology 2015*, pages 1–4.

[13] Ayotte, P., Smith, R. S., Stevenson, K. P., DohnÃąlek, Z., Kimmel, G. A., and Kay, B. D. (2001). Effect of porosity on the adsorption, desorption, trapping, and release of volatile gases by amorphous solid water. *Journal of Geophysical Research: Planets*, 106(E12):33387–33392.

[14] Bally, J. (2016). Protostellar outflows. *Annual Review of Astronomy and Astrophysics*, 54(1):491–528.

[15] Barnes, J., Chi, A., Cutler, L., Healey, D., Leeson, D., MCGunigal, T., Mullen, J., Smith, W., Sydnor, R., Vessot, R., and WINKLER, G. (1971a). Characterization of frequency stability. *IEEE Transactions on Instrumentation and Measurement*, IM20(2):105+.

[16] Barnes, J. A., Chi, A. R., Cutler, L. S., Healey, D. J., Leeson, D. B., McGunigal, T. E., Mullen, J. A., Smith, W. L., Sydnor, R. L., Vessot, R. F. C., and Winkler, G. M. R. (1971b). Characterization of frequency stability. *IEEE Transactions on Instrumentation and Measurement*, IM-20(2):105–120.

[17] Belloche, A., Garrod, R., Muller, H., Menten, K., Comito, C., and Schilke, P. (2009). Increased complexity in interstellar chemistry: detection and chemical modeling of ethyl formate and n-propyl cyanide in Sagittarius B2(N). *Astronomy and Astrophysics*, 499:215–232.

[18] Bergin, E. A., Melnick, G. J., and Neufeld, D. A. (1998). The postshock chemical lifetimes of outflow tracers and a possible new mechanism to produce water ice mantles. *The Astrophysical Journal*, 499(2):777.

[19] Bergin, E. A., Phillips, T. G., Comito, C., Crockett, N. R., Lis, D. C., Schilke, P., Wang, S., Bell, T. A., Blake, G. A., Bumble, B., Caux, E., Cabrit, S., Ceccarelli, C., Cernicharo, J., Daniel, F., de Graauw, T., Dubernet, M. L., Emprechtinger, M., Encrenaz, P., Falgarone, E., Gerin, M., Giesen, T. F., Goicoechea, J. R., Goldsmith, P. F., Gupta, H., Hartogh, P., Helmich, F. P., Herbst, E., Joblin, C., Johnstone, D., Kawamura, J. H., Langer, W. D., Latter, W. B., Lord, S. D., Maret, S., Martin, P. G., Melnick, G. J., Menten, K. M., Morris, P., Müller, H. S. P., Murphy, J. A., Neufeld, D. A., Ossenkopf, V., Pagani, L., Pearson, J. C., Pérault, M., Plume, R., Roelfsema, P., Qin, S. L., Salez, M., Schlemmer, S., Stutzki, J., Tielens, A. G. G. M., Trappe, N., van der Tak, F. F. S., Vastel, C., Yorke, H. W., Yu, S., and Zmuidzinas, J. (2010). Herschel observations of EXtra-Ordinary Sources (HEXOS): The present and future of spectral surveys with Herschel/HIFI. *Astronomy and Astrophysics*, 521:L20.

[20] Bernd Klein, Sabine D. Philipp, R. G. I. K. D. S. (2006). A new generation of spectrometers for radio astronomy: fast fourier transform spectrometer. volume 6275, pages 6275 – 6275 – 12.

[21] Beuther, H., Klessen, R. S., Dullemond, C. P., and Henning, T. (2014). Protostars and Planets VI. *Protostars and Planets VI*.

[22] Black, H. K., van Praagh, G., and Topley, B. (1930). Note on the vapour pressure of solid nitrous oxide. *Trans. Faraday Soc.*, 26:196–197.

[23] Blue, R. W. and Giauque, W. F. (1935). The heat capacity and vapor pressure of solid and liquid nitrous oxide. the entropy from its band spectrum. *Journal of the American Chemical Society*, 57(6):991–997.

[24] Bolina, A. S. (2005). *Adsorption of astrochemically relevant molecules on interstellar dust grain analogue surfaces*. PhD thesis, University of London, University College London (United Kingdom.

[25] Bolina, A. S., Wolff, A. J., and Brown, W. A. (2005). Reflection absorption infrared spectroscopy and temperature programmed desorption investigations of the interaction of methanol with a graphite surface. *Journal of Chemical Physics*, 122(4):044713–044713.

[26] Bonev, B. P., Mumma, M. J., Villanueva, G. L., Disanti, M. A., Ellis, R. S., Magee-Sauer, K., and Russo, N. D. (2007). A search for variation in the h2o ortho-para ratio and rotational temperature in the inner coma of comet c/2004 q2 (machholz). *The Astrophysical Journal Letters*, 661(1):L97.

[27] Boogert, A. C. A., Huard, T. L., Cook, A. M., Chiar, J. E., Knez, C., Decin, L., Blake, G. A., Tielens, A. G. G. M., and van Dishoeck, E. F. (2011). Ice and dust in the quiescent medium of isolated dense cores. *The Astrophysical Journal*, 729(2):92.

[28] Born, M. and Oppenheimer, R. (1927). Zur quantentheorie der molekeln. *Annalen der Physik*, 389(20):457–484.

[29] Bremer, J. C. (1979). Improvement of scanning radiometer performance by digital reference averaging. *IEEE Transactions on Instrumentation and Measurement*, 28(1):46–54.

[30] Brogi, M., Snellen, I. A. G., de Kok, R. J., Albrecht, S., Birkby, J., and de Mooij, E. J. W. (2012). The signature of orbital motion from the dayside of the planet $\tau$ boötis b. *Nature*, 486:502–504.

[31] Brown, J. C., Potts, H. E., Porter, L. J., and Chat, G. l. (2011). Mass Loss, Destruction and Detection of Sun-grazing and -impacting Cometary Nuclei. *Astron. Astrophys.*, 535:A71.

[32] Brown, J. M. and Carrington, A. (2003). *Rotational Spectroscopy of Diatomic Molecules*. Cambridge Molecular Science. Cambridge University Press.

[33] Brown, W. A. and Bolina, A. S. (2007). Fundamental data on the desorption of pure interstellar ices. *Monthly Notices of the RAS*, 374:1006–1014.

[34] Brown, W. A., Viti, S., Wolff, A. J., and Bolina, A. S. (2006). Laboratory investigations of the role of the grain surface in astrochemical models. *Faraday Discuss.*, 133:113–124.

[35] Bryson, C. E., Cazcarra, V., and Levenson, L. L. (1974a). Sublimation rates and vapor pressures of water, carbon dioxide, nitrous oxide, and xenon. *Journal of Chemical & Engineering Data*, 19(2):107–110.

[36] Bryson, C. E., Cazcarra, V., and Levenson, L. L. (1974b). Sublimation rates and vapor pressures of water, carbon dioxide, nitrous oxide, and xenon. *Journal of Chemical & Engineering Data*, 19(2):107–110.

[37] Burke, D. J. and Brown, W. A. (2010). Ice in space: surface science investigations of the thermal desorption of model interstellar ices on dust grain analogue surfaces. *Phys. Chem. Chem. Phys.*, 12:5947–5969.

[38] Burke, P. J., Schoelkopf, R. J., Prober, D. E., Skalare, A., Karasik, B. S., Gaidis, M. C., McGrath, W. R., Bumble, B., and LeDuc, H. G. (1999). Mixing and noise in diffusion and phonon cooled superconducting hot-electron bolometers. *Journal of Applied Physics*, 85(3):1644–1653.

[39] Camps, A. and J., M. T. (2010). Microwave radiometer resolution optimization using variable observation times. *Remote Sensing*, 2(7):1826–1843.

[40] Caselli, P., Walmsley, C. M., Zucconi, A., Tafalla, M., Dore, L., and Myers, P. C. (2002). Molecular ions in l1544. ii. the ionization degree. *The Astrophysical Journal*, 565(1):344.

[41] Chamberlain, J. W. and Hunten, D. M. (1987). *Theory of planetary atmospheres. An introduction to their physics andchemistry.*

[42] Chang, T., Wu, X., and Weng, F. (2013). Metop-b avhrr ir channel postlaunch calibration and verification tests. In Scholl, M. and Paez, G., editors, *Infrared Remote Sensing and Instrumentation XXI*, volume 8867 of *Proceedings of SPIE*.

[43] Chantzos, J., Spezzano, S., Caselli, P., Chacon-Tanarro, A., Bizzocchi, L., Sipila, O., and Giuliano, B. M. (2018). A study of the c-c3hd/ c-c3h2 ratio in low-mass star-forming regions. *The Astrophysical Journal*, 863(2):126.

[44] Charnley, S. B., Tielens, A. G. G. M., and Rodgers, S. D. (1997). Deuterated methanol in the orion compact ridge. *The Astrophysical Journal Letters*, 482(2):L203.

[45] Chen, Y.-J., Nuevo, M., Hsieh, J.-M., Yih, T.-S., Sun, W.-H., Ip, W.-H., Fung, H.-S., Chiang, S.-Y., Lee, Y.-Y., Chen, J.-M., and Wu, C.-Y. R. (2007). Carbamic acid produced by the UV/EUV irradiation of interstellar ice analogs. *Astronomy and Astrophysics*, 464:253–257.

[46] Cheung, A., Rank, D., Townes, C., Thornton, D., and Welch, W. (1969). Detection of water in interstellar regions by its microwave radiation. *Nature*, 221:626–628.

[47] Christmann, K. and Demuth, J. E. (1982). The adsorption and reaction of methanol on Pd(100). I. Chemisorption and condensation. *Journal of Chemical Physics*, 76:6308–6317.

[48] Cieza, L., Casassus, S., Tobin, J., Bos, S., Williams, J., Perez, S., Zhu, Z., Caceres, C., Canovas, H., Dunham, M., Hales, A., Prieto, J., Principe, D., Schreiber, M., Ruiz-Rodriguez, D., and Zurlo, A. (2016). Imaging the water snow-line during a protostellar outburst. *Nature*, 535(7611):258–261.

[49] Cohn, M., Degenford, J. E., and Newman, B. A. (1975). Harmonic mixing with an antiparallel diode pair. *IEEE Transactions on Microwave Theory and Techniques*, 23(8):667–673.

[50] Collings, M., Anderson, M., Chen, R., Dever, J., Viti, S., Williams, D., and McCoustra, M. (2004). A laboratory survey of the thermal desorption of astrophysically relevant molecules. *Monthly Notices of the RAS*, 354:1133–1140.

[51] Collings, M., Dever, J., Fraser, H., and McCoustra, M. (2003a). Laboratory studies of the interaction of carbon monoxide with water ice. *Astrophysics and Space Science*, 285(3):633–659.

[52] Collings, M., Dever, J., Fraser, H., and McCoustra, M. (2003b). Laboratory studies of the interaction of carbon monoxide with water ice. *Astrophysics and Space Science*, 285(3):633–659.

[53] Collings, M., Dever, J., Fraser, H., McCoustra, M., and Williams, D. (2003c). Carbon monoxide entrapment in interstellar ice analogs. *Astrophysical Journal*, 583(2, 1):1058–1062.

[54] Collings, M. P., Dever, J. W., Fraser, H. J., McCoustra, M. R. S., and Williams, D. A. (2003d). Carbon monoxide entrapment in interstellar ice analogs. *The Astrophysical Journal*, 583(2):1058.

[55] Collins, C. E., Pollard, R. D., Miles, R. E., and Dildine, R. G. (1996). On the measurement of ssb noise figure using sideband cancellation. *IEEE Transactions on Instrumentation and Measurement*, 45(3):721–727.

[56] Cornish, J. C. and Avery, N. R. (1990). Adsorption of n2, o2, n2o and no on ir(111) by eels and tpd. *Surface Science*, 235(2):209 – 216.

[57] Cruikshank, D., Roush, T., Owen, T., Geballe, T., De Bergh, C., Schmitt, B., Brown, R., and Bartholomew, M. (1993). Ices on the surface of triton. *Science*, 261(5122):742–745.

[58] Cuppen, H. M., Walsh, C., Lamberts, T., Semenov, D., Garrod, R. T., Penteado, E. M., and Ioppolo, S. (2017). Grain surface models and data for astrochemistry. *Space Science Reviews*, 212(1):1–58.

[59] Daniels, C. C., Braun, M. J., Oravec, H. A., Mather, J. L., and Taylor, S. C. (2017). Leak-rate-quantification method for gas pressure seals with controlled pressure differential. *Journal of Spacecraft and Rockets*, 54(6):1228–1234.

[60] de Jong, A. and Niemantsverdriet, J. (1990). Thermal desorption analysis: Comparative test of ten commonly applied procedures. *Surface Science*, 233(3):355 – 365.

[61] Dicke, R. (1946). The measurement of thermal radiation at microwave frequencies. *Review of Scientific Instruments*, 17:268–275.

[62] Domingo Beltran, M., Luna Molina, R., Satorre Aznar, M. A., Santonja Molto, C., and Millan Verdu, C. (2015). Double laser for depth measurement of thin films of ice. *Sensors*, 15(10):25123–25138.

[63] Draper, D. W., Newell, D. A., Teusch, D. A., and Yoho, P. K. (2013). Global precipitation measurement microwave imager prelaunch hot load calibration. *IEEE Transactions on Geoscience and Remote Sensing*, 51(9, SI):4731–4742.

[64] Drawin, H. W. (1969). Validity conditions for local thermodynamic equilibrium. *Zeitschrift für Physik*, 228(2):99–119.

[65] Drouet, C., Alphonse, P., Fierro, J., and Rousset, A. (2001). Adsorption of nitric oxide and temperature programmed desorption on nonstoichiometric nickel-copper manganites. *Applied Surface Science*, 174(3):289 – 295.

[66] Dudhia, A. (2016). The reference forward model (rfm). 186.

[67] Dudhia, A. (2017). The reference forward model (rfm). *Journal of Quantitative Spectroscopy and Radiative Transfer*, 186:243 – 253.

[68] Dulieu, F., Amiaud, L., Congiu, E., Fillion, J. H., Matar, E., Momeni, A., Pirronello, V., and Lemaire, J. L. (2010). Experimental evidence for water formation on interstellar dust grains by hydrogen and oxygen atoms. *Astronomy and Astrophysics*, 512:A30.

[69] Dulieu, F., Congiu, E., Noble, J. A., Baouche, S., Chaabouni, H., Moudens, A., Minissale, M., and Cazaux, S. (2013). How micron-sized dust particles determine the chemistry of our universe. In *Scientific reports*.

[70] E. H. Rhoderick, R. H. W. (1988). *Metal-semiconductor contacts*. Clarendon Press.

[Ecosorb.] Ecosorb. http://www.eccosorb.comm.

[72] E.Habenschaden, J. (1984). Evaluation of flash desorption spectra. *Surface Science*, 138(1):L147 – L150.

[73] Einstein, A. (1905). ÃIJber einen die erzeugung und verwandlung des lichtes betreffenden heuristischen gesichtspunkt. *Annalen der Physik*, 322(6):132–148.

[74] Ellison, B., Valavanis, A., Auriacombe, O., Rawlings, T., Oldfield, M., Han, Y., Linfield, E., Davies, A., and Saenz, E. (2018). 3.5-thz quantum-cascade laser emission from dual diagonal feedhorns. In *12th European Conference on Antennas and Propagation (EuCAP 2018)*, pages 248 (4 pp.)–248 (4 pp.)(1).

[75] Emprechtinger, M. (2009). Deuterium fractionation as evolutionary tracer of class 0 protostars. In *American Astronomical Society Meeting Abstracts 214*, volume 214 of *American Astronomical Society Meeting Abstracts*, page 760.

[76] Emprechtinger, M., Lis, D. C., Rolffs, R., Schilke, P., Monje, R. R., Comito, C., Ceccarelli, C., Neufeld, D. A., and van der Tak, F. F. S. (2013). The abundance, ortho/para ratio, and deuteration of water in the high-mass star-forming region ngc 6334 i. *The Astrophysical Journal*, 765(1):61.

[77] Emrich, A. (1997). Autocorrelation Spectrometers for Space Borne (sub) Millimetre Astronomy. In Wilson, A., editor, *The Far Infrared and Submillimetre Universe.*, volume 401 of *ESA Special Publication*, page 361.

[78] Emrich, A. (1997). Autocorrelation spectrometers for space borne (sub) millimetre spectroscopy.

[79] Endres, C. P., Schlemmer, S., Schilke, P., Stutzki, J., and Muller, H. S. (2016). The cologne database for molecular spectroscopy, cdms, in the virtual atomic and molecular data centre, vamdc. *Journal of Molecular Spectroscopy*, 327:95 – 104.

[80] Ernicharo, J., Agundez, M., Kahane, C., Guelin, M., Goicoechea, J., Marcelino, N., De Beck, E., and Decin, L. (2011). Probing the dust formation region in irc +10216 with the high vibrational states of hydrogen cyanide. *Astronomy and Astrophysics*, 529:L3.

[81] Evans, II, N. J. (1999). Physical Conditions in Regions of Star Formation. *Annual Review of Astron and Astrophys*, 37:311–362.

[82] Faber, M., Chramiec, J., and Adamski, M. (1995). *Microwave and millimeter-wave diode frequency multipliers*. Artech House microwave library. Artech House.

[83] Falconer, J. L. and Schwarz, J. A. (1983). Temperature-programmed desorption and reaction: Applications to supported catalysts. *Catalysis Reviews*, 25(2):141–227.

[84] Fano, R. (1950). Theoretical limitations on the broadband matching of arbitrary impedances. *Journal of the Franklin Institute*, 249(1):57 – 83.

[85] Fayolle, E. C., Balfe, J., Loomis, R., Bergner, J., Graninger, D., Rajappan, M., and ÃŰberg, K. I. (2016). N2 and co desorption energies from water ice. *The Astrophysical Journal Letters*, 816(2):L28.

[86] Fayolle, E. C., Bertin, M., Romanzin, C., Michaut, X., Oberg, K. I., Linnartz, H., and Fillion, J.-H. (2011). Co ice photodesorption: A wavelength-dependent study. *The Astrophysical Journal Letters*, 739(2):L36.

[87] Fayolle, E. C., Öberg, K. I., Cuppen, H. M., Visser, R., and Linnartz, H. (2011). Laboratory $h_2o$:$co_2$ ice desorption data: entrapment dependencies and its parameterization with an extended three- phase model. *Astronomy and Astrophysics*, 529:A74.

[88] Feistel, R. and Wagner, W. (2007). Sublimation pressure and sublimation enthalpy of h2o ice ih between 0 and 273.16k. *Geochimica et Cosmochimica Acta*, 71(1):36 – 45.

[89] Fraser, H., Collings, M., McCoustra, M., and Williams, D. (2001). Thermal desorption of water ice in the interstellar medium. *Monthly Notices of the RAS*, 327:1165–1172.

[90] Fraser, H. J., Collings, M. P., and McCoustra, M. R. S. (2002). Laboratory surface astrophysics experiment. *Review of Scientific Instruments*, 73(5):2161–2170.

[91] Fray, N. and Schmitt, B. (2009). Sublimation of ices of astrophysical interest: A bibliographic review. *Planetary and Space Science*, 57(14):2053 – 2080.

[92] Friberg, P., Madden, S. C., Hjalmarson, A., and Irvine, W. M. (1988). Methanol in dark clouds. *Astronomy and Astrophysics*, 195:281–289.

[93] Friis, H. T. (1944). Noise figures of radio receivers. *Proceedings of the IRE*, 32(7):419–422.

[94] Frisk, U., Hagström, M., Ala-Laurinaho, J., Andersson, S., Berges, J. C., Chabaud, J. P., Dahlgren, M., Emrich, A., Florén, H. G., Florin, G., Fredrixon, M., Gaier, T., Haas, R., Hirvonen, T., Hjalmarsson, Å., Jakobsson, B., Jukkala, P., Kildal, P. S., Kollberg, E., Lassing, J., Lecacheux, A., Lehikoinen, P., Lehto, A., Mallat, J., Marty, C., Michet, D., Narbonne, J., Nexon, M., Olberg, M., Olofsson, A. O. H., Olofsson, G., Origné, A., Petersson, M., Piironen, P., Pons, R., Pouliquen, D., Ristorcelli, I., Rosolen, C., Rouaix, G., Räisänen, A. V., Serra, G., Sjöberg, F., Stenmark, L., Torchinsky, S., Tuovinen, J., Ullberg, C., Vinterhav, E., Wadefalk, N., Zirath, H., Zimmermann, P., and Zimmermann, R. (2003). The Odin satellite. I. Radiometer design and test. *Astronomy and Astrophysics*, 402:L27–L34.

[95] Fritsche, D., Li, S., Joram, N., Carta, C., and Ellinger, F. (2016). Design and characterization of a 190 ghz voltage-controlled oscillator. In *2016 46th European Microwave Conference (EuMC)*, pages 493–496.

[96] Fuchs, G. W., Acharyya, K., Bisschop, S. E., Öberg, K. I., van Broekhuizen, F. A., Fraser, H. J., Schlemmer, S., van Dishoeck, E. F., and Linnartz, H. (2006). Laboratory experiments on interstellar ice analogs: The sticking and desorption of small physisorbed molecules. In *NASA LAW 2006*, page 73.

[97] Fuchs, G. W., Cuppen, H. M., Ioppolo, S., Romanzin, C., Bisschop, S. E., Andersson, S., van Dishoeck, E. F., and Linnartz, H. (2009a). Hydrogenation reactions in interstellar CO ice analogues. *ArXiv e-prints*.

[98] Fuchs, G. W., Cuppen, H. M., Ioppolo, S., Romanzin, C., Bisschop, S. E., Andersson, S., van Dishoeck, E. F., and Linnartz, H. (2009b). Hydrogenation reactions in interstellar CO ice analogues. A combined experimental/theoretical approach. *Astronomy and Astrophysics*, 505:629–639.

[99] Gallego, J. D., Lopez, I., Diez, C., and Barcia, A. (2006). Alma memo, 560 methods for the characterization and measurement of the gain fluctuations of cryogenic amplifiers.

[100] Garcia-Hernandez, D. A., Rao, N. K., and Lambert, D. L. (2011). Are c60 molecules detectable in circumstellar shells of r coronae borealis stars? *The Astrophysical Journal*, 729(2):126.

[101] Garrod, R., Park, I. H., Caselli, P., and Herbst, E. (2006). Are gas-phase models of interstellar chemistry tenable? The case of methanol. *Faraday Discussions*, 133:51.

[102] Garrod, R. T., Wakelam, V., and Herbst, E. (2007). Non-thermal desorption from interstellar dust grains via exothermic surface reactions. *Astronomy and Astrophysics*, 467:1103–1115.

[103] Garrod, R. T., Widicus Weaver, S. L., and Herbst, E. (2008). Complex Chemistry in Star-forming Regions: An Expanded Gas-Grain Warm-up Chemical Model. *The Astrophysical Journal*, 682:283–302.

[104] Geppert, W. D., Thomas, R. D., Ehlerding, A., Hellberg, F., ÃŰsterdahl, F., Hamberg, M., Semaniak, J., Zhaunerchyk, V., Kaminska, M., KÃďllberg, A., Paal, A., and Larsson, M. (2005). Dissociative recombination branching ratios and their influence on interstellar clouds. *Journal of Physics: Conference Series*, 4(1):26.

[105] Gibb, E. L., Whittet, D. C. B., Schutte, W. A., Boogert, A. C. A., Chiar, J. E., Ehrenfreund, P., Gerakines, P. A., Keane, J. V., Tielens, A. G. G. M., van Dishoeck, E. F., and Kerkhof, O. (2000). An inventory of interstellar ices toward the embedded protostar w33a. *The Astrophysical Journal*, 536:347–356.

[106] Giesen, T. F., Brunken, S., Caris, M., Neubauer-Guenther, P., Fuchs, U., Fuchs, G. W., and Lewen, F. (2005). Terahertz rotational spectroscopy. *Proceedings of the International Astronomical Union*, 1(S231):87–96.

[107] Goldsmith, P. F. (1992). Quasi-optical techniques. *Proceedings of the IEEE*, 80(11):1729–1747.

[108] Goldsmith, P. F., Liseau, R., Bell, T. A., Black, J. H., Chen, J.-H., Hollenbach, D., Kaufman, M. J., Li, D., Lis, D. C., Melnick, G., Neufeld, D., Pagani, L., Snell, R., Benz, A. O., Bergin, E., Bruderer, S., Caselli, P., Caux, E., Encrenaz, P., Falgarone, E., Gerin, M., Goicoechea, J. R., Hjalmarson, Å., Larsson, B., Le Bourlot, J., Le Petit, F., De Luca, M., Nagy, Z., Roueff, E., Sandqvist, A., van der Tak, F., van Dishoeck, E. F., Vastel, C., Viti, S., and Yıldız, U. (2011). Herschel Measurements of Molecular Oxygen in Orion. *The Astrophysical Journal*, 737:96.

[109] Gonzalez, A., Kaneko, K., and Asayama, S. (2017). Receiver optics for alma band 11 (1.25 2013;1.57 thz). In *2017 42nd International Conference on Infrared, Millimeter, and Terahertz Waves (IRMMW-THz)*, pages 1–2.

[110] Gordon, I., Rothman, L., Hill, C., Kochanov, R., Tan, Y., Bernath, P., Birk, M., Boudon, V., Campargue, A., Chance, K., Drouin, B., Flaud, J.-M., Gamache, R., Hodges, J., Jacquemart, D., Perevalov, V., Perrin, A., Shine, K., Smith, M.-A., Tennyson, J., Toon, G., Tran, H., Tyuterev, V., Barbe, A., Csaszar, A., Devi, V., Furtenbacher, T., Harrison, J., Hartmann, J.-M., Jolly, A., Johnson, T., Karman, T., Kleiner, I., Kyuberis, A., Loos, J., Lyulin, O., Massie, S., Mikhailenko, S., Moazzen-Ahmadi, N., MÃijller, H.,

Naumenko, O., Nikitin, A., Polyansky, O., Rey, M., Rotger, M., Sharpe, S., Sung, K., Starikova, E., Tashkun, S., Auwera, J. V., Wagner, G., Wilzewski, J., WcisÅĆo, P., Yu, S., and Zak, E. (2017). The hitran2016 molecular spectroscopic database. *Journal of Quantitative Spectroscopy and Radiative Transfer*, 203:3 – 69.

[111] Gottlieb, C. A., Ball, J. A., Gottlieb, E. W., and Dickinson, D. F. (1979). Interstellar methyl alcohol. *The Astrophysical Journal*, 227:422–432.

[112] Goumans, T. P. M. and KÃďstner, J. (2011). Deuterium enrichment of interstellar methanol explained by atom tunneling. *The Journal of Physical Chemistry A*, 115(39):10767–10774.

[113] Green, S. D., Bolina, A. S., Chen, R., Collings, M. P., Brown, W. A., and McCoustra, M. R. S. (2009). Applying laboratory thermal desorption data in an interstellar context: sublimation of methanol thin films. *Monthly Notices of the Royal Astronomical Society*, 398(1):357–367.

[114] Guillem, M. P. (2010). Multiscale soil moisture retrievals from microwave remote sensing observations.

[115] Halfen, D. T., Apponi, A. J., and Ziurys, L. M. (2001). Evaluating the n/o chemical network: The distribution of n2o and no in the sagittarius b2 complex. *The Astrophysical Journal*, 561(1):244.

[116] Han, Y., Partington, J., Chhantyal Pun, R., Henry, M., Auriacombe, O., Rawlings, T., Li, L., Keeley, J., Oldfield, M., Brewster, N., Rui, D., Dean, P., Davies, A., Ellison, B., Linfield, E., and Valavanis, A. (2018). Gas spectroscopy through multimode self-mixing in a double-metal terahertz quantum cascade laser. *Optics Letters*.

[117] Hardy, W. N. (1973). Precision temperature reference for microwave radiometry (short papers). *IEEE Transactions on Microwave Theory and Techniques*, 21(3):149–150.

[118] Harris, F. J. (1978). On the use of windows for harmonic analysis with the discrete fourier transform. *Proceedings of the IEEE*, 66(1):51–83.

[119] Hayes, D. D. (1966). *High Gain antenna techniques. System gain-to-noise temeprature ratio measurements on an adaptively phased array.* Technical Report No ADC-TR-66-125, Vol I.

[120] Haynes, D. R., Tro, N. J., and George, S. M. (1992). Condensation and evaporation of H2O on ice surfaces. *Journal of Physical Chemistry*, 96:8502–8509.

[121] Hedges, C. and Madhusudhan, N. (2016). Effect of pressure broadening on molecular absorption cross sections in exoplanetary atmospheres. *Monthly Notices of the RAS*, 458:1427–1449.

[122] Henning, J. W., Ade, P., Aird, K. A., Austermann, J. E., Beall, J. A., Becker, D., Benson, B. A., Bleem, L. E., Britton, J., Carlstrom, J. E., Chang, C. L., Cho, H.-M., Crawford, T. M., Crites, A. T., Datesman, A., de Haan, T., Dobbs, M. A., Everett, W., Ewall-Wice, A., George, E. M., Halverson, N. W., Harrington, N., Hilton, G. C., Holzapfel, W. L., Hubmayr, J., Irwin, K. D., Karfunkle, M., Keisler, R., Kennedy, J., Lee, A. T., Leitch, E., Li, D., Lueker, M., Marrone, D. P., McMahon, J. J., Mehl, J., Meyer, S. S., Montgomery, J., Montroy, T. E., Nagy, J., Natoli, T., Nibarger, J. P., Niemack, M. D., Novosad, V., Padin, S., Pryke, C., Reichardt, C. L., Ruhl, J. E., Saliwanchik, B. R., Sayre, J. T., Schaffer, K. K., Shirokoff, E., Story, K., Tucker, C., Vanderlinde, K., Vieira, J. D., Wang, G., Williamson, R., Yefremenko, V., Yoon, K. W., and Young, E. (2012). Feedhorn-coupled TES polarimeter camera modules at 150 GHz for CMB polarization measurements with SPTpol. In *Millimeter, Submillimeter, and Far-Infrared Detectors and Instrumentation for Astronomy VI*, volume 8452, page 84523A.

[123] Henry, M., Worley, R., Willegers, M., Cahill, F., Green, R., Huggard, P. G., Ellison, B., and Winser, M. (2016). Design and development of ground calibration targets for the metop-sg microwave sounder payload. In *2016 41st International Conference on Infrared, Millimeter, and Terahertz waves (IRMMW-THz)*, pages 1–2.

[124] Herbst, E. and Cuppen, H. M. (2006). Monte carlo studies of surface chemistry and nonthermal desorption involving interstellar grains. *Proceedings of the National Academy of Sciences*, 103(33):12257–12262.

[125] Herbst, E. and van Dishoeck, E. F. (2009). Complex Organic Interstellar Molecules. *Annual Review of Astron and Astrophys*, 47:427–480.

[126] Hersman, M. and Poe, G. (1981a). Sensitivity of the total power radiometer with periodic absolute calibration. *IEEE TRANSACTIONS ON MICROWAVE THEORY AND TECHNIQUES*, 29(1):32–40.

[127] Hersman, M. S. and Poe, G. A. (1981b). Sensitivity of the total power radiometer with periodic absolute calibration. *IEEE Transactions on Microwave Theory and Techniques*, 29(1):32–40.

[Hewison and Gaffard] Hewison, T. J. and Gaffard, C. Radiometrics mp3000 microwave radiometer performance assessment. Technical report tr29, Met Office, Observations/Development.

[129] Hogerheijde, M. R., Bergin, E. A., Brinch, C., Cleeves, L. I., Fogel, J. K. J., Blake, G. A., Dominik, C., Lis, D. C., Melnick, G., Neufeld, D., Panić, O., Pearson, J. C., Kristensen, L., Yıldız, U. A., and van Dishoeck, E. F. (2011). Detection of the water reservoir in a forming planetary system. *Science*, 334(6054):338–340.

[130] Hooge, F. (1976). 1/f noise. *Physica B+C*, 83(1):14 – 23.

[131] Huang, J., Öberg, K. I., Qi, C., Aikawa, Y., Andrews, S. M., Furuya, K., Guzmán, V. V., Loomis, R. A., van Dishoeck, E. F., and Wilner, D. J. (2017). An alma survey of dcn/h$^{13}$cn and dco$^+$/h$^{13}$co$^+$ in protoplanetary disks. *The Astrophysical Journal*, 835:231.

[132] Hwang, D.-Y. and Mebel, A. (2000). Ab initio study of the reaction mechanism of singlet and triplet N $_2$O and their intersystem crossing. *Chemical Physics*, 259:89–97.

[133] Ioppolo, S., Cuppen, H. M., Romanzin, C., van Dishoeck, E. F., and Linnartz, H. (2010). Water formation at low temperatures by surface o2 hydrogenation i: characterization of ice penetration. *Phys. Chem. Chem. Phys.*, 12:12065–12076.

[134] Ioppolo, S., McGuire, B. A., Allodi, M. A., and Blake, G. A. (2014). Thz and mid-ir spectroscopy of interstellar ice analogs: methyl and carboxylic acid groups. *Faraday discussions*, 168:461–84.

[135] Iturbide-Sanchez, F., Reising, S. C., and Padmanabhan, S. (2007). A miniaturized spectrometer radiometer based on mmic technology for tropospheric water vapor profiling. *IEEE Transactions on Geoscience and Remote Sensing*, 45(7):2181–2194.

[136] Jackson, B. D., de Korte, P. A. J., van der Kuur, J., Mauskopf, P. D., Beyer, J., Bruijn, M. P., Cros, A., Gao, J. R., Griffin, D., den Hartog, R., Kiviranta, M., de Lange, G., van Leeuwen, B. J., Macculi, C., Ravera, L., Trappe, N., van Weers, H., and Withington, S. (2012a). The spica-safari detector system: Tes detector arrays with frequency-division multiplexed squid readout. *IEEE Transactions on Terahertz Science and Technology*, 2(1):12–21.

[137] Jackson, B. D., de Korte, P. A. J., van der Kuur, J., Mauskopf, P. D., Beyer, J., Bruijn, M. P., Cros, A., Gao, J. R., Griffin, D., den Hartog, R., Kiviranta, M., de Lange, G., van Leeuwen, B. J., Macculi, C., Ravera, L., Trappe, N., van Weers, H., and Withington, S. (2012b). The spica-safari detector system: Tes detector arrays with frequency-division multiplexed squid readout. *IEEE Transactions on Terahertz Science and Technology*, 2(1):12–21.

[138] Jacobs, D. C., Kolasinski, K. W., Shane, S. F., and Zare, R. N. (1989). Rotational population and alignment distributions for inelastic scattering and trapping/desorption of no on pt(111). *The Journal of Chemical Physics*, 91(5):3182–3195.

[139] Jamieson, C. S., Bennett, C. J., Mebel, A. M., and Kaiser, R. I. (2005). Investigating the mechanism for the formation of nitrous oxide [n2o(x 1Îč+)] in extraterrestrial ices. *The Astrophysical Journal*, 624(1):436.

[140] Jansen, P., Bethlem, H., and Ubachs, W. (2014). Perspective: Tipping the scales: Search for drifting constants from molecular spectra. *The Journal of chemical physics*, 140:010901.

[141] Jarnot, R. F., Perun, V. S., and Schwartz, M. J. (2006). Radiometric and spectral performance and calibration of the ghz bands of eos mls. *IEEE Transactions on Geoscience and Remote Sensing*, 44(5):1131–1143.

[142] Jenniskens, P. and Blake, D. (1996). Crystallization of amorphous water ice in the solar system. *The Astrophysical Journal*, 473:1104.

[143] Johansson, J. F. (1995). A Comparison of Some Feed Types. In Emerson, D. T. and Payne, J. M., editors, *Multi-Feed Systems for Radio Telescopes*, volume 75 of *Astronomical Society of the Pacific Conference Series*, pages 82–89.

[144] Johansson, J. F. and Whyborn, N. D. (1992). The diagonal horn as a sub-millimeter wave antenna. *IEEE Transactions on Microwave Theory and Techniques*, 40(5):795–800.

[145] Johnson, J. B. (1928). Thermal agitation of electricity in conductors. *Phys. Rev.*, 32:97–109.

[146] Jørgensen, I., Bergmann, M., Davies, R., Barr, J., Takamiya, M., and Crampton, D. (2005). RX J0152.7-1357: Stellar Populations in an X-Ray Luminous Galaxy Cluster at z = 0.83. *Astronomical Journal*, 129:1249–1286.

[147] Kaisti, M., Altti, M., and Poutanen, T. (2014). Uncertainty of radiometer calibration loads and its impact on radiometric measurements. *IEEE Transactions on Microwave Theory and Techniques*, 62(10):2435–2446.

[148] Kalenskii, S. and Kurtz, S. (2016). Analytical methods for measuring the parameters of interstellar gas using methanol observations. *Astronomy Reports*, 60:702–717.

[Keating] Keating, T. http://www.terahertz.co.uk.

[150] Kennedy, G. and Kenyon, S. (2008). Planet formation around stars of various masses: The snow line and the frequency of giant planets. *The Astrophysical Journal*, 673:502–512.

[151] Kerr, A. R., Feldman, M. J., and Pan, S.-K. (1997). *Eighth International Symposium on Space Terahertz Technology*.

[152] Kerr, A. R., Feldman, M. J., and Pan, S.-K. (1997). Receiver Noise Temperature, the Quantum Noise Limit, and the Role of the Zero-Point Fluctuations. In *Eighth International Symposium on Space Terahertz Technology*, pages 101–111.

[153] Kerr, A. R., Feldman, M. J., and Pan, S.-K. (1997). Receiver noise temperature, the quantum noise limit, and the role of the zero-point fluctuations. In *Eighth International Symposium on Space Terahertz Technology*, page 101.

[154] Kerr, A. R., Pan, S., Claude, S. M. X., Dindo, P., Lichtenberger, A. W., Effland, J. E., and Lauria, E. F. (2014). Development of the alma band-3 and band-6 sideband-separating sis mixers. *IEEE Transactions on Terahertz Science and Technology*, 4(2):201–212.

[155] Kerr, A. R., Pan, S. K., and E., E. J. (2003). Sideband calibration of millimeter-wave receivers. Memo 357, ALMA, NRAO.

[156] Kerr, A. R., Pan, S.-K., and Effland, J. E. (2001). Alma memo 357 sideband calibration of millimeter-wave receivers.

[157] King, D. A. (1975). Thermal desorption from metal surfaces: A review. *Surface Science*, 47:384–402.

[158] Kiss, J., Lennon, D., Jo, S. K., and White, J. M. (1991). Photoinduced dissociation and desorption of nitrous oxide on a platinum(111) surface. *The Journal of Physical Chemistry*, 95(21):8054–8059.

[159] Klein, B., Hochgürtel, S., Krämer, I., Bell, A., Meyer, K., and Güsten, R. (2012). High-resolution wide-band fast Fourier transform spectrometers. *Astronomy and Astrophysics*, 542:L3.

[160] Klugmann, D., Rea, S., Moyna, B., Parow-Souchon, K., Henry, M., Wang, H., Oldfield, M., Brewster, N., Hunyor, P., Merritt, M., Green, R., Smith, D., Davis, B., Obeed, A., Phillips, M., Beardsley, M., Hampton, J., Ellison, B., Howe, C., Burton, G., Marshall, A., Thomas, B., Brandt, M., Philipp, M., Sonnabend, G., Stangier, T., Hammett, R., Decoopman, T., Kangas, V., D'Addio, S., and Piironen, P. (2017). Millimetre wave front end receivers for the mws and mwi instruments onboard metop-sg satellites. In *2017 42nd International Conference on Infrared, Millimeter, and Terahertz Waves (IRMMW-THz)*, pages 1–2.

[161] Koch, K., Hunger, B., Klepel, O., and Heuchel, M. (1997). A new method of analysing temperature-programmed desorption (tpd) profiles using an extended integral equation. *Journal of Catalysis*, 172(1):187 – 193.

[162] Kojima, T., Kroug, M., Uemizu, K., Niizeki, Y., Takahashi, H., and Uzawa, Y. (2017). Performance and characterization of a wide if sis-mixer-preamplifier module employing high-j c sis junctions. *IEEE Transactions on Terahertz Science and Technology*, 7(6):694–703.

[163] Kokalj, A., Kobal, I., and Matsushima, T. (2003). A dft study of the structures of n2o adsorbed on the pd(110) surface. *The Journal of Physical Chemistry B*, 107(12):2741–2747.

[164] Kong, S., Tan, J. C., Caselli, P., Fontani, F., and Goodson, M. D. (2016). The physics and chemistry of massive starless cores. In *American Astronomical Society Meeting Abstracts 227*, volume 227 of *American Astronomical Society Meeting Abstracts*, page 418.05.

[165] Konvalinka, J., Scholten, J., and Rasser, J. (1977). Analysis of second-order desorption kinetics in temperature-programmed desorption. *Journal of Catalysis*, 48(1):365 – 373.

[166] Kurth, D. G. and Bein, T. (1995). Optical effects in reflection-absorption ir spectroscopy of thin films of silane coupling agents on metallic surfaces. *Langmuir*, 11(2):578–584.

[167] Kurtz, D. S., Crowe, T. W., Hesier, J. L., and Porterfield, D. W. (2005). Frequency domain terahertz spectroscopy. *30th Int Conference on Infrared and Millimeter Waves*, 1:76–77.

[168] Lamberts, T., Cuppen, H. M., Ioppolo, S., and Linnartz, H. (2013). Water formation at low temperatures by surface o2 hydrogenation iii: Monte carlo simulation. *Phys. Chem. Chem. Phys.*, 15:8287–8302.

[169] Lee, Y.-S. (2009). *Principles of Terahertz Science and Technology*. Springer, New York.

[170] Leger, A., Jura, M., and Omont, A. (1985). Desorption from interstellar grains. *Astronomy and Astrophysics*, 144:147–160.

[171] Leupers, R., Bhattacharyya, S. S., and Deprettere, E. F. (2013). *Handbook of Signal Processing Systems*, volume 2. Springer Science.

[172] Lian, J. C., Kieseritzky, E., Gonchar, A., Sterrer, M., Rocker, J., Gao, H.-J., and Risse, T. (2010). N2o adsorption on the surface of mgo(001) thin films: An infrared and tpd study. *The Journal of Physical Chemistry C*, 114(7):3148–3151.

[173] Lide, D. (2007). *CRC Handbook of Chemistry and Physics*. CRC Press.

[174] Linnartz, H., Ioppolo, S., and Fedoseev, G. (2015). Atom addition reactions in interstellar ice analogues. *ArXiv e-prints*.

[175] Lisowski, E., Stobinski, L., and Dus, R. (1987). On the influence of the way of thin gold films preparation on the character of hydrogen adsorption. *Surface Science*, 188(3):L735 – L741.

[176] Maestrini, A., Thomas, B., Wang, H., Jung, C., Treuttel, J., Jin, Y., Chattopadhyay, G., Mehdi, I., and Beaudin, G. (2010). Schottky diode-based terahertz frequency multipliers and mixers. *Comptes Rendus Physique*, 11(7):480 – 495.

[177] Maiolino, R. (2008). Prospects for agn studies with alma. *New Astronomy Review*, 52:339–357.

[178] Marti, J. and Mauersberger, K. (1993). A survey and new measurements of ice vapor pressure at temperatures between 170 and 250k. *Geophysical Research Letters*, 20(5):363–366.

[179] Martín-Doménech, R., Munoz Caro, G. M., Bueno, J., and Goesmann, F. (2014). Thermal desorption of circumstellar and cometary ice analogs. *Astronomy and Astrophysics*, 564:A8.

[180] Maschwitz, G., Loehnert, U., Crewell, S., Rose, T., and Turner, D. D. (2013a). Investigation of ground-based microwave radiometer calibration techniques at 530 hpa. *Atmospheric Measurement Techniques*, 6(10):2641–2658.

[181] Maschwitz, G., Löhnert, U., Crewell, S., Rose, T., and Turner, D. D. (2013b). Investigation of ground-based microwave radiometer calibration techniques at 530 hpa. *Atmospheric Measurement Techniques*, 6(10):2641–2658.

[182] Mason, N. J., Dawes, A., Holtom, P. D., Mukerji, R. J., Davis, M. P., Sivaraman, B., Kaiser, R. I., Hoffmann, S. V., and Shaw, D. A. (2006). Vuv spectroscopy and photo-processing of astrochemical ices: an experimental study. *Faraday Discuss.*, 133:311–329.

[183] McCoustra, M. R. S. and Collings, M. P. (2013). Laboratory studies of desorption in model astrophysical ice systems. *AIP Conference Proceedings*, 1543(1):289–306.

[184] McCullough, P. (1992). The interstellar deuterium-to-hydrogen ratio - a reevaluation of lyman absorption-line measurements. *The Astrophysical Journal*, 390:213–218.

[185] McGrath, A. and Hewison, T. (2001). Measuring the accuracy of marssâĂŤan airborne microwave radiometer. *Journal of Atmospheric and Oceanic Technology*, 18(12):2003–2012.

[186] McGuire, B. A., Brogan, C. L., Hunter, T. R., Remijan, A. J., Blake, G. A., Burkhardt, A. M., Carroll, P. B., van Dishoeck, E. F., Garrod, R. T., Linnartz, H., Shingledecker, C. N., and Willis, E. R. (2018). First results of an alma band 10 spectral line survey of ngc 6334i: Detections of glycolaldehyde (hc(o)ch 2 oh) and a new compact bipolar outflow in hdo and cs. *The Astrophysical Journal Letters*, 863(2):L35.

[187] McKellar, A. (1940). Evidence for the Molecular Origin of Some Hitherto Unidentified Interstellar Lines. *Publications of the Astronomical Society of the Pacific*, 52:187.

[188] Medvedev, I. R., Neese, C. F., Plummer, G. M., and Lucia, F. C. D. (2010). Submillimeter spectroscopy for chemical analysis with absolute specificity. *Opt. Lett.*, 35(10):1533–1535.

[189] Mejia, C. F., de Barros, A. L. F., Bordalo, V., da Silveira, E. F., Boduch, P., Domaracka, A., and Rothard, H. (2013). Cosmic ray-ice interaction studied by radiolysis of 15 k methane ice with mev o, fe and zn ions. *Monthly Notices of the Royal Astronomical Society*, 433(3):2368–2379.

[190] Mendoza, E., Bronfman, L., Duronea, N. U., Lepine, J. R. D., Finger, R., Merello, M., Hervias-Caimapo, C., Gama, D. R. G., Reyes, N., and Ake-Nyman, L. (2018). G331.512-0.103: An interstellar laboratory for molecular synthesis. i. the ortho-to-para ratios for ch3oh and ch3cn. *ASTROPHYSICAL JOURNAL*, 853(2).

[191] Menten, K. M., Melnick, G. J., Phillips, T. G., and Neufeld, D. A. (1990). A new submillimeter water maser transition at 325 ghz. *The Astrophysical Journal Letters*, 363:L27–L31.

[192] Mezger, P. G. (1990). The interstellar radiation field and its interaction with the interstellar matter. In *The Galactic and Extragalactic Background Radiation*, volume 139 of *IAU Symposium*, pages 63–73.

[193] Mihalas, D., Auer, L. H., and Mihalas, B. R. (1978). Two-dimensional radiative transfer. i - planar geometry. *The Astrophysical Journal*, 220:1001–1023.

[194] Mihalas, D., Barnard, A. J., Cooper, J., and Smith, E. W. (1975). He i lambda 4922 profiles in b stars - calculations with an improved line broadening theory. *The Astrophysical Journal*, 197:139–142.

[195] Millar, T. (2005). Millar: Deuterium in interstellar space: Deuterium in interstellar clouds. *Astronomy and Geophysics*, 46(2):2.29–2.32.

[196] Mittleman, D., Jacobsen, R., Neelamani, R., Baraniuk, R., and Nuss, M. (1998). Gas sensing using terahertz time-domain spectroscopy. *Applied Physics B*, 67(3):379–390.

[197] Munoz Caro, G. M., Jiménez-Escobar, A., Martín-Gago, J. Á., Rogero, C., Atienza, C., Puertas, S., Sobrado, J. M., and Torres-Redondo, J. (2010). New results on thermal and photodesorption of CO ice using the novel InterStellar Astrochemistry Chamber (ISAC). *Astronomy and Astrophysics*, 522:A108.

[198] Murphy, J. A. and Padman, R. (1990). Phase centers of horn antennas using gaussian beam mode analysis. *IEEE Transactions on Antennas and Propagation*, 38(8):1306–1310.

[199] N. Wehres, B. Heyne, F. L. M. H. B. S. C. E. U. U. G. D. R. H. and Schlemmer, S. (2017). 100 ghz room-temperature laboratory emission spectrometer. In *IAU Symposium*, volume 332.

[200] Nishimura, S. Y., Gibbons, R. F., and Tro, N. J. (1998). Desorption kinetics of methanol from al2o3(0001) studied using temperature-programmed desorption and isothermal desorption. *The Journal of Physical Chemistry B*, 102(35):6831–6834.

[201] Noble, J. A., Congiu, E., Dulieu, F., and Fraser, H. J. (2012). Thermal desorption characteristics of CO, $O_2$ and $CO_2$ on non-porous water, crystalline water and silicate surfaces at submonolayer and multilayer coverages. *Monthly Notices of the RAS*, 421:768–779.

[202] Nystrom, O., Murtagh, D., and Belitsky, V. (2012). Phocus radiometer. *Atmospheric Measurement Techniques*, 5(6):1359–1373.

[203] Oberg, K. (2009). *Complex processes in simple ices : laboratory and observational studies of gas-grain interactions during star formation.* PhD thesis, Leiden University.

[204] Oberg, K. I. (2016). Photochemistry and astrochemistry: Photochemical pathways to interstellar complex organic molecules. *Chemical Reviews*, 116(17):9631–9663.

[205] Öberg, K. I., Bottinelli, S., Jørgensen, J. K., and van Dishoeck, E. F. (2010). A Cold Complex Chemistry Toward the Low-mass Protostar B1-b: Evidence for Complex Molecule Production in Ices. *The Astrophysical Journal*, 716:825–834.

[206] Öberg, K. I., Fuchs, G. W., Awad, Z., Fraser, H. J., Schlemmer, S., van Dishoeck, E. F., and Linnartz, H. (2007). Photodesorption of CO Ice. *The Astrophysical Journal Letters*, 662:L23–L26.

[207] Öberg, K. I., Garrod, R. T., van Dishoeck, E. F., and Linnartz, H. (2009a). Formation rates of complex organics in UV irradiated CH_3OH-rich ices. I. Experiments. *Astronomy and Astrophysics*, 504:891–913.

[208] Oberg, K. I., van Broekhuizen, F., Fraser, H. J., Bisschop, S. E., van Dishoeck, E. F., and Schlemmer, S. (2005). Competition between co and n2 desorption from interstellar ices. *The Astrophysical Journal Letters*, 621(1):L33.

[209] Öberg, K. I., van Dishoeck, E. F., and Linnartz, H. (2009b). Photodesorption of ices I: CO, $N_2$, and $CO_2$. *Astronomy and Astrophysics*, 496:281–293.

[210] Oort, J. H. and van de Hulst, H. C. (1946). Gas and smoke in interstellar space. *Bulletin of the Astronomical Institutes of the Netherlands*, 10:187.

[Origins-Space-Telescope] Origins-Space-Telescope. https://asd.gsfc.nasa.gov/firs/.

[212] Otoshi, T. Y. (1968). The effect of mismatched components on microwave noise-temperature calibrations. *IEEE Transactions on Microwave Theory and Techniques*, 16(9):675–686.

[213] Paine, S. N., Turner, D. D., and Kuchler, N. (2014). Understanding thermal drift in liquid nitrogen loads used for radiometric calibration in the field. *Journal of Atmospheric and Oceanic Technology*, 31(3):647–655.

[214] Parczewski, K. I. (1972). Thermal radiation heat transfer, robert siegel and john r. howell, mcgraw-hill book company, new york. 814 pages. $18.50. *AIChE Journal*, 18(2):463–463.

[215] Park, G. B. and Field, R. W. (2016). Perspective: The first ten years of broadband chirped pulse fourier transform microwave spectroscopy. *The Journal of Chemical Physics*, 144(20):200901.

[216] Parkes, S., Dunstan, M., Scott, P., Dillon, D., Spark, A., Ellison, B., and Auriacombe, O. (2018). A wideband spectrometer in the microsemi rtg4 fpga. In *Data Systems in Aerospace (DASIA)*.

[Parks] Parks, S. www.star-dundee.com.

[218] Pearson, J. C., Mehdi, I., Ward, J. S., Maiwald, F., Ferber, R., Leduc, H. G., Schlecht, E., Gill, J. J., Hatch, W., Kawamura, J. H., Stern, J. A., Gaier, T. C., Samoska, L., Weinreb, S., Bumble, B., Pukala, D., Javadi, H. H. S., Finamore, B., Lin, R. H., Dengler, R. J., Velebir, J. R., Luong, E. M.,

Tsang, R. S. W., Peralta, A., Wells, M., Chun, W., Zmuidzinas, J., Karpov, A. V., Phillips, T. G., Miller, D. L., Maestrini, A., Erickson, N., Swift, G., Liao, K. T., and Paquette, M. (2004). Thz instrumentation for the herschel space observatory's heterodyne instrument for far infrared.

[219] Pickett, H. M., Poynter, R. L., Cohen, E. A., Delitsky, M. L., Pearson, J. C., and Müller, H. S. P. (1998). Submillimeter, millimeter and microwave spectral line catalog. *Journal of Quantative Spectroscopy and Radiative Transfer*, 60:883–890.

[220] Pike, J., Calvert, T., and Maaskant, P. (2000). Reliability of THz Whisker Contacted Schottky Diodes. In *European Space Components Conference : ESCCON 2000*, volume 439, page 309.

[221] Planck, M. (1901). Ueber das Gesetz der Energieverteilung im Normalspectrum. *Annalen der Physik*, 309:553–563.

[222] Plíva, J. (1968). Molecular constants of nitrous oxide, $^{14}N\ _2{}^{16}O$. *Journal of Molecular Spectroscopy*, 27:461–488.

[223] Polanyi, M. and Wigner, E. (1925). Bildung und zerfall von molekülen. *Zeitschrift für Physik*, 33(1):429–434.

[224] Pozar, D. (2004). *Microwave Engineering*. Wiley.

[225] Prialnik, D., Benkhoff, J., and Podolak, M. (2004). *Modeling the structure and activity of comet nuclei*.

[226] Price, D. C. (2016). Spectrometers and Polyphase Filterbanks in Radio Astronomy. *ArXiv e-prints*.

[227] Qasim, D., Chuang, K.-J., Fedoseev, G., Ioppolo, S., Boogert, A. C. A., and Linnartz, H. (2018). Formation of interstellar methanol ice prior to the heavy CO freeze-out stage. *Astronomy and Astrophysics*, 612:A83.

[228] Qi, C., Öberg, K. I., Wilner, D. J., D'Alessio, P., Bergin, E., Andrews, S. M., Blake, G. A., Hogerheijde, M. R., and van Dishoeck, E. F. (2013). Imaging of the co snow line in a solar nebula analog. *Science*, 341(6146):630–632.

[229] Randa, J., Walker, D., Cox, A., and Billinger, R. (2005). Errors resulting from the reflectivity of calibration targets. *IEEE Transactions on Geoscience and Remote Sensing*, 43(1):50–58.

[230] Randall, K., Scarratt, M., Levasseur, M., Michaud, S., Xie, H., and Gosselin, M. (2012). First measurements of nitrous oxide in arctic sea ice. *Journal of Geophysical Research: Oceans*, 117(C9).

[231] Rea, S., Ellison, B., Swinyard, B., Valavanis, A., Han, Y., Linfield, E., Davies, A., Saunders, C., Parkes, S., Gerber, D., Henry, M., Wang, H., Alderman, B., Auriacombe, O., Rawlings, T., Crooke, M., and Bradshaw, T. (2015). The low-cost upper-atmosphere sounder (locus).

[232] Rea, S., Moyna, B., Parow-Souchon, K., Henry, M., Wang, H., Oldfield, M., Brewster, N., , P., Merritt, M., Green, R., Smith, D., Davis, B., Obeed, A., Klugmann, D., Phillips, M., , M., Hampton, J., Ellison, B., Howe, C., and Piironen, P. (2017). In *165-229 GHz Front End Receivers for the Microwave Sounder and Microwave Imager Instruments onboard MetOp-SG satellites Preliminary Design and Results*.

[233] Rea, S., Oldfield, M., Moyna, B., Gerber, D., Whale, M., and Murk, A. (2012). First-light atmospheric observations with a 340 ghz sideband-separating schottky diode receiver. *Infrared, Millimeter, and Terahertz Waves (IRMMW-THz)*.

[234] Rea, S. P., Alderman, B., Henry, M., Matheson, D. N., and Munro, Y. (2009). A 320-360 ghz subharmonically pumped image rejection mixer using planar schottky diodes. *IEEE Microwave and Wireless Components Letters*, pages 101–103.

[235] Reboussin, L., Wakelam, V., Guilloteau, S., and Hersant, F. (2014). Grain-surface reactions in molecular clouds: the effect of cosmic rays and quantum tunnelling. *Monthly Notices of the RAS*, 440:3557–3567.

[236] Richards, A. M. S., Impellizzeri, C. M. V., Humphreys, E. M., Vlahakis, C., Vlemmings, W., Baudry, A., De Beck, E., Decin, L., Etoka, S., Gray, M. D., Harper, G. M., Hunter, T. R., Kervella, P., Kerschbaum, F., McDonald, I., Melnick, G., Muller, S., Neufeld, D., O'Gorman, E., Parfenov, S. Y., Peck, A. B., Shinnaga, H., Sobolev, A. M., Testi, L., Uscanga, L., Wootten, A., Yates, J. A., and Zijlstra, A. (2014). Alma sub-mm maser and dust distribution of vy canis majoris. *Astronomy and Astrophysics*, 572:L9.

[237] Rigopoulou, D., Caldwell, M., Ellison, B., Pearson, C., Caux, E., Cooray, A., Gallego, J. D., Gerin, M., Goicoechea, J. R., Goldsmith, P., Kramer, C., Lis, D. C., Molinari, S., Ossenkopf-Okada, V., Savini, G., Tan, B. K., Tielens, A., Viti, S., Wiedner, M., and Yassin, G. (2016). The far infrared spectroscopic explorer (firspex): Probing the lifecycle of the ism in the universe. In *Space Telescopes and Instrumentation 2016: Optical, Infrared, and Millimeter Wave*, volume 9904 of *Proceedings of SPIE*.

[238] Roberts, H., Herbst, E., and Millar, T. J. (2004). The chemistry of multiply deuterated species in cold, dense interstellar cores. *Astronomy and Astrophysics*, 424:905–917.

[239] Rogalski, A. and Sizov, F. (2011). Terahertz detectors and focal plane arrays. *Opto-Electronics Review*, 19(3):346–404.

[240] Roueff, E. and Gerin, M. (2003). Deuterium in molecules of the interstellar medium. *Space Science Reviews*, 106(1):61–72.

[241] Rubiola, E. (2006). Tutorial on the double balanced mixer. *ArXiv Physics e-prints*.

[242] Rybicki, G. B. and Lightman, A. P. (1986). *Radiative Processes in Astrophysics*.

[243] Sack, N. J. and Baragiola, R. A. (1993). Sublimation of vapor-deposited water ice below 170 K, and its dependence on growth conditions. *Physical Review B*, 48:9973–9978.

[244] Sandford, S. and Allamandola, L. (1990). The volume- and surface-binding energies of ice systems containing co, co2, and h2o. *Icarus*, 87:188âĂŤ192.

[245] Sandford, S. A. and Allamandola, L. J. (1988). The condensation and vaporization behavior of H2O:CO ices and implications for interstellar grains and cometary activity. *ICARUS*, 76:201–224.

[246] Sandford, S. A. and Allamandola, L. J. (1993). Condensation and vaporization studies of CH3OH and NH3 ices: Major implications for astrochemistry. *The Astrophysical Journal*, 417:815–825.

[247] Saunders, R., Hewison, T., Atkinson, N., and Stringer, S. (1993). Radiometric characterisation of amsu-b. In Shiue, J., editor, *Microwave Instrumentation for Remote Sensing of the Earth*, volume 1935 of *Proceedings of the Society of Photo-optical Instrumentation Engineers (SPIE)*, pages 148–159.

[248] Saunders, R. W., Hewison, T. J., Stringer, S. J., and Atkinson, N. C. (1995). The radiometric characterization of amsu-b. *IEEE Transactions on Microwave Theory and Techniques*, 43(4):760–771.

[249] Savini, G., Brooks, D., Zhu, L., Ellison, B., Auriacombe, O., Bradshaw, T., Crook, M., Gerber, D., Henry, M., Rawlings, T., Wang, H., Charlton, J., Tun, S. M., Emes, M., Hunt, T., Winter, B., Linfield, E., Davies, G., Valavanis, A., Parkes, S., Walker, D., and Yu, G. (2016). Recent progress in the elegant breadboard supra-thz activities for locus and a view to an astronomy application. In *2016 IEEE 9th UK-Europe-China Workshop on Millimetre Waves and Terahertz Technologies (UCMMT)*, pages 1–5.

[250] Sawabe, K. and Matsumoto, Y. (1992). Structure of adsorbed n2o on a pt(111) surface and photodissociation at 193 nm: effective formation of oxygen adatoms. *Chemical Physics Letters*, 194(1):45 – 50.

[251] Sawabe, K. and Matsumoto, Y. (1993). Laser-induced photochemistry of nitrous oxide on a pt(111) surface. *Surface Science*, 283(1):126 – 131.

[252] Saxena, P. P. (2004). On the possibility of nitrous oxide ($n_2o$) as a cometary parent molecule in comet 1p/halley. *Bulletin of the Astronomical Society of India*, 32:185.

[253] Sceats, M. (1982). Sa rice in water, a comprehensive treatise, vol. 7.

[254] Schieder, R. and Kramer, C. (2001). Optimization of heterodyne observations using allan variance measurements. *Astron. Astrophys.*, 373:746–756.

[255] Schieder, R., Stutzki, J., and Winnewisser, G. (1997). Terahertz Spectroscopy at the University of Cologne. In *The Far Infrared and Submillimetre Universe.*, volume 401, page 425.

[256] Schlecht, E., Gill, J., Siegel, P. H., Oswald, J., and Mehdi, I. (2004). Novel designs for submillimeter subharmonic and fundamental schottky mixers.

[257] Schottky, W. (1942). Vereinfachte und erweiterte theorie der randschichtgleichrichter. *Zeitschrift für Physik*, 118(9):539–592.

[258] Sewiło, M., Indebetouw, R., Charnley, S., Zahorecz, S., Oliveira, J., van Loon, J., Ward, J., Chen, C.-H., Wiseman, J., Fukui, Y., Kawamura, A., Meixner, M., Onishi, T., and Schilke, P. (2018). The detection of hot cores and complex organic molecules in the large magellanic cloud. *The Astrophysical Journal Letters*, 853:L19.

[259] Sharma, A., Saurabh, and Biswas, S. (2014). A low power cmos voltage controlled oscillator in 65 nm technology. In *2014 International Conference on Computer Communication and Informatics*, pages 1–5.

[260] Shu, F., Najita, J., Ostriker, E., Wilkin, F., Ruden, S., and Lizano, S. (1994). Magnetocentrifugally driven flows from young stars and disks. 1: A generalized model. *The Astrophysical Journal*, 429.

[261] Shu, F. H., Adams, F. C., and Lizano, S. (1987). Star formation in molecular clouds - Observation and theory. *Annual Review of Astron and Astrophys*, 25:23–81.

[262] Shu, F. H. and Terebey, S. (1984). The formation of cool stars from cloud cores. In *Cool Stars, Stellar Systems, and the Sun*, volume 193 of *Lecture Notes in Physics, Berlin Springer Verlag*, page 78.

[263] Siebertz, O., SchmÃijlling, F., Gal, C., Schloeder, F., Hartogh, P., Natale, V., and Schieder, R. (2007). The wide-band spectrometer (wbs) for the hifi instrument of herschel. *Proceedings of the Eighteenth International Symposium on Space Terahertz Technology 2007, ISSTT 2007.*

[264] Siles, J. V., Grajal, J., and Krozer, V. (2006). Design of subharmonically pumped schottky mixers for submillimetre-wave applications. In *2006 European Microwave Integrated Circuits Conference*, pages 145–148.

[265] Simon M. Sze, K. K. N. (2006). *Physics of Semiconductor Devices.* Wiley.

[266] Sliter, R., Gish, M., and Vilesov, A. F. (2011). Fast nuclear spin conversion in water clusters and ices: A matrix isolation study. *The Journal of Physical Chemistry A*, 115(34):9682–9688.

[267] S.Maas (1993). *Microwave Mixers.* Artech House.

[268] Smith, R. S., Huang, C., Wong, E. K. L., and Kay, B. D. (1997a). The molecular volcano: Abrupt $ccl_4$ desorption driven by the crystallization of amorphous solid water. *Phys. Rev. Lett.*, 79:909–912.

[269] Smith, R. S., Huang, C., Wong, E. K. L., and Kay, B. D. (1997b). The molecular volcano: Abrupt $ccl_4$ desorption driven by the crystallization of amorphous solid water. *Phys. Rev. Lett.*, 79:909–912.

[270] Smith, R. S., Matthiesen, J., and Kay, B. D. (2014). Desorption kinetics of methanol, ethanol, and water from graphene. *The Journal of Physical Chemistry A*, 118(37):8242–8250.

[271] Snow, T. P. and McCall, B. J. (2006). Diffuse Atomic and Molecular Clouds. *Annual Review of Astron and Astrophys*, 44:367–414.

[272] Snyder, L. and Buhl, D. (1971). Observations of radio emission from interstellar hydrogen cyanide. *The Astrophysical Journal Letters*, 163:L47.

[273] Snyder, L. E., Kuan, Y.-J., Ziurys, L. M., and Hollis, J. M. (1993). New 3 millimeter observations of interstellar hno - reinstating a discredited identification. *The Astrophysical Journal Letters*, 403:L17–L20.

[274] Sobis, P. (2011). *Advanced Schottky diode receiver front-ends for terahertz applications*. PhD thesis, Thesis Doctoral, Chalmers University of Technology.

[275] Sobis, P., Bryllert, T., Olsen, A., Vukusic, J., Drakinskiy, V., Cherednichenko, S., Emrich, A., and Stake, J. (2009). Compact 340 ghz receiver front-ends.

[276] Song, H.-J. (2017). Packages for terahertz electronics. *Proceedings of the IEEE*, 105.

[277] Speedy, R. J., Debenedetti, P. G., Smith, R. S., Huang, C., and Kay, B. D. (1996). The evaporation rate, free energy, and entropy of amorphous water at 150 K. *Journal of Chemical Physics*, 105:240–244.

[278] Srivani, K. S., Girish, B. S., Shankar, N. U., and Subrahmanyan, R. (2014). A precision spectrometer for measuring signals from the epoch of cosmological recombination. In *2014 XXXIth URSI General Assembly and Scientific Symposium (URSI GASS)*, pages 1–4.

[279] Svoboda, V., Horka-Zelenkova, V., Rakovsky, J., Pracna, P., and Votava, O. (2015). Oh-stretch overtone of methanol: empirical assignment using a two temperature technique in a supersonic jet. *Phys. Chem. Chem. Phys.*, 17:15710–15717.

[280] Swinyard, B., Auriacombe, O., Bradshaw, T., Brooks, D., Charlton, J., Crook, M., Davies, G., Ellison, B., Emes, M., Friend, J., Gerber, D., Gray, C., Henry, M., Hunt, T., Linfield, E., Navarathinam, N., Parks, S., Rawlings, T., Rea, S., Saunders, C., Savini, G., Tun, S. M., Walker, D., Wang, H., and Winter, B. (2015a). In *The LOw Cost Upper atmosphere Sounder: the "Elegant Breadboard programme.*, UK Europe China Millimeter Waves and THz Technology Workshop.

[281] Swinyard, B., Auriacombe, O., Bradshaw, T., Brooks, D., Charlton, J., Crook, M., Davies, G., Ellison, B., Emes, M., Friend, J., Gerber, D., Gray, C., Henry, M., Hunt, T., Linfield, E., Navarathinam, N., Parks, S., Rawlings, T., Rea, S., Saunders, C., Savini, G., Tun, S. M., Walker, D., Wang, H., and Winter, B. (2015b). The low cost upper atmosphere sounder: The "elegant breadboard" programme. In *2015 8th UK, Europe, China Millimeter Waves and THz Technology Workshop (UCMMT)*, pages 1–4.

[282] Tanarro, I., Alemán, B., de Vicente, P., Gallego, J. D., Pardo, J. R., Santoro, G., Lauwaet, K., Tercero, F., Díaz-Pulido, A., Moreno, E., Agúndez, M., Goicoechea, J. R., Sobrado, J. M., López, J. A., Martínez, L., Doménech, J. L., Herrero, V. J., Hernández, J. M., Peláez, R. J., López-Pérez, J. A., Gómez-González, J., Alonso, J. L., Jiménez, E., Teyssier, D., Makasheva, K., Castellanos, M., Joblin, C., Martín-Gago, J. A., and Cernicharo, J. (2018). Using radio astronomical receivers for molecular spectroscopic characterization in astrochemical laboratory simulations: A proof of concept. *Astronomy and Astrophysics*, 609:A15.

[283] Tevar, N., Mehta, P., and Bhatt, K. (2016). A review paper on conical corrugated horn antenna. In *2016 International Conference on Wireless Communications, Signal Processing and Networking (WiSPNET)*, pages 889–892.

[284] Teyssier, D., Dartois, E., Deboffle, D., Crussaire, J.-P., Longval, Y., Boulanger, F., and Perault, M. (2004). A multi-path Far-infrared and Submm gas cell for spectral tests of Herschel/HIFI. In *Fifteenth International Symposium on Space Terahertz Technology*, page 306.

[285] Thomas, B., Gill, J., Maestrini, A., Lee, C., Lin, R., Sin, S., Peralta, A., and Mehdi, I. (2010a). An integrated 520-600 ghz sub-harmonic mixer and tripler combination based on gaas mmic membrane planar schottky diodes. In *35th International Conference on Infrared, Millimeter, and Terahertz Waves*, pages 1–2.

[286] Thomas, B., Maestrini, A., Gill, J. J., Lee, C., Lin, R. H.-J., Mehdi, I., and de. Maagt, P. (2010b). A broadband 835-900 ghz fundamental balanced mixer based on monolithic gaas membrane schottky diodes. *IEEE Transactions on Microwave Theory and Techniques*, 58:1917–1924.

[287] Thomas, B., Rea, S., Moyna, B., Alderman, B., and Matheson, D. (2009). A 320âĂŞ360 ghz subharmonically pumped image rejection mixer using planar schottky diodes. *IEEE Microwave and Wireless Components Letters*, 19(2):101–103.

[288] Thrower, J. D., Collings, M. P., Rutten, F. J. M., and McCoustra, M. R. S. (2009). Thermal desorption of c6h6 from surfaces of astrophysical relevance. *The Journal of Chemical Physics*, 131(24):244711.

[289] Tielens, A. G. G. M. and Hagen, W. (1982). Model calculations of the molecular composition of interstellar grain mantles. *Astronomy and Astrophysics*, 114:245–260.

[290] Tiuri, M. (1964). Radio astronomy receivers. *IEEE Transactions on Military Electronics*, MIL8(3-4):264–&.

[291] Toker, G., Sagi, R., Bar-Nachum, S., and Asscher, M. (2013). Highly efficient photoinduced desorption of n2o and co from porous silicon. *The Journal of Chemical Physics*, 138(4):044710.

[292] Tolls, V., Melnick, G. J., Ashby, M. L. N., Bergin, E. A., Gurwell, M. A., Kleiner, S. C., Patten, B. M., Plume, R., Stauffer, J. R., Wang, Z., Zhang, Y. F., Chin, G., Erickson, N. R., Snell, R. L., Goldsmith, P. F., Neufeld, D. A., Schieder, R., and Winnewisser, G. (2004). Submillimeter wave astronomy satellite performance on the ground and in orbit. *The Astrophysical Journal Supplement Series*, 152(1):137.

[293] Townes, C. and Schawlow, A. (2013). *Microwave Spectroscopy*. Dover books on physics. Dover Publications.

[294] Tsybulev, P. G., Dugin, M. V., Berlin, A. B., Nizhelskij, N. A., Kratov, D. V., and Udovitskiy, R. Y. (2014). 1/f-type noise in a total power radiometer. *Astrophysical Bulletin*, 69(2):240–246.

[295] Valavanis, A., Henry, M., Han, Y., Auriacombe, O., Dong, R., Rawlings, T., Li, L. H., Oldfield, M., Brewster, N., Davies, A. G., Ellison, B. N., and Linfield, E. H. (2016). Feedhorn-integrated thz qcl local oscillators for the locus atmospheric sounder. In *2016 41st International Conference on Infrared, Millimeter, and Terahertz waves (IRMMW-THz)*, pages 1–2.

[296] van der Merwe, M. (2002). *Harmonic mixer analysis and design*. PhD thesis, Stellenbosch University. Faculty of Engineering. Dept. of Electrical and Electronic Engineering.

[297] van der Ziel, A. (1970). *Noise : sources, characterization, measurement*. Englewood Cliffs, N.J. : Prentice-Hall.

[298] van Dishoeck, E. (2017). Astrochemistry: overview and challenges. *ArXiv e-prints*.

[299] van Dishoeck, E. F. (2014). Astrochemistry of dust, ice and gas: introduction and overview. *Faraday Discussions*, 168:9.

[300] van Dishoeck, E. F., Herbst, E., and Neufeld, D. A. (2013a). Interstellar water chemistry: From laboratory to observations. *Chemical Reviews*, 113(12):9043–9085.

[301] van Dishoeck, E. F., Herbst, E., and Neufeld, D. A. (2013b). Interstellar water chemistry: From laboratory to observations. *Chemical Reviews*, 113(12):9043–9085.

[302] van Vliet, K. and van der Ziel, A. (1977). The quantum correction of the einstein relation for high frequencies. *Solid-State Electronics*, 20(11):931 – 933.

[303] Vassilev, V., Henke, D., Lapkin, I., Nystrom, O., Monje, R., Pavolotsky, A., and Belitsky, V. (2008). Design and characterization of a 211âĂŞ275 ghz sideband separating mixer for the apex telescope. *IEEE Microwave and Wireless Components Letters*, 18(1):58–60.

[304] Vidali, G., Roser, J. E., Congiu, E., Li, L., Manicò, G., and Pirronello, V. (2006). Use of Laboratory Data to Model Interstellar Chemistry. In Weck, P. F., Kwong, V. H. S., and Salama, F., editors, *NASA LAW 2006*, page 77.

[305] Wakelam, V., Cuppen, H. M., and Herbst, E. (2013). Astrochemistry: Synthesis and Modelling.

[306] Watanabe, N. and Kouchi, A. (2002). Efficient formation of formaldehyde and methanol by the addition of hydrogen atoms to co in h2o-co ice at 10 k. *The Astrophysical Journal Letters*, 571(2):L173.

[307] Wehres, N., Maßen, J., Borisov, K., Schmidt, B., Lewen, F., Graf, U. U., Honingh, C. E., Higgins, D. R., and Schlemmer, S. (2018). A laboratory heterodyne emission spectrometer at submillimeter wavelengths. *Physical Chemistry Chemical Physics (Incorporating Faraday Transactions)*, 20:5530–5544.

[308] Weinreb, S. (1961). Digital radiometer. *Proc. IEEE*, 49:1099.

[309] Weinreb, S., Barrett, A. H., Meeks, M. L., and Henry, J. C. (1963). Radio Observations of OH in the Interstellar Medium. *Nature*, 200:829–831.

[310] Weissbrodt, E., Kallfass, I., Huelsmann, A., Tessmann, A., Leuther, A., Massler, H., and Ambacher, O. (2011). W-band radiometer system with switching front-end for multi-load calibration. In *2011 IEEE INTERNATIONAL GEOSCIENCE AND REMOTE SENSING SYMPOSIUM (IGARSS)*, IEEE International Symposium on Geoscience and Remote Sensing IGARSS, pages 3843–3846.

[311] Weissbrodt, E., Leuther, A., Schlechtweg, M., Kallfass, I., and Ambacher, O. (2012). In *Highly Integrated Switching Calibration Front-End MMIC with Active Loads for W-Band Radiometers*, European Microwave Integrated Circuits Conference - Proceedings, pages 203–206.

[312] Wengler, M. and Woody, D. (1987). Quantum noise in heterodyne detection. *IEEE Journal of Quantum Electronics*, 23(5):613–622.

[313] Werwein, V., Brunzendorf, J., Serdyukov, A., Werhahn, O., and Ebert, V. (2016). First measurements of nitrous oxide self-broadening and self-shift coefficients in the 0002-0000 band at 2.26Îijm using high resolution fourier transform spectroscopy. *Journal of Molecular Spectroscopy*, 323(C):28–42.

[314] W.F. Huebner, J. Benkhoff, M.-T. C. A. C. C. D. S. R. O. D. P. (2006). Heat and gas diffusion in comet nuclei. *The International Space Science Institute Report, ESA Publications*.

[315] Wiedner, M. C. (2002). Noise characterization and allan variances of water vapor monitors. Technical report, SMA memo 148.

[316] Wolff, A. J., Carlstedt, C., and Brown, W. A. (2007). Studies of binary layered ch3oh/h2o ices adsorbed on a graphite surface. *The Journal of Physical Chemistry C*, 111(16):5990–5999.

[Wolff] Wolff, I. Microwave mixers, second edition, by stephen a. maas, artech house, boston, london 1993. *International Journal of Microwave and Millimeter-Wave Computer-Aided Engineering*, 3(4):471–471.

[318] Wootten, A. (1987). Deuterated molecules in interstellar clouds. In Vardya, editor, *Astrochemistry*, volume 120 of *IAU Symposium*.

[319] Yoon, D. and Rieh, J. (2014). A 200 ghz heterodyne image receiver with an integrated vco in a sige bicmos technology. *IEEE Microwave and Wireless Components Letters*, 24(8):557–559.

[Zafar et al.] Zafar, E., Auriacombe, O., Rawlings, T., Brewster, N., Oldfield, M., Han, Y., Li, L., Linfield, E., Davies, A., Dean, P., Ellison, B., and Valavanis, A. Quantum cascade laser emission at 3.5 thz from dual diagonal feedhorns. In *UK Semiconductors 2018*.

[321] Zheng, W., Kim, Y. S., and Kaiser, R. I. (2011). Formation of nitric oxide and nitrous oxide in electron-irradiated h218o/n2 ice mixturesâĂŤevidence for the existence of free oxygen atoms in interstellar and solar system analog ices. *Phys. Chem. Chem. Phys.*, 13:15749–15754.

[322] Zhou, X.-L., White, J., and Koel, B. (1989). Chemisorption of atomic hydrogen on clean and cl-covered ag(111). *Surface Science*, 218(1):201 – 210.

[323] Ziurys, L. M., Apponi, A. J., Hollis, J. M., and Snyder, L. E. (1994). Detection of interstellar n2o: A new molecule containing an n-o bond. *The Astrophysical Journal Letters*, 436:L181–L184.

[324] Ziurys, L. M., McGonagle, D., Minh, Y., and Irvine, W. M. (1991). Nitric oxide in star-forming regions - further evidence for interstellar n-o bonds. *The Astrophysical Journal*, 373:535–542.

# Publications

1. Auriacombe, O., Fraser, H., Ellison, B., Ioppolo, S., and Rea, S. (2016). Terahertz desorption emission spectroscopy (thz des) - alma in the lab. In *American Astronomical Society Meeting Abstracts #228*, volume 228 of *American Astronomical Society Meeting Abstracts*, page 104.03

2. Auriacombe, O., Fraser, H., Ellison, B., and Rea, S. (2015). Desorption emission spectroscopy using thz radiometry (thz des). In *IET Colloquium on Millimetre-Wave and Terahertz Engineering Technology 2015*, pages 1–4

3. Ellison, B., Valavanis, A., Auriacombe, O., Rawlings, T., Oldfield, M., Han, Y., Linfield, E., Davies, A., and Saenz, E. (2018). 3.5-thz quantum-cascade laser emission from dual diagonal feedhorns. In *12th European Conference on Antennas and Propagation (EuCAP 2018)*, pages 248 (4 pp.)–248 (4 pp.)(1)

4. Han, Y., Partington, J., Chhantyal Pun, R., Henry, M., Auriacombe, O., Rawlings, T., Li, L., Keeley, J., Oldfield, M., Brewster, N., Rui, D., Dean, P., Davies, A., Ellison, B., Linfield, E., and Valavanis, A. (2018). Gas spectroscopy through multimode self-mixing in a double-metal terahertz quantum cascade laser. *Optics Letters*

5. Rea, S., Ellison, B., Swinyard, B., Valavanis, A., Han, Y., Linfield, E., Davies, A., Saunders, C., Parkes, S., Gerber, D., Henry, M., Wang, H., Alderman, B., Auriacombe, O., Rawlings, T., Crooke, M., and Bradshaw, T. (2015). The low-cost upper-atmosphere sounder (locus)

6. Savini, G., Brooks, D., Zhu, L., Ellison, B., Auriacombe, O., Bradshaw, T., Crook, M., Gerber, D., Henry, M., Rawlings, T., Wang, H., Charlton, J., Tun, S. M., Emes, M., Hunt, T., Winter, B., Linfield, E., Davies, G., Valavanis, A., Parkes, S., Walker, D., and Yu, G. (2016). Recent progress in the elegant breadboard supra-thz activities for locus and a view to an astronomy application. In *2016 IEEE 9th UK-Europe-China Workshop on Millimetre Waves and Terahertz Technologies (UCMMT)*, pages 1–5

7. Swinyard, B., Auriacombe, O., Bradshaw, T., Brooks, D., Charlton, J., Crook, M., Davies, G., Ellison, B., Emes, M., Friend, J., Gerber, D., Gray, C., Henry, M., Hunt, T., Linfield, E., Navarathinam, N., Parks, S., Rawlings, T., Rea, S., Saunders, C., Savini, G., Tun, S. M., Walker, D., Wang, H., and Winter, B. (2015b). The low cost upper atmosphere sounder: The "elegant breadboard" programme. In *2015 8th UK, Europe, China Millimeter Waves and THz Technology Workshop (UCMMT)*, pages 1–4

8. Valavanis, A., Henry, M., Han, Y., Auriacombe, O., Dong, R., Rawlings, T., Li, L. H., Oldfield, M., Brewster, N., Davies, A. G., Ellison, B. N., and Linfield, E. H. (2016). Feedhorn-integrated thz qcl local oscillators for the locus atmospheric sounder. In *2016 41st International Conference on Infrared, Millimeter, and Terahertz waves (IRMMW-THz)*, pages 1–2

9. Zafar, E., Auriacombe, O., Rawlings, T., Brewster, N., Oldfield, M., Han, Y., Li, L., Linfield, E., Davies, A., Dean, P., Ellison, B., and Valavanis, A. Quantum cascade laser emission at 3.5 thz from dual diagonal feedhorns. In *UK Semiconductors 2018*